# Remote Sensing of Boreal Forest Terrain: Sub-Pixel Scale Mixture Analysis of Land Cover and Biophysical Parameters at Forest Stand and Regional Scales

by

**Derek Roland Peddle**

A thesis
presented to the University of Waterloo
in fulfilment of the
thesis requirement for the degree of
Doctor of Philosophy
in
Geography

Waterloo, Ontario, Canada, 1997

The University of Waterloo requires the signatures of all persons using or photocopying this thesis. Please sign below, and give address and date.

## ABSTRACT

Increasing concentrations of atmospheric carbon dioxide and other greenhouse gases have focused attention on the global carbon cycle. Predicted climate change scenarios indicate the release of large stores of organic carbon in boreal forest regions could have profound ecological, cultural and economic impacts on agricultural, boreal and Arctic tundra zones. Remote sensing provides the only comprehensive information to monitor such large tracts of land, however, conventional NDVI vegetation index approaches have been shown to be unreliable for extracting required biophysical parameters such as biomass, leaf area index and productivity. In this research, spectral mixture analysis (SMA) and geometric-optical reflectance models provide sub-pixel scale forest information such as sunlit canopy, background and shadow fractions which yield improved biophysical estimates when compared to NDVI. This was validated first for individual forest stands using the NASA COVER data set from the Superior National Forest, Minnesota USA. Best results were obtained from shadow fraction using a spheroid based reflectance model with corrections for mutual shadowing and solar zenith angle variations. Following this, a regional scale methodology was implemented in the Boreal Ecosystem Atmosphere Study (BOREAS) which coupled canopy reflectance models, spectral mixture analysis, and a powerful evidential reasoning classifier into an integrated, physically based land cover and biophysical algorithm (the M⊕P software package). Field spectrometer data processed to end-member reflectance and stand level tree geometry were input to canopy optical models to produce spectral trajectories of reflectance and forest scene components over a full range of stand densities. These trajectories were input to the new M⊕P software to produce land cover and sub-pixel scale outputs for predicting biophysical parameters. Improved classification accuracies and biophysical estimates were obtained compared to conventional approaches, with a potential shown for estimating tree height and stem diameter.

## ACKNOWLEDGEMENTS

I express my sincere gratitude to Professor Ellsworth LeDrew, academic supervisor of this thesis research, for his support and guidance and for creating such diverse and valuable research opportunities. Thank you for exposing me to science from a true geographical perspective. I also thank my thesis committee members, Dr. LeDrew, Dr. Phil Howarth and Dr. Doug Dudycha of Geography, Dr. Ric Soulis of Civil Engineering, and the external examiner, Dr. Larry Band (University of Toronto), for their valuable insights and comments on this research which have helped strengthen and clarify the thesis.

I am very grateful to Dr. Forrest Hall, who was my research advisor during the summer of 1994 as part of a NASA Visiting Scientist Award through the Universities Space Research Association (USRA) Earth System Science Education Program at the Goddard Space Flight Center, Greenbelt Maryland USA. This opportunity provided excellent experience and training, and I greatly appreciate his dedication to education and research integrity as well as his support, initiative, and wisdom. I thank Dr. Michael Kalb, Director of the USRA-Goddard Visiting Scientist Program (GVSP), for his contributions to creating and maintaining that program, and Paula Webber, USRA-GVSP Administrator, for sorting out the extra arrangements involved with having a Canadian participate in the program. Dr. Hall provided the Superior National Forest (SNF) data set from the NASA COVER Project, and access to BOREAS data and resources specific to this research as P.I. of BOREAS Project TE-18. Thanks to Carla and Rock for their hospitality in College Park.

Dr. Alan Strahler and Dr. Xiaowen Li of the Center for Remote Sensing at Boston University kindly provided geometric-optical reflectance models to this research while I was at Goddard, and encouraged their use in subsequent BOREAS work. I thank Dr. Wolfgang Wanner of that Center for assistance with model specifications and for information about the software and algorithms which helped in my development of the GOMS interface and M⊕P programs.

I am grateful to Dr. John Miller (York University), the P.I. of BOREAS Project RSS-19 for which I am a member. His many and varied contributions to RSS-19 and his

encouragement of student participation are appreciated, as are valuable discussions about field methods.

I acknowledge with gratitude the support of several scholarships and fellowships during my doctoral program. These include: a Natural Sciences and Engineering Research Council of Canada (NSERC) Post-Graduate Scholarship, a NSERC-SSHRC-MRC Eco-Research Doctoral Fellowship, a NSERC-Forestry Canada Research Award (collaborating Research Scientist: Dr. Mike Apps, Canadian Forestry Service, Edmonton), a Sir James Lougheed Award of Distinction through the Alberta Heritage Scholarship Fund, an Atmospheric Environment Service Forest Climatology Scholarship, three Davis Memorial Scholarships in Ecology from the University of Waterloo, and University of Waterloo Graduate Scholarships and Teaching Assistantships. I also acknowledge funding from the Institute for Space and Terrestrial Science (ISTS), the Universities Space Research Association at the NASA Goddard Space Flight Center, and a Northern Sciences Training Program (NSTP) Fieldwork Grant. I thank Dr. Bob Sharpe and Dr. Al Hecht, Department of Geography, Wilfrid Laurier University, for the opportunity to gain valuable teaching experience as a sessional instructor during the final year of my doctoral program. Equipment purchased from a University of Lethbridge Faculty Start-up Grant and an Alberta Research Excellence Grant was essential to completing the latter stages of this research and producing the final thesis.

This research was also supported by funding to Dr. E.F. LeDrew through NSERC Research Grants, the Atmospheric Environment Service, and ISTS. Dr. LeDrew is co-investigator of BOREAS Project RSS-19, which is supported in part by the NSERC Collaborative Special Projects program.

This research is a contribution to the BOREAS project, within which I collectively acknowledge all individuals and agencies involved. A number of individuals made direct contributions of data or resources which were essential to completing the BOREAS analysis presented here. I am particularly grateful to David Knapp (NASA-GSFC: TE-18 / BOREAS Staff), who was most helpful in providing remote sensing imagery and sample data, as well as a variety of other pertinent information. I also thank Dr. Fred Huemmrich (NASA-GSFC: TE-18 / BOREAS Staff) for helpful discussions on BOREAS field

methods as well as insight into the SNF data set. Greg McDermid provided expert field assistance during the BOREAS FFC-T and IFC-3 field campaigns in 1994, and directions to Mr. Ribs in Thompson Manitoba. I thank Peter White (York University), Ray Soffer (ISL-York), and Greg McDermid for their contributions and assistance with processing the large volume of BOREAS field spectrometer data, and Roger De Abreu and Dr. Mike Morassutti for providing comparative ASD KGC lab calibration spectra at the University of Waterloo.

Additional BOREAS data were obtained from the following colleagues or science teams, to whom I express thanks: Dr. Richard Fournier (RSS-19, TE-23, P.I. Dr. Paul Rich, Kansas University); Dr. Mike Apps and Dr. Dave Halliwell (TE-13, Canadian Forestry Service, Edmonton); Dr. Janet Hardy (HYD-3, P.I. Dr. Bert Davis, CRREL, USA) in collaboration with members of Dr. Alan Strahler's group at Boston University, Dr. Curtis Woodcock and Dr. Wenge Ni; members of TE-06 (P.I. Dr. Tom Gower, University of Wisconsin-Madison); and members of RSS-8 / TE-21 (P.I. Dr. Steven Running, University of Montana).

I am grateful to Dr. Claude Duguay, Université Laval, for his valued support and collaboration on several projects in Colorado and elsewhere during my doctoral studies. I also thank Professor Steven Franklin for first mentioning Waterloo Geography to me while I was an undergraduate student, and for his motivation during those early years of my studies.

Thanks to Keith Storey, Professor of Geography at Memorial University of Newfoundland and Feildian's Soccer Full-back, who, while jogging around Quidi Vidi Lake during a late evening practice, told me of a new Undergraduate Joint Program in Computer Science and Geography - as a Computer Scientist I joined shortly thereafter and quickly discovered the world of Geography that lay outside the small, windowless rooms that I had become accustomed. I am very grateful for that initial opportunity, and to Drs. Franklin, Duguay, and LeDrew for keeping me interested and outdoors ever since !

Thanks to friends and colleagues at the University of Waterloo, and to the

Grasshopper's Soccer squad.

To my family, Pauline and Mahaliah - thank you. I love you. You have provided me the central motivation to pursue this degree, and your love and support have been instrumental in completing it. To my parents, Barbara and Roland Peddle, thank you for always encouraging me to pursue my interests and dreams. Your love, trust, and kindness have created a wonderful example to follow, now that I am a parent. Mahaliah is fortunate to have such special grandparents, just as I had. Special thanks to Michaeline and Brendan, Janice and Andy, and my parents, for your love, support and help, particularly during this past year when we gave birth to Mahaliah and moved west shortly thereafter. We could not have done this without your help and care. Thanks also to the 4-legged members of our family, Amber and George, who shared more than a few late thesis nights with me, and to Sammy, who didn't.

## DEDICATION

To Jeff Jessen,

whose character, bravery and courage saved my life shortly after I had started my doctorate.

## TABLE OF CONTENTS

## LIST OF TABLES

## LIST OF FIGURES

# CHAPTER I

# INTRODUCTION

## 1.1 INTRODUCTION

Remote sensing is a powerful tool in the environmental sciences which has profoundly changed the way we view planet Earth. With mounting concern over the state of the environment, the need for remote sensing has increased, as evidenced by the central role of remote sensing in a number of large, international global change projects. Fortunately, concurrent advances in airborne and satellite sensor systems and computing architectures have also evolved to provide data, algorithms and equipment appropriate to meeting these expectations.

In this thesis, remote sensing image processing methods are developed and applied within the context of a specific global change study. The cycling of carbon between the biosphere and atmosphere is a focal point of concern due to observed increases in atmospheric greenhouse gases such as carbon dioxide, and the resulting potential for global warming and change beyond the natural variability of the physical climate system. This is of particular importance in the vast boreal forest region, within which large amounts of carbon are stored. Remote sensing imagery is a key data source for carbon models which require forest land cover and biophysical information. Accordingly, the development of improved remote sensing methods for obtaining this information within the larger context of the biospheric-atmospheric cycling of carbon and global environmental change creates the fundamental construct for this thesis.

In this research, we address problems identified with conventional approaches to obtaining forest biophysical information from remotely sensed digital imagery. It will be shown that a variety of factors which affect pixel level spectral response in forested terrain, such as the forest understorey and background, tree shadows, canopy geometry, and tree density, all combine to make significant and sometimes dominant contributions to the overall signal received at a remote sensing platform. However, as shall be discussed, in current remote sensing methods for estimating forest biophysical information, such as vegetation indices (e.g. NDVI), these factors are ignored or not accounted for explicitly, thus leading to errors in the analysis that are well documented in the literature. Put simply, we need to obtain information on trees, but the trees are much smaller than the fundamental spatial unit of measure of a remote sensing device - the pixel. Therefore, the thrust of this research is to implement ways of separating individual components that exist at *sub-pixel spatial scales*, such as trees, shadows, understorey vegetation and soils, and use this different approach to obtain quantitative area measures of forest components for providing better information about important forestry attributes of interest over a variety of spatial scales. The basis for this work is the concept of spectral mixture analysis, in which the spectral properties of scene components are isolated, measured, and used to quantify scene fractions from digital remote sensing data. These scene component fractions are used together with physical descriptors of tree form and geometry to provide a more appropriate framework for providing estimates of forest structural and biophysical parameters.

The concept of improved forestry analysis through sub-pixel scale analysis of remotely sensed imagery is applicable at the spatial scales of satellite sensors and airborne systems, and is also appropriate for spatial resolutions planned for the future Earth

Observing System of NASA. Even for very high spatial resolution aerial sensors, these concepts apply since shadowing and background effects are important at spatial scales that encompass partial canopies of individual trees. These concepts are also applicable in other research problems and environments, as discussed briefly near the end of the thesis.

## 1.2 RESEARCH CONTEXT

The central research context for this thesis work is set within the Boreal Ecosystem Atmosphere Study (BOREAS), a large, international global change research project with the broad objective being to clarify the role of the boreal forest in global change, as described in greater detail in Chapter II. The author is a member of BOREAS Remote Sensing Science project #19 (RSS-19), and is also a collaborating scientist with BOREAS Terrestrial Ecology project #18 (TE-18). The title of project RSS-19 is "Variation in Radiometric Properties of the Boreal Forest Landscape as a Function of Ecosystem Dynamics". The Principal Investigator (P.I.) of RSS-19 is Dr. John Miller, York University, Ontario, with University of Waterloo involvement through RSS-19 co-investigator Dr. Ellsworth LeDrew, the academic supervisor of this thesis research. The title of project TE-18 is "Regional Scale Carbon Flux from Modeling and Remote Sensing" and the P.I. is Dr. Forrest Hall, NASA Goddard Space Flight Center (GSFC), Greenbelt, Maryland USA. Collaboration with project TE-18 commenced in 1994 while the author held a Visiting Scientist post at GSFC through the NASA-Universities Space Research Association Visiting Scientist Program, for which Dr. Hall was the research advisor. As the main field and remotely sensed data collection efforts in BOREAS occurred that year, suitable data were not available while the author was at Goddard. Instead, an established remote sensing and field data set collected at the Superior National Forest (SNF) in

Minnesota USA as part of the NASA COVER project (Characterization of Vegetation with Remote Sensing, see Hall *et al.*, 1992) was made available to this research. Accordingly, in this thesis the research problems identified in the previous section are addressed in two forested environments, namely the southern limit of the boreal forest in Minnesota as part of the NASA COVER project, and the northern boreal forest in Canada as part of BOREAS. Further, two spatial scales are addressed. The Minnesota work was performed first and addressed the forest stand level as a means to test the spectral mixture analysis approach (Chapter IV). Successes in that project led to expanded objectives in BOREAS which considered the regional scale and a variety of terrain and forest land cover types (Chapters V and VI). In addition to membership in RSS-19, this research has gained considerable benefit from collaboration with Dr. Hall and members of TE-18 as a result of common research interests held by investigators involved. Therefore, as appropriate, the contributions from this research are also explained within that context in Chapters IV and V for the NASA COVER and BOREAS projects, respectively.

A number of reasons support the rationale for considering two projects and study areas in this research. Firstly, this provided an opportunity to test and refine new methods and modelling approaches in SNF prior to the larger BOREAS analysis. The earlier SNF analysis also helped define strategies and priorities for BOREAS field work. Secondly, it was advantageous to be able to test the sub-pixel scale methods implemented in this research using data acquired at different scales and from airborne and satellite platforms in the SNF and BOREAS projects, respectively. Thirdly, it was very useful to be able to perform a full analysis of the NASA COVER data set at a time when the extensive 1994 BOREAS data set was not yet available for release to BOREAS scientists. Finally, it was deemed acceptable, and indeed desirable, to test the remote sensing methodologies

implemented in this research in more than one forested environment, as one of the longer term goals of this line of research is to apply these methods to larger and more diverse regions in the boreal forest of North America, as well as to other forested settings elsewhere. The specific research objectives pursued in this thesis as part of these projects are described next.

## 1.3 THESIS RESEARCH OBJECTIVES

The main research objective of this thesis is to:

- Provide improved methods for estimating boreal forest biophysical variables from digital remotely sensed imagery over different spatial scales.

Towards this goal, a number of secondary objectives have been identified:

- Identify and document problems with existing techniques and pose an alternative framework for quantifying forest scene component fractions at sub-pixel scales using spectral mixture analysis.

- Test this approach in a controlled experiment at the scale of individual forest stands. Assess the importance of accounting for sun-sensor position in the analysis using different canopy reflectance models and provide a method for

scene fraction validation. Compare biophysical results with those obtained using more traditional vegetation index approaches.

- Following the analysis of individual forest stands, expand the approach to implement a new software system for estimating biophysical variables at regional scales. Investigate both the importance of integrating land cover stratification directly into this method, and the advantages of providing a physical basis to the analysis. Assess the impact of classification error on the biophysical analysis and compare results to those obtained from a vegetation index.

## 1.4 ORGANISATION OF THE THESIS

This thesis has been organised into seven Chapters. In this Chapter, an introduction to the thesis has been provided, as well as a statement of the research context and objectives for this work.

In Chapter II, a review of the relevant literature is provided. First, the broader research context of global change and the carbon cycle is developed and reviewed, with a focus on the boreal forest as a key component in this cycle. The role of remote sensing in global change studies is then introduced, together with the Boreal Ecosystem Atmosphere Study, a global change project which involves substantial remote sensing of boreal forest terrain and which forms the context for a large part of the analysis presented in this thesis. Following this, forest biophysical remote sensing issues are presented. The fundamentals

of optical remote sensing of vegetation are addressed together with factors affecting the reflectance of forest canopies. A critical review of current remote sensing techniques for estimating biophysical variables is provided as a means to identify the problems this thesis will address.

In Chapter III, spectral mixture analysis is introduced as a suitable methodology for overcoming several important problems identified with current approaches to estimating forest biophysical variables from remotely sensed data. The ability to obtain information at sub-pixel scales is described and related to the forested environment. Background information and the theory of spectral mixing models are provided.

Chapter IV is the first of two analysis sections presented in the thesis. The first analysis is designed to test spectral mixture analysis for estimating forest biophysical parameters at the scale of individual forest stands using a data set from the Superior National Forest, Minnesota USA. New corrections for solar zenith angle variation, sophisticated geometric optical reflectance models, as well as new methods for scene fraction validation are implemented and shown to be important for improving both the accuracy of spectral mixture analysis results and the relationship of component fractions with forest biophysical variables.

In Chapter V, a regional scale methodology is presented for the Boreal Ecosystem Atmosphere Study (BOREAS). The methodology builds on successful results obtained from the analysis of individual forest stands presented in Chapter IV, and is set within a new framework for estimating biophysical parameters at regional scales. Analytical issues that arise when considering the regional scale are first identified. Then, the study area, field

techniques, and field data analysis methods are presented. These are followed by descriptions of optical modelling methods and the implementation of a new software package that provides a physically based approach for unifying land cover classification and biophysical parameter estimation.

In Chapter VI, the results of the BOREAS land cover classification and biophysical parameter analysis are presented for the southern study area using data from the 1994 late summer intensive field campaign. Land cover results using a more traditional training mode approach to classification are compared to results obtained from the new physically based software implemented in Chapter V. Using sub-pixel scale mixture fraction outputs from the new software, equations for biophysical parameters are derived and used to produce estimates which are compared to both ground data and vegetation index approaches.

In Chapter VII, a summary of the thesis is presented, conclusions are drawn, and areas for future research are identified.

Near the end of the thesis, several appendices and a glossary of terms are provided.

# CHAPTER II

# A REVIEW OF REMOTE SENSING OF VEGETATION AND FOREST BIOPHYSICAL VARIABLES

## 2.1 INTRODUCTION

This Chapter contains a review of literature dealing with the remote sensing of forest biophysical variables. It begins with a discussion of the much broader research context, that of global change and carbon cycling in the boreal forest, from which the forest biophysical variables of interest are defined. The review then moves on to the focus of this thesis, which deals with the remote sensing of these variables. It begins by considering some of the fundamentals of optical remote sensing of vegetation as well as the properties of vegetation that affect their spectral response. This is followed by a detailed treatment of forest canopies and the set of factors that together contribute to the integrated pixel level reflectance signal received by a remote sensing instrument on an airborne or satellite platform. The intention of the review is to present the issues involved in estimating complex biophysical variables of forest canopies, beyond the more common use of remote sensing data for applications such as land cover classification. The Chapter concludes with a review of several different approaches which have been used to estimate these biophysical variables. In considering these approaches, a number of the factors that affect forest canopy reflectance (as reviewed in the fourth section of this Chapter) are identified as being inadequately addressed by current methods, thereby limiting their usefulness for estimating biophysical variables. The identification of problems with current techniques forms the motivation for research methodologies presented later in the thesis.

## 2.2 THE CARBON CYCLE AND GLOBAL CHANGE

### 2.2.1 The Global Carbon Cycle

Carbon is the key element of life (Bolin *et al.*, 1979). It is found in all organic matter in varying levels and with multiple functions, and in its purest form is diamond. For humans, approximately 10% of our bodies are comprised of carbon, with carbon dioxide being an essential component of our life-sustaining respiratory and circulatory systems (Farish, 1986). From this first perspective, we as humans already have a vested interest in carbon, and its exchange in nature. However, the role of carbon extends well beyond basic human biological functioning. It also plays a significant role in our physical climate system through linkages to the atmosphere, lithosphere and hydrosphere - the key components of the biosphere in which all life is contained.

For example, a striking correlation between climatic variations over the past 160,000 years and the atmospheric concentration of carbon dioxide ($CO_2$) and methane ($CH_4$) has been inferred and documented by Chappellaz *et al.* (1990) based on analysis of Antarctic ice cores (Figure 2.1). Although the major climatic changes were likely initiated by oscillations in the Earth's orbit and possibly other factors, the important point is that concentrations of these gases varied as the land and ocean adapted to these changes - the long-term responses and feedbacks between atmospheric carbon concentration and the physical climate system are evident. The global carbon cycle links these major components and drives these responses.

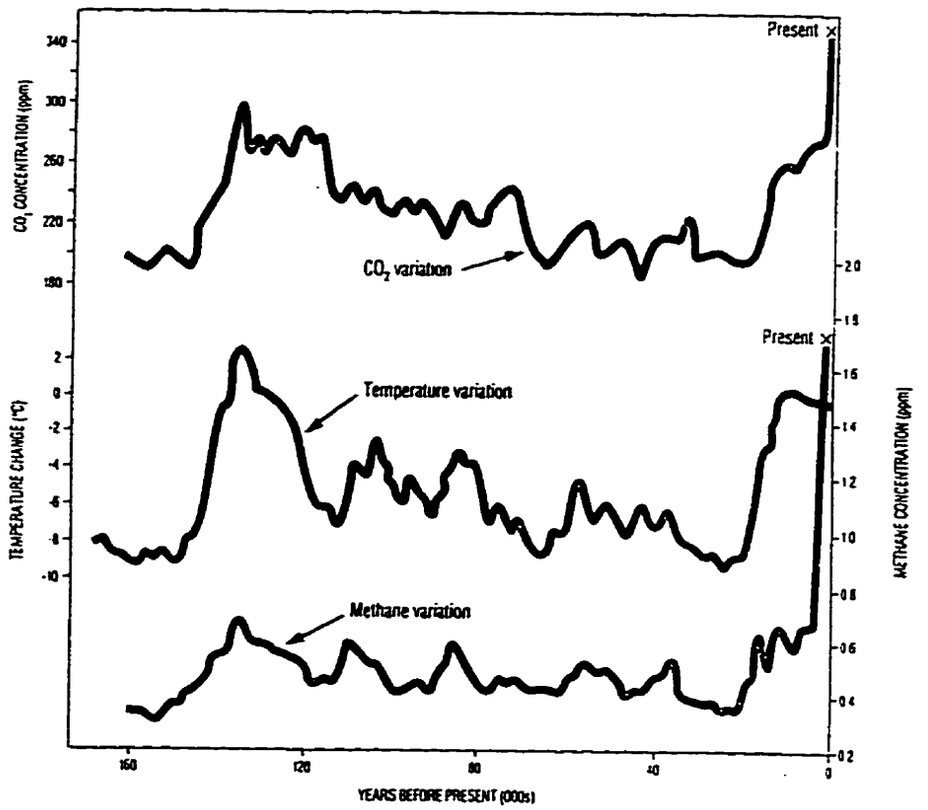


Figure 2.1. Variation in temperature over Antarctica and of global atmospheric carbon dioxide and methane for the last 160,000 years (modified from Chappellaz *et al.* 1990).

This global cycle is one of the many unique features of our terrestrial environment - with the element carbon being continuously and sometimes rapidly exchanged among a number of global reservoirs. The atmosphere serves as the principle point of transfer for carbon, which is exchanged among: (i) the biosphere, through the processes of

photosynthesis and decay, (ii) the oceans, by gaseous exchange, and (iii) the Earth's crust, by weathering and volcanic emission. Of the three, the oceans cover the largest area, and have the greatest volume of carbon exchange (Bolin, 1981), however, this does not imply a hierarchy of importance since all three reservoirs are vital links in the carbon cycle. The global carbon cycle has been in a natural balance for thousands of years, with the distribution of carbon varying among these major reservoirs with changes in climate, as seen in Figure 2.1. This cycle is complex and we do not as yet understand how all of its components interact nor have we been able to definitively quantify or balance even the major components. For example, current understanding suggests the existence of a large but as yet unknown or missing sink of carbon.

However, what is known is that humans as a species have been inadvertently modifying the climate system for some time, and thus affecting the global carbon cycle. Perhaps the earliest observation linking human activities to climatic impacts can be traced to the Swedish chemist, Svante August Arrhenius, who, in 1896, reported the notion that increased fossil fuel usage associated with the industrial revolution was creating increased concentrations of 'carbonic acid' (carbon dioxide) in the atmosphere, and that this could cause the global mean temperature to rise with unknown but significant consequences (Arrhenius, 1896). This followed earlier work by Tyndall (1861), who attempted to measure the absorption of long-wave radiation by atmospheric gases, which had previously been linked to changes in ground temperature by Fourier in 1827 (Mitchell, 1989).

What Arrhenius and others had observed was a potential change in what was later to be known as the 'Greenhouse Effect'. This is the effect caused by certain atmospheric gases which absorb and reradiate long-wave radiation emitted from the Earth's surface,

thus creating warmer temperatures near the surface and resulting in our planet being suitable for human habitation (Mitchell, 1989). The principal greenhouse gases, several of which contain carbon (C), are water vapour, carbon dioxide ($CO_2$), methane ($CH_4$), nitrous oxide ($N_2O$), and, in recent years, chlorofluorocarbons (CFCs). Increases in these atmospheric gases from anthropogenic sources are causing an enhanced Greenhouse Effect, in which additional warming is being induced - a process often referred to as 'Global Warming'.

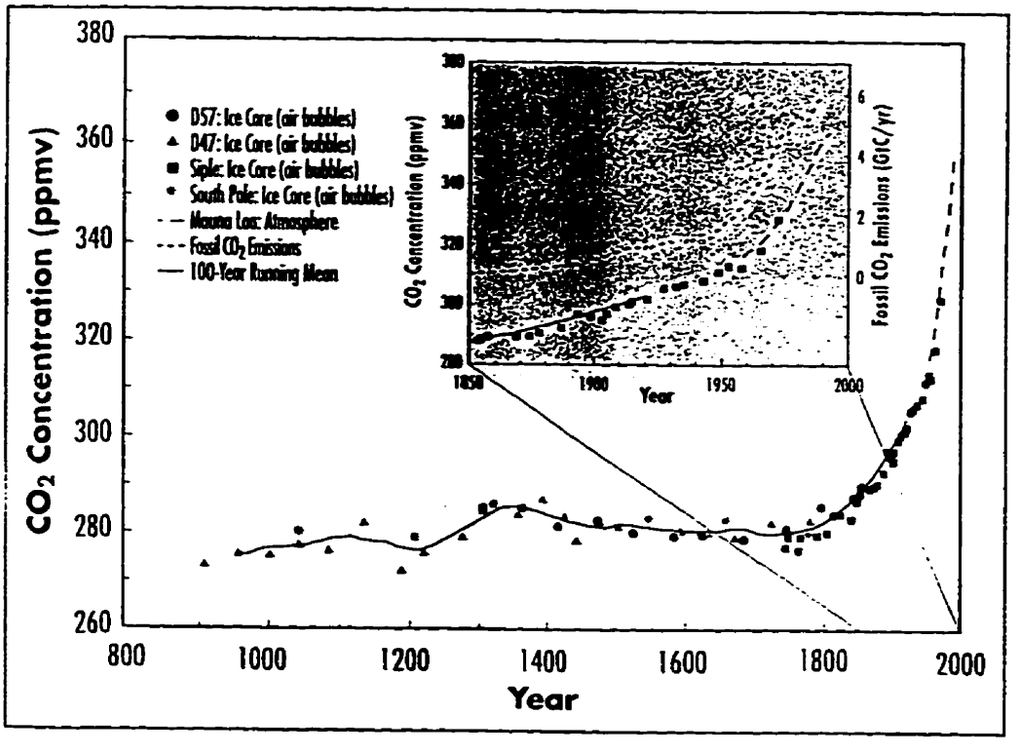


Figure 2.2. Long term atmospheric $CO_2$ concentration (modified from IPCC, 1995).

A look to the far right hand side of Figure 2.1 illustrates these recent changes that were first realised in the late 19th century. Closer observation of the last 200 years (as shown in Figure 2.2) reveals a steady increase in modelled atmospheric $CO_2$ concentrations which are in close agreement with observations made at the Mauna Loa Observatory in Hawaii during the period 1958 - 1978 (Keeling, 1983), shown in Figure 2.3. Although it is difficult to be certain, the increases in the past 200 years may be leading to climatic change, that is, outside the natural variability of the system as depicted over the last 160,000 years. However, due to these uncertainties, the time scales of relevant observation are decreasing; periods of several decades instead of centuries are now very much of interest. Given the observations of the past two centuries, the longer these trends continue (which can be observed over relatively short time periods), the more concerned we become.

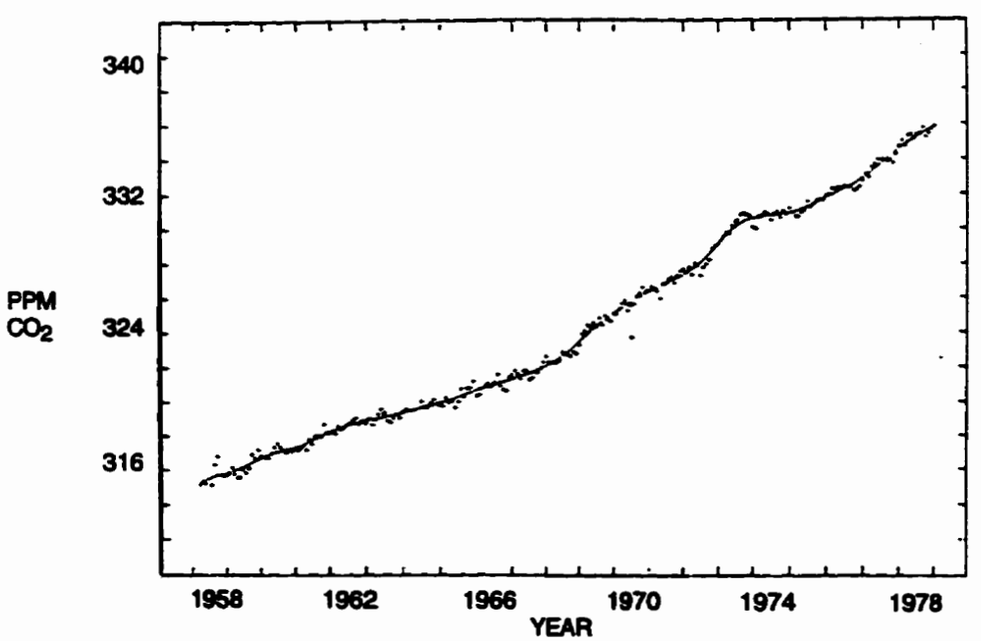


Figure 2.3. Observed increases in atmospheric $CO_2$ concentration at Mauna Loa Observatory, 1958 to 1978 (modified from Keeling, 1983).

This trend over the past 200 years coincides with the period of the industrial revolution and also when a sharp increase in world population began. Since then, the opportunity and capacity for humans to increase the concentrations of atmospheric $CO_2$ has further increased through the burning of fossil fuels and by other activities such as large scale deforestation. It now seems clear that humans are having a significant impact on the Earth's physical climate system and the global carbon cycle.

### 2.2.2 Carbon Cycling in the Boreal Forest

The second largest reservoir of carbon associated with the Earth system is found in the terrestrial biosphere, which, according to Mitchell (1989), contains a total of 1500 Gigatons of carbon (1 Gt = $10^9$ metric tons). Forests cover about 42% of the Earth's land surface yet they contain 86% of the 562 Gt of above-ground carbon, while 73% of the carbon in the world's soil is located in forested regions (Sedjo and Solomon, 1988). Forests directly affect climate at the global scale by modifying the Earth's hydrological regimes, albedo, and atmospheric $CO_2$ (trees sequester $CO_2$ to grow), while at larger scales, forests alter factors such as humidity, temperature and solar radiation (LeDrew, 1986; Graham *et al.*, 1990). In particular, forests and activities in the forest sector play an integral role in short term (<100 years) dynamics of the global carbon cycle (Kurz *et al.*, 1992; Apps *et al.*, 1995). Through photosynthesis, trees remove $CO_2$ from the atmosphere and retain some of this carbon for several decades or more. Carbon is released back to the atmosphere through disturbances, fire, harvesting, and the decomposition of organic matter after tree mortality. This cycling of carbon and, in particular, changes in the main components of that cycle, can have profound affects with the physical climate system. For example, results from a number of climate models suggest the greatest increases in

temperature from increasing $CO_2$ will occur at high northern latitudes (45-65°N), ranging from 6 to 12°C in winter and 2-6°C in summer (Bonan *et al.*, 1990; Pastor and Post, 1988; Kauppi and Posch, 1985), with the most marked effects in continental interiors where much of the boreal forest is located (Mitchell, 1989), see Figure 2.4.

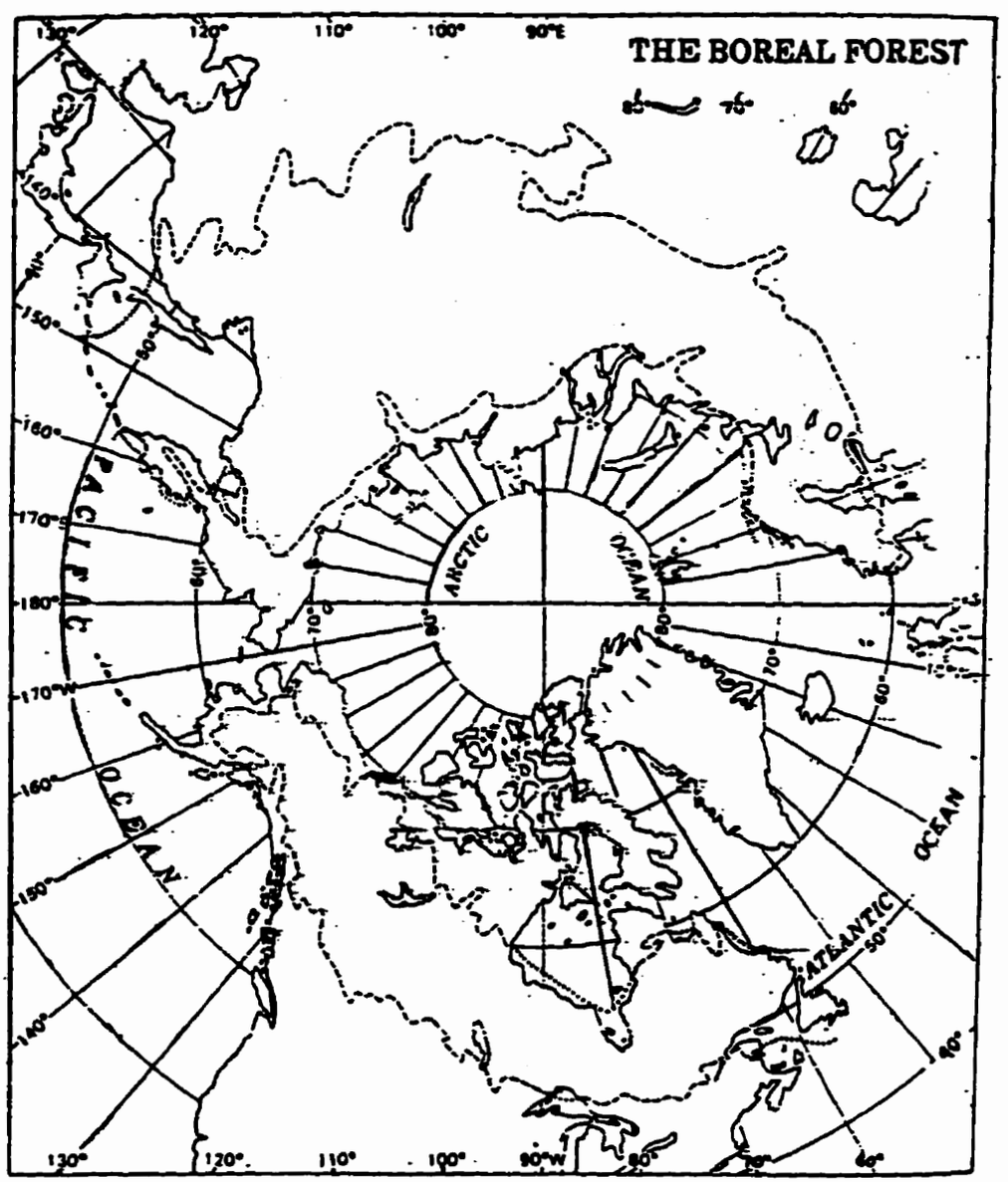


Figure 2.4. The northern hemisphere boreal forest in polar projection (modified from Hare and Ritchie, 1972)

As a result of these effects on the physical climate system, the northern boreal forest is thought to play a particularly large role in the global carbon cycle (Bonan, 1991a,b). In a study of global carbon sources and sinks, Tans *et al.* (1990) found that a large terrestrial sink for fossil fuel carbon currently exists in the mid-latitudes of the northern hemisphere, and that boreal forest areas may account for part of the missing sink of carbon, while D'Arrigo *et al.* (1987) reported that large scale changes in the growth of boreal forests may already be contributing to the observed increasing trend of $CO_2$ amplitude. It is further hypothesised that these changes will cause a northward migration of the boreal forest on the order of 2.5 km/year (Gates, 1990), with some forest scientists suggesting that global warming will outpace the northward migration of these forests (Harrington, 1987; Pollard, 1989; Hendrickson, 1990). Although from a strict atmospheric viewpoint, suitable climatic regimes may become available at increasingly northern locations, other factors such as unfavourable soil conditions and melting permafrost may complicate such a transition, resulting in an overall reduction in timber volume in the boreal forest. This has major implications for the net carbon regime of the boreal forest, since under a warming climate, the southern boreal regions will release much of its stored carbon as trees die or are cleared to give way to agricultural zones, which would also be advancing northward. Therefore, the boreal forest biome could become a net source of carbon from its current state of carbon retention, with a distinct potential for profound long-term cultural, economic and ecological impacts on agricultural zones, the boreal forest, and Arctic tundra ecosystems (Apps *et al.*, 1993).

Clearly, the boreal forest is a focal point of concern regarding future climate scenarios and the carbon cycle. As a result, it is important to be able to understand and monitor the carbon cycle in the boreal forest. In Canada, the boreal forest covers 29% of

the total land mass and represents one of the world's significant carbon storage areas, with approximately 35 billion tonnes of carbon stored in this forest (Government of Canada, 1991). A tract of land of this size is too large and inaccessible to study by traditional field methods. Remote sensing provides suitable sources of data to address a variety of global change issues and over a large range of scales. In the next section, the role of remote sensing in global change studies is outlined, and followed by an introduction to the scope and objectives of the BOREAS project within which some of this thesis research has been carried out.

### 2.2.3 The Role of Remote Sensing

Remote sensing imagery provides the only source of digital, spatially comprehensive, consistent, multiscale information necessary for studying a variety of environmental change issues (Asrar, 1990). The importance of remote sensing to studies of global change can further be realised by the significant role it plays in a number of large, international and interdisciplinary global change research programs (CGCP, 1989; IGBP, 1990; LTER, 1991; NBIOME, 1993; Apps, 1993; USGCRP, 1994; LeDrew *et al.*, 1995a; [acronyms defined in glossary]), and in particular, the co-ordinating research program now underway by NASA entitled 'Mission to Planet Earth' which contributes to a variety of research programs and large scale projects (NASA, 1988; Asrar and Dozier, 1994).

One of these projects is the Boreal Ecosystem-Atmosphere Study (BOREAS), which is a major interdisciplinary research effort involving over 500 scientists divided into approximately 80 groups (Sellers *et al.*, 1995). The project is focused on two study sites located in Saskatchewan and Manitoba near the southern and northern boundaries of the

boreal forest zone, respectively (Figure 2.5). BOREAS includes a large diversity of individuals and scientific focii, which have been divided into six main categories: (i) airborne flux and meteorology (AFM), (ii) remote sensing science (RSS), (iii) terrestrial ecology (TE), (iv) tower fluxes (TF), (v) trace gas biogeochemistry (TGB), and (vi) snow and hydrology (HYD). The goal of BOREAS is to "improve our understanding of the interactions between the boreal forest biome and the atmosphere in order to clarify their roles in global change" (BOREAS, 1994), with three major scientific issues at stake, as follows:

1. Sensitivity of the boreal forest to changes in the physical climate system

2. The carbon cycle and biogeochemistry in the boreal forest, and

3. Biophysical feedbacks on the physical climate system.

Within the context of the above scientific issues, two main objectives have been identified (BOREAS, 1994):

(i) improve the process models which describe the exchanges of energy, water, heat, and carbon between the boreal forest and the atmosphere, and

(ii) develop and test remote sensing methods for providing key forestry information over a variety of scales, and specifically, to develop and evaluate remote sensing algorithms that relate spectral, spatial and temporal patterns of surface spectral response to the required biophysical parameters of interest.

These major scientific issues and objectives address the broad global change issues discussed earlier in this section. In terms of the present thesis, the scope of this research would be categorised as falling within the second BOREAS objective to develop remote sensing algorithms for deriving biophysical information over a variety of scales. Consistent with this emphasis, the main part of this review which follows is focused on issues in remote sensing of forest biophysical variables. In the next section, these variables are defined and following that, issues involved with using remote sensing to obtain estimates of these variables are presented.

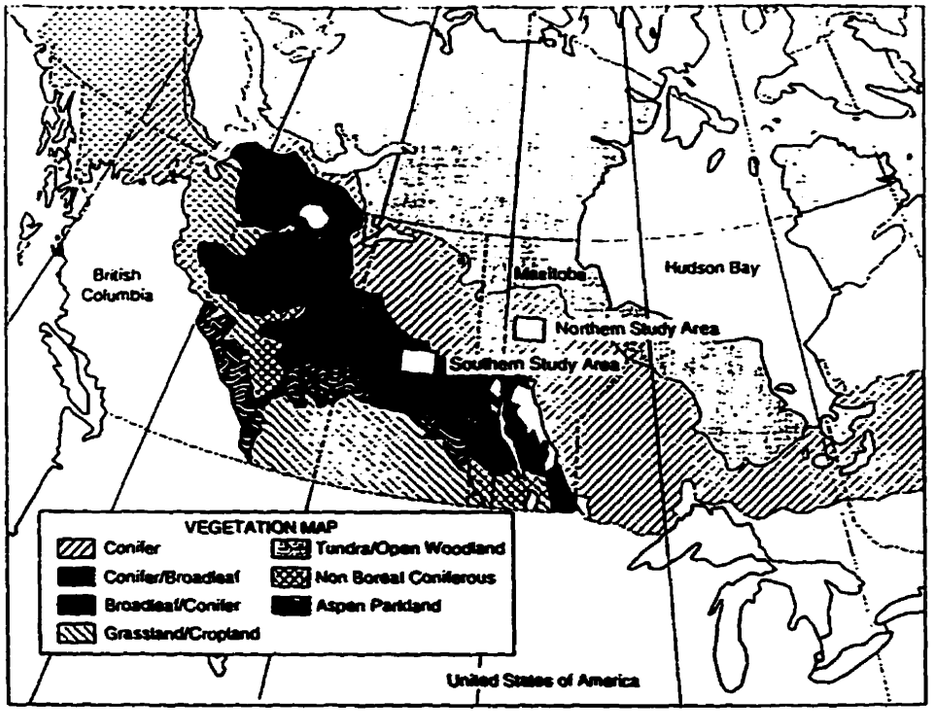


Figure 2.5. Map of western Canada showing the major vegetation zones in the area, as well as the location of the BOREAS northern and southern study areas (modified from Sellers *et al.*, 1995)

### 2.2.4 Forest Biophysical Variables

#### 2.2.4.1 Selection of Variables

Some of the major conclusions and recommendations from an International Conference on the Global Carbon Cycle (Bolin *et al.*, 1979) were that comprehensive, regional scale measures of carbon cycle parameters such as net primary productivity, biomass amount, and leaf area index are urgently needed, and that reliable methods to obtain these parameters from remotely sensed data sources require investigation (Bolle, 1991; Skole, 1992). These parameters are key variables in a variety of intricate carbon cycle and ecological models (Bolle, 1991; Skole, 1992; Rasool, 1992; Sellers and Shimel, 1993), such as FOREST-BGC (Running and Coughlan, 1988; Running and Gower, 1991), BIOME-BGC (Running and Hunt, 1993), RESSys (Running *et al.*, 1989) and RHESSys (Band *et al.*, 1991a,b; Nemani *et al.*, 1993). Although there are a number of additional remote sensing biological variables of interest in studies of carbon cycling in forested settings, such as canopy closure, stand density, canopy gap fraction, and tree diameter at breast height, the recommended variables of leaf area index (LAI), biomass, and net primary productivity (NPP) are the most important, for several reasons: (i) these measures can be applied to any plant canopy and are therefore compatible with results from other environments, whereas variables such as stand density, tree diameter, gap fraction, and canopy closure are usually specific to forested areas, and less so to areas such as grasslands and low vegetation; (ii) many of these other variables are correlated with LAI, NPP and biomass; and (iii) these key variables identified here are required for a number of regional scale models, as discussed earlier. Therefore, the variables LAI, NPP and biomass

are the main carbon cycle parameters of interest in this study, with additional variables considered where appropriate.

These parameters provide us with different types of information, with the following definitions from Bonham (1989) adopted for use in this study. Leaf area index refers to the area of foliage per unit area of ground and therefore includes a component of unit density related to carbon storage and allocation; biomass is the total or absolute amount of vegetation present, which here will strictly refer to above ground biomass, or standing biomass; while net primary productivity has a distinct temporal component as it is related to the amount of biomass accumulated over a given time period, which is usually specified for a growing season, or over several years. Similar to biomass, NPP in this context refers to productivity above ground, which is sometimes called ANP, or above ground net primary productivity. Each of these variables provide important information of interest to the exchange of carbon between the forest and the atmosphere, namely the density of foliage, the amount of vegetation matter, and their temporal characteristics. These biological-physical, or biophysical, variables therefore are of interest in terms of being estimated from remote sensing data. In the following sections, issues involved in using remote sensing data for extracting and estimating such information from forest canopies will be reviewed.

#### 2.2.4.2 Optical and Radar Remote Sensing of Biophysical Variables

A variety of optical and radar remote sensing systems have been used in monitoring forest and vegetation of the Earth's surface, a review of which is well beyond the scope of this research. Instead, in this section an overview of the use of radar imagery is provided

for this application as a means of comparison with optical remote sensing strategies which form the focus in this work.

In recent years, there has been increasing research into the use of radar for obtaining forest biophysical estimates (e.g. Sader, 1987; Ahern *et al.*, 1993, 1995; Franklin *et al.* 1994; Ranson *et al.* 1995; Wilson, 1996), given the advantages of cloud penetration compared to optical sensors and the availability of radar satellite sensors such as ERS, JERS, and RADARSAT . A useful overview of radar capabilities in this regard has been provided by Waring *et al.* (1995), who concluded that variable results have been found to date in terms of land cover classification and biophysical parameter estimation using synthetic aperture radar (SAR) instruments. For example, it was mentioned that classification accuracies of up to 66% were reported by Ranson and Sun (1994) for distinguishing classes of coniferous and deciduous trees, as well as mixed forest and regeneration classes using one radar image. In that study, using sets of multi-temporal imagery the accuracy was increased to over 80%. C-band radar can be capable of discerning major land cover classes under dry conditions, however for deciduous forests it can be difficult to estimate LAI due to the orientation of leaves which limits penetration (Waring *et al.* 1995). For coniferous forests, results by Ulaby and Dobson (1993) and Franklin *et al.* (1994) indicate estimates of LAI up to values of 4 are possible, while for biomass, SAR is better suited for areas of low to moderate standing biomass, beyond which detection is problematic (Waring *et al.* 1995). Variations in moisture status of leaves and conifer needles has also been found to limit biophysical estimates (Sader, 1987). Encouraging results have been obtained recently from BOREAS Shuttle Imaging Radar (SIR-C) data by Ranson *et al.* (1995). In that study, overall classification accuracy was on the order of 80%, however, individual class accuracies ranged from 62% for black spruce

to 87% for jack pine within a class structure that considered five forest classes. Biomass estimates from individual bands had errors in excess of 6 kg/m$^2$, however, using ratios of different radar bands the highest sensitivity to biomass of ±2.13 kg/m$^2$ was attained. It was concluded that when using SAR imagery, multiple polarization and multiple frequency data are required to obtain acceptable results for these forestry variables. In a detailed study by Ahern *et al.* (1996), it was found that multidate and multipolarization airborne SAR data provided good discrimination of major boreal forest cover types, but that single polarization data for one date could not be considered adequate for this task in an operational setting. Weak relationships were found between the multi-date, multi-polarization data set and a comprehensive set of stand structure measures, and these relationships were deemed to be not strong enough to provide reliable estimates. Similar to previous studies, the use of multi-date and multi-polarization data was advocated to achieve more acceptable results. This is consistent with conclusions made by Ahern *et al.* (1995), who recommended future satellite radar sensors be configured to provide multiple frequencies and polarizations compared to existing satellite sensors such as ERS-1, JERS-1 and RADARSAT, all of which provide single frequency, single polarization data.

In this thesis research, optical remote sensing data from field-based, airborne, and satellite platforms that operate over a variety of spatial scales are used. The remainder of this Chapter provides a detailed treatment of a number of issues inherent to the use of optical remote sensing systems in forestry applications.

## 2.3 OPTICAL REMOTE SENSING OF VEGETATION

### 2.3.1 Spectral Reflectance

The interpretation of remotely sensed data is based on our understanding of how different materials with different properties absorb, transmit and reflect electromagnetic radiation in different amounts at different wavelengths with respect to the amount of incident energy (Curran, 1985). For optical remote sensing systems, an important parameter of interest is the reflectance of a surface, feature, or area. Reflectance at a given angle is defined as the ratio (often expressed as a percentage) of the amount of radiation reflected by a surface, termed radiance, to that which is incident upon that surface, or its irradiance. Radiance is measured with respect to an angular component and specified as radiance per steradian. Angular measures of radiance can be converted to bidirectional reflectance factors (BRF), that is, the ratio between spectral radiance measured at a specified viewing angle to the object of interest and the incident irradiance at a given angle. It is important to make explicit the distinction between radiance and reflectance, since (i): our knowledge and information on the optical properties of vegetation components is expressed in terms of reflectance to facilitate comparisons of information from different sensors and different environments; (ii) most optical remote sensing devices mounted on airborne or satellite platforms measure radiance only (resulting in a significant amount of remote sensing research devoted to converting or estimating reflectance from radiance data); and, (iii): perhaps in part due to the above reasons, the terms reflectance and radiance are often confused or used interchangeably and incorrectly in the literature, as also noted by Curran (1985). In this research, the term reflectance will be used in most cases, since it will be assumed that a suitable correction from radiance to reflectance is possible for the

given topic under consideration. Also, in this work, reflectance is the remote sensing quantity of primary interest since it is the form of most of the spectral data used in this study. For example, as we shall see later in the thesis, a number of procedures and computer programs have been implemented in this research for the collection of field data and processing of these data to reflectance values. Airborne and satellite imagery used in this research analysis are also converted to reflectance. Measurements of reflectance form the basis for our understanding of the spectral characteristics of vegetation, to be summarised next.

### 2.3.2 Reflectance Characteristics of Vegetation

The spectral reflectance of vegetation varies by wavelength in unique and known ways throughout the electromagnetic spectrum, and forms the basis for our ability to discriminate them from other surface features using multispectral sensors mounted on remote platforms (Lillesand and Kieffer, 1979). The main sources of variation (sometimes referred to as spectral signatures) associated with different vegetation types and biophysical properties exist within the visible and infrared portions of the electromagnetic spectrum and will be briefly reviewed here. It is in these regions of the spectrum that spectral contrasts between and among vegetation species and other surface features are maximised (Curran 1985), which explains why optical remote sensing systems that operate in these regions are preferred for terrestrial vegetation studies of the major biomes of the Earth (forests, savanna, grasslands, as well as vegetated sectors of desert and tundra - see Strahler and Strahler, 1987, Chapter 26; Plate M2). It should be noted, however, that more precise spectral signatures have been derived for detailed biogeochemical cycling

applications (e.g. Wessman *et al.*, 1988a,b) which deal with vegetation properties at the molecular level using very narrow portions of the electromagnetic spectrum (e.g. Curran, 1989).

### 2.3.3 Leaf and Needle Optical Properties

Leaves and needles are comprised of layers of organic material containing pigments, water, and air spaces, all of which affect their spectral reflectance, absorbance and transmittance properties (Curran, 1985). Controlled laboratory measurements at the leaf level have indicated that, in the visible portion of the electromagnetic spectrum, light is absorbed at wavelengths centered around 400 nanometres (nm) and 690 nm where chlorophyll is acquiring light for photosynthesis, while at about 552 nm (the green peak), leaf pigments are responsible for the scattering of light which causes vegetation to appear green (Gates *et al.*, 1965). Visible reflectance decreases exponentially with the number of leaf layers (i.e. increased LAI) as a result of this absorption by chlorophyll (Hall, 1994). In the near-infrared (NIR) portion of the spectrum, beyond 700 nm, needle and leaf cell structure tend to dominate reflectance - at these wavelengths, light absorption is minimal, while scattering from cell walls governs light reflectance. Multiple scattering associated with additional layers of leaves (i.e. higher LAI) results in increased canopy level reflectance (Hall, 1994). In the mid-infrared portion of the spectrum (1600-2000 nm), the key feature which dominates reflectance is the absorption of light by leaf water content, with primary applications to studies of leaf moisture stress (e.g. Cohen, 1991).

In terms of reflectance, the combined effects of leaf pigments and physiological structure result in healthy green leaves having low reflectance of red and blue light, medium

reflectance of green light, and high reflectance of near-infrared radiation (Curran, 1985). Of particular importance is the rather significant and sharp change in reflectance between 680-740 nm, which marks the boundary between chlorophyll absorption in red wavelengths and leaf scattering in the NIR (Figure 2.6). This region of maximum slope in vegetation reflectance spectra is known as the 'red edge' (Horler *et al.*, 1983; Curran *et al.*, 1991), and is the basis for a number of vegetation indices and spectral derivative techniques used to estimate forest biophysical parameters, as discussed in §2.5. The optical properties of individual leaves and needles can also be influenced by disease (Ahern *et al.*, 1991; Franklin, 1989; Rock *et al.*, 1988; Franklin *et al.*, 1995), nutrient deficiencies (Guyot *et al.*, 1989), age, and time of season, for example, vegetation senescence (Curran, 1985).

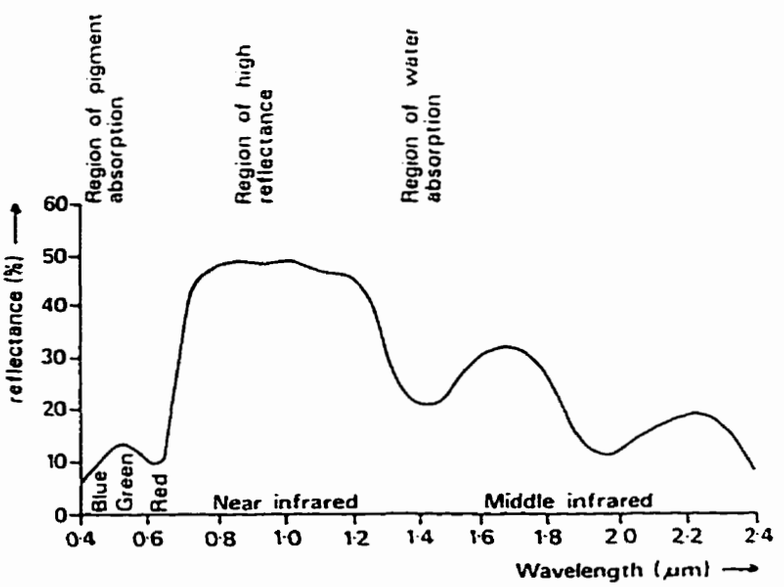


Figure 2.6. Typical reflectance distribution for leaves. Note the sharp increase in reflectance in the red portion of the spectrum, the 'red edge' (modified from Curran, 1985).

## 2.4 FACTORS AFFECTING REMOTELY SENSED FOREST REFLECTANCE

Up until now, the discussion of vegetation reflectance in this Chapter has dealt with vegetation components and their optical properties at the scale of individual needles and leaves. However, remote sensing systems collect data at the scale of forest stands and canopies, with pixel level reflectance signals derived from a composite of ground, tree, canopy, and other components, and not just needles and leaves. Nonetheless, current methods of analysing these data for estimating biophysical variables are based largely on those optical properties known at the needle and leaf level (discussed above), which are applied at the scales of canopies and forest stands. However, this link is confounded by a number of important factors which have a critical influence on forest canopy reflectance.

A number of factors affect the spectral reflectance of trees, forest canopies and forest stands (Table 2.1). These factors are very important since they represent some of the problems and challenges which have hindered a variety of remote sensing techniques for estimating biophysical variables from pixel level reflectance values - problems which current research seeks to overcome. These can be grouped into factors which are internal and external to the forest canopy (Guyot *et al.*, 1989).

### 2.4.1 Factors External to the Forest Canopy

Sensor spatial resolution will affect the reflectance of a forest canopy. The instantaneous field of view (IFOV) of a remote sensor defines the area on the ground from which the pixel reflectance signal is obtained. In a large IFOV (coarse spatial resolution, e.g. 1 km × 1 km), a pixel could likely encompass a myriad of surface features such as lakes, roads, non-forested areas, etc., in addition to the forest stands of interest. In these cases, one might expect a great deal of uncertainty in terms of the contribution of the forested portion of the IFOV to the overall pixel reflectance. At the more common intermediate scales (i.e. 20 - 30 m resolution of satellite imagery), a pixel which encompasses a pure forest stand can include reflectance from the ground, understorey, shadows cast by tree crowns, as well as the reflectance of trees, which itself is influenced by tree geometry and structure. Also, at these scales, some pixels will contain several distinct ground covers when the IFOV is located in mixed stands, at boundaries between forests, or near open areas. With a small IFOV, such as that found with high resolution imaging spectrometers (e.g. 1 - 5m), an individual tree or a partial tree crown might comprise a significant portion of a pixel, although it will also include some degree of shadowing as well as understorey and soil reflectance contributions, depending on local conditions. At these high spatial resolutions, one might expect pixel level reflectance to be more closely related to leaf and needle optical properties, although this is influenced significantly by canopy structure, density, and imaging geometry (discussed later). Also, in certain cases, bark and branch reflectance can also be a factor at these scales (Guyot *et al.*, 1989). In any case, regardless of the spatial resolution, a remotely sensed pixel is comprised of a mixture of surface elements.

| External Factors | Internal Factors |
|---|---|
| Sensor resolution | Background influence |
| Solar zenith angle | Canopy geometry |
| Solar Azimuth | Branch and bark reflectance |
| View zenith | Canopy spatial arrangement |
| View azimuth | |
| Topography | |

Table 2.1. Factors affecting forest canopy spectral reflectance at the pixel level.

The position of the sun and the sensor relative to the target plays an important role in affecting the pixel level reflectance of a forest. This is because forests are non-Lambertian surfaces, meaning that they do not reflect radiation equally in all directions, thereby affecting its bidirectional reflectance (Smith *et al.*, 1980). The elevation of the sun in the sky, often expressed as its solar zenith angle (SZA, the angular offset of the sun's position from vertical) will affect the amount of illumination reaching various parts of the forest canopy and ground surface. At a low SZA (high sun elevation), solar radiation will penetrate more deeply into the canopy, resulting in bidirectional reflectance decreasing at visible and increasing at infrared wavelengths as the SZA increases (Kimes, 1983). Syrén (1994) reported that, on average, reflectance factors increased by 1-2% for each degree of decreasing SZA at certain wavelengths for spruce and pine. Also, the proportion of shadowed and illuminated surfaces will change significantly with changing SZA throughout the day (or by season and latitude), for example, there will be more shadowing

of canopies at higher SZAs (Guyot *et al.*, 1989). This is of particular importance at visible wavelengths where leaf transmittance is low, causing shadows to be dark (Curran, 1985).

Differences in the view angle of the remote sensor also result in variations in spectral reflectance. Today, many remote sensing systems are nadir viewing (e.g. NOAA AVHRR, Landsat MSS and TM, airborne AVIRIS, MEIS, NS001-TMS), however, an increasing number of satellite (e.g. SPOT), specialised airborne (e.g. ASAS, CASI) and field sensors (e.g. PARABOLA, Deering and Leone, 1986) also provide off-nadir viewing capabilities to increase target-specific data collection opportunities and to capture and utilise the differences in bidirectional reflectance with view angle. These reflectance values will also be affected by the solar azimuth with respect to the off-nadir sensor look direction. For example, the bidirectional reflectance of a forest canopy is usually lower when the sensor is pointed towards the sun, as opposed to looking away from the sun in the anti-solar direction (Deering *et al.*, 1994). Further variations in reflectance also result at intermediate angles, oblique to the solar azimuth angle and target of interest. When the sensor look angle corresponds to the solar azimuth illumination angle, directional reflectance in the anti-solar direction is maximised (Li and Strahler, 1992), which is sometimes referred to as the "hotspot" effect (Jupp and Strahler, 1991).

Topography can also be an important component in defining overall sun-sensor-target geometry which affects forest reflectance (Cibula and Nyquist, 1987). The above discussion of solar and sensor parameters assumed flat terrain, however, two different topographic orientations (e.g. different slope, aspect, curvature) when viewed

under identical sun and sensor angles will have very different reflectance values (Frank, 1988). In cases of variable terrain it may be necessary to account for topography, either through attempts to minimise its influence through normalisation (Justice *et al.*, 1981), or by explicitly characterising topography through geomorphometric analyses (Fleming and Hoffer, 1979; Franklin, 1987,1992; Jones *et al.*, 1988; Duguay and LeDrew, 1991; Franklin and Wilson, 1991; Peddle and Franklin, 1993).

### 2.4.2 Factors Internal to the Forest Canopy

The background beneath a forest canopy can have a large effect on overall forest reflectance. In the case of open canopies, the effect of background soils and vegetation can dominate and, for sparse forests (e.g. high latitude boreal conifers and subarctic forests) almost completely mask the contribution of trees to the pixel level reflectance (Dean *et al.*, 1986). The background is typically comprised of either bare soil, surface cover vegetation (e.g. grasses, lichens, moss), understorey vegetation (e.g. herbs, shrubs, bushes), other materials (e.g. rock, deadfall), or, a combination of some or all of these. The effect of different backgrounds was studied by Ranson *et al.* (1986) in a controlled setting by placing identical forested canopies over different backgrounds of natural sod, a pure black surface, and then a white surface. They noted substantial differences in reflectance attributed solely to the background influence. The magnitude of background effects on pixel level reflectance depends on the proportion of the background exposed to the sensor, and this in turn is a function of canopy closure, stand density, and sun and sensor position. Guyot *et al.* (1989) report that with low vegetation, the background will significantly affect visible reflectance up to an LAI of about 3.0, after which the background is largely

obscured, while in the infrared, this saturation occurs beyond LAI values of 5.0 due to increased leaf transmittance, and that similar properties will hold for forested canopies in terms of canopy closure. Further, the amount of spectral contrast between background and canopy is important. For example, Ranson *et al.* (1986) concluded that, of the backgrounds they studied, the white background with the highest contrast to the forest canopies maximised the potential for information extraction throughout the forest canopies being studied. Li and Strahler (1985, 1986) also chose high contrasting backgrounds similar to that of pure snow to optimise model simulations of forest canopies based on conical objects. Otherwise, in cases where the background is spectrally similar to the forest canopy, interpretation of reflectance values can be compromised (Curran, 1985). Consistent with these results, and also based on their own experimentation, both Guyot *et al.* (1989) and Ranson *et al.* (1986) recommended the use of snow covered terrain to best characterise forest stands from a remote sensing perspective, due to the high contrast between snow and trees, and also because the snow cover will mask the variability of surface vegetation and understorey.

According to Guyot *et al.* (1989), canopy geometry is the most important factor which influences the reflectance of an individual canopy. This geometry modifies the amount of shadow presented to a sensor, and therefore affects the sensitivity of bidirectional reflectance to solar and sensor position (Curran, 1985). The geometrical structure of a canopy is determined by several factors. One of the more important is the leaf inclination angle (e.g. Verhoef, 1984), and, at the canopy level, the mean inclination of leaves, characterised by the leaf inclination distribution function. For example, when leaves are predominantly vertical, visible reflectance increases for low LAI due to increased background effects, while it decreases at higher values of LAI due to shadow effects

(Guyot *et al.*, 1989). Other structural factors such as crown shape (Goel and Grier, 1988; Goel, 1989) tree size, as well as tree spacing and the spatial arrangement of trees are important (Li and Strahler, 1985). Another important canopy geometry factor is the multiple scattering of radiation, both within a canopy and among adjacent trees. The implications of this are that the overall effect of individual factors on pixel level forest reflectance (discussed above) will be either amplified or dampened as they combine in complex ways with respect to forest canopy radiative transfer. Intricate models have been designed in attempts to capture the essence of this multiple scattering, and to account for its effects on reflectance (e.g. Goel *et al.*, 1991).

Guyot *et al.* (1989) also mention several other factors which affect forest canopy reflectance. These include external factors such as atmospheric aerosol effects, clouds and cloud shadows, and the effects of wind on modifying canopy geometry, as well as internal factors such as the orientation of tree rows (plantations), and the effect of exposed bark and branches on canopy reflectance.

## 2.5 REMOTE SENSING OF FOREST BIOPHYSICAL VARIABLES

Forest biophysical variables cannot be obtained directly using remote sensing but instead must be inferred from forest reflectance data. As a result, several information processing techniques have been used for this purpose. These methods are largely based on attempts to indirectly minimise the effect of factors which influence forest pixel level reflectance (§2.4), so that we can apply our knowledge of leaf and needle optical properties (§2.3) with greater confidence.

Since this thesis research is based on the development of new techniques for the remote sensing of forest biophysical variables, the focus in this review will be directed towards assessing existing techniques, with the parameters they estimate commented on as appropriate. The emphasis will be to provide an overview of the level of results obtained, and the nature of the problems or difficulties encountered.

### 2.5.1 Vegetation Indices

A popular approach to estimating biophysical variables has been the use of transformations and vegetation indices interpreted from band ratios (i.e. one spectral band divided by another). They are all, in one form or another, based on the different spectral response of vegetation in the visible (usually red) and near-infrared portions of the electromagnetic spectrum, as reviewed earlier. Two of the most common vegetation indices are the Simple Ratio (SR), defined as (Jordan, 1969):

$$SR = \frac{R_n}{R_V} \tag{2.1}$$

where, $R_n$ = radiance in the near-infrared spectral region

$R_V$ = radiance in the visible spectral region

and the Normalised Difference Vegetation Index (NDVI, Rouse *et al.*, 1974), defined as:

$$NDVI = \frac{R_n - R_v}{R_n + R_v} \qquad (2.2)$$

These rather simple formulations have nonetheless become quite popular as a quick, easy and straight-forward method of capturing the effect of the red-edge contrast as it is manifested in broad-band (usually satellite) imagery. For example, the studies of Tucker (1977, 1979) contributed to land cover classification and vegetation indices derived from regional scale NOAA AVHRR (1 km and 4 km spatial resolution) which were related to estimates of biomass and LAI over Africa (Tucker *et al.*, 1986). As a result of the high temporal resolution of these data from meteorological satellites, it was possible to construct cloud-free data sets from daily imagery. Both the simple ratio and NDVI were found to be virtually equivalent, however it was difficult to know how accurate the results were due to a lack of ground data and the difficulties in collecting these data for the broad region being considered (Tucker *et al.*, 1986). Further issues such as off-nadir viewing, sun angle, canopy morphology, shadowing, background effects, and atmospheric aerosols were identified as affecting the indices derived, and these issues were magnified by daily variations throughout a composite image. In addition, it was pointed out that all spectral green leaf indices become saturated (and therefore unusable) at higher levels of green leaf area and biomass (Tucker *et al.*, 1986). Despite the number of factors and limitations involved, these studies have been quite valuable since they demonstrate the possibility for quick, broad scale estimates of important parameters which cannot be obtained by means other than remote sensing, particularly at continental to global scales. These observations are supported by work done by Cihlar *et al.* (1991) who studied the Canadian landmass using NDVI computed from AVHRR data to provide estimates of ecological variables and evapotranspiration over a growing season. It was concluded that NDVI values provide

important information on the seasonal development of northern latitudes, and they illustrated how a large area could be monitored throughout an extended period and linked with detailed meteorological and ecological data and a soil moisture model.

In addition to these indices, there have been many other related band ratios proposed in attempts to reduce some of the problems found with NDVI and SR, although virtually all of these are functionally related (Asrar, 1990), with minimal improvements found. Many of these earlier developments were made in the agricultural field, from which additional work in the area of transformations evolved. One example of this is the "Tasseled Cap" image transformation (Kauth and Thomas, 1976), so named because of its characteristic shape in spectral space which resembles that of a hat, with a tassel. Also known as the 'greenness-brightness' transform, the Tasseled Cap orients the data planes in multispectral space in a way which can be interpreted with respect to physical scene characteristics (Crist and Cicone, 1984). Brightness is the weighted sum of all the bands (e.g. applied to either the Landsat MSS or Thematic Mapper, TM) and was defined in the direction of maximum variation in soil reflectance. The second feature, greenness, is then the contrast between the near-infrared and visible bands. Although Li and Strahler (1985) mention that this transform is useful for separating tree crowns from background, its practical application to determining biophysical variables in forested areas has not met with success (Hall *et al.*, 1995). More recently, there has been some renewed interest towards improving vegetation indices. Two notable developments are the soil adjusted vegetation index, or SAVI (Huete, 1988) and the atmospherically resistant vegetation index, or ARVI (Kaufman and Tanre, 1992). The SAVI formulation serves to reduce the contribution of background soil reflectance to the overall signal through the addition of a constant to the NDVI equation. However, this index was developed for areas of partial vegetation cover

and therefore is of limited utility in forested areas. The ARVI adds the radiance difference between the red and blue wavelengths to minimise atmospheric effects, and is a useful improvement on NDVI in many cases.

Vegetation indices have been applied in a number of forest studies with varying levels of success. Chen (1996) has provided a comprehensive overview and evaluation of a variety of vegetation indices and also introduced a new index called the modified simple ratio (MSR). In that work, it was pointed out that refinements to NDVI designed to reduce background influence have had the negative effect of also reducing the sensitivity to the overstorey conditions of interest. The MSR index is expressed as a function of the simple ratio but provides for a different rate of change as reflectance values increase. Using late spring BOREAS data from IFC-1, a higher correlation coefficient with ground measured LAI (Chen and Cihlar, 1995) was found using MSR (~0.59) compared to NDVI (~0.51). Also, the set of vegetation indices tested provided better results in the late spring compared to mid-summer (IFC-2) as a result of the increase in the understorey signal as it developed to maturity, resulting in the indices being less sensitive to forest canopy and overstorey conditions (Chen and Cihlar, 1996). In another study, Running and Nemani (1988) studied the use of vegetation indices for seven sites with different climatic characteristics distributed around North America. They obtained $r^2$ values of 0.72 between the vegetation index and NPP, and found overall results to be rather variable. In a European coniferous forest study, Rosema *et al.* (1992) concluded that the forest green biomass is not uniquely related to NDVI, and that errors of up to 50% can be expected. The reason for this was that the variations within pixels which affected the signal response, which they reported would be better dealt with through separating out the individual components which combine to make that signal. Spanner *et al.* (1990) did substantial preprocessing of Landsat TM image data

to compensate for atmospheric effects and sun-surface-sensor geometry prior to deriving vegetation indices, which were then related to LAI. They obtained reasonable results in some areas, but found that the background reflectance of litter and soils in old-growth stands posed problems. In all cases, the effects of canopy closure, understorey vegetation and background reflectance were significant, and it was recommended that these factors should be explicitly accounted for. They concluded that to use Landsat Thematic Mapper data effectively, alternative approaches such as mixture modelling which capture these effects directly should be investigated.

There are a number of fundamental problems with using vegetation indices in general, and for estimating forest biophysical variables, in particular. Several investigators have commented or offered explanations for this. Lathrop and Pierce (1991) found relationships between vegetation indices and LAI were complicated by the heterogeneity of canopy cover and leaf optical properties, canopy geometry effects, and background reflectance, while Spanner *et al.* (1990) and Hall *et al.* (1990) found background variations to be particularly problematic. Several authors concluded that NDVI was useful for estimating absorbed photosynthetically active radiation (APAR) but that it was not well suited for LAI and biomass (Baret and Guyot, 1991; Hall *et al.*, 1990). In several comprehensive studies, vegetation indices were found to be highly nonlinear and therefore unreliable predictors of both LAI and biomass (Sellers, 1985, 1987). Curran and Williamson (1987) reported that LAI varied by up to 100% using vegetation indices, and that these indices tend to saturate at high values of LAI. Wickland (1989), in a commentary outlining future directions in optical remote sensing, mentioned that alternatives to vegetation indices should be sought, and that in the meantime, it would be highly desirable to attach a rigorous measure of accuracy with vegetation indices as a result of the

uncertainties and problems experienced. In terms of future sensors, another argument for moving on from vegetation indices is the fact that they use only two information channels. This is reasonable with broad-band, low spectral resolution data, however, with current and future hyperspectral imaging systems providing hundreds of channels, the use of only two of them would seem to be less than optimal.

### 2.5.2 Spectral Derivatives

A number of approaches to the problem of obtaining biological variables from remote sensing imagery have used more sophisticated manipulations of the data beyond that of simple band ratio techniques. These methods have largely been in response to higher quality image data becoming available in the past several years, and in particular, higher spectral resolution (hyperspectral) imagery.

The spectral derivative approach has been applied in a number of remote sensing studies in which hyperspectral data were available to provide detailed spectral information. This technique is related to spectral curve matching (Goetz *et al.*, 1985) in that the shape of the distribution by wavelength is associated with materials of interest, however, it differs in that it manipulates that distribution by taking derivatives of the curve (Adams *et al.*, 1993). The spectral derivative approach is used to suppress the contribution of scene features considered to be extraneous, or noise, to the application. In the case of estimating biophysical variables, the noise would be the spectral response of the background (soils, understorey). The technique is based on the assumption that the spectra of the components of interest must vary at different rates with wavelength, and specifically, that the spectra of the target (in this case, vegetation) varies at a higher rate than that of the background noise.

If these assumptions are true, then by taking derivatives of these spectra, the effects of the background can partly be eliminated (Demetriades-Shah *et al.*, 1990). The calculation of derivative spectra eliminates additive constants (e.g. caused by illumination differences) while reducing linear functions, such as the linear variation of background reflectance with wavelength (Curran *et al.*, 1990).

Most of the work concerning this technique has been applied in biogeochemical applications such as estimating leaf chemical constituents and chlorophyll content (Wessman *et al.*, 1988b, 1989; Miller *et al.*, 1990, 1991; Rock *et al.*, 1988), water suspended sediment analysis (Chen *et al.*, 1992; Dick and Miller, 1991) and to the estimation of absorbed photosynthetically active radiation (Hall *et al.*, 1990). Gong *et al.* (1992) used this approach to estimate LAI in open canopy Ponderosa Pine stands in Oregon. Using examples of vegetation and bare soil spectra, they found that the influence of the bare soil spectra was reduced to a constant after taking the first derivative, implying that its effect on the target was manifested as a constant gain added to the vegetation signal. By taking the second derivative, the influence of the simulated background soil was removed. This enabled correlation between Compact Airborne Spectrographic Imager (CASI, see Babey and Anger, 1989) spectra and LAI to be increased from 0.68 using the original pixels to 0.90 when the background effects were removed by derivative processing. It was concluded that this approach is suitable for situations where the variability of background soil and atmospheric effects is less than that of the signal spectra (vegetation). However, if this is not the case (and presumably it would be desirable to ascertain this beforehand), then the technique will not work. Furthermore, if the reflectance of the background features does not vary in a linear fashion, then the assumptions inherent to this approach will be invalid and the derivatives will not be independent of the

background signal (Curran *et al.*, 1990). Also, this technique is very sensitive to real noise in the data (i.e. noise at the sensor level; not to be confused with the spectral contributions from unwanted portions of the image pixel), which could further reduce the effectiveness of the derivative technique (Hall *et al.*, 1990), especially when higher order derivatives are required. Due to these limitations, spectral derivative methods can only be considered useful under certain specific conditions. The approach does not have widespread application to a number of environments nor would it be as suitable in parts of the boreal forest, particularly where understorey vegetation is complex and varied.

### 2.5.3 Canopy Optical Reflectance Models

Biophysical parameters can also be estimated using physical models of spectral reflectance (Strahler and Woodcock, 1986). Physical approaches attempt to understand the physics of interactions between solar radiation and objects, which are then built into a model relating vegetation characteristics to spectral response (Strahler and Jupp, 1990). Models are typically initialised and validated using known characteristics of a given interaction medium or environment, from which unknown characteristics can be estimated (Monteith and Unsworth, 1990). This determination is based on solving for unknowns in equations which relate spectral response to canopy characteristics as a function of a variety of physical factors (some of which were discussed in §2.4) as well as scale (Woodcock and Strahler, 1987). Through an understanding of physical properties and by measurements of spectral reflectance, the equations can be rearranged in terms of the canopy characteristics of interest, through a process known as model inversion.

Different types of geometric optical canopy reflectance models are of particular relevance to this research since they consider individual components of a scene as a function of scene geometry and lighting. A geometric optical reflectance model regards vegetation (e.g. forest crowns) as a collection of discrete objects such as cylinders, cones, spheres, or ellipsoids placed on a simulated background of known reflectance. Through knowledge of the geometry of light interaction and shadowing with these objects, it is possible to model a variety of canopy geometries which might occur in nature. One of the most simple geometric canopy forms used is the cylinder model, as in Jasinski and Eagleson (1989, 1990), Jasinski (1990), and Hall *et al.* (1995). This model requires a small number of inputs, namely the ratio of height to width of the cylinders, and the solar zenith angle of illumination. Component fractions are computed over a range of specified canopy density values. The height-to-width ratio can be obtained from field measurements, and these need not be particularly detailed as it is the ratio that must be provided, not actual measures, and since only one ratio is required this parameter can represent an averaged case of a real forest stand. The advantage of the model, therefore, is it's simplicity and ease of use, however, modelling the shape of canopies as cylinders is somewhat crude and not applicable to a wide range of tree types, and further, this model does not have a good representation of canopy shadow in all cases.

Conical geometry has provided an improved representation of forest canopies, and is the basis of the earlier canopy reflectance models of Li and Strahler (1985, 1986). In that work, coniferous forest canopies were modelled as a collection of cones on a white background to improve understanding of the nature of bidirectional reflectance of forest canopies under a variety of lighting conditions and viewing angles. This model can be run in one of two modes. In forward mode, the model requires as input the crown density as

well as the size and shape of trees (tree height, tree width), the size of the pixel, and the angle of illumination (e.g. solar zenith angle, SZA). The relative brightness of the cone objects and the background under conditions of direct and shadowed illumination are also required. When these inputs are provided in forward mode, the model produces as output the average brightness of the pixel (e.g. pixel level reflectance) and estimates of component fractions. This model is also invertible. In that mode, the inputs include the pixel level brightness values, cell size, the angle of illumination, and the reference brightness values of the illuminated and shadowed cones and background. The model is thus inverted to provide average outputs of tree height, cone shape, and the density of trees. The flexibility of being able to run this model in forward or inverse mode is an advantage to this approach, as is the more representative geometry of cones in terms of modelling coniferous forests. However, the model is not equipped to handle off-nadir view angles, topographic variations, or atmospheric effects. Further, in areas of more dense forests, and also when illumination angles are lower (e.g. higher solar zenith angles), the overlapping of shadows on adjacent crowns becomes problematic in this model as these cases are not accounted for explicitly.

More sophisticated models of canopy geometry which improve upon the cone model have been developed. For example, Franklin and Strahler (1988) used an ellipsoid model developed by Li and Strahler (1988) and applied it to a study of semi-arid woodland in Africa. Using Landsat TM imagery as input, the model was inverted to derive estimates of tree size and density. This canopy geometry model, which also permits the specification of stem or trunk length, was designed to consider additional environments such as vegetated areas of forest, savanna, and shrub-land. In another study, Wu and Strahler (1994) used this model to estimate crown size, tree density and biomass on a transect of different forest types in Oregon. By inverting the canopy reflectance model, estimates of

crown radius and stand density were computed and these were related to biomass using allometric equations. Using that approach, foliage biomass was estimated with a $r^2$ value of 0.75, while standing biomass had a $r^2$ value of 0.63. Issues involved in the study included model inversion, topographic correction, and component signature estimation. This type of model was further enhanced by Li and Strahler (1992) to use spheroids with corrections implemented for higher stand densities as well as illumination conditions such as higher solar zenith angles. In these cases, shadows increasingly tend to fall on adjacent crowns instead of background, yet at higher densities, these shadows themselves will become increasingly obscured, particularly those shadows which fall on lower portions of adjacent canopies. These issues of mutual shadowing are particularly important in boreal areas which characterize higher latitude zones and therefore have larger solar zenith angles. These effects can be further magnified when viewed at off-nadir sensor orientations. The Li-Strahler (1992) geometric-optical mutual shadowing (GOMS) model considers this, and also includes formulations to account for the 'hot-spot' effect, that is, when the view angle and illumination angle converges resulting in a reduction in shadows created. The basic geometric form parameters used in the GOMS model are shown in Figure 2.7. These include the horizontal crown radius (r), which essentially specifies the tree width dimension, the vertical crown radius (b), which specifies the canopy size from the lowest live branch to the crown apex, and the height to the center of the crown (h), which together with the vertical crown radius describes the stem length and tree height. When run in forward mode, these form parameters are required input variables. When the model is inverted, these parameters are estimated. Additional inputs such as spectral component reflectance and illumination and view angle inputs are also required, regardless of which mode is used. Additional information on these models, and in particular, the GOMS model, is provided later in the thesis when these models are incorporated into the analysis of

remotely sensed imagery for biophysical parameters. As we shall see later, the fact that these models consider sub-pixel scale forest scene components in their specification enables them to be used effectively as part of a larger approach based on spectral mixture analysis concepts used in this research.

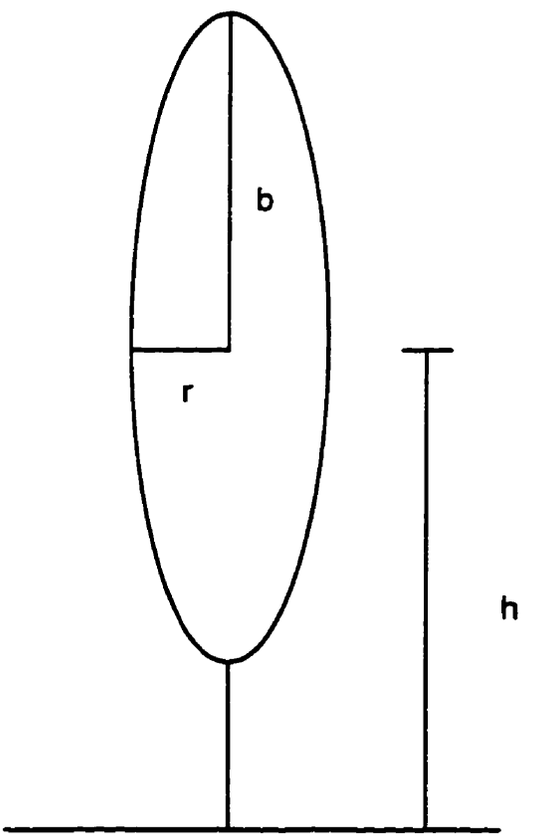


Figure 2.7. Geometric form parameters in GOMS reflectance model for modelling tree canopy geometry as a spheroid placed on a stick. Horizontal crown radius (r), vertical crown radius (b), and height to center of crown (h) shown.

These modelling research efforts continue to evolve, with recent advances in this area being based on a hybrid geometric optical - radiative transfer model (Li *et al.*, 1995). In previous geometric optical models (Li and Strahler, 1986, 1992) the objects modelled as trees were treated as opaque bodies which did not account for scattering that occurs internal to the tree. The hybrid approach initially treats incoming light using geometric optics, however, once light reaches one of the spheroids (simulated trees), the algorithm uses radiative transfer principles to model the internal scattering of light by the objects, in similar ways to that of turbid media radiative transfer models (e.g. Verhoef, 1984; Goel and Grier, 1988). Future work will likely evolve into the incorporation of complex computer simulation models, which essentially trace the entire path of a photon throughout a canopy (Goel *et al.*, 1990, 1991; Nilson, 1990; Nilson and Peterson, 1991).

## 2.6 CHAPTER SUMMARY

In this Chapter, a review of forest biophysical parameters and factors involving their estimation using remote sensing techniques has been presented within the broad context of the role of the boreal forest in the global carbon cycle and environmental change. The extraction of useful forest information from remote sensing signals involves knowledge of the spectral properties of vegetation over different wavelengths, with an important consideration being the spatial scale of observation. The basis for interpretation of remote sensing signals is rooted in knowledge of the optical properties of vegetation at the scale of needles and leaves. When the scale of observation becomes that of a forest canopy or stand, many factors are introduced which affect the spectral reflectance of the target of interest. The most significant of these is the role of background vegetation, the

affect of tree size, shape, and distribution, as well as sun-sensor-surface geometry and the presence of shadows. Several remote sensing techniques have been applied to ascertain forest biophysical variables, yet an approach which deals with many of these factors directly and explicitly has not been forthcoming. The most common approach, vegetation indices, was shown to be limited in that it does not adequately account for background reflectance, shadows, or canopy geometry, as well as being restricted to two spectral bands. Studies which used this approach have encountered significant problems and error in biophysical parameter estimation. These limitations are particularly problematic in boreal forest areas where canopy coverage is often sparse (i.e. large background influence), and where shadows are significant due to the higher solar zenith angles which typify boreal latitudes. Methods involving spectral derivatives were also considered, and found to be useful but not robust in terms of dealing with more complex environments. The major conclusion from this review of the literature is that an alternative method which deals with these problems is required for improved estimation of forest biophysical variables. Physical optical models which simulate canopy geometry were also reviewed and shown to provide an effective means of relating vegetation structure to overall pixel level reflectance. As we shall see later, these models are related to the spectral mixture analysis concepts used to deal explicitly with the problems that confound methods such as vegetation indices. These methods form the context of the next Chapter as well as the underlying basis for the analyses presented later in the thesis.

# CHAPTER III

## SPECTRAL MIXTURE ANALYSIS METHODS FOR ESTIMATING SUB-PIXEL SCALE FOREST COMPONENTS

### 3.1 INTRODUCTION

In the review of existing approaches to determining forest biophysical variables in Chapter II, it was found that these generally rely on some manipulation of spectral response in different portions of the electromagnetic spectrum which can be related to vegetation properties and biophysical parameters. In all cases, the pixel level reflectance acquired over the entire IFOV of the given remote sensing system was used as measures of vegetation and input to the various techniques. In doing so, different methods were used in attempts to minimise the effect of some of the factors which influence the spectral reflectance of forest stands (e.g. background influence, shadows, structure). However, this research seeks to account for these factors explicitly and directly in order to understand their influence, and to estimate forest biophysical variables with greater confidence, particularly with respect to new opportunities available through higher spatia! and spectral resolution data. This is achieved by quantifying the fundamental components of a forested scene which combine to make up the signal received as pixel level reflectance by the remote sensor.

In this Chapter, spectral mixture analysis (SMA) is presented as a methodology for overcoming a number of problems which limit existing techniques. In the following sections, the important aspects of this methodology are presented and described with reference to previous applications in other fields to provide insight into how this method can be applied in boreal forest terrain. Following this, the theory behind this method is presented in preparation for its use in the analysis chapters which follow. As this thesis contains two separate chapters which present data analysis using these concepts, specific methodological details pertaining to the experimental design, data sets, and inputs to the spectral mixture analysis methodology are contained within the two analysis chapters themselves.

## 3.2 SPECTRAL MIXTURE ANALYSIS

Spectral Mixture Analysis (SMA) of remotely sensed image data is based on the fact that the instantaneous field of view (IFOV) of a pixel contains a number of individual surface components which together contribute to the overall pixel level reflectance received by the remote detection instrument (Adams *et al.*, 1993). This can occur in several ways, and is related to the spatial resolution of image acquisition and the scale and nature of the surface features being considered. Figure 3.1 illustrates how pixels over a variety of image scales contain a number of surface features within the patch of ground covered by a pixel. Three pixels are shown at the coarse one-kilometre spatial resolution of the NOAA AVHRR satellite sensor, with scales of the Landsat MSS (80 m), Thematic Mapper (30 m) and high resolution imaging spectrometers (e.g. CASI) also indicated. Though the scene elements as drawn may not be to scale in some or all cases, the concept of their spatial heterogeneity over a variety of imaging scales and their mixing within pixels is nonetheless portrayed.

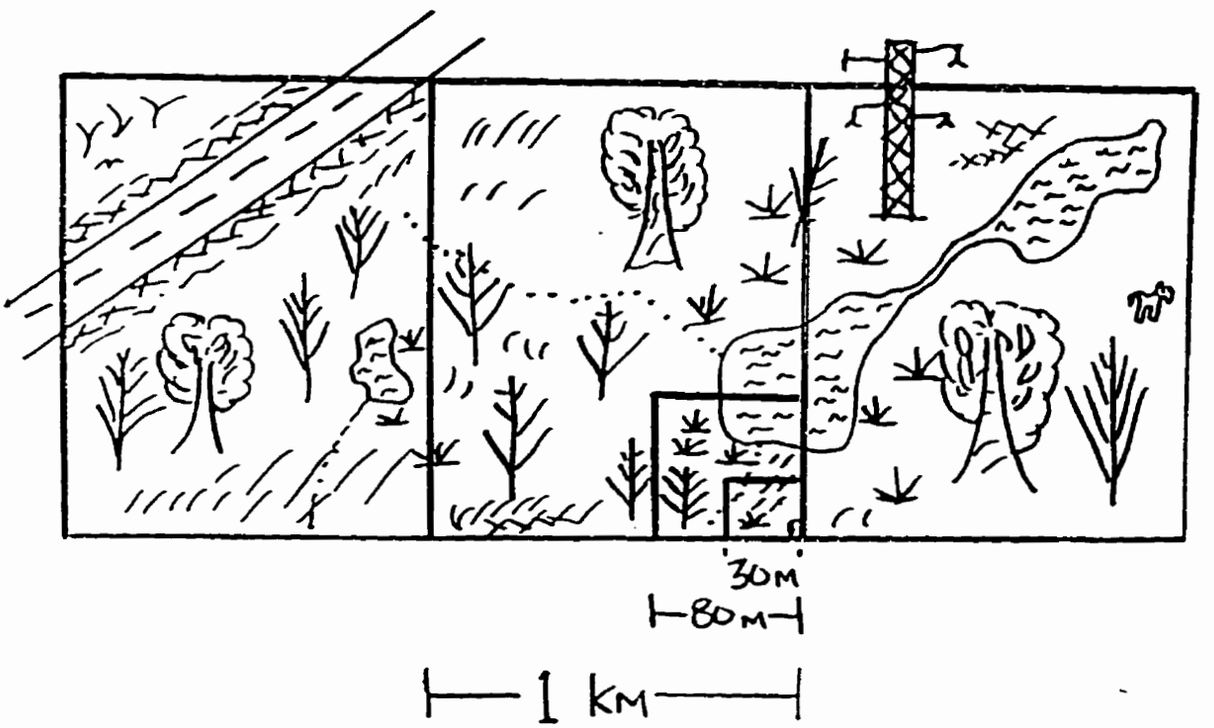


Figure 3.1. Spectral mixing over different imaging scales. Three NOAA AVHRR pixels are shown (1 km × 1 km ground resolution), with Landsat MSS, TM and imaging spectrometer scales also indicated. At each scale, a variety of scene elements are contained within any given pixel.

In general, two scenarios of mixing are possible. More commonly, spectral mixing occurs when individual objects and surface cover components are smaller than the pixel spatial resolution. In this case, pixel level reflectance will be determined from a mixture of radiation from all materials within a given IFOV. The same is also found when the

instrument IFOV overlaps boundaries between homogeneous surface elements which are larger than the pixel resolution. In both cases, the remotely sensed signals cannot be considered as uniquely representative of any one of the materials or surface cover features present. This is because the radiation received by the sensor is a mixture of radiation from those objects within the IFOV. In this sense, for a given surface component of interest (e.g. needles or leaves of a tree which constitute LAI and contribute to biomass), the overall pixel reflectance recorded by a remote sensor is actually a signal contaminated by other surface features and scene factors. It would therefore be desirable to separate out the individual spectral contributions of each component of interest. This is a powerful concept with many implications for improved remote sensing image analysis and interpretation beyond the forestry applications pursued in this research.

## 3.3 EVOLUTION AND DEVELOPMENT

Spectral mixture analysis grew out of the need to account for the rather fundamental aspect of the physics of image data acquisition discussed in the previous sections. These issues were first identified by Horwitz *et al.* in 1971, who recognised the implications of the mixing problem in an agricultural setting and developed a number of fundamental mathematical relationships between mixtures (these will be elaborated upon later). Other early works in this area which make reference to mixing effects for simple plant canopies (e.g. agricultural areas, grasslands) can be traced to Detchmendy and Pace (1972), Salvato (1973), Tucker and Miller (1977), Tucker (1979) and Jackson *et al.* (1979). However, the overall results obtained from these early studies were complicated by a number of factors such as the spectral similarity of the vegetation components considered (Hall *et al.*, 1995), lower spectral resolution of image data (e.g. Landsat MSS), and perhaps less well

developed techniques for acquiring component spectra and applying them to SMA. It is apparent from the small number of related applications reported in the literature that this approach did not receive very much attention in the 1970s, as evidenced further by the comment of Schowengerdt in 1983, that "these techniques are not widely used" (Schowengerdt, 1983, p. 141).

However, interest in this approach to image analysis was renewed in the mid-1980s, perhaps as a result of new sensors with increased spectral resolution becoming available (e.g. Landsat TM), continued advances in the maturing field of digital remote sensing, the availability of better field and laboratory equipment to obtain component spectra in support of mixture analyses, and different applications more suited to the input requirements of SMA. This could be considered the second generation of spectral mixture analysis, in which the problem was formalised and definitive approaches to its solution began to evolve. Much of the work in this period was done by Dr. John Adams and his group at the University of Washington in Seattle (Adams and Adams, 1984; Adams *et al.*, 1986; Shipman and Adams, 1987; Johnson *et al.*, 1983), with a very strong focus on geological applications in which the proportions of individual minerals were analysed from surface mixtures.

Today, a number of new applications for SMA are emerging in a variety of fields. This is partly due to the rapid increase in the number and quality of very high spectral resolution imaging spectrometers which provide detailed spectral data rich in information content. Digital image analysis techniques designed for lower spatial and spectral resolution data are not well suited to extracting the rich information content of these new data sources, and as a result, new and different approaches such as SMA are increasingly attractive and

well suited to these tasks, particularly as other disciplines become more demanding of remote sensing science to provide baseline results and analyses as our concern heightens over increasingly complex environmental phenomena.

It should be noted that these procedures, which by preference are referred to here as spectral mixture analysis (after Adams *et al.*, 1993), have also been referred to by other names, such as 'spectral unmixing' (e.g. Gong *et al.*, 1994), 'spectral mixture modelling' (Adams *et al.*, 1986; Lenningston *et al.*, 1984), 'spectral decomposition' (Hall *et al.*, 1995), and even 'pixel splitting' (Foschi, 1993), with individual scene elements sometimes referred to as suffering from the 'pixel mixing effect' (Birnie, 1986) and deemed 'mixed pixels' (Chikara, 1984) , which, on occasion have been reduced to 'mixels' (Matsumoto *et al.*, 1992) with 'mixing ratios' (Terayama *et al.*, 1992).

## 3.4 FORESTRY APPLICATIONS

Forests are comprised of trees, with a background cover of low vegetation, and these can be either sunlit or shadowed. Therefore, the fundamental components of a forested scene are sunlit canopy, sunlit background, and shadow. This is shown clearly in Figures 3.2 - 3.4, a series of three vertical colour photographs of varying density black forest stands taken at a nominal altitude of 120 m from a helicopter platform over the Superior National Forest, Minnesota. The area covered in each photo is approximately 30 × 30 m, the size of a Landsat TM pixel. These figures amply illustrate how a pixel IFOV will include many more items than just trees (which is what we are interested in for determining the biophysical variables such as LAI, NPP and biomass). The background

Figure 3.2. Nadir view of low density SNF Black Spruce forest stand taken from a helicopter platform at an altitude of 120m (Site #62). Area shown is approximately 30m × 30m. The fundamental scene components of sunlit canopy, sunlit background, and shadow are evident, with radiation from all three contributing to pixel level reflectance received by a remote sensing instrument.

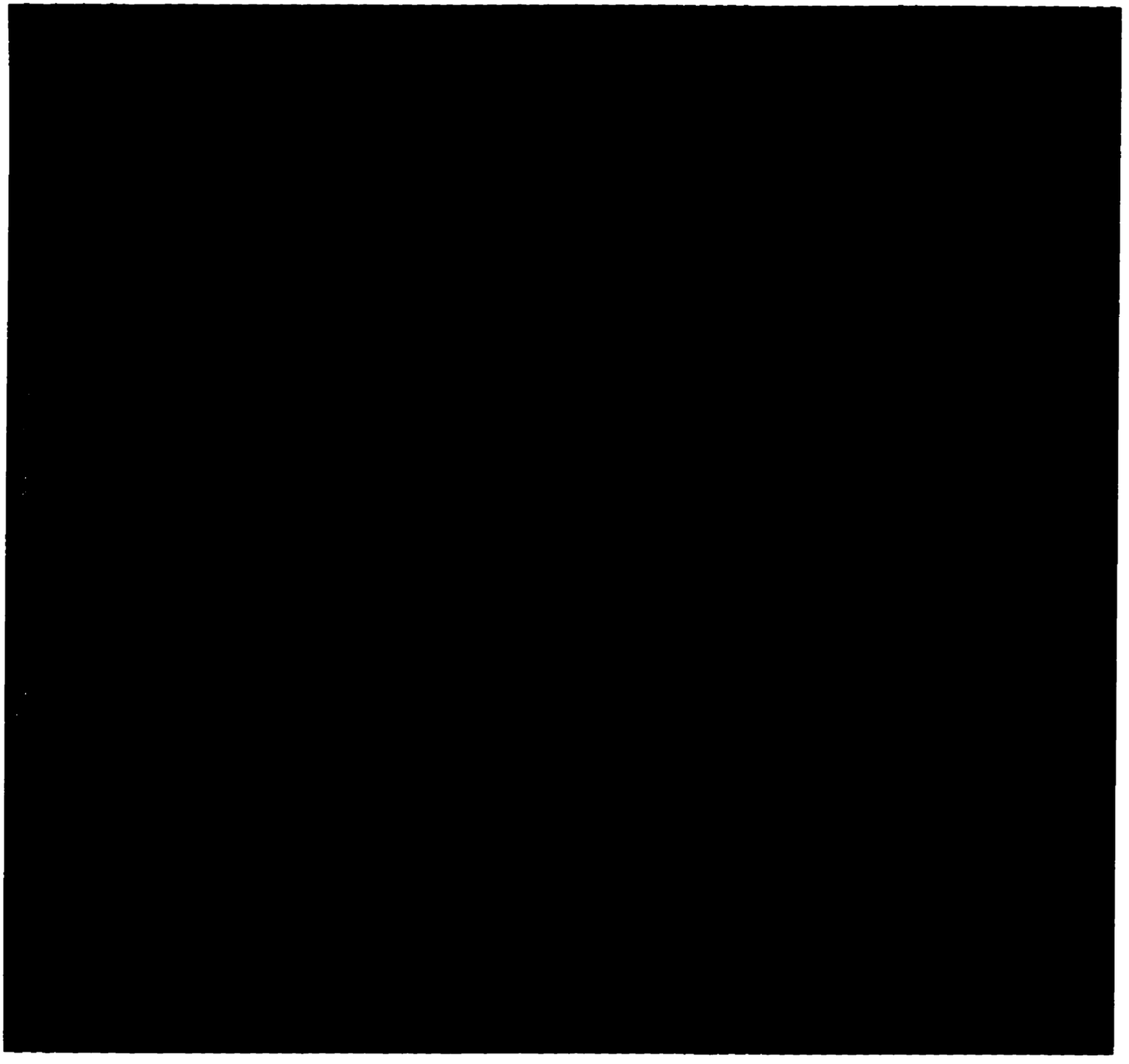

Figure 3.3. Nadir view of medium density SNF Black Spruce forest stand taken from a helicopter platform at an altitude of 120m (Site #54). Area shown is approximately 30m × 30m.

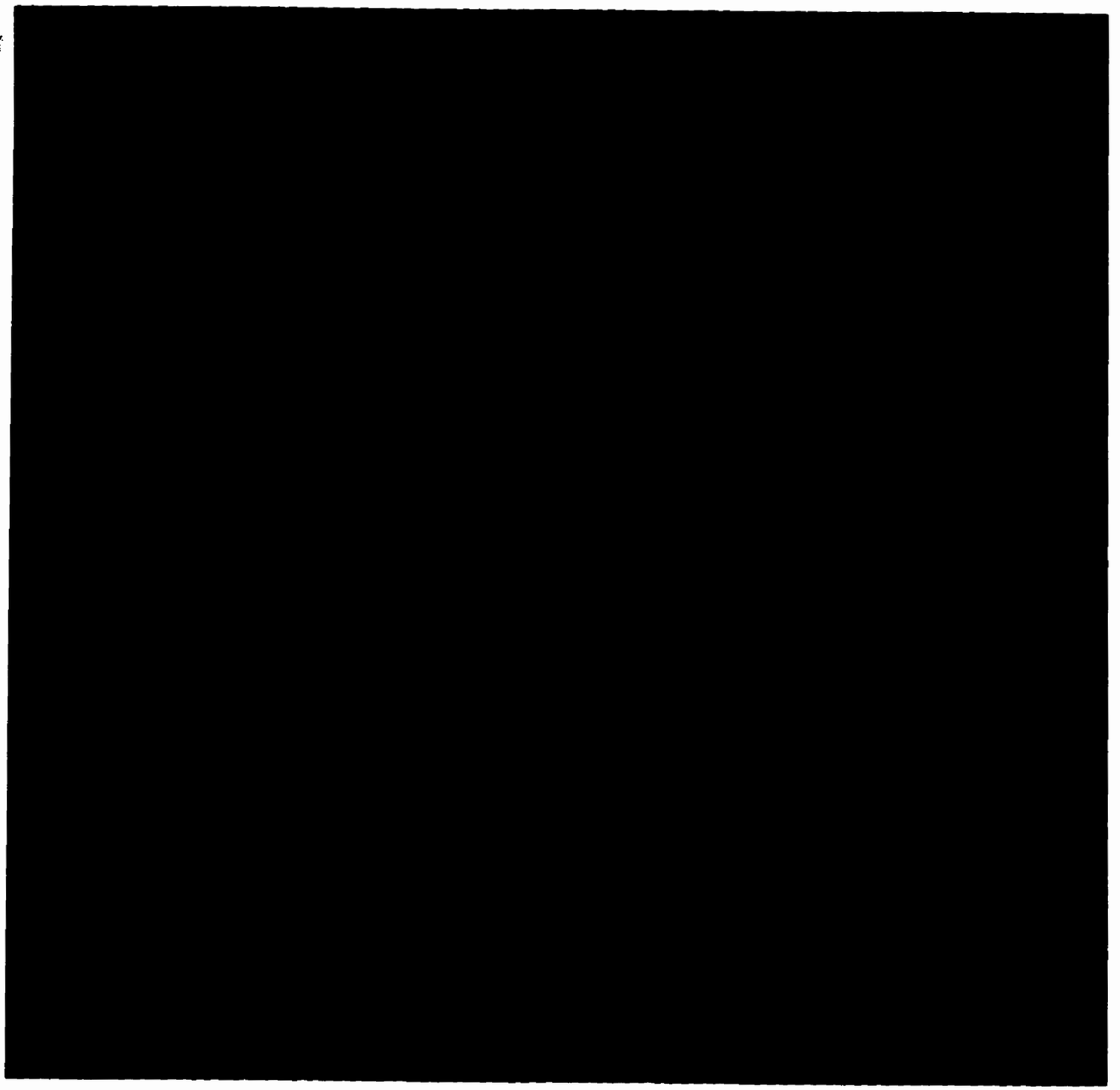

Figure 3.4. Nadir view of high density SNF Black Spruce forest stand taken from a helicopter platform at an altitude of 120m (Site #14). Area shown is approximately 30m × 30m.

cover (sphagnum moss) clearly contributes to the overall signal, and the prominence of shadows on both the background and the canopy can be seen. By using spectral mixture analysis, the proportions of each of these components that exist within a pixel can be determined. This represents, both spatially and intuitively, a more logical approach to analysing the fundamental unit of measure from a remote sensing instrument (the pixel). The idea then is to relate these proportions, or sub-pixel fractions, to the biophysical parameters of interest. This represents an explicit and direct way of understanding and accounting for some of the very important factors which affect pixel level reflectance; factors which have limited the success of other approaches based on overall pixel level reflectance values alone.

In recent years, spectral mixture analysis has been used in several forestry studies. Cross *et al.* (1991) applied a linear mixture model to two test sites in Africa using 1 km resolution NOAA AVHRR data. They used mixture fractions as a means of producing a classification based on the highest fraction present in a given pixel. Higher classification accuracies were reported using the mixture model compared to a maximum likelihood classification. The latter tended to underestimate forest cover as a result of its inability to consider sub-pixel surface features. Mixture model results from the AVHRR scale were also found to be well correlated with per-pixel classifications of a Landsat TM (30m) scene of the same area. Shimabukuro and Smith (1991) tested linear mixing models for deriving forest structure from Landsat MSS data in a Eucalyptus forest near São Paulo, Brazil. Three components were considered: Eucalyptus, soil, and shadow. It was found that the shadow fraction was well correlated with a distribution of Eucalyptus tree ages across the study site. In particular, areas of smaller (younger) trees had lower shadow fractions than the older trees which cast larger shadows and therefore had greater shadow fractions at the

pixel level. Nelson *et al.* (1994) used a linear spectral mixing technique to quantify the occurrence of widespread blowdowns in the Brazilian Amazon caused by severe windstorms. By including spectral components for green vegetation and nonphotosynthetic material, they were able to successfully identify areas of damage, including those occurring at sub-pixel scales. This was verified by field visits to remote locations and from knowledge gained in earlier related studies (Richey *et al.*, 1990). Using Landsat TM data from 1988 to 1991, they also performed a change detection analysis to identify areas of alteration as being potential new blowdowns. Roberts *et al.* (1993) used a similar approach to component identification to perform spectral mixture analysis in a forested preserve in California based on AVIRIS hyperspectral imagery. They first tested a linear mixing model and found it accounted for 98% of the spectral variation for the three components: green vegetation, soil, and shadow. However, nonlinear mixing effects were found to be significant for distinct communities of green vegetation, expressed as variations in fractions obtained using spectral subsets. In general, the soil and shade components were linear, however, within-canopy variations rendered the green vegetation component nonlinear. It was also concluded that high spectral resolution AVIRIS data was quite favourable and amenable to the spectral mixture analysis approach. Gong *et al.* (1994) compared classification and spectral unmixing procedures applied to colour infrared photography and airborne CASI and AVIRIS data for estimating forest canopy closure in an open canopy environment in Oregon. Both techniques were able to determine forest canopy closure, to within 3% agreement, when suitable inputs were available. It was easier to obtain image end-members from the high spatial resolution CASI data compared to the 20 m AVIRIS imagery, which made spectral mixture analysis of the AVIRIS data less straight forward. The importance of proper image conversion from radiance to reflectance as well as the need to carefully select or derive end-member spectra was stressed. They concluded that more

research is warranted to fully understand how spectral mixture analyses operate in complex forested terrain, and that issues such as image calibration, obtaining accurate estimates of scene fractions for comparison to fractions obtained by SMA, and the accurate specification and measurement of end-member spectra were important research issues to investigate.

In a more recent paper, Hall *et al.* (1995) presented an approach for estimating forest biophysical variables based on spectral mixture analysis. Component reflectances obtained by both measurement and a simple cylinder-based geometric-optical reflectance model were input to the spectral mixture analysis from which the areal proportions of scene components were determined and shown to be useful in predicting the biophysical variables of interest. This study demonstrated potential for using mixture analysis for estimating biophysical parameters; although a number of important factors rendered the results less than optimal. However, as we will see in the next chapter, these results have been improved upon significantly through a number of new techniques and methods introduced to this approach.

## 3.5 THEORY

SMA works by first identifying the various individual components of the surface which may be expected to be present within any given pixel IFOV. This can be done from field observation, aerial photo interpretation, or other sources of knowledge about a given environment. Once these have been identified, the spectral properties of each component (or spectral end-member) are obtained. These sets of component spectra are then applied to each pixel, from which the proportion of reflectance contributed by each component is

ascertained. The end result, for a given pixel, is a set of fractions (one fraction per component) which indicate the abundance of each component present.

One of the most important aspects of SMA is end-member specification. This task, if not done properly, can compromise the entire SMA procedure since these form the critical spectral inputs upon which the rest of the analysis is based. Some issues and approaches to this follow.

### 3.5.1 Spectral End-members

The individual components of the surface which are present within a pixel are called spectral end-members (Adams *et al.*, 1993), or simply end-members (abbreviated here as EM). These are members in the sense that they belong to the cluster or grouping of spectral properties associated with a given material or phenomenon of interest. For SMA, the purest spectral forms of these materials are required, and thus they occur at the 'end' of a spectral continuum associated with that material. Other materials increasingly mix with the given component as spectral space is traversed away from the end-member. These end-members can exist at different scales and can be measured or modelled in a variety of ways, but in general there are two types. These are reference end-members and image end-members (Farrand *et al.*, 1994).

#### 3.5.1.1 Reference End-members

Reference end-members are obtained typically at larger scales and usually represent the most fundamental components in a given scene. These are normally measured either in

a field setting with a portable field spectrometer (e.g. ASD, 1993), or in a laboratory with controlled hemispherical or bidirectional illumination (Adams *et al.*, 1993). The goal with reference EMs is to obtain the spectral properties of a material of interest in its pure form, that is, without the presence of any mixing with other materials. An example of a reference EM would be the pure occurrence of a given mineral located in nature and measured *in situ*, or extracted and transported to a laboratory for spectral analysis. In forestry applications, various components of trees, understorey, and background can be isolated for measurement in the field, or they can be removed for more detailed assays of their optical properties in a laboratory setting. Figure 3.5 illustrates the concept of reference EMs with respect to pixel level reflectance measurements in the boreal forest for the two-dimensional case of red and near-infrared reflectance. These are Black Spruce stands with a background cover of sphagnum moss, and so the end-member components of interest are sunlit canopy, sunlit background, and shadow. The pixel level reflectance measurements of individual stands, which were taken from a helicopter, are shown as a cluster in the middle of the plot. The reference EM spectral reflectance in the red and near-infrared are labeled on the graph, and form a characteristic triangle shape around the cluster of pixel reflectance values. End-members of each component are found at the vertices of the triangle. In this case, all of the pixels are comprised of mixtures of these individual components, since they all fall within the triangle. The location of the pixel level reflectance values in spectral space (on the graph) is related to the proportions of the individual components in nature which comprise the overall reflectance. In addition to illustrating reference EMs in spectral space, Figure 3.5 provides additional insight into the information content and composition of a pixel. If, for example, we are interested in analysing a forest canopy, it is clear that other materials such as background reflectance and shadows are very much a part of the signal which has been recorded. SMA seeks to separate these components such that, for any

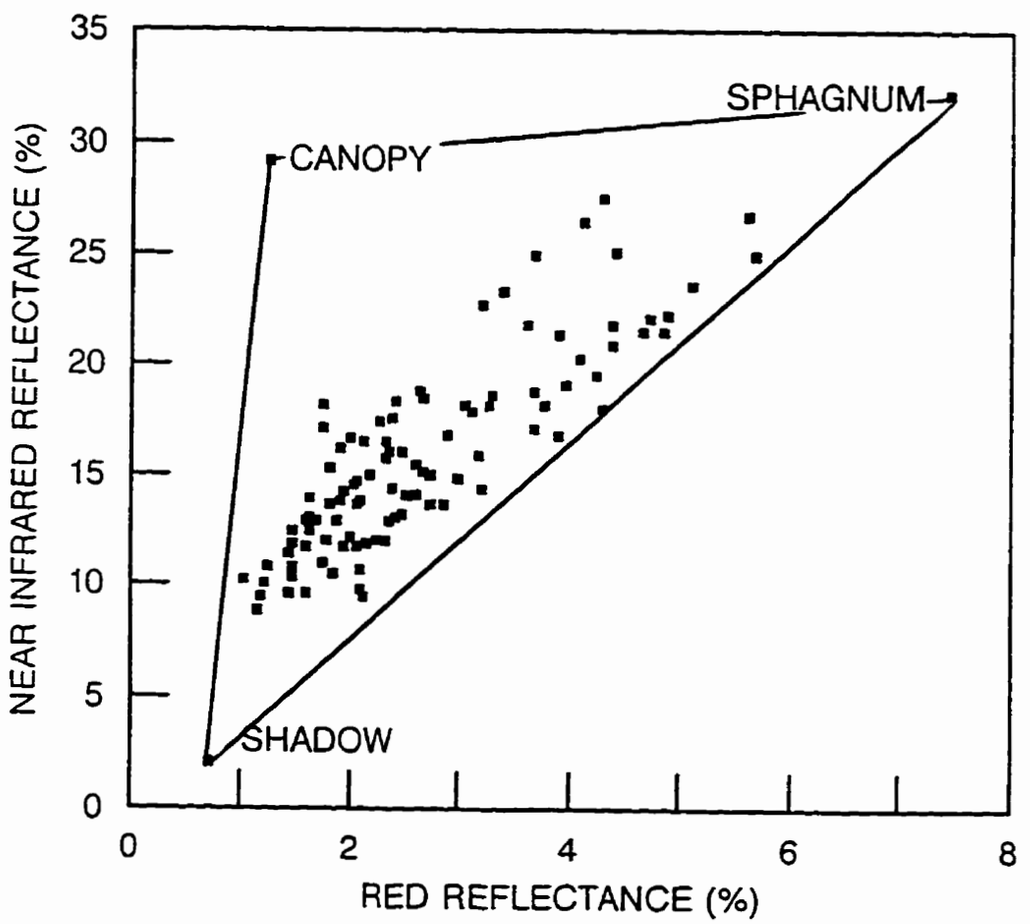


**Figure 3.5. Infrared versus red reflectance for 31 Black Spruce stands in the Superior National Forest, Minnesota. Data from helicopter MMR (modified from Hall *et al.*, 1995).**

given application, the data upon which the interpretation is to be conducted corresponds to the phenomena being studied.

Regardless of what the reference EMs are or how they are acquired, it is important that their spectral measurements be consistent with the spectral range of the remote sensing device to which the SMA procedure will be applied. As well, the reference EM spectra should be calibrated to a known standard, and ideally to the same or similar standard used by the remote sensing instrument (this is often possible with co-ordinated airborne remote sensing campaigns). In this regard, it is highly desirable to convert both image data and field or laboratory EM spectra from radiance to reflectance (Adams *et al.*, 1993). Methods have been developed to use SMA as a means of converting radiance to reflectance which are appropriate for this task (Farrand *et al.*, 1994).

3.5.1.2 Image End-members

The second type of end-member is the image end-member. As the name might imply, image EMs are selected directly from the image, with no requirement for field measurement or laboratory analysis. Individual or groups of pixels deemed to contain homogeneous or near homogeneous surface elements at the image scale are suitable candidate image EMs (i.e. the purest pixels). This can be done in consultation with knowledge of the area (e.g. supplemental data, reports, field observations, if available), and in making final selections it is advisable to select image EMs from areas of maximum illumination (except for the shadow end-member). This avoids having other pixels of the same material with reflectance values higher than the image EM (Adams *et al.*, 1993). The advantages to using image EMs are that they can be determined relatively quickly and

without the need for field or laboratory spectral measurements, and there is no need for extensive calibration of EM spectra to the image spectra, since the EMs are obtained from the image directly. The process of selecting an image end-member is similar to that of defining training areas for a supervised classification, although it is quite a bit more focused in the sense that it is concerned more with individual pixels than the more typical procedure which involves groups or blocks of pixels being delineated. However, Gong and Howarth (1990) determined that the use of single-pixels for training instead of block training was the most significant factor for improving classification accuracies for a given classifier. This better way of selecting training data is also more consistent with the needs of spectral mixture analysis, although the objectives differ in that training pixels for classification are selected to capture the variability within a class, whereas an image end-member is selected to represent the purest occurrence of a given material or surface feature. Much of the variability desired in training pixels is necessary to account for background and other effects that increase within-class variance, and therefore must be present in the training data to characterise a given class.

However, there are several disadvantages to the use of image EMs. Since the procedure works at the image scale, it is usually not possible to capture fundamental scene elements which are smaller than the pixel IFOV, unless there happens to be a known and identifiable instance of that element which is anomalously large and which is encompassed by an image pixel. Even in this case, it is unlikely that other EMs can be identified at a similar scale. With reference to Figure 3.3, image EMs for the three components would likely be identified as those stands which define the outer limits of the cluster of pixel level reflectances. However, these image EMs are not pure occurrences of their respective scene elements, since they do not match the pure reference spectral EMs discussed earlier

(located at the vertices of the triangle in Figure 3.3). So, for example, the best available sunlit sphagnum background pixel for use as an image EM might actually be comprised of 80% background, 15% sunlit canopy, and 5% shadow. When image EMs are themselves comprised of mixtures, any analysis based on SMA fractions derived from them would have to be interpreted with caution. In these cases, it would be helpful if the proportions of mixtures can be determined for a mixed image EM, although this can be difficult to quantify. In any case, even if a given pixel is thought to be a pure case of a given material, there will likely be sub-pixel shadow that cannot be detected at the image pixel scale (Adams *et al.*, 1993), particularly for rough surfaces such as forests. These problems can sometimes limit the usefulness of image EMs for detailed, sub-pixel scale analyses, however, for applications at the image scale (and beyond), the use of image EMs is often appropriate.

In practice, it is not always possible to obtain EM spectra using the same method for all materials in a given area, and in these cases a combination of reference and image end-members can be derived, although this is not ideal. For example, in areas of difficult terrain, it may not be possible to access or transport field spectra equipment to occurrences of certain materials, thereby preventing the collection of a complete set of reference spectra. In some cases, it may be possible to obtain reference spectra from existing spectral libraries, although to date most of these formal developments have been in the field of geology (e.g. Clark *et al.*, 1993). Another alternative is to model the end-member reflectance. It may also be possible to identify image EMs from higher spatial resolution imagery and use those with coarser resolution data, if a suitable multiscale data set exists. In this case, issues of calibration (similar to that with reference EMs) must be dealt with. In any case, it is usually best to obtain end-member spectra directly from the area being

studied, and in a consistent and careful manner, since this aspect of the analysis is critical to the overall success of SMA. In cases where the phenomena or surface features exist at sub-pixel scales, it is highly desirable to obtain reference end-members.

3.5.1.3 Convex-Hull Approach

One additional and recent area of theoretical investigation into spectral mixture analysis involves the unmixing of scene components without the *a priori* specification of end-members. This idea, first put forth by Craig (1990) as unsupervised unmixing but developed more significantly in Boardman (1993) and Craig (1994), involves algorithms which attempt to locate end-members in spectral space based on the shape of the pixel level data clusters, using principles of convex geometry (Lay, 1982). This can be visualised with reference to Figure 3.3 by removing the reference end-member vertices of the triangle, and instead, trying to fit a triangle around the cluster of pixel reflectances based only on the shape of the cluster, thereby creating new end-points which describe the locations of end-members. The concept is analogous to unsupervised classification, in which statistical clustering techniques are applied to identify data groupings, which are then identified *a posteriori*. As with unsupervised classification, the end-members so determined may or may not be related to real surfaces, since the statistics of the spectral domain are usually not directly related to the spatial domain (Curran, 1985). This is particularly important when considering mixtures. End-members determined in this way may not be pure, but instead are more likely to be comprised of mixtures themselves, although hopefully one material will be prominent in its spectral definition. The success of such a technique is clearly data dependent, and, for example, could also be sensitive to noise in the data which typically lie outside data clusters and therefore may confound the fitting of a convex hull around the

data space. Noise recognition and reduction algorithms (e.g. Curran and Dungan, 1989) can be employed in attempts to avoid this (Boardman, 1993). However, perhaps the most significant problem which confounds the unsupervised approach at the statistical level (aside from the natural interpretation issues mentioned above) is the difficulties encountered in positioning the convex hull around data clusters which possess varying levels of symmetry in spectral space. In this case, there can be significant discrepancies among a potentially large number of analytical solutions to the problem. This can be more easily understood with reference to the simple two-dimensional data cluster in Figure 3.3. If the pixel level reflectances formed a circular shape, there is an infinite number of solutions to the convex hull location problem (i.e. no solution); if the shape formed an ellipse, or square etc., there would also be a number of possible solutions. In any case, although the idea of unsupervised SMA is interesting and could be of interest to some applications in which end-member identification is not critical, or where *a posteriori* spectral identification is straight forward, it is not suitable for use in environments of even moderate complexity due to the uncertainty associated with end-member spectra, which as mentioned earlier, drives the SMA approach. It is definitely not suitable for the complex forested environment, and in particular, the application of SMA concepts to determining carbon cycling parameters. For these applications, the end-member spectra must be identified *a priori*, and in a controlled and well understood setting.

### 3.5.2 Spectral Mixing Models

Once a set of end-members has been determined (reference or image EMs), the next step is to invoke a model or algorithm which describes the spectral mixing, and from which component fractions can be derived from pixel level reflectance. There are two types of

spectral mixtures - macroscopic and intimate (Farrand *et al.*, 1994), and they are modelled as linear and non-linear combinations of material reflectances, respectively.

3.5.2.1 Linear Model

Macroscopic mixtures occur when there is only a single set of interactions between incoming radiation and the surface, in which a given incident photon is reflected or absorbed by one type of material only. Although this is not always the case in nature, linear models of macroscopic mixtures are used almost exclusively at present in mixture analysis (Hanan *et al.*, 1991; Arai and Terayama, 1992; Quarmby *et al.*, 1992; Settle and Drake, 1993). The overall pixel level reflectance is considered to be the sum of all component (end-member) reflectances weighted by their fractional area. The general form of the equation for linear mixing by area (after Adams *et al.*, 1989), for a given channel c and N end-members, is:

$$DN_c = \sum_{i=1}^{N} F_i DN_{i,c} + E_c \qquad (3.1)$$

where:

$DN_c$ = the digital number of the pixel level reflectance in channel c

$F_i$ = the fraction of end-member i

$DN_{i,c}$ = the reflectance of end-member i in channel c

N = the number of end-members

$E_c$ = the error for channel c

with the following constraints:

$$\sum_{i=1}^{N} F_i = 1 \tag{3.2}$$

and

$$0 \leq F_i \leq 1 \tag{3.3}$$

For the specific case of a forest stand, end-members can be identified as sunlit canopy, sunlit background, and shadow, with pixel level reflectance expressed as a function of individual component reflectances and their areal fractions as per equation 3.1.

Equation (3.1) is for one channel. For multispectral or hyperspectral data, there will be as many equations of the form (1-3) as there are channels, thus creating a linear set of equations to be solved for the unknown fractions, which can be done in a variety of ways (e.g. Adams *et al.*, 1993; Shimabukuro and Smith, 1991; Holben and Shimabukuro, 1993; Zhang, 1994). The fractions determined can be displayed as images either individually or as selected subsets to produce a spatial rendition of individual component abundances of interest. Further, individual or sets of fractions can be related to physical processes or phenomena of interest within a pixel area (e.g. biophysical parameters).

All fractions necessarily sum to one (equation 3.2), which is the unit area of the pixel, and, given a proper and comprehensive set of end-member spectra, any given

fraction should lie between 0 and 1 (equation 3.3). A component fraction lying outside this range usually means one or more of the following problems exist with the SMA: (i) an end-member spectra is inappropriate for the data under consideration (i.e. a pixel lies outside the triangle defined by the reference EM vertices in Figure 3.3), (ii) an important part of the signal has been overlooked (i.e. a missing end-member), (iii) other issues, such as atmospheric effects or instrumental problems, need to be addressed, or (iv) the assumption of macroscopic (linear) mixing has been violated severely.

3.5.2.2 Non-Linear Model

The second type of mixing is intimate mixing (Farrand *et al.*, 1994), which occurs when an incoming photon of radiation interacts with more than one type of material. Unlike macroscopic mixtures, these more complex interactions can only be modelled accurately as non-linear processes. Intimate mixing of incident radiation occurs in areas of rough surfaces, and can also occur where a surface may be penetrated to different depths by radiation at different wavelengths (e.g. water, snow, sea ice volumes). Many types of high vegetation, including trees and forests, create rough surfaces in which intimate mixing occurs. In a forest canopy, the multiple scattering of radiation amongst leaves, branches, trunks, understorey and background (Williams, 1991) results in non-linear mixing which is complex and difficult to model. This was demonstrated by Borel and Gerstl (1994), who used a single layer model of vegetation to show that radiation interactions within the canopy were not additive amongst components, but instead involved the products of individual reflectance values. They also showed that NDVI and biophysical parameters such as LAI had a complex, non-linear relation to modeled reflectance. Non-linear mixing can be visualised in spectral space with reference to Figure 3.3, by first removing the straight lines

which join the vertices of the triangle formed by the three end-members for the linear mixing model case shown, and replacing them by curves or some other warped shape connecting the vertices according to some non-linear criterion. Although several authors have made reference to non-linear spectral mixing (e.g. Farrand *et al.*, 1994; Borel and Gerstl, 1994; Roberts *et al.*, 1993; Portigal and Harrill, 1996), there has been no formal specification of a non-linear mixing model or algorithm, despite the abundance of natural surfaces in which intimate mixing would be expected to occur. However, Borel and Gerstl (1994) concluded that further research is needed in this area, which could possibly lead to improved vegetation indices and non-linear mixing algorithms.

## 3.6 CHAPTER SUMMARY

In this Chapter, spectral mixture analysis has been presented as a more suitable conceptual methodology for estimating forest biophysical variables compared to traditional methods. Through its ability to quantify the areal abundance of individual scene components at sub-pixel scales, spectral mixture analysis provides an explicit framework for analysis that addresses several of the problems inherent to previous approaches. Specifically, the ability to account for background reflectance, shadows, and canopy geometry are three immediate advantages to this approach as these are important factors affecting pixel level reflectance that other methods do not account for directly, if at all. In addition to providing the background to the evolution and development of this technique, this chapter has also presented the theory of spectral mixture analysis in preparation for applying this methodology in the analysis presented in the following chapter.

# CHAPTER IV

## SPECTRAL MIXTURE ANALYSIS OF BOREAL STANDS FOR ESTIMATING FOREST BIOPHYSICAL VARIABLES

### 4.1. INTRODUCTION

In this Chapter, a detailed study using spectral mixture analysis is presented for estimating biophysical variables in a boreal forest setting. As this is a new approach to the problem of estimating these variables in complex forest stands, the analysis presented in this chapter is intended to serve as a "proof of concept" for first deriving forest component fractions and then relating these to the biophysical variables of interest. Consistent with this purpose, an established, high quality data set from the Superior National Forest (SNF), Minnesota, was obtained and used in a controlled experiment designed to minimise the influence of many of the factors which normally must be dealt with in larger remote sensing studies (e.g. large spatial area, different forest species, atmospheric corrections). This data set was originally used by Hall *et al.* (1995) in a related study which this work builds upon in several respects, including the introduction of solar zenith angle corrections, sophisticated canopy reflectance models and inter-comparisons, and methods for scene validation and component accuracy assessment. The motivation for developing these new methods is to establish this as a viable approach for estimating biophysical parameters.

These improvements are also necessary to provide a basis for a more extensive analysis in BOREAS. Further, since the major field and remote sensing data collection components of the BOREAS project occurred while this thesis research was in progress, the availability of the SNF data set represented an opportunity to perform a significant analysis while simultaneously participating in BOREAS data collection efforts, with the expectation that BOREAS data would become available for the latter stages of this thesis research. The SNF data set was made available to the author while at GSFC under the NASA/USRA Visiting Scientist Program, as explained in Chapter I. During that internship, the Li-Strahler (1992) geometric-optical mutual shadowing (GOMS) canopy reflectance model was made available to this research by Dr. Alan Strahler at Boston University and obtained with the assistance of staff-member Dr. Wolfgang Wanner.

In this Chapter, the SNF study area and data set are first described, and followed by the experimental design implemented for the analysis. Of particular importance are the methods used to obtain end-member spectra. Also, a new method is presented for validating scene fractions from the spectral mixture analysis, a task which is often difficult or impossible but which is important in understanding the use of scene fractions in follow-on analyses. In the next section the results of the analysis are presented, which includes an assessment of the accuracy of the component fractions using the scene fraction validation methodology, as well as a study of the effects of solar zenith angle. The component fractions obtained are then used to predict the forest biophysical variables biomass, leaf area index and net primary productivity. A common vegetation index, NDVI, is also derived from the data set and compared with mixture fractions in terms of their ability to predict these biophysical parameters.

## 4.2. STUDY AREA AND DATA SET

The study area is centred at 48°N, 92°W in the Superior National Forest (SNF), northeastern Minnesota USA. This region is near the southern limit of the North American boreal forest, and therefore may be particularly sensitive to climatic variability and change (Hall *et al.*, 1992). The 40 × 120 km study area overlaps the Boundary Waters Canoe Area Wilderness, north of the town of Ely, and adjoins Canada at Quetico Provincial Park, about 200 km west of Thunder Bay, Ontario. Stands of black spruce, jack pine, and trembling aspen are dominant in this region, and exist over a range of densities, successional stages, age classes, and rates of productivity.

Field inventories and remote sensing imagery were collected during the summers of 1983 and 1984 by personnel associated with the NASA Johnson Space Center. Quantitative estimates of biomass, leaf area index (LAI), and net primary productivity (NPP) were obtained by dimension analysis of sacrificed trees using standard allometric techniques, described in Hall *et al.* (1992). This study deals with black spruce (*picea mariana*), the most common boreal forest dominant, for which field and remote sensing data are available for 31 stands based on 80 × 80m plots. For each of these stands, spectral reflectance measurements were obtained over a variety of solar zenith angles using a Modular Multi-band Radiometer (MMR) at spectral bands equivalent to NS001 Thematic Mapper Simulator and Landsat TM data. The MMR was mounted on a helicopter platform hovering at a nominal altitude of 120m a.g.l., producing an effective instantaneous field of view (IFOV) of approximately 30m in diameter, similar to the spatial resolving power of Landsat TM and SPOT satellite sensors. All MMR data used in this study were acquired with a nadir view angle. As part of the MMR data collection, nadir view colour

photographs were also acquired coincident with spectral measurements for the purpose of recording the spatial distribution of trees and the nature of the forest floor and canopy geometries throughout each site.

## 4.3. EXPERIMENTAL DESIGN

### 4.3.1. Spectral Mixture Analysis

The basis for the remote sensing image processing is spectral mixture analysis (SMA), which builds on the fact that the IFOV of a pixel contains a number of individual surface components which together contribute to the overall pixel level reflectance received by a remote detection instrument (Adams *et al.*, 1993). Through SMA, the areal abundance of these components can be quantified at sub-pixel scales, from which selected scene fractions are interpreted as surrogates for the biophysical attributes of interest. In the boreal forest, pixel level reflectance ($R_p$) can be expressed as linear combinations of the individual component (end-member) reflectances weighted by their areal fractions, as follows:

$$R_p = C \cdot R_c + S \cdot R_s + B \cdot R_b \qquad (4.1)$$

where:

$R_p$ = pixel level reflectance

$R_c$ = sunlit canopy reflectance

$R_b$ = sunlit background reflectance

$R_s$ = shadow reflectance

C = areal proportion of sunlit canopy

B = areal proportion of sunlit background

S = areal proportion of shadow

A system of equations similar to (4.1) was developed over all spectral bands from remotely sensed pixel level reflectance values (in this study, MMR band 3 red and band 4 NIR) together with input component reflectances, from which the unknown fractions were determined using a constrained least squares approach (Shimabukuro and Smith, 1991).

### 4.3.2. Component End-member Specification

Component end-member spectra ($R_c$,$R_b$,$R_s$) drive the SMA procedure, and therefore their quality is critical to the success of any spectral mixture analysis (Adams *et al.*, 1993). In this study, different approaches to obtaining each component spectra were used. Sunlit background reflectance (sphagnum moss) was obtained as an *in situ* reference end-member using measurements from a hand-held field radiometer. Shadowed background and shadowed canopy reflectances were assumed to be approximately equal to that of deep, clear lake, for which helicopter MMR image end-member spectra were available. However, there were no available spectral measurements of sunlit canopy structures - these are smaller than the MMR IFOV and were impractical for direct, hand-held radiometer measurements in the field. Instead, geometric-optical (G-O) canopy reflectance models were used to estimate values for $R_c$ at specified solar zenith angles. In this study, a simple cylinder model (Jasinski and Eagleson, 1989) was used, as well as more advanced models of canopy geometry based on a cone representation (Li and Strahler, 1985) and that of a spheroid with additional corrections for canopy mutual shadowing (Li and Strahler, 1992), which are particularly important at higher solar zenith angles and for denser stands. Sunlit canopy reflectance was estimated from each G-O model by solving equation (4.1) for $R_c$ at the maximum shadow point of pixel level reflectance for $R_p$ (minimum MMR red and NIR reflectance values), and using the

reference and image end-member spectra for $R_b$ and $R_s$, as above. Values of C, B and S were obtained for the maximum shadow point by running the G-O models over the full range of simulated canopy densities corresponding to the actual range of densities (ranging from 0.15 to 1.07 stems/$m^2$ for the SNF Black Spruce sites (Hall *et al.*, 1992)), from which the set of fractions were derived which correspond to the maximum shadow point in each case.

Since it is known that sunlit canopy reflectance increases with SZA (Li and Strahler, 1985, 1992; Barker Schaaf and Strahler, 1993; Syrén, 1994), $R_c$ was solved at individual SZA according to the time of MMR acquisition. These corrections are evaluated by comparing results to those obtained without such corrections.

### 4.3.3. Scene Fraction Validation

In many applications of spectral mixture analysis, it is difficult or impossible to determine the accuracy of the component fractions produced at sub-pixel resolutions. Although component end-member reflectance is often measured in the field, simultaneous ground truthing of their fractions over a given area (e.g. equivalent to a remote sensing system's IFOV) is confounded by factors such as canopy accessibility, understorey characteristics, tree size, distribution, and the spatial heterogeneity and arrangement of the components of interest. In this analysis, ground validation of component fractions was instead determined using nine high resolution helicopter photographs representing a gradient of Black Spruce stand densities in the Superior National Forest. The photos were acquired 12 August 1983, with the exception of site 14, which was taken 2 days later. All photos were taken near solar noon on these dates, at solar zenith angles of 33° and 34°.

The individual mixture components of interest to this study (sunlit canopy, sunlit background, shadow) are clearly evident in these 9 × 9 inch format photos (see Figure 3.2), from which it was possible to determine these fractions as 'ground truth' information for assessing the accuracy of scene fractions produced by SMA. This was done by overlaying, on each photograph, a transparent 16 $cm^2$ dense grid containing 400 cells of 2mm dimension, and tabulating the occurrence of components by cell. As a result of the low altitude of the helicopter platform (~120 m), some relief displacement was evident near the edges of the photographs. The size of the grid was chosen to minimise these effects, such that the fractions would be determined for essentially a nadir view with an orthographic projection for use with helicopter MMR data as well as with higher altitude C-130 Thematic Mapper Simulator (TMS) data and Landsat and SPOT satellite imagery of the SNF area. The dense grid was centered on the principal point of each air-photo to further reduce radial effects of the perspective projection, and oriented parallel to the direction of shadowing to aid visual interpretation. In most cases, the cell size was sufficiently small and the tree canopies sufficiently well defined such that only one component was present within a cell; in cases where this was not true, proportion counts of the observed components were recorded by cell and averaged over quadrants of 25 cells. In the original grid counts, both shadowed background and shadowed canopy components were counted, however these class counts were aggregated to be consistent with the shadow component used in this analysis.

This set of ground validation fractions provides an opportunity to independently assess both the importance of solar zenith angle effects, and to compare the use of different geometric-optical reflectance models for estimating component end-member reflectance

values. This is done in the following section, after which these factors are evaluated further in terms of predicting boreal forest biophysical parameters.

## 4.4. ANALYSIS OF SPECTRAL MIXTURE FRACTIONS

### 4.4.1 Accuracy Assessment of Component Fractions

In Table 4.1, the 'ground truth' grid fractions from the helicopter photos are compared to the fractions obtained from spectral mixture analysis of the helicopter MMR spectral data. In the SMA, cylinder, cone and spheroid models of sunlit canopy reflectance were used as separate inputs to the analysis. Each model was run for SZA=33°, corresponding to the SZA at the time of MMR data collection for the nine stands in the density gradient. For the individual results by site, the cone and spheroid model difference to grid fraction was better than the cylinder model for over two-thirds of the components tested. Results by component indicate that both the sunlit background and shadow fractions were determined with considerably greater accuracy using the spheroid and cone models compared to the cylinder model, while for sunlit canopy fraction, the spheroid model was best, followed by the cylinder and cone model. In terms of consistency among sites, the spheroid model produced the smallest standard deviations for both the sunlit canopy and shadow fraction.

Overall, the best results were obtained using the mutual shadowing spheroid model, as it had the smallest total mean difference from the ground truth data aggregated over the nine sites and averaged for the three components. Further, the overall standard deviation was also lowest for the spheroid model, which, when combined with the overall difference

results, illustrates how this model is the most appropriate representation of canopy geometry of the three models tested, both in terms of correspondence to grid fractions and with respect to its stability over the gradient of stand densities tested, expressed as a smaller

| Comparison of Cylinder, Cone, and Spheroid Geometric-Optical Models | | | | | |
|---|---|---|---|---|---|
| REFLECTANCE MODEL | Difference from Grid Fraction C | B | S | Fraction Total | Fraction Mean |
| Total Difference: | | | | | |
| CYLINDER | 0.810 | 0.710 | 1.010 | 2.530 | 0.845 |
| CONE | 0.920 | 0.370 | 0.700 | 1.990 | 0.665 |
| SPHEROID | 0.801 | 0.441 | 0.720 | 1.953 | 0.648 |
| Mean Difference: | | | | | |
| CYLINDER | 0.090 | 0.079 | 0.112 | 0.281 | 0.094 |
| CONE | 0.102 | 0.041 | 0.078 | 0.221 | 0.074 |
| SPHEROID | 0.089 | 0.049 | 0.080 | 0.217 | 0.072 |
| Standard Deviation: | | | | | |
| CYLINDER | 0.061 | 0.025 | 0.100 | 0.162 | 0.055 |
| CONE | 0.051 | 0.036 | 0.064 | 0.103 | 0.034 |
| SPHEROID | 0.042 | 0.030 | 0.071 | 0.098 | 0.033 |

Table 4.1. Cumulative differences between SMA scene fractions and grid count fractions ("ground-truth") for sunlit canopy (C), sunlit background (B), and shadow (S) components from spectral mixture analysis using cylinder, cone and spheroid geometric-optical models of sunlit canopy end-member reflectance. Results from Helicopter MMR spectra of 9 Black Spruce sites along a gradient of stand densities; solar zenith angle = 33° in all cases. Results shown represent totals over 9 sites, where the maximum difference per site equals 1.0, corresponding to the maximum fraction value of 1.0 (or 100% spatial coverage for a given component).

variability in the magnitude of error over all sites. The results of these tests also show the importance of component signature estimation - in this case, the sunlit background and shadow reflectance values were held constant, while only the sunlit canopy reflectance was varied according to the geometric-optical model outputs. Differences in one input set of reflectance values result in significant differences among all component fractions generated through the spectral mixture analysis.

### 4.4.2 Effect of Solar Zenith Angle on Component Fraction Accuracy

Table 4.2 provides results on the effect of solar zenith angle on the accuracy of component fractions derived from SMA, for the cylinder, cone and spheroid G-O models of canopy reflectance. Of the 9 sites in the density gradient with grid-counted fractions, only site 14 had additional MMR data collected over a range of SZAs; MMR data for the other 8 sites were at SZA=33° only. Therefore, a detailed study of SZA effects is only possible for site 14 - a dense, mature stand of black spruce trees averaging 60 feet in height (Hall *et al.*, 1992). Results corrected for SZA from all three G-O models driven by MMR site 14 pixel reflectances were obtained for the SZA range 30°-37°. To evaluate the importance of SZA corrections, results were also obtained over the full range of SZA using a constant $R_C$, from which the differences to grid fractions were averaged from individual MMR reflectances acquired at each of 6 SZA median intervals from 30°-75°, at 7° increments, to produce results without SZA corrections.

Table 4.2 shows the importance of correcting for SZA. For the cylinder model, SZA corrections produced better results for 2 of the 3 components, and also for the overall case in which the component differences were totaled and combined by averaging. For

both the cone and spheroid models, considerably better correspondence was also found between SMA scene fractions and grid count ground truth fractions when SZA corrections

| Solar Zenith Angle Effects on Forest Component Fraction Accuracy | | | | | | |
|---|---|---|---|---|---|---|
| REFLECTANCE MODEL | SZA | Difference from Grid Fraction C | B | S | Total | Average |
| CYLINDER | 30°-75° | 0.140 | 0.200 | 0.060 | 0.400 | 0.133 |
| CYLINDER | 30°-37° | 0.045 | 0.128 | 0.155 | 0.329 | 0.109 |
| CONE | 30°-75° | 0.150 | 0.076 | 0.092 | 0.318 | 0.106 |
| CONE | 30°-37° | 0.093 | 0.071 | 0.025 | 0.189 | 0.063 |
| SPHEROID | 30°-75° | 0.143 | 0.068 | 0.105 | 0.315 | 0.105 |
| SPHEROID | 30°-37° | 0.093 | 0.057 | 0.037 | 0.187 | 0.062 |

Table 4.2. Forest component fractions from Helicopter MMR reflectance data at different solar zenith angle (SZA) ranges for sunlit canopy (C), sunlit background (B), and shadow (S) components from cylinder, cone and spheroid geometric-optical reflectance models of sunlit canopy end-member reflectance ($R_c$). Component fractions averaged over given SZA range and compared with grid counts ("ground truth") at SZA 33° for SNF Black Spruce site 14. Values shown are areal fractions, with a maximum possible value of 1.0.

are applied. For each model, improvements are found for all three of the forest components sunlit canopy, sunlit background, and shadow, compared to the results

without SZA corrections. The largest improvements realised through the SZA corrections were for the shadow fraction, with the two smallest overall differences found for shadow fraction produced by the cone and spheroid models corrected for SZA. The high correspondence of shadow fraction with ground data is quite significant since, as we shall see in the next section, shadow fraction is the most important component for predicting forest biophysical variables. The best overall results were obtained from the spheroid model with SZA corrections (overall difference of 0.187), while the cone model corrected for SZA also performed quite well. The uncorrected cone model and the cylinder model for SZA=30°-37° were similar, while the uncorrected cylinder model had the largest divergence values of the six models tested.

These comparisons are consistent with the results from Table 4.1, which showed the spheroid model to be superior to the other two G-O models in terms of component signature estimation and the mixture fractions produced. However, it is interesting to note that, in comparisons between the cone and spheroid results in Table 4.2, larger improvements are produced from the correction for SZA than by the use of a more sophisticated model. The average difference attributed to SZA corrections applied to both the cone and spheroid models is 0.129, while the improvement found by using the spheroid model compared to cone (for both the SZA corrected and uncorrected cases) is not as great. Individual results by component show greater improvements through use of the more sophisticated spheroid model, as discussed earlier, however, this set of results clearly shows that it is very important to consider the solar zenith angle of spectral measurements when estimating component reflectance signatures using geometric-optical models for input to spectral mixture analyses.

## 4.5. PREDICTING FOREST BIOPHYSICAL VARIABLES

### 4.5.1. Comparison of Canopy Reflectance Model Inputs to SMA

Tables 4.3 - 4.5 present results of relating the forest component fractions and the biophysical structural variables biomass, LAI, and NPP for 149 MMR data acquisitions over a variety of SZAs for all 31 black spruce sites. In all cases, solar zenith angle corrections were applied, following the results obtained in the previous section in which a greater correspondence to ground truth data was found when such corrections were applied. In this section, different models of canopy geometry, used for the purpose of deriving one of the three end-member reflectance values (sunlit canopy) for input to the spectral mixture analysis, are evaluated and compared in terms of the resulting ability to predict forest biophysical variables. Linear regression analysis is used to test the relationships between the spectral mixture fractions and biophysical variables, with a level of significance of $\alpha = 0.05$ used for all regressions reported in this Chapter.

The results from the cylinder model are shown in Table 4.3. In general, the magnitude of $r^2$ coefficients is low to moderate, and these often tended to vary in strength of relationship at different SZA. Further, in many cases the results also vary by component, with no clear trend evident as to a preferred component or solar zenith angle. A possible reason for these varied results is the relative simplicity of using a cylinder model of boreal conifers. In particular, the cylinder model does not provide a realistic treatment of shadows since it fails to recognise shadowed crown as shadow, particularly at higher SZA. These results show the overall limitations of the cylinder model itself as a representation of boreal forest canopy geometry.

| REFLECTANCE MODEL | | BIOMASS | | NPP | | LAI | |
|---|---|---|---|---|---|---|---|
| | | $r^2$ | S.E. | $r^2$ | S.E. | $r^2$ | S.E. |
| **CYLINDER** | | | | | | | |
| SZA=30° | C | 0.34 | 3.40 | 0.47 | 0.11 | 0.48 | 0.84 |
| | B | 0.66 | 2.40 | 0.76 | 0.07 | 0.76 | 0.57 |
| | S | 0.34 | 3.40 | 0.25 | 0.13 | 0.24 | 1.01 |
| SZA=45° | C | 0.20 | 3.93 | 0.22 | 0.12 | 0.22 | 0.99 |
| | B | 0.76 | 2.17 | 0.80 | 0.06 | 0.78 | 0.53 |
| | S | 0.52 | 3.03 | 0.54 | 0.10 | 0.52 | 0.78 |
| SZA=60° | C | 0.60 | 2.99 | 0.66 | 0.11 | 0.60 | 0.94 |
| | B | 0.55 | 3.19 | 0.62 | 0.11 | 0.66 | 0.86 |
| | S | 0.42 | 3.60 | 0.49 | 0.13 | 0.57 | 0.98 |

Table 4.3. Linear regression analyses of forest component fractions (C,B,S) with biomass, NPP, and LAI. Component fractions derived from spectral mixture analysis using cylinder G-O models of sunlit canopy end-member reflectance ($R_c$). Results obtained using values of $R_c$ computed individually for each SZA. A level of significance of $\alpha = 0.05$ was used for all regressions shown.

The results using the cone and spheroid models are provided in Tables 4.4 and 4.5. In almost all cases, the $r^2$ values from the cone and spheroid models provided better results than the cylinder model. The magnitude of $r^2$ values were generally low to moderate with the cylinder model, whereas the cone and spheroid results were considerably higher. In terms of individual component fractions, the cylinder and cone models both exhibit more variability among fractions. For example, the best results with the cylinder model were found for sunlit background fractions at lower SZA, with mixed results found for the other two components. The cone and spheroid models were more consistent in that each produced the highest $r^2$ values with shadow fraction, except for the cone model at SZA=60° for which the results vary by component for each variable considered. The

spheroid model produced the most consistent and highest results by individual components over the full range of SZA. In all cases, the shadow fraction produced the best $r^2$ result for a given variable and sun angle, while the sunlit background and sunlit canopy values were always the second and third highest results, respectively. This consistency is quite important, since it provides a more substantive result from which it is possible to recommend the use of a given model and a particular component fraction over a variety of solar zenith angles, compared to the other models for which no clear trend emerges as to which component is optimal for a given model or set of sun angles.

| REFLECTANCE MODEL | | BIOMASS | | NPP | | LAI | |
|---|---|---|---|---|---|---|---|
| | | $r^2$ | S.E. | $r^2$ | S.E. | $r^2$ | S.E. |
| **CONE** | | | | | | | |
| SZA=30° | C | 0.34 | 3.40 | 0.47 | 0.11 | 0.48 | 0.84 |
| | B | 0.65 | 2.48 | 0.75 | 0.08 | 0.75 | 0.58 |
| | S | 0.73 | 2.16 | 0.76 | 0.07 | 0.76 | 0.57 |
| SZA=45° | C | 0.20 | 3.93 | 0.22 | 0.12 | 0.22 | 0.99 |
| | B | 0.70 | 2.41 | 0.74 | 0.07 | 0.72 | 0.59 |
| | S | 0.81 | 1.92 | 0.85 | 0.05 | 0.82 | 0.47 |
| SZA=60° | C | 0.60 | 2.99 | 0.66 | 0.11 | 0.60 | 0.94 |
| | B | 0.55 | 3.16 | 0.63 | 0.11 | 0.67 | 0.86 |
| | S | 0.51 | 3.31 | 0.59 | 0.12 | 0.64 | 0.89 |

Table 4.4. Linear regression analyses of forest component fractions (C,B,S) and biophysical variables. Component fractions derived from spectral mixture analysis using a cone based geometric-optical reflectance model of sunlit canopy end-member reflectance ($R_C$) derived separately at three solar zenith angles (SZA). A level of significance of $\alpha = 0.05$ was used for all regressions shown.

In comparing the cone and spheroid results, it is apparent that at SZAs of 30° and 45°, the results are similar, with the spheroid model providing slightly higher overall $r^2$ values for a given SZA and biophysical variable in cases where the results differ. However, at SZA=60°, the spheroid model is clearly superior to both the cone and cylinder model results. This can be attributed to the improved representation of canopy geometry through the use of spheroids instead of cones or cylinders, and, in particular, the explicit formulations to account for mutual shadowing amongst adjacent crowns which occur with increased frequency at higher SZA (Li and Strahler, 1992). These improvements found at higher SZA are of particular significance to studies in the boreal forest, since these ecosystems are found at higher latitudes where solar zenith angles are higher in comparison to lower latitudes. Further, since it is sometimes desirable to use winter time imagery of forested areas to maximise the spectral contrast between the snow covered forest floor and the exposed tree canopy, a sophisticated treatment of high SZA shadowing would be critical to the analysis owing to the particularly high zenith angles during that time of year. The mutual shadowing spheroid geometric-optical model by Li and Strahler (1992) has been specifically designed to handle cases such as this. In addition to this, the spheroid model can also be used over a variety of view zeniths. Although this analysis is concerned only with nadir view angle imagery, the ability to advance the approaches developed here to other types of imaging systems represents a natural next step in the evolution of this research. Off-nadir and multi-angle imaging systems are available from both satellite and airborne platforms, and these configurations will become increasingly available in future sensor systems such as EOS to take advantage of the increased information content offered through a more thorough characterisation of bidirectional reflectance properties of surface targets.

| REFLECTANCE MODEL | | BIOMASS | | NPP | | LAI | |
|---|---|---|---|---|---|---|---|
| | | $r^2$ | S.E. | $r^2$ | S.E. | $r^2$ | S.E. |
| **SPHEROID** | | | | | | | |
| SZA=30° | C | 0.34 | 3.40 | 0.47 | 0.11 | 0.48 | 0.84 |
| | B | 0.62 | 2.56 | 0.73 | 0.08 | 0.73 | 0.60 |
| | S | 0.73 | 2.16 | 0.76 | 0.07 | 0.76 | 0.57 |
| SZA=45° | C | 0.19 | 3.74 | 0.21 | 0.12 | 0.20 | 0.98 |
| | B | 0.68 | 2.33 | 0.72 | 0.07 | 0.69 | 0.61 |
| | S | **0.83** | **1.73** | **0.86** | **0.05** | **0.82** | **0.46** |
| SZA=60° | C | 0.21 | 3.82 | 0.38 | 0.12 | 0.40 | 1.01 |
| | B | 0.61 | 2.68 | 0.76 | 0.08 | 0.78 | 0.62 |
| | S | 0.65 | 2.53 | 0.77 | 0.07 | 0.79 | 0.61 |

Table 4.5. Linear regression analyses of forest component fractions (C,B,S) and biophysical variables. Component fractions derived from spectral mixture analysis using spheroid geometric-optical reflectance models of sunlit canopy end-member reflectance ($R_c$) derived separately at three solar zenith angles (SZA). Numbers in bold denote best result over all models tested (Tables 4.3 - 4.5) for each biophysical variable. A level of significance of $\alpha = 0.05$ was used for all regressions shown.

In terms of the overall ability for predicting variables related to boreal forest photosynthetic activity, the best results for all three biophysical variables were obtained, in each case, from the shadow fraction using the spheroid model corrected for SZA=45°. Linear regression analyses showed that biomass could be estimated with $r^2$ values of 0.83 and a standard error (S.E.) of 1.7 kg/m$^2$; LAI: $r^2$=0.82, S.E.=0.46; and NPP: $r^2$=0.86, S.E.=0.05 kg/m$^2$/year. For biomass, LAI and NPP, these S.E. values were the lowest

obtained for all models and all SZAs. These results are quite positive and significant in terms of the absolute magnitude of predictive capability expressed through the $r^2$ coefficients. They also represent significant improvements to the results reported by Hall *et al.* (1995) in which the shadow fraction was determined to be the best component, from which biomass was estimated with a standard error of 2.0 kg/m$^2$ and a $r^2$ value of 0.76; LAI estimates had a standard error (S.E.) of 0.58, and $r^2$=0.72; and NPP: S.E.=0.07 kg/m$^2$/year, $r^2$=0.74.

The forest component fractions derived from spectral mixture analysis in this analysis are clearly related and highly suitable for predicting the biophysical variables of interest. In particular, the shadow fraction was found to be optimal for predicting biophysical variables over a full range of stand densities. The physical basis from which shadow fraction is expected to be more robust over a variety of stand densities and SZAs stems from its greater sensitivity to tree size and morphology. The other forest components are less indicative of tree size, since, for even-aged stands (which typify many forested settings), sunlit canopy fraction will tend to be more constant over a variety of tree sizes, while sunlit background fraction will become smaller and more prone to error with larger trees and denser stands. Essentially, as the number of trees increase per unit area, there will be more sunlit canopy, more shadow, and less sunlit background, and these should be related to increasing biomass for stands of low to moderate density. However, at higher biomass densities where the trees are larger and more numerous, the amount of sunlit canopy does not increase in relative proportion to the increase in biomass, due to shadowing amongst trees. Further, in this case where shadow includes both background shadow and shadowed canopy, at higher densities the shadow fraction will be primarily canopy shadow because less background (sunlit or shadowed) will be visible, while at

lower stand densities, where most tree shadow is directed to the background, the shadow component will be primarily background shadow. Either way, the amount of shadow will vary more with tree size over a larger range of stand densities compared to the other component fractions. Since tree size directly conditions biomass amount, this greater sensitivity to tree size explains why shadow fraction is optimal. In this section, shadow fraction was also shown to be more robust over a variety of tree sizes, stand densities and canopy geometries. This explains why shadow fraction produced the best results in relation to the set of biophysical parameters tested.

As a result, geometric-optical models with more realistic representations of canopy shadow are preferable for these objectives. Consistent with this, the theoretical basis for the geometric-optical mutual shadowing model by Li and Strahler (1992) has been shown, in practice, to provide an appropriate model of canopy geometry for providing good estimates of sunlit canopy reflectance for input to the spectral mixture analyses.

### 4.5.2. Comparison of Spectral Mixture Analysis and Vegetation Indices

Having developed a methodology for estimating forest biophysical variables based on spectral mixture analysis and presenting a series of results using that approach, it is now of interest to explore how these results compare to more traditional ways of biophysical parameter estimation. As discussed earlier, vegetation indices have been the most common method for estimating forest biophysical variables, and therefore in this section a full vegetation index analysis is presented and compared to the results from the spectral mixture analysis presented earlier in this Chapter.

In this section, the normalised difference vegetation index (NDVI) was computed for the full set of MMR sites, using the formula:

$$NDVI = \frac{MMR_{NIR} - MMR_{RED}}{MMR_{NIR} + MMR_{RED}} \qquad (4.2)$$

After NDVI was computed, a linear regression analysis of NDVI with biomass, LAI and NPP was performed over the full set of MMR sites. The analysis was done for all SZA, and also for three 7° SZA ranges centered at 30°, 45° and 60° for the sake of direct comparison with mixture analysis results in previous sections, even though the computation of NDVI is the same regardless of SZA.

The results of the analysis using NDVI are shown in Table 4.6. None of the results indicate a strong predictive capability among NDVI and any of the biophysical variables at any of the three ranges of SZA analysed.

| NDVI | BIOMASS | | NPP | | LAI | |
|---|---|---|---|---|---|---|
| | $r^2$ | S.E. | $r^2$ | S.E. | $r^2$ | S.E. |
| SZA = 30° | 0.39 | 3.25 | 0.53 | 0.10 | 0.54 | 0.79 |
| SZA = 45° | 0.44 | 3.11 | 0.46 | 0.10 | 0.44 | 0.82 |
| SZA = 60° | 0.37 | 3.41 | 0.56 | 0.10 | 0.60 | 0.83 |

Table 4.6. Linear regression coefficients ($r^2$) and standard error (S.E.) for NDVI with biomass, net primary productivity (NPP), and leaf area index (LAI). Results shown for MMR data collected at solar zenith angles ranging from 30° to 60°. A level of significance of $\alpha = 0.05$ was used for all regressions shown.

Table 4.7 provides more detailed results as it reports different SZA used in the three canopy geometric-optical reflectance models as part of the SMA. Clearly, SZA is important in the overall rankings obtained. In virtually all cases, the best results from SMA were obtained when sunlit canopy reflectance was estimated using canopy models run at SZA=45°. Similarly, the spheroid-based geometric-optical mutual shadowing (GOMS)

| **BIOMASS** | | **NPP** | | **LAI** | |
|---|---|---|---|---|---|
| Ranking | $r^2$ | Ranking | $r^2$ | Ranking | $r^2$ |
| 1. SMA-GOMS 45° | 0.83 | 1. SMA-GOMS 45° | 0.86 | 1. SMA-GOMS 45° | 0.82 |
| 2. SMA-CONE 45° | 0.81 | 2. SMA-CONE 45° | 0.85 | 2. SMA-CONE 45° | 0.82 |
| 3. SMA-CYL 45° | 0.76 | 3. SMA-CYL 45° | 0.80 | 3. SMA-GOMS 60° | 0.79 |
| 4. SMA-GOMS 30° | 0.73 | 4. SMA-GOMS 60° | 0.77 | 4. SMA-CYL 45° | 0.78 |
| 5. SMA-CONE 30° | 0.73 | 5. SMA-GOMS 30° | 0.76 | 5. SMA-GOMS 30° | 0.76 |
| 6. SMA-CYL 30° | 0.66 | 6. SMA-CONE 30° | 0.76 | 6. SMA-CONE 30° | 0.76 |
| 7. SMA-GOMS 60° | 0.65 | 7. SMA-CYL 30° | 0.76 | 7. SMA-CYL 30° | 0.76 |
| 8. SMA-CONE 60° | 0.60 | 8. SMA-CONE 60° | 0.66 | 8. NDVI 60° | 0.60 |
| 9. SMA-CYL 60° | 0.60 | 9. SMA-CYL 60° | 0.66 | 9. SMA-CONE 60° | 0.60 |
| 10. NDVI 45° | 0.44 | 10. NDVI 60° | 0.56 | 10. SMA-CYL 60° | 0.60 |
| 11. NDVI 30° | 0.39 | 11. NDVI 30° | 0.53 | 11. NDVI 30° | 0.54 |
| 12. NDVI 60° | 0.37 | 12. NDVI 45° | 0.46 | 12. NDVI 45° | 0.44 |

Table 4.7. Results from linear regression analysis for predicting biophysical variables from NDVI and spectral mixture analyses at different solar zenith angles. Spheroid-based geometric-optical mutual shadowing (GOMS), and cone and cylinder (CYL) models of canopy geometry were tested in the SMA. Rankings shown by SZA and for all 12 test cases (ties resolved based on standard error values, not shown). A level of significance of $\alpha = 0.05$ was used for all regressions shown.

model provided better results compared to the cone and cylinder representation of canopy geometry. As with the overall results, NDVI was ranked in the last three positions in all but one case. It is clear from these results that (i) NDVI is not capturing the full information content available from these remotely sensed data sets in terms of biophysical variables, and (ii) the spectral mixture fractions provide significantly improved results which are consistent over a range of solar zenith angles and forest stand densities.

Table 4.8 presents a summary of overall results obtained from mixture analysis and NDVI. In both cases, results are shown for the analysis of all black spruce stands over the full range of solar zenith angles. Since the SMA results were obtained at specific SZA, they were averaged to obtain the reported summary values. For all three biophysical parameters, overall results show that SMA provides significantly better correspondence with biophysical parameters compared to NDVI.

| APPROACH | BIOMASS | | NPP | | LAI | |
|---|---|---|---|---|---|---|
| | $r^2$ | S.E. | $r^2$ | S.E. | $r^2$ | S.E. |
| SMA | 0.74 | 2.14 | 0.80 | 0.06 | 0.79 | 0.55 |
| NDVI | 0.40 | 3.26 | 0.47 | 0.11 | 0.47 | 0.85 |

Table 4.8. Overall results summarised from linear regression coefficients ($r^2$) and standard error (S.E.) for NDVI and spectral mixture analysis (SMA) with biomass, net primary productivity (NPP), and leaf area index (LAI). Results from all MMR data with solar zenith angles ranging from 30° to 60°. SMA results from shadow fraction using a spheroid model of canopy geometry. A level of significance of $\alpha = 0.05$ was used for all regressions shown.

## 4.6. CHAPTER SUMMARY

In this chapter, the viability of spectral mixture analysis has been demonstrated for deriving component scene fractions in boreal forest terrain for the purpose of predicting

forest biophysical variables. Particular attention was given to the methods of spectral end-member specification and also to creating a method to assess the accuracy of mixture fractions as a means for quantitatively validating forest scene components produced in the analysis. Several different canopy geometric optical reflectance models were used to derive sunlit canopy reflectance for input to the analysis, and these were compared both in terms of mixture fraction accuracy and the effects of accounting for solar zenith angle and with respect to predicting forest biophysical variables. From those assessments, and from linear regression analyses of forest biophysical variables, it was found that the spheroid model was superior to the cone and cylinder models; that it is important to account for SZA; and that the shadow fraction is optimal for predicting biophysical variables. In particular, the spheroid model for estimating sunlit canopy end-member reflectances produced the most consistent results amongst the forest components, while providing significantly improved results at higher solar zenith angles which typify boreal forest latitudes. A common vegetation index, NDVI, was also derived for the SNF data set and compared to the SMA approach for estimating biophysical parameters. Spectral mixture analysis provided significantly improved results in all cases compared to the results provided by NDVI.

Having shown that the concept of using individual forest components is an attractive approach for estimating biophysical variables in boreal forests, the next step in this research is to apply these ideas to the regional scale. In so doing, the true power of remote sensing over vast areas can be realised. However, in considering much larger areas, new challenges and important factors are introduced to the analysis. Building on the results from this Chapter, these challenges are addressed in the next Chapter where new methods for regional scale analysis of boreal forest biophysical parameters are presented for a 10,000 $km^2$ area of forest as part of the Boreal Ecosystem-Atmosphere Study (BOREAS).

# CHAPTER V

# A REGIONAL SCALE METHODOLOGY FOR THE BOREAL ECOSYSTEM ATMOSPHERE STUDY (BOREAS)

## 5.1 INTRODUCTION

In the previous Chapter, a methodology based on spectral mixture analysis was validated at the forest stand level using low altitude imagery for homogeneous forests over a range of densities. In this Chapter, the issue of performing similar analyses at the regional scale is considered. It will be shown that, while the concept of computing sub-pixel scale mixture fractions holds, the methods used to achieve this at the regional scale are different than that demonstrated at the scale of forest stands. In this work, a methodology for regional scales is presented for applying the concepts of spectral mixture analysis, but set within the framework of a physical approach to the problem first documented in Hall (1996) and Hall *et al.* (1996), and linked here to a knowledge-based evidential reasoning framework modified from Peddle (1995a,b) which now integrates geometric-optical reflectance models (Li and Strahler, 1992) directly into the analysis. In this Chapter, the issues of scaling to regional areas are first addressed, following which an outline of the overall methodology is presented. Details of the method are then presented as part of the Boreal Ecosystem Atmosphere Study (BOREAS). The study area and field data collection methods are described, and followed by a presentation of laboratory and computer methods for processing the extensive set of field spectrometer data collected

during two BOREAS field campaigns. The use of geometric-optical reflectance models as part of the methodology is then described, and followed by a presentation of a new software implementation which provides an integrated land cover and biophysical estimation capability. As the methodology is somewhat involved, a full Chapter has been devoted to its description, with results of applying this methodology placed in Chapter VI. A general overview of this methodology is provided as part of the discussion which addresses scaling issues, presented next.

## 5.2 REGIONAL SCALE CLASSIFICATION AND BIOPHYSICAL ESTIMATION ISSUES

### 5.2.1 Issues from Forest Stand to Regional Scales

At the forest stand scale, spectral mixture analysis was shown in Chapter IV to provide forest scene components at sub-pixel scales that were useful predictors of forest biophysical variables. However, the true power of remote sensing lies in the ability to provide consistent information over broad, synoptic scales. It is at these scales where many important environmental processes can be studied, yet these scales are largely inaccessible by means other than satellite remote sensing. Unfortunately, the application of remote sensing image analysis methods from larger scales to smaller scales is not always straight forward, creating the need for sophisticated methods particularly for more complex applications (Franklin, 1995). When moving to larger study areas, it is often appropriate to use coarser spatial resolution imagery as these will usually provide greater spatial coverage. However, in doing so, pixel level information is reduced, and further, the incidence of spectral mixing within a pixel area will increase. Regional scale sensors often have a lower

spectral resolution and, as they are acquired at satellite altitudes, often require atmospheric correction if more complex information is to be extracted.

In terms of the estimation of biophysical parameters being studied here, a key consideration is the need to know land cover type as part of the biophysical estimation process. In the SNF study, all forest stands considered were black spruce and so a land cover stratification was implicit to that analysis (Peddle *et al.*, 1996b). However, over any large forested area, variability of land cover types is common, with the North American boreal forest no exception as it comprises a patchwork of coniferous and deciduous forest stands of varying species, age classes and stand densities, as well as occurrences of mixed forest land cover. As reviewed earlier, most of the work done in the area of biophysical parameter estimation has relied on the use of vegetation indices. At regional scales, the need for prior land cover information has usually been met by first doing a land cover classification and then, within each land cover class, developing relationships between a vegetation index and the biophysical parameters of interest. This approach is explored in the next section where BOREAS NDVI and LAI data are presented and evaluated. However, in addition to the problems illustrated in Chapter IV with NDVI at the forest stand level, which also hold at more regional scales, the added need for land cover classification further complicates the issue. The methods used for land cover classification typically rely upon statistical supervised classification techniques such as the maximum likelihood algorithm in which training areas are identified for each forest class. One of the advantages of this approach is that no physical understanding of the forest stands is required. Instead, in the creation of training sites the analyst selects representative pixels for each class without direct reference or need for any forest mensuration data. However, there are several problems with this approach. Firstly, the possibility of bias in training data

exists due to factors such as ground sampling schemes (inaccessibility to certain areas), reference and image co-registration error, and the chance location of pixels included in a sample, all of which may result in misrepresentation of certain attributes of a forest class (e.g. an over representation of higher density stands, resulting in classification error for lower density occurrences of that forest class). It is more difficult to specify a comprehensive training sample which represents the full range of variability which characterises a class, yet from a statistical standpoint, this is the requirement of the algorithm. Further, statistical classifiers such as maximum likelihood require that the data adhere to the Gaussian (normal) distribution, however, as we shall see later, the spectral properties of forest stands at the scale of satellite pixels can be highly non-linear and do not always follow a normal distribution. Another problem with the training data approach is that a sample derived from one date or area is likely unsuitable for use at another time of year, or even at a different study site. This is because training samples are site specific, and are therefore less amenable to larger, regional or global scale applications or multi-temporal studies where the generation of adequate training samples can become prohibitive. Also, there is no explicit way of dealing with variations in forest understorey, canopy structure, optical properties, and other environmental factors, nor is there a way of specifying important sun-sensor-view angles or topographic variations which may further affect pixel level reflectance. All of these problems point to a need for a physical understanding and characterisation of forest stands to provide improved classifications and biophysical estimates beyond that provided by empirically based training and vegetation index methods. In particular, given the physical and structural nature of the biophysical parameters being estimated, a physical understanding and specification of forest targets would seem to be implicit to a successful approach. Prior to exploring such an approach, however, we first evaluate the relationships between BOREAS NDVI and LAI data to illustrate the problem.

5.2.1.1 Graphic Evaluation of Vegetation Indices and LAI

Prior to exploring a physical approach to the remote estimation of biophysical parameters, it is useful to first evaluate vegetation index data with respect to biophysical information since this is a common approach to the problem. This evaluation is achieved here using graphic plots of NDVI and LAI data from BOREAS. For the purpose of this initial qualitative analysis, leaf area index has been chosen for evaluation as this is one of the more important biophysical variables of interest (Running and Hunt, 1993). Later, these relationships are explored extensively and quantitatively using a full regression analysis involving a variety of remote sensing products and biophysical variables (§6.3). As part of that full analysis, the methods of acquiring and processing the full biophysical and remotely sensed data set (including vegetation indices) are described in detail. However, for the purpose of this initial evaluation of the NDVI vegetation index, these details are less important here and instead we focus on illustrating these relationships and identifying any potential problems that may exist.

As discussed earlier, it is important to stratify the forest landscape by land cover class prior to performing a biophysical analysis. Therefore, in this evaluation of NDVI and LAI data, the data were first categorised into the four major forest cover classes in BOREAS. These classes are Old Black Spruce (OBS), Old Jack Pine (OJP), mixed forest (MIX), and Old Aspen (OA). As the full data set was quite large, a smaller number of sites was sampled randomly from the set of tower flux and auxiliary sites to provide a reasonable number of data points for graphic display and interpretation. By evaluating the scatter of plotted data for each class, we can obtain early insight into the utility of vegetation indices for predicting biophysical variables. The results of plotting LAI and NDVI data for each major forest class are shown in Figures 5.1 - 5.4. In the case of OBS (Figure 5.1),

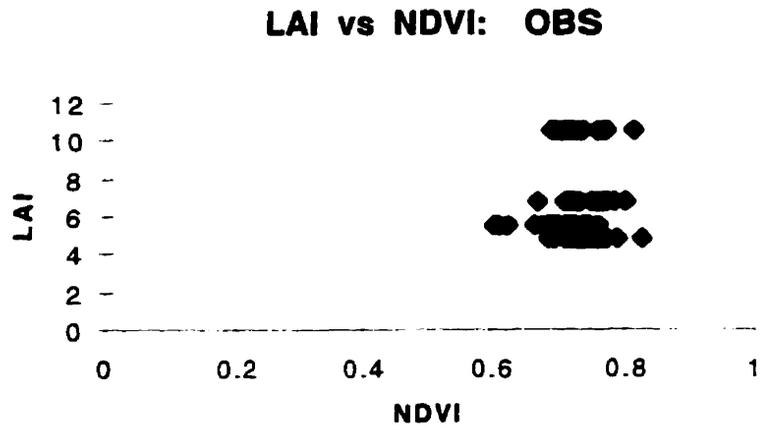


Figure 5.1. Plot of LAI data versus NDVI from a sample of BOREAS Old Black Spruce (OBS) sites.

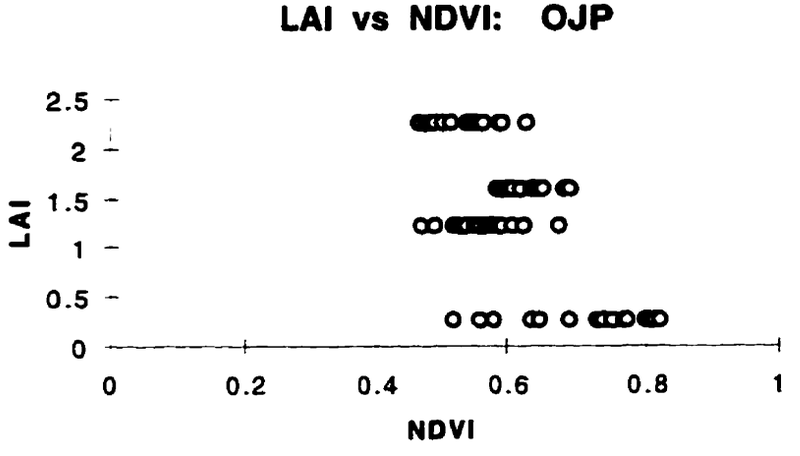


Figure 5.2. Plot of LAI data versus NDVI from a sample of BOREAS Old Jack Pine (OJP) sites.

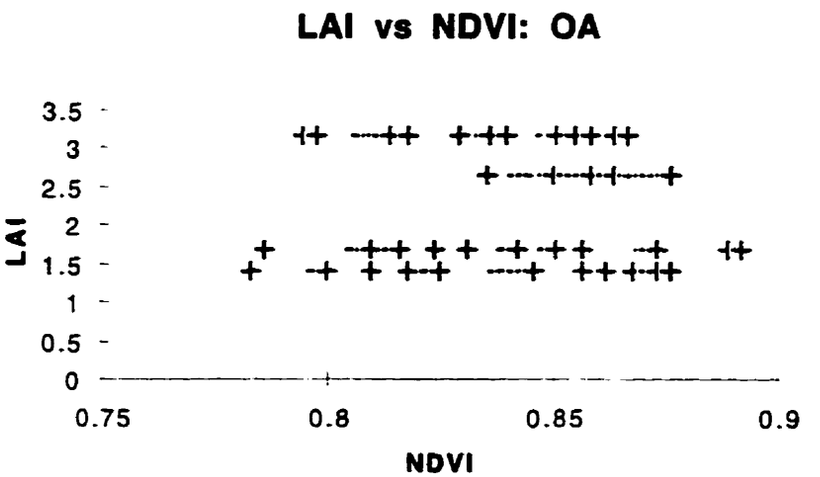


Figure 5.3. Plot of LAI data versus NDVI from a sample of BOREAS Old Aspen (OA) sites.

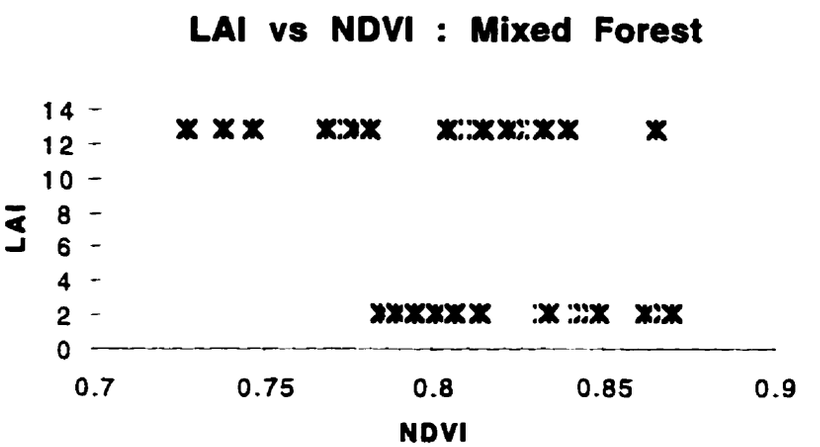


Figure 5.4. Plot of LAI data versus NDVI from a sample of BOREAS mixed forest sites.

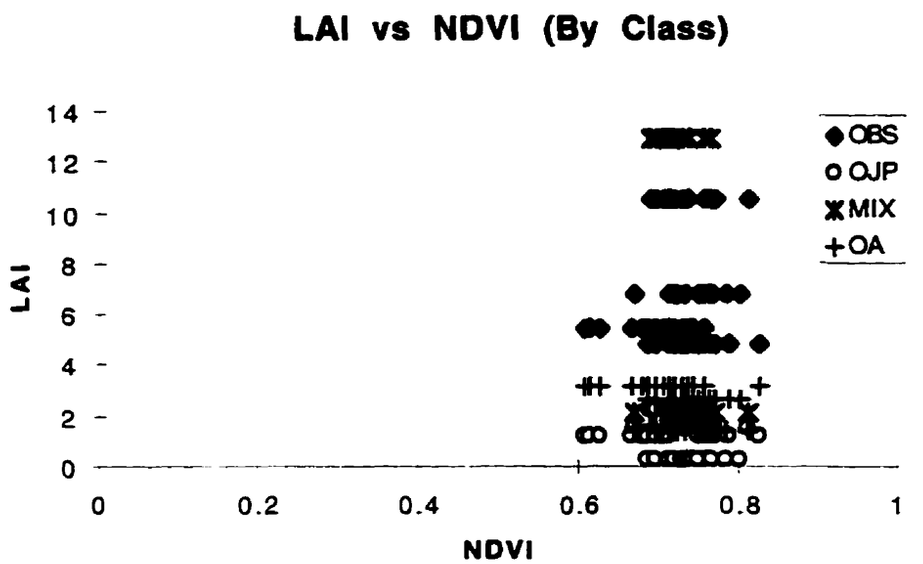


Figure 5.5. Summary plot of LAI data versus NDVI from a sample of BOREAS sites from the four major forest cover classes.

the NDVI data appear to range between 0.6 and 0.8 with no apparent trend associated with changing LAI values, which vary between 4 and 12. At each LAI value, almost the entire range of NDVI values are found. This suggests that NDVI may not provide adequate information content for predicting LAI throughout the range of values in the sample. The same is true for the other three classes. In the case of OJP (Figure 5.2), there appears to be a slight trend of decreasing NDVI with increasing LAI, however, as with OBS, the spread of NDVI values at any given LAI point would suggest that any predictive capability may be weak, at best. The Old Aspen plot (Figure 5.3) contains a considerable amount of scatter, with the mixed forest graph (Figure 5.4) also showing no distinct pattern between NDVI and LAI. This latter result would not be unexpected given the apparent unsuitability of NDVI for predicting LAI for the other three classes. In Figure 5.5, the full data set from all four classes is displayed together, with different classes plotted with different symbols.

This plot serves to summarise the observations made from the individual class plots. In this figure, we see the full range of LAI values represented, yet at each LAI value the values of NDVI appear to range from the minimum NDVI value of 0.60, to a maximum of about 0.82. From this initial qualitative analysis of plotted NDVI and LAI values, it appears that a different approach is needed to provide improved estimates of biophysical variables such as LAI. In the next section, a physically based approach is presented which addresses a number of the theoretical and empirical problems encountered with vegetation indices that have been discussed earlier in the thesis, and which have been observed from the results of this evaluation of NDVI data in BOREAS.

### 5.2.2 Overview of Methodology: a Physically Based Approach

In this research, an alternative methodology has been implemented which involves a physically based approach to land cover classification and biophysical parameter estimation first documented by Hall (1996) and Hall *et al.*, (1996) and set within the processing environment of an evidential reasoning image processing software package modified from Peddle (1995a,b). The approach implemented here is designed to address, explicitly and directly, problems identified above with the statistical supervised training and vegetation index methods. The method pursued here builds on the work presented in Chapter IV, however, it is somewhat different in that several new aspects have been required. The spectral mixture analysis approach, and, in particular, the need to provide forest component fractions for predictive estimates of biophysical parameters forms the conceptual basis for the regional scale application presented here. However, spectral mixture analysis, by itself, was deemed to be incomplete for providing a full land cover and biophysical analysis. The main reason is that, in terms of providing a suitable regional scale classification, a relatively large number of classes are involved, however, not all of these classes are suitable for mixture analysis, and further, the necessary end-member spectra were neither collected nor were available for such a purpose. Additionally, the number of end-members required for all classes would be excessive for a mixture analysis, making it impossible to solve the system of equations necessary to determine scene fractions. Additionally, as the goal is to include an explicit physical basis to the new approach, this would not be possible using spectral mixture analysis alone. However, as was seen in the previous Chapter, SMA can be used in conjunction with canopy geometric-optical reflectance models which provide a physical description of forest canopies in relation to stand level and individual forest component reflectance values. This has led to the development of an alternate method for

providing a linked, physically based land cover classification and biophysical parameter estimation approach.

The regional scale methodology applied in this research uses canopy reflectance models to generate forest reflectance values which characterise different forest land cover classes. These modelled values effectively serve and replace the role of training data. In this work, the classification and biophysical parameter estimation information has been integrated into a knowledge-based evidential reasoning image processing framework which has been substantially modified to deal with these values (together with also providing a training based capability). Based on a physical description of trees which characterise forest stands in a given class, together with a specification of the end-member reflectance values of forest components (similar to SMA), and a full description of the sun-sensor-viewing angles and topography, the canopy reflectance model simulates forest stands over a full range of stand densities, and, at each stand density produces a set of reflectance values and component fractions (sunlit canopy, sunlit background, shadow) which are computed as a function of the end-member reflectances, tree dimensions, the illumination conditions, and the tree density. The resulting set of spectral reflectance values computed over a full range of stand densities is called a *spectral trajectory*, so named because of the trajectory through spectral space that is produced when modelling forest reflectance over progressively increasing stand densities. In this study, the spheroid based canopy geometric-optical reflectance model which corrects for mutual shadowing (GOMS model) is used, since it was shown to be the best model compared to the cylindrical and conical model representations of canopy geometry tested in the previous Chapter. These spectral trajectories are then used for two purposes. First, the spectral reflectance values along the trajectories are used to drive land cover stratification. Essentially, a given input pixel

reflectance value is evaluated against each spectral trajectory with class membership assigned to the class with the trajectory which most closely represents that spectral reflectance value being classified. This achieves the land cover classification component. Then, to provide biophysical estimates, the other data associated with the selected spectral trajectory are consulted. This works by determining exactly which point along the spectral trajectory the input reflectance values have the greatest proximity to. The mixture fractions and tree density value for the trajectory point so identified constitutes the output for that pixel, together with the land cover class. This set of mixture fractions can then be used for predicting biophysical parameters, in the same way as with the stand level forest analysis in the SNF study.

The advantages to this method are that, firstly, the land cover classification and biophysical parameter estimation processes are directly linked to form an integrated, coupled image processing environment. Through this direct linkage, the effect of misclassification error can be more readily assessed since the classification and biophysical parameter estimation process both evolve from the same trajectory based data set and processing methodology. Secondly, the approach is based on a physical representation of tree canopies and forest stands, thus making the approach well suited for the physical and structural variables being studied. Thirdly, this method provides a way to account for variations in solar position, view angle and topography, all of which affect pixel level reflectance. Related to this, the ability to quantify forest component fractions at sub-pixel scales is a distinct advantage - this and the previously mentioned points make this approach more appealing than the use of vegetation indices. Through the use of spectral trajectories, the need for training data is reduced or eliminated, which is particularly advantageous when dealing with large study areas, different regions, multi-temporal analyses, or remote or

poorly known areas where training data might be difficult to compile with confidence. Fourthly, the integration of these methods within a knowledge-based evidential reasoning processing environment (after Peddle 1995a,b) provides a powerful classification system which has now been modified to provide the required sub-pixel scale mixture fractions through the integration of sophisticated geometric-optical reflectance models into the analysis. Using reflectance models, trajectories can be generated from either field measured inputs or from values obtained from the literature or other sources. The ability to model spectral trajectories as a function of tree density makes it possible to represent highly non-linear multi-spectral distributions which may otherwise complicate traditional algorithms, and these are well suited to the non-parametric evidential reasoning approach, as discussed later in this Chapter. This is particularly important given that it is difficult or impossible to obtain a representative sample of training data over the full range of forest stand densities. Further, using these models it is possible to create different sets of trajectories for different dates, or for different times of the day corresponding to image acquisition. Finally, as we shall see later in this Chapter, the ability to integrate this approach into a powerful evidential reasoning classification framework is a further advantage with respect to future work and other data sets, as this approach has been shown to be superior to a variety of other classification and statistical pattern recognition algorithms when dealing with multisource data sets (e.g. Peddle, 1993; Duguay and Peddle, 1996). In the next section, further information about each part of the methodology is presented.

## 5.3 STUDY AREA AND DATA COLLECTION

### 5.3.1 BOREAS Field Work

The Boreal Ecosystem-Atmosphere Study (BOREAS) is a major international, interdisciplinary project designed to improve our understanding of the interactions between the boreal forest biome and the atmosphere in order to clarify their roles in global change (Sellers *et al.*, 1995). The BOREAS study region covers a 1000km × 1000km expanse of boreal forest in northern Saskatchewan and Manitoba, and encompasses two main study areas: the southern study area (SSA) located north of Prince Albert, Saskatchewan, and the northern study area (NSA), west of Thompson, Manitoba. Field work for the project ran from August 1993 through September 1996, with the bulk of activities concentrated in two focused field campaigns (winter and spring thaw: FFC-W and FFC-T) and three intensive field campaigns (early, middle, and late summer: IFC-1, 2 and 3) during 1994.

The regional scale component of this research is being conducted as part of the BOREAS project. As a member of BOREAS project RSS-19, the author conducted field work at the SSA and NSA field sites during each of FFC-T (12 April - 2 May) and IFC-3 (30 August - 19 September). The main objective of the field work was to collect field spectrometer measurements of the boreal forest as a contribution to the RSS-19 data submission to the BOREAS information system (BORIS), and also to support individual investigator research. In both field campaigns, field understorey measurements were obtained as part of a larger effort throughout RSS-19 to characterise the mean spectral properties of the understorey (Miller *et al.*, 1996; White *et al.*, 1995) in support of the other RSS-19 main deliverable which was the acquisition of an extensive set of airborne imagery

during all FFCs and IFCs (Miller *et al.*, 1995) using a Compact Airborne Spectrographic Imager (CASI) sensor (Babey and Anger, 1989; Anger *et al.*, 1994; Mah *et al.*, 1995). The RSS-19 mean understorey work in FFC-T involved the collection of field spectra at regular intervals along a predefined transect established at each BOREAS Tower Flux site in NSA and SSA in support of RSS-19 cryospheric objectives and other BOREAS investigations. These spectral measurements included both snow covered and vegetated background surfaces, depending on snow melt progression. The objectives and data collection methods used in FFC-T differed somewhat from the methods used to collect end-member spectra for this research in IFC-3. The goal of the understorey work was to determine an average set of spectral values to characterise the understorey of each TF site. In contrast to this, the goal of end-member spectra collection is not to obtain an average signal, but instead to collect spectra from pure, individual samples of the forest components of interest. In IFC-3, spectra were collected in both the understorey and also from samples removed from the understorey. These methods are described in § 5.3.4.

In terms of the timing of field research, the IFC-3 field campaign was chosen for several reasons. Firstly, a full set of spectral end-members were collected in IFC-3 but not in FFC-T. This is because in FFC-T the University of Waterloo field objectives were focused on the understorey measurement campaign for RSS-19 and this did not leave ample opportunity to collect a rigorous set of end-member spectra as well. In IFC-3, some understorey spectra were collected and submitted to BOREAS, however there was also opportunity to collect the necessary end-member spectra. In terms of the summer time IFCs, IFC-3 was chosen for the second field campaign primarily due to logistical reasons. The original plan was to focus this study on the mid-summer IFC-2 field campaign since it was nearer the time of peak greenness and also because the largest array of BOREAS

remote sensing instruments were deployed during that time. IFC-1 (24 May - 16 June) was not considered since that field campaign started only 22 days after we had returned from FFC-T and it was decided that more time to synthesize data and review field techniques would be appropriate. However, the original plan to do field work during IFC-2 was changed to IFC-3 when it became apparent that the author would not be available during IFC-2 due to the USRA/NASA visiting scientist internship position held at the Goddard Space Flight Center during that time. The decision to shift the field plan was simplified by the fact that the IFC-3 time period still provided suitable foliage conditions for this research, and in fact the higher solar zenith angles at this later time in the summer provided an interesting challenge to this research compared to the mid-summer time period which is more typical for this type of work. Furthermore, a full fleet of remote sensing instruments was scheduled to fly during IFC-3, so there was no disadvantage to changing from IFC-2 to IFC-3.

### 5.3.2 Study Area

The spatial focus of this thesis research is the BOREAS southern study area (SSA). Although suitable field measurements were acquired for both the northern and southern study areas in IFC-3, the SSA was chosen for use in this research because a suitable regional scale satellite image product was available for IFC-3 SSA when the analysis phase of this work was being conducted. At that time, there was no such image data available for IFC-3 NSA.

The BOREAS southern study area encompasses an area of 130 km × 90 km located 40 km north of Prince Albert, Saskatchewan (see Figure 2.5). The study area is

near the southern limit of the boreal forest with transitional areas to prairie grassland located about 15 km to the southeast. The primary climatological variable controlling the biophysical and ecological functioning of this area is moisture (precipitation, snow hydrology, surface properties), in contrast to the northern study area where temperature (length of growing season) is the governing variable (Sellers *et al.*, 1995). The western part of the SSA encompasses Prince Albert National Park while the eastern part includes the Narrow Hills Provincial Forest. Topography throughout the SSA is flat to gently rolling terrain with glacial till deposits and moraine features of Pleistocene age overlaying bedrock from the Cretaceous period. The vegetation of the SSA includes a variety of tree and understorey species. On poorly drained sites common in boreal terrain, black spruce (*Picea mariana*) is dominant with an understorey typified by an understorey of sphagnum/feather moss with Labrador tea. Fens also occur in areas of poor drainage and contain a variety of sedge and grass vegetation, as well as some occurrences of trees such as black spruce. On well drained and sandy soil, the dominant species is jack pine (*Pinus banksiana*), with a typical understorey of lichens, bearberry and moss. In upland areas of well drained glacial deposits, deciduous stands of aspen (*Populus tremuloides*) are more common, and these have an understorey composition of hazelnut, wild rose, leaf litter and a variety of herbs and grasses. The SSA, as with many parts of the boreal forest, contains a patchwork of pure stands as well as occurrences of mixed forest stands where a variety of tree species coexist. In addition, logging activities and fire result in smaller areas of regeneration for all species.

In BOREAS, individual sites of each of these major species types have been identified for intensive study. At each site, a significant infrastructure of towers, boardwalks, paths and other facilities have been constructed to support a large variety of

scientific instrumentation for measuring key parameters in the boreal forest. These tower flux sites are listed in Table 5.1 together with the corresponding BOREAS acronym for

| Site | Abbreviation |
|---|---|
| Old Black Spruce | OBS |
| Old Jack Pine | OJP |
| Young Jack Pine | YJP |
| Old Aspen | OA |
| Fen | FEN |

Table 5.1. BOREAS Tower Flux sites and abbreviations.

each. Three of the sites (OBS, OJP, OA) are located in areas of mature, mostly homogeneous occurrences of the target tree species. Figures 5.6 - 5.13 contain photographs of these sites in the SSA taken in the late summer. In addition to the five TF sites in each of SSA and NSA, a variety of Auxiliary (AUX) sites were also identified in BOREAS to provide a set of additional sample sites, albeit without the large infrastructure of towers and equipment found at the TF sites.

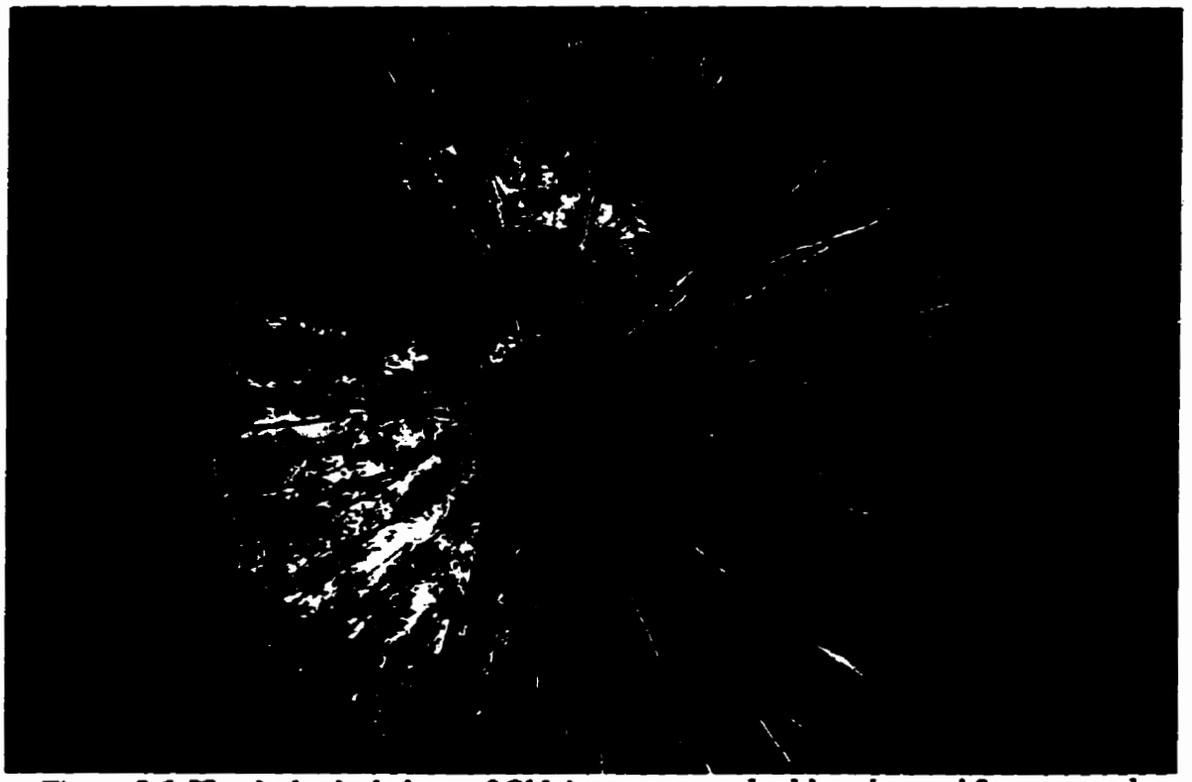

Figure 5.6. Hemispherical photo of Old Aspen canopy looking skyward from ground.

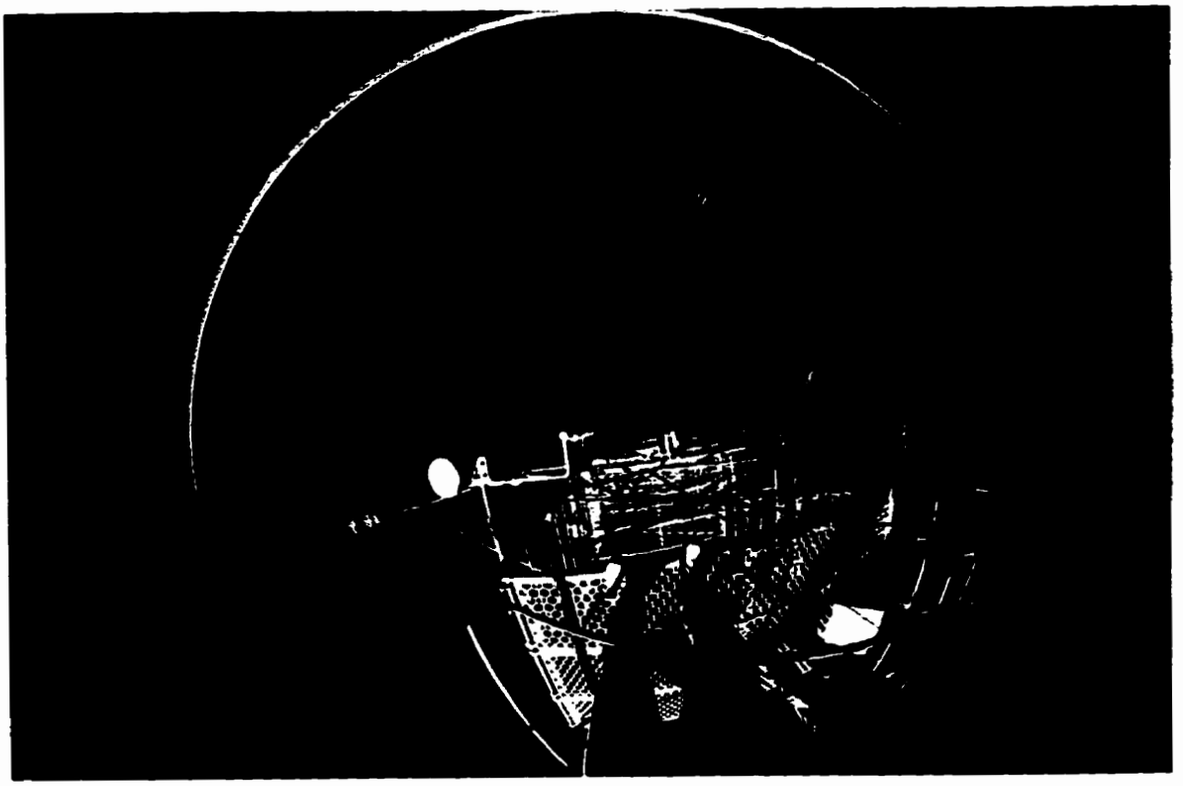

Figure 5.7. Hemispherical photo of Old Aspen canopy looking down from tower top.

Figure 5.8. Hemispherical photo of Old Aspen canopy and understorey from ground.

Figure 5.9. Oblique photograph of Old Black Spruce forest from tower top.

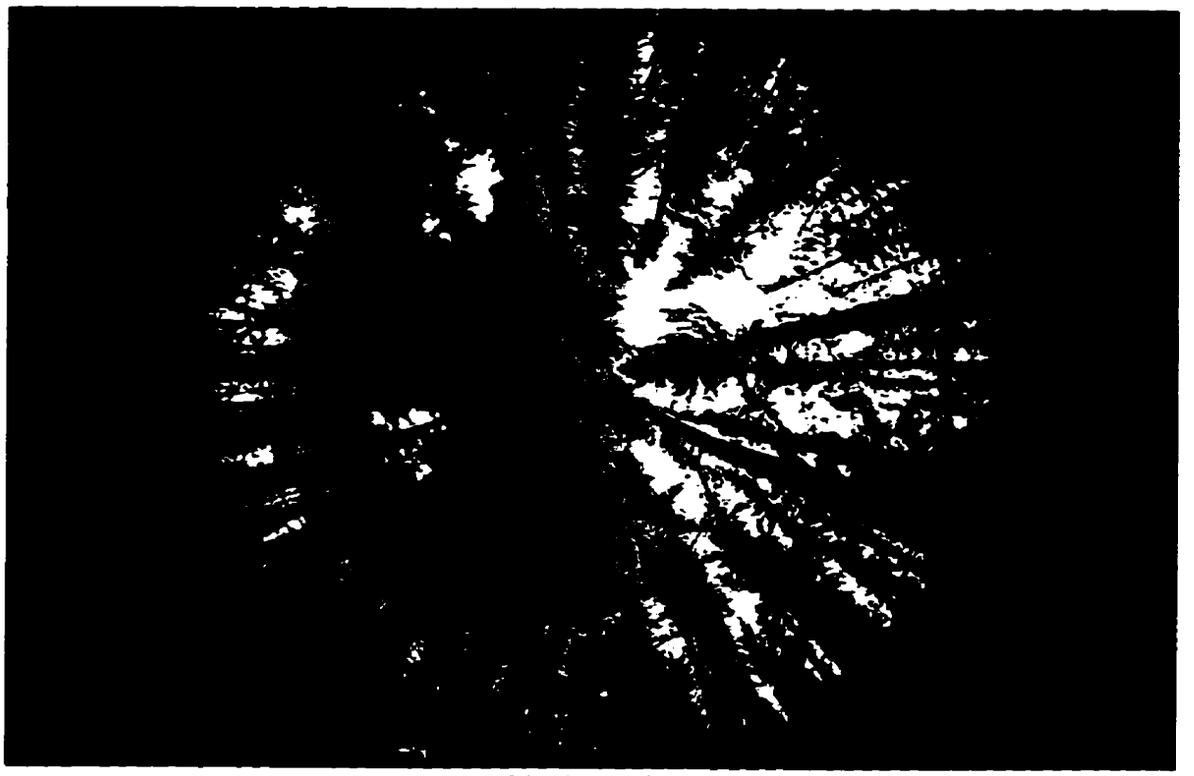

Figure 5.10. Hemispherical photo of Old Black Spruce looking skyward from ground.

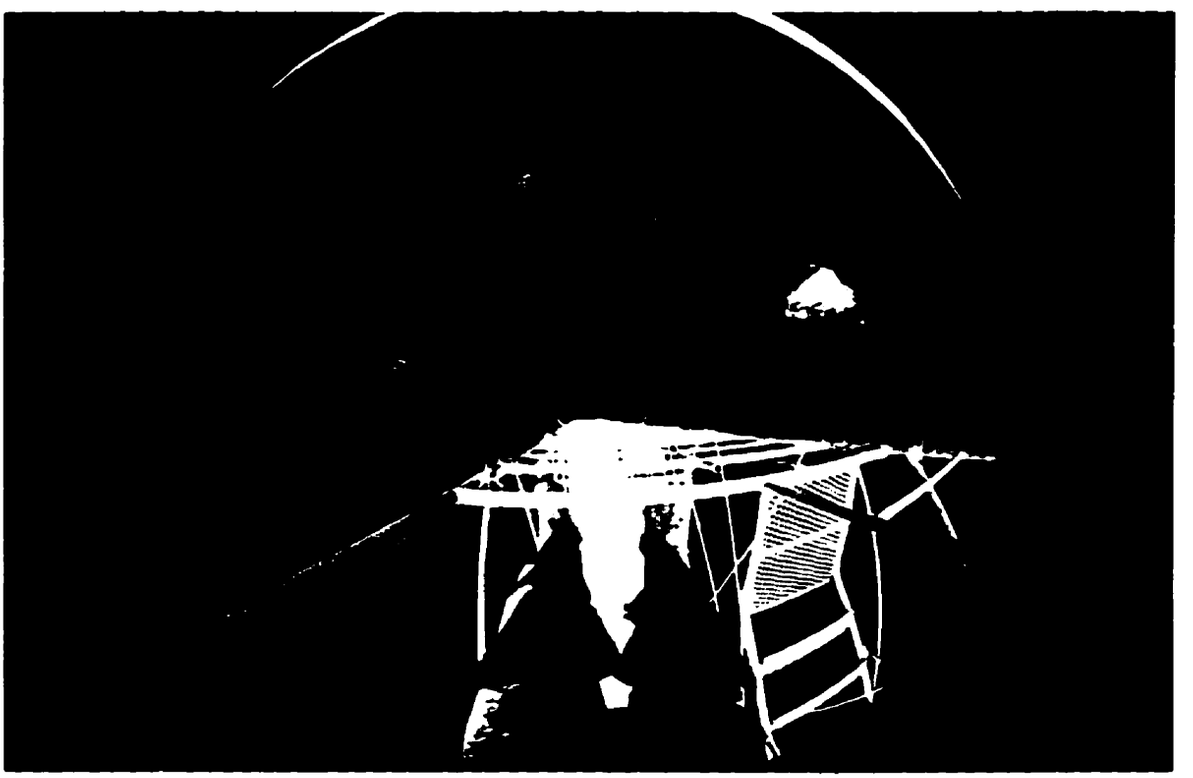

Figure 5.11. Hemispherical photo of Old Black Spruce looking down from tower top.

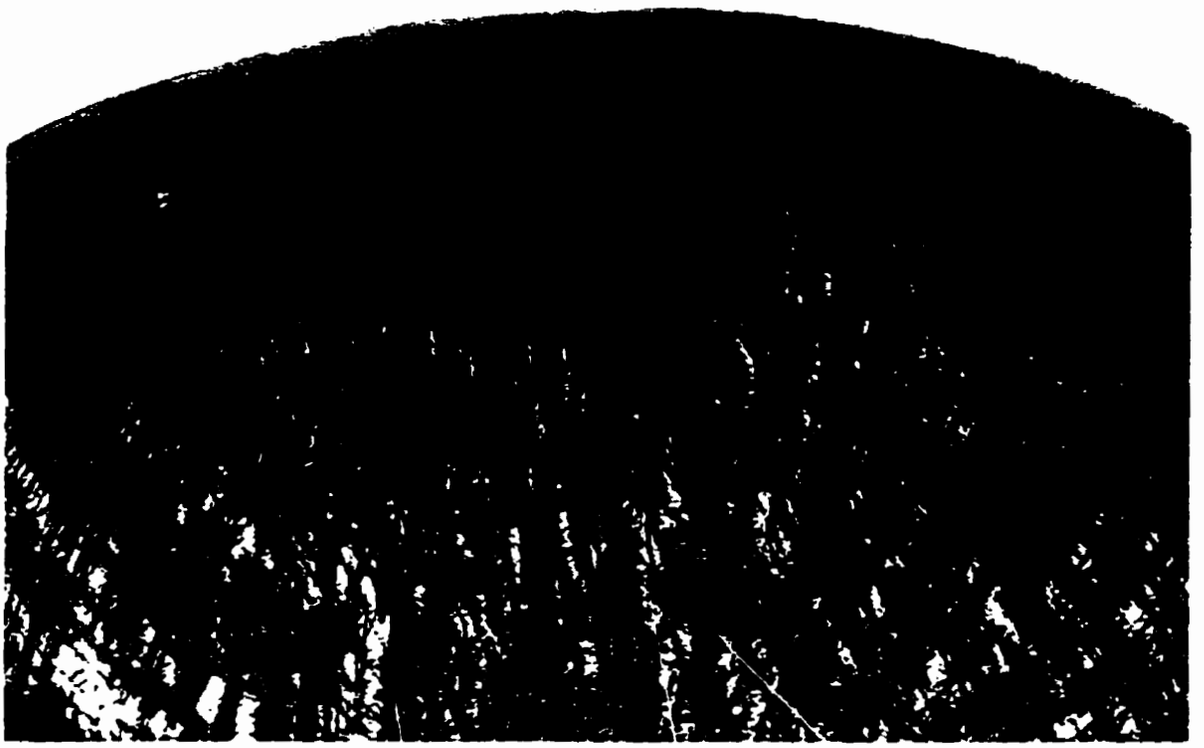

Figure 5.12. Oblique hemispherical photo of Old Jack Pine forest from tower top.

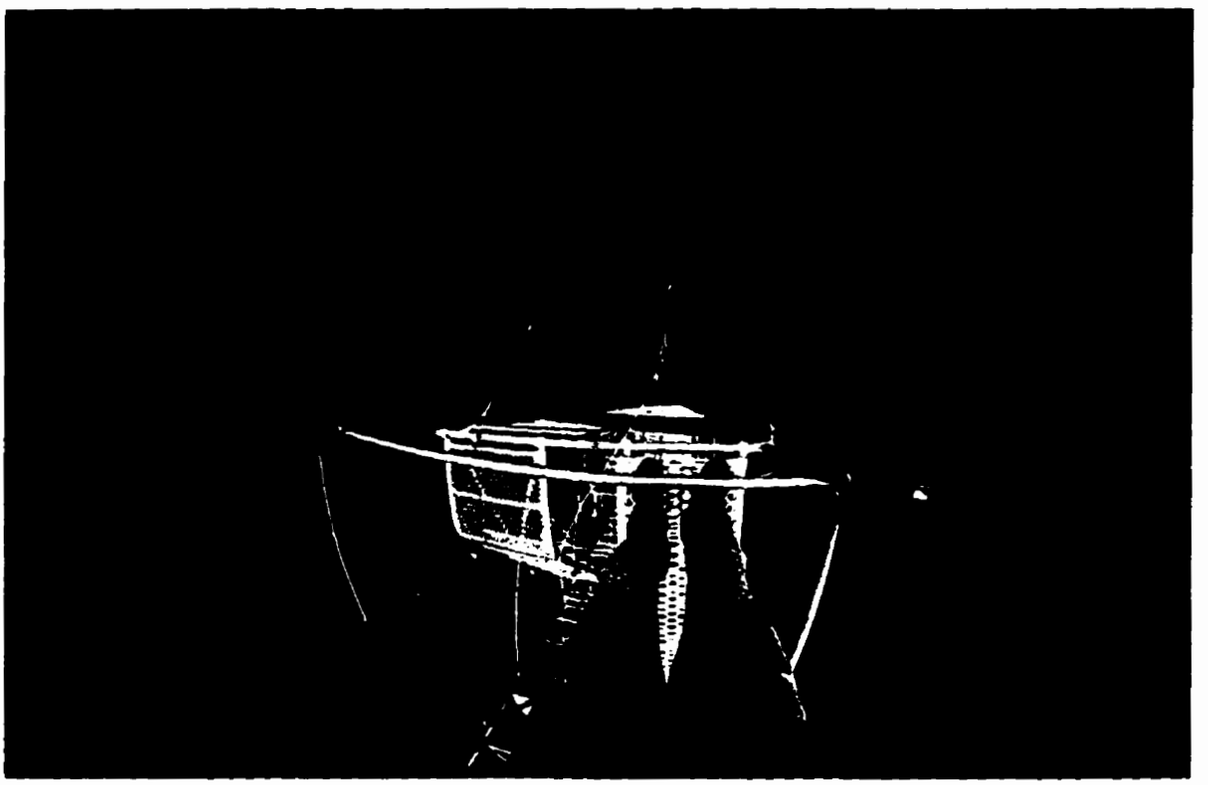

Figure 5.13. Hemispherical photo of Old Jack Pine canopy looking down from tower.

### 5.3.3 Remote Sensing Imagery

As a result of the regional scale objectives of this research, remote sensing imagery covering a large part of the BOREAS SSA was required for the IFC-3 field campaign. Further, image reflectance values were required to link the field based reflectance data collection program to the regional scale remote sensing imagery. The only BOREAS image product for SSA IFC-3 that met these criteria was a Landsat Thematic Mapper (TM) image acquired 2 September 1994. The very large volume of remotely sensed data collected by a variety of sensors and project teams together with unique processing requirements of certain sensors meant that processed image data products took some time to become available to BOREAS scientists. Future research will address use of a variety of image products from BOREAS, particularly AVIRIS (Airborne Visible Infrared Imaging Spectrometer), MAS (MODIS Airborne Simulator) and CASI (Compact Airborne Spectrographic Imager). These data exist for several field campaigns in the SSA and NSA.

Landsat TM imagery is acquired in 7 spectral bands (Table 5.2) at a spatial resolution of 30 x 30m (thermal band 6 has a resolution of 120m). The 2 September 1994

| Band | Wavelength (μm) |
|---|---|
| 1 | 0.45 - 0.52 |
| 2 | 0.52 - 0.60 |
| 3 | 0.63 - 0.69 |
| 4 | 0.76 - 0.90 |
| 5 | 1.55 - 1.72 |
| 6 | 10.4 - 12.5 |
| 7 | 2.08 - 2.35 |

Table 5.2. Landsat Thematic Mapper bands and wavelengths (micrometers, μm).

image was acquired by the Landsat-5 satellite on orbital Path 37, Row 22-23 and covered an area of 129 × 86 km, or 11,094 km$^2$ of the BOREAS southern study area. At the time of image acquisition, the solar zenith angle was 50.71° and solar azimuth angle 146°. This image was acquired by BOREAS Staff, who deemed the radiometric quality of the data to be acceptable for use in BOREAS. They performed an atmospheric correction of scene radiance to surface reflectance for bands 3, 4 and 5 using BOREAS sun photometer data input to the 6S atmospheric correction model (Markham *et al.*, 1992; Vermote *et al.*, 1994). This 3 band TM image was made available to this research in 16-bit format. As the ASD field spectrometer data did not cover the spectral range of band 5, only TM bands 3 (red) and 4 (NIR) were used in this study. These are the same bands which were used in Chapter IV with the MMR data set in the SNF NASA COVER Project. Also, the TM spatial resolution is virtually the same as the instantaneous field of view of the helicopter mounted MMR sensor used in that work. This provides a useful means for comparison between results obtained from the two separate study areas analysed in this research.

### 5.3.4 Field Spectrometer Data Collection

#### 5.3.4.1 Instrumentation and Portable Field Laboratory

High resolution field measurements of forest reflectance components are a key input to the spectral mixture analysis methodologies used in this research. Such measurements also have important applications to a number of remote sensing image analysis and modeling applications such as canopy reflectance modeling, image classification, as well as more detailed ecological studies of individual forest species. The instrument used for field spectral data collection was the ASD Personal Spectrometer II manufactured by Analytical

Spectral Devices Inc. (ASD, 1993) in Boulder, Colorado USA. This instrument detects radiation in the range of 350nm to about 1050nm in wavelength intervals of 1.423nm. The unit was linked to a Poqet palmtop computer running MS-DOS and contains a good software user interface for the display and capture of spectra. The ASD is also portable and compact making it reasonable to carry and set-up in a variety of environments. A fibre-optic cable extends from the spectrometer to the sensor head, which in this research was fitted with a pistol grip and field-of-view barrels to control target viewing specification. In all cases, the pistol grip was fixed to a tripod to ensure sensor stability during acquisition.

Field spectra were acquired at nadir angle over the target of interest. An inclinometer containing a small sight was attached to the ASD field of view (FOV) fore-optic barrel. The inclinometer was used to determine the angle of spectral measurement with the sight used to help ensure proper inclusion of the target in the sensor field of view for each measurement. As the latter is critical to proper target measurements, a plumb line was also rigged from the FOV barrel at initial site set-up to ensure the projected principal point from the sensor FOV corresponded with the target center for both the panel and forest component target measurements. A 10° FOV barrel was used for all spectral acquisitions to permit good coverage of the target while staying well within its dimensions to ensure the signal was not contaminated. For all spectra, dark current corrections were applied and the average of 10 spectral scans was recorded to minimise the effect of any internal signal noise produced by the sensor.

The ASD field spectrometer was used to collect spectral radiance measurements of a variety of forest targets. For each spectral target measurement taken, irradiance spectra were acquired by coincident measurement of the white side of a Kodak Gray Card (KGC)

reference panel so that reflectance measurements could be derived (Teillet, 1995), as described in §5.4 . Kodak Gray Cards have been shown to be spectrally stable in the wavelengths used in this research (400nm-900nm) (Milton, 1989). This, together with their versatility, low cost, and ease of use in the field made them a desirable choice.

To achieve experimental control, a Portable Field Laboratory (PFL) was designed and constructed to create a controlled environment for field spectral measurement which could also be transported to various sites and set up with ease (Figure 5.14). The PFL consisted of two wooden platforms with an adjustable support system for adjusting the surfaces such that they would lie flat. The two platforms were joined and a black rubber sheet was placed over each segment. One platform was used for the ASD sensor tripod, while the other platform was used for mounting the target sample for measurement. The rubber surface overlaid on the platform segments provided a suitable, non-slippery surface on which various items could be placed, with the black colour minimising reflection from objects near the PFL. The platforms were leveled using a leveling bubble in conjunction with the adjustable supports. For obtaining reference irradiance spectra, the Kodak Gray Card was placed over the target using a small stand which was also kept flat using the level bubble. A white reference panel measurement was acquired with each target spectra. At each TF site, the PFL was situated in an open area near to the sampling sites yet far enough away from the forest canopy such that no direct tree shadows were present and any scattering of radiation from the forest was negligible. The operator was situated out of the sensor field of view and away from the PFL configuration during data acquisition. The PFL setup allowed rapid data acquisition such that the collection of target and reference spectra could be done efficiently and also under the same illumination conditions due to the very small amount of time between acquisitions. In all cases, measurements were taken

under open skies with direct solar illumination available. If this was not present, data collection was suspended until conditions returned to ideal, clear skies.

5.3.4.2 Field End-member Sampling Design

As mentioned earlier, the author collected field spectra at all tower flux sites in the SSA and NSA during FFC-T and IFC-3 as part of BOREAS project RSS-19. In this section, the sampling strategy used for acquiring field spectra used in this research from IFC-3 SSA is described.

At each TF site, the dominant understorey and canopy species were first identified. For each component, both sunlit and shadowed measurements were required. In acquiring end-member spectra, an individual sample of each forest component of interest was identified and measured. By definition, an end-member in this research is a pure, homogeneous occurrence of the species target of interest. The first task in the field, therefore, was to locate an appropriate sample which met this criterion. Great care was taken in the selection of target samples for measurement. Once an appropriate sample site was found, the next task was to measure its spectral properties. For the understorey, one option would be to measure the forest floor directly at the location where the sample was found. A great deal of experience with this approach was obtained during the FFC-T campaign. However, there are a number of problems with this approach in terms of acquiring quality end-member spectra. For example, with a sunlit background end-member, maximum solar illumination would be required to capture the "most extreme" or brightest possible naturally occurring situation for acquiring end-member reflectance

such that the case of an open (treeless) occurrence of the background material would produce a component fraction of 1.0. In the understorey, natural solar illumination is rarely at a maximum but instead contains a significant diffuse component created by the overstorey and multiple scattering of radiation within the canopy. Further, movements of trees caused by wind alter the location of pockets of sunlight (or sunflecks) which reach the ground. In the same way, it was difficult to define a situation of end-member shadow (minimum) illumination in a consistent way. Also, the forest floor sometimes had uneven terrain which rendered the consistent set-up of the field spectrometer more difficult. In cases of dense stands (particularly OBS), the understorey was more difficult to walk through which further compromised data collection as a result of many tightly spaced branches near the ground.

To overcome these problems, a sampling strategy was devised whereby component samples were removed from the problematic understorey environment, and taken to an open site for measurement. The idea was to eliminate the effects of the forest canopy which lies between the target and the illumination source (sun) to provide a way of measuring a pure sample without any intervening objects. The acquisition of spectra for each end-member is described in the next section.

### 5.3.5 Acquisition of Forest Component Spectra

#### 5.3.5.1 Sunlit Background End-member Spectra

The acquisition of sunlit background component spectra was straight-forward with the understorey sampling design and PFL configuration in place, as described above. Sampling in the understorey involved cutting a square block of turf ≈40 × 40 cm dimension, digging around the square to provide access under the turf, and carefully removing the square sample using a shovel. The sample was transported by foot directly to the open site (Figure 5.14). A potential drawback to this method is that it involves a small amount of disturbance of the forest understorey. However, with proper care in selecting an appropriate sample, the amount of disturbance is limited to less than a 3 $m^2$ area per site, and when possible the measured understorey sample was returned to its original location and the natural setting restored as much as possible so that regrowth or re-establishment of the disturbed area might occur. Samples used for OJP and OBS are shown in Figure 5.15.

#### 5.3.5.2 Sunlit Canopy End-member Spectra

Obtaining direct measures of the canopy for the sunlit canopy end-member was not as straightforward. Attempts were made to obtain direct measures from TF towers, however the canopy target could not be isolated with sufficient confidence to ensure the sensor field of view contained only trees, even when very narrow FOV barrels were used. Also, it was difficult to obtain the necessary nadir measures from the tower top for consistent use with nadir satellite imagery. Tower measures with the ASD were better suited for angular bi-directional reflectance measurements, however these were not required

for this research. Instead, canopy samples were measured using the optically thick stack method (Goward *et al.*, 1994). This method involved clipping branches from trees at various heights throughout the canopy and assembling them together on the PFL platform into a compact, opaque configuration such that the platform background was obscured prior to acquiring spectra, with the branches positioned with the proper side of each clipping facing upwards as found on the tree (see Figures 5.14 and 5.15). The advantage is that a reasonably consistent method of acquiring canopy reflectance is provided, with the proper target ensured for the sensor. The disadvantage of this method is that the natural structure and geometry of the branches on trees is not preserved. As a result, the reflectance factors obtained may be overestimated somewhat as a result of the greater concentration of branches per unit area compared to what is found in a natural stand of trees. However, from the end-member stand-point, this is not a problem and in fact could be considered appropriate for this technique since the goal of any end-member spectral measurement is to obtain spectra for the most pure occurrence of the target as possible. There is no implicit assumption that the target actually occurs in nature at that level of purity, and in fact component fractions equal to one are rare, even at fine spatial resolutions. This fact lends itself well to being able to obtain quality end-member spectra. All that is required is for the field scientist to shift their normal way of thinking in terms of field measurement away from the traditional approach of selecting representative samples (i.e. the 'average' case) to instead focus on samples which are homogeneous and measured under conditions of maximum illumination.

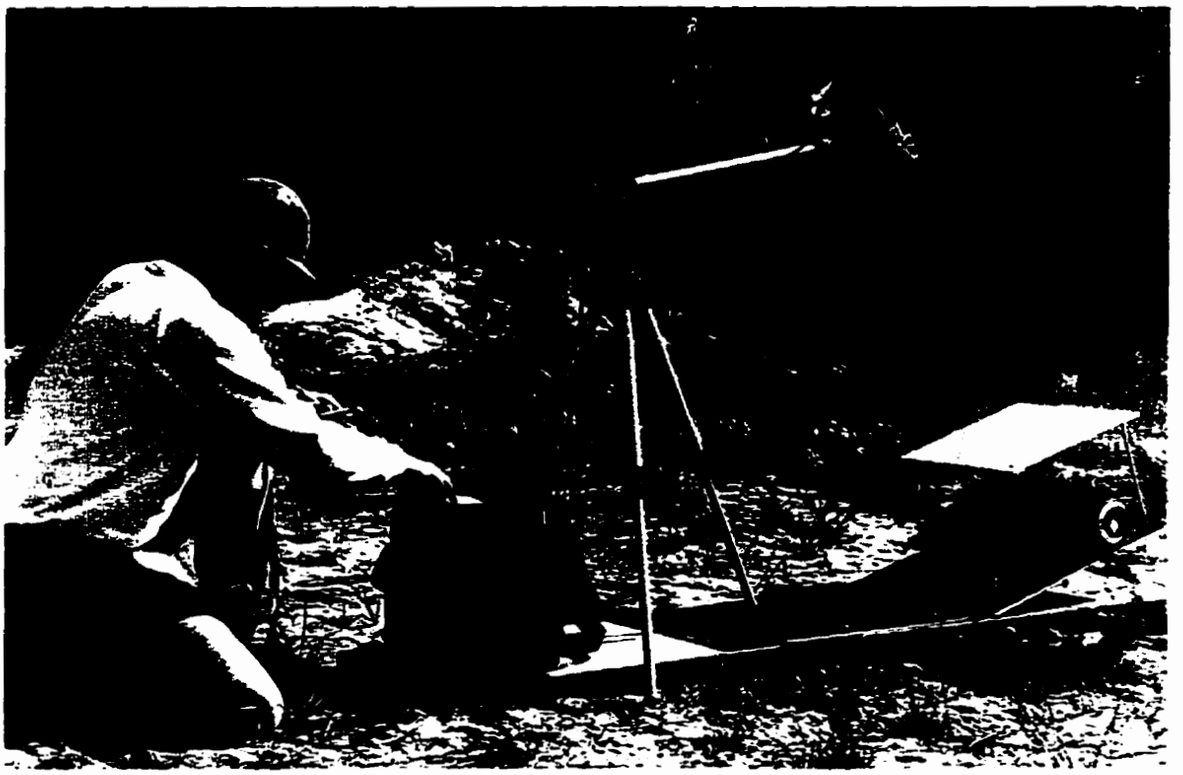

Figure 5.14. Portable Field Laboratory set-up for spectrometer.

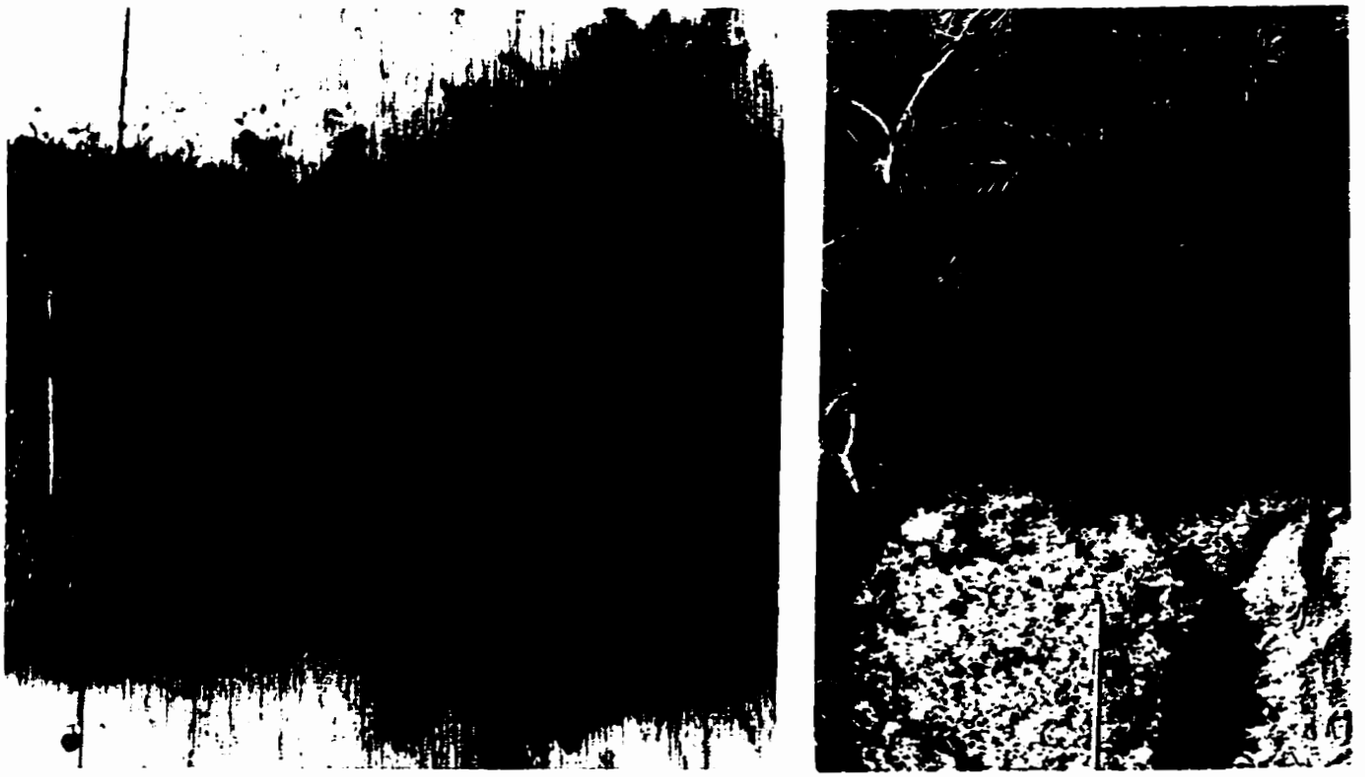

Figure 5.15. End-member samples: OBS sphagnum and branch stack (left photo). OJP cladina lichen and branch stack (right photo). Pen shown for scale.

5.3.5.3 Shadowed Component End-member Spectra

The shadowed end-member case provided different challenges since the nature of shade and shadowing can be highly variable within forest stands and canopies, and further, this can vary significantly over different spatial scales (Ranson and Daughtry, 1987; Franklin *et al.*, 1991; Hanan *et al.*, 1993; Leblon *et al.*, 1996). For example, within the forest understorey, diffuse (shadowed) radiance can vary inside and outside shadows and also within the shadowed area itself according to areas in the umbra and penumbra with respect to the direct beam, and this can be further affected by complex interactions of radiation with surrounding canopy features. As a result, the specification and measurement of shadow end-member spectra in the natural forest understorey and canopy environment can be difficult to achieve in a consistent manner. Accordingly, in this research, an addition to the PFL was used to create a more standardised and consistent environment for measurement of shadow spectra instead of obtaining spectral measurements directly in the forest canopy and understorey.

For shadowed target spectra, a portable wall of dimension 2 × 2m and consistent spectral properties was erected perpendicular to the sample plane and oriented to block direct solar illumination. This set-up was used to acquire target radiance measurements of samples of background materials and optically thick stacks, using the same samples as used for collecting sunlit component reflectance spectra. The PFL was situated away from the canopy and any other surface features to avoid diffuse light from other sources. The only variable illumination condition created was the possibility of small variations in the magnitude of sky light (excluding direct solar illumination) reaching the target at different times (different SZA). This is due to the fact that it was not possible to change the size of the portable wall according to solar zenith angle such that an identical portion of the

hemisphere was obstructed for each measurement. However, this factor was deemed relatively insignificant since measurements were acquired near solar noon within a relatively narrow temporal window in IFC-3 (i.e. small differences in SZA), and further, SZA is accounted for in the computation of reflectance.

Using the above PFL configuration provided a useful set-up for acquiring radiance spectra of target samples under shadowed illumination. However, reflectance is an inherent property of a material which is invariant of illumination. Accordingly, the ratio of target radiance to incident irradiance measured within the same sunlit illumination conditions or within the same shadowed conditions should produce a consistent reflectance spectra. For the purpose of obtaining end-member component reflectance spectra, in this research shadow spectra were defined as target radiance obtained in shadow with respect to the total amount of incident illumination available. Accordingly, target radiance spectra were obtained in the PFL shadow configuration as described above, while incident irradiance was measured from the unobscured KGC reference, which comprises the total direct plus diffuse irradiance. As this differs from the classical definition of reflectance, in which radiance and irradiance are obtained under the same illumination conditions, the computed ratio of target radiance and reference irradiance is instead referred to as *apparent reflectance*.

The methods developed for field collection of end-member spectral data provided an efficient, controlled setting for acquiring a large number of spectra in a consistent and repeatable fashion under natural illumination conditions. The raw ASD spectra collected at each site were archived for post-field processing at the University of Waterloo to convert the target and panel spectra to measures of reflectance. The procedures to do this are described in the next section, following which example end-member spectra are presented for the understorey and canopy species analysed.

## 5.4 REFLECTANCE PROCESSING OF FIELD SPECTROMETER DATA

### 5.4.1. Background and Rationale

The large effort expended in field data collection, coupled with the need for high quality field spectrometer data for use by RSS-19 investigators and for release to the BOREAS information system meant that the development of an efficient, highly accurate method for processing large volumes of reflectance data was of vital importance to this research and RSS-19 science objectives. As a result, considerable effort was put forth to design an efficient system for processing reflectance spectra. Accordingly, these developments are described in some detail here.

In this section, field techniques for data collection are presented, and followed by a description of the approach for converting raw target and panel radiance spectra to calibrated reflectance. This conversion involves five major processing stages: (i) panel calibration, (ii) solar zenith angle computations, (iii) spectral and angular interpolation, (iv) computation of reflectance, and (v) automated batch mode execution of stages ii-iv for processing large data volumes. Equipment, methods, and computer programs for achieving these stages are presented.

### 5.4.2. Panel Calibration

It is essential that reference panel measurements be calibrated since panels and KGCs do not reflect all of the incident radiation, and further, their reflectance is highly dependent on illumination angle (solar zenith angle). A laboratory panel calibration facility was developed by personnel at the Instrument Services Laboratory of York University for characterising the spectral properties of Kodak Gray Cards in terms of bidirectional reflectance factors (BRF). A full description of this facility is contained in Soffer *et al.* (1995), and summarised here. The facility used an Ocean Optics ST1000 spectrometer (1024 channels between 360 nm and 860 nm) connected to a detector head mounted on a precision controlled rotational stage to permit spectral acquisition over a range of user specified view angles. The panel is secured to a second rotational stage for setting the illumination angle. The small size of the detector head and the positional flexibility of the system permits reliable measurement in the case of near-coincident view and illumination angles. Using nadir illumination (to minimise experimental error), a series of KGCs were characterised at view angles between 15°-80°, at 5° increments. Then, according to the Helmholz reciprocity principle (which states that a BRF at view angle $\delta$ and nadir illumination is equivalent to that obtained at nadir view angle and illumination angle $\delta$), we interpret these view angles as solar zenith angles (SZA) for the purpose of deriving panel calibrations over the wide range of SZAs encountered in the field. Validation of the system was accomplished through comparisons of facility results for a 99% Spectralon Panel with published BRFs of that material, and with facility results from BOREAS instrument calibrations at the University of Nebraska, USA.

The BRFs of the white side of the rectangular KGCs differ significantly between the two orthogonal panel orientations, suggesting that this parameter should be noted in the field and accounted for in the lab. In our field work, the narrow dimension of the KGC was always positioned perpendicular to incoming solar illumination, allowing us to use the BRFs obtained from the view angle plane oriented 90° to the KGC narrow dimension. Once these panel orientation effects were separated, the combined variability of BRFs among the 5 white cards used in the field was assessed together with a new, clean KGC in terms of spatial differences within each card, differences between cards, and experimental error. The variability was very low, which, in addition to producing the first quantitative evidence of the careful treatment of KGCs in the field, permitted one BRF to be generated for use with all 6 cards. An inter-sensor comparison was also performed between the Ocean Optics spectrometer used in the lab, and the ASD spectrometer used in the field. The size of the ASD FOV barrel made it impractical to obtain a full range of angular measurements in the lab necessary for panel BRF characterisation over the wide range of SZAs encountered during BOREAS. Instead, several ASD spectra of KGCs were collected in the panel calibration facility at nadir illumination and view angles between 50° and 60° (Morassutti and De Abreu, pers. coms., 1995), for comparison with similarly acquired spectra using the methods described here. The results were consistent between the ASD and Ocean Optics instruments tested. The final output of the panel calibration process is an Excel spreadsheet containing target BRFs between 350 nm and 850 nm at 14 view angles (SZAs) for 11 spectral wavebands at 50 nm intervals, plus an additional 4 wavebands at MMR wavelengths. Degrading the spectral resolution to 50 nm made the panel calibration files more manageable. This was done after results from high order interpolations of the 15 wavebands (discussed later) showed a very high correspondence with the high spectral resolution raw spectra.

### 5.4.3. Solar Zenith Angle Computations

Field spectrometer measurements were acquired by RSS-19 personnel during all 5 of the 1994 BOREAS field campaigns (February - September), resulting in a wide range of solar zenith angles encountered throughout the year. Knowledge of the SZA for a given field measurement is critical as a result of the reflectance anisotropy for nadir observations of coniferous forest canopies (Syrén, 1994). However, since it is difficult or impossible to determine directly the SZA with any degree of confidence while mired in the boreal forest understorey, an alternative method was required to allow accurate specification of SZA for the reflectance processing software.

To accurately determine the solar zenith and azimuth angles for a given spectral observation, one only requires the date and time of measurement, and its latitude and longitude. The date and local time are stored automatically in the header of each ASD spectra file, and the exact latitude and longitude of the tower flux sites are known in BOREAS. Determining the solar position from time and location is a standard computation in astronomical and planetary studies (Duffett-Smith, 1990; Observers Handbook, 1994). An overview of this approach with a full set of equations is contained in Peddle *et al.* (1995b) and is not repeated here.

### 5.4.4. Spectral and Angular Interpolation

The result of the panel calibration is a matrix of BRFs for the KGCs at 50 nm wavelength intervals for 15 view angles. However, panel calibration data were required for the specific SZA encountered in the field (computed as above for each field measure), and

further, these data must be determined at very high spectral resolutions matching that of the field spectrometers. To achieve this, spectral and angular interpolations were applied to the original panel calibration results using an Excel spreadsheet, a portion of which is shown in Figure 5.16. Although much of the Excel code and formulations are hidden or contained elsewhere in the document, a number of important functions are illustrated. The angular interpolation is performed first. For each center wavelength (column B in Figure 5.16), an equation describing the BRFs over the 15 angular measures is determined using a fourth order polynomial fit applied to the panel calibration data (read from a separate worksheet, not shown). Using these equations, Target BRFs (col. F) are calculated for each center wavelength for the input SZA (obtained by referencing the linked SZA worksheet which computes the solar position for the field spectral measurement). Next, the spectral interpolation is performed over these Target BRFs for the specified SZA. This is done by fitting an equation to the points described by the Target BRFs at MMR and standard wavelengths (STD), again, using a fourth order polynomial. The coefficients of that equation, their standard errors, and the $r^2$ value for the equation are depicted in Figure 5.16 in the box above the chart. In the example shown, the $r^2$ value is very high (0.9963), which is a typical result as the fourth order polynomials provide highly accurate spectral and angular interpolations. This is expected, given the stable spectral response observed for a variety of panels over a range of view angles, and allowed the panel calibration process to be simplified in terms of the number of spectra and bandwidths required to produce optimal spectral characterisations in the lab.

| Input Solar Zenith Angle : | 53.43 | | | Panel: KGC - Gray Side | | | |
|---|---|---|---|---|---|---|---|
| A | B | C | D | E | F | G | H |
| Band Designation | Center Wavelength (nm) | Start Wavelength (nm) | End Wavelength (nm) | | | | |
| MMR1-485 | 484.8400 | 449.5900 | 520.0900 | | 0.17221 | 0.17481 | 1.51% |
| MMR2-560 | 560.5100 | 520.0900 | 600.9300 | | 0.16977 | 0.16970 | -0.04% |
| MMR3-660 | 660.0750 | 629.2900 | 690.8600 | | 0.17285 | 0.17055 | -1.33% |
| MMR4-809 | 809.2100 | 760.2300 | 858.1900 | | 0.21398 | 0.21599 | 0.94% |
| STD01-358 | 358.1450 | 341.3500 | 374.9400 | | 0.08093 | 0.08246 | 1.89% |
| STD02-400 | 400.3000 | 374.9400 | 425.6600 | | 0.14194 | 0.13947 | -1.74% |
| STD03-450 | 450.5550 | 425.6600 | 475.4500 | | 0.17194 | 0.16930 | -1.54% |
| STD04-500 | 499.8750 | 475.4500 | 524.3000 | | 0.17250 | 0.17496 | 1.43% |
| STD05-550 | 549.2900 | 524.3000 | 574.2800 | | 0.17074 | 0.17089 | 0.09% |
| STD06-600 | 599.7700 | 574.2800 | 625.2600 | | 0.16685 | 0.16684 | -0.01% |
| STD07-650 | 650.2000 | 625.2600 | 675.1400 | | 0.17133 | 0.16911 | -1.30% |
| STD08-700 | 700.4850 | 675.1400 | 725.8300 | | 0.17624 | 0.17976 | 2.00% |
| STD09-750 | 750.5850 | 725.8300 | 775.3400 | | 0.19814 | 0.19666 | -0.75% |
| STD10-800 | 800.4100 | 775.3400 | 825.4800 | | 0.21344 | 0.21366 | 0.10% |
| STD11-850 | 841.8350 | 825.4800 | 858.1900 | | 0.22215 | 0.22086 | -0.58% |
| | | | | | | | |
| 4th Order Equation of Fit: | | y=Ax^4+Bx^3+Cx^2+Dx+E | | | | | |
| | | Coefficient | St. Error | | | ASD Wavelength | 4th Order Fit BRF |
| | A= | -2.6908E-11 | 2.05627E-12 | | | 400.01 | 0.1454 |
| | B= | 5.9999E-08 | 4.92391E-09 | | | 401.42 | 0.1462 |
| | C= | -6.6562E-05 | 4.3178E-06 | | | | |
| | D= | 0.027493102 | 0.001640413 | | | | |
| | E= | -3.999268049 | 0.227450551 | | | | |
| | R2= | 0.996287914 | | | | | |
| | | | | | | 848.61 | 0.2298 |
| | | | | | | 850.02 | 0.2314 |

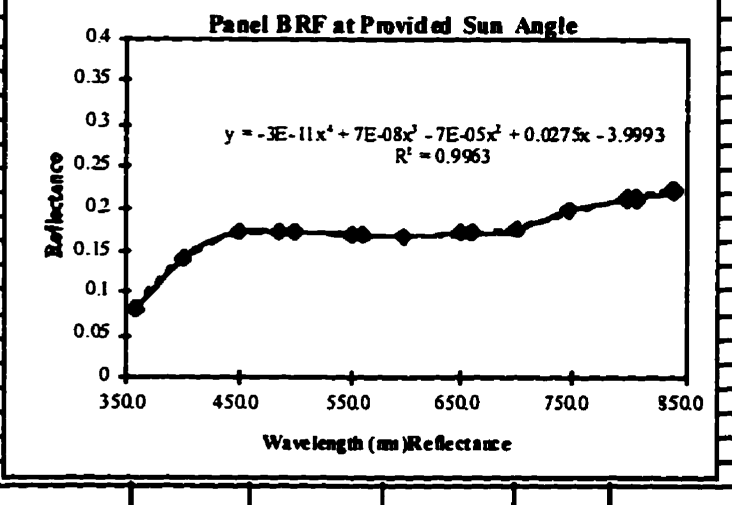


Figure 5.16. Spreadsheet for spectral and angular interpolation of calibration BRFs.

The results of applying these equations back to the original wavelength centers are displayed in Figure 5.16 (top portion of column G), with the associated standard error for each estimate shown (col. H). The chart includes the full equation, its $r^2$ value, and a plot of the curve for the equation fit to the Target BRF points, displayed as diamonds along the curve. These equations were then applied to compute panel calibration BRFs at each wavelength band of the field spectrometer which, for the ASD, is at 1.423nm intervals. These results, shown in the bottom right of Figure 5.16, represent the output from the spectral and angular interpolation of the panel calibration data used in computing reflectance.

### 5.4.5. Automated Batch Mode Processing of Reflectance

An Excel macro program was written to control batch mode execution of reflectance processing for the large volume of data collected by RSS-19. The process involves three linked Excel spreadsheets, each with different functions, together with input spectra files and a series of batch command modules. The spreadsheets contain: (i) the laboratory panel calibration BRFs of the KGCs, as discussed in §5.4.2; (ii) the solar zenith angle computations, as presented in section §5.4.3; and, (iii) the angular and spectral interpolation routines, discussed in §5.4.4. The external files, which are read into the macro program for input to the spreadsheets, include the target and panel spectra files collected in the field (converted from binary to ASCII format using the ASD (1993) Portspec command), each of which contains important header information, as well as batch files (created using standard word processing editors) which specify the latitude and

longitude of the field measurements (in the case of RSS-19, the BOREAS tower flux sites), target and panel file names, output reflectance file names, and text describing the field spectral acquisition (e.g. target species, sampling design, site description, illumination conditions, KGC panel information, spectrum characteristics etc.) for inclusion as header information in each reflectance output file. Examples of the two levels of batch files as well as the header template developed for this procedure are listed in Appendix A. The macro program itself makes extensive use of a variety of low-level Excel functions. Additional information about this program is contained in Appendix A, together with the source code listing of the Excel macro developed for this application. Once the various files have been coordinated and the necessary data processed, the program computes a reflectance value. Spectral reflectance for a given SZA ($\sigma$) and at nadir view angle ($\theta$) is computed over the full wavelength range at the spectral resolution of the field spectrometer as:

$$\text{Reflectance}_{(\sigma,\theta)} = \frac{\text{target radiance}}{\text{panel radiance}} \times \text{panel calibration BRF} \qquad (5.1)$$

An example reflectance output file is shown in Appendix A. Example plots of reflectance spectra curves processed using these procedures can be found later in this Chapter.

The end result of this aspect of the research is a flexible and automated approach to producing spectral reflectance values from field radiance data. These methods were used both in this research and also to process the larger data set of field spectral data as part of the University of Waterloo's contribution to BOREAS RSS-19. The approach is quite flexible in that panel calibration data for any solar zenith angle can be derived based on a

highly accurate procedure for spectral and angular interpolation of panel measurements obtained over a range of view angles. An extensive macro program controls batch processing of large volumes of spectral data in an automated environment - the user need only generate a batch file specifying the location of spectral measurements and file names for processing. The approach permits high quality reflectance values to be obtained from the data collected in the field. In the next section, end-member spectra produced using these procedures are presented.

### 5.4.6. End-member Reflectance Spectra

#### 5.4.6.1 Component Spectra Specification

Reflectance spectra were produced from end-member radiance and irradiance measurements acquired at all TF sites in SSA IFC-3. Sunlit canopy, sunlit background and shadow component spectra were generated for the dominant species in each case for input to the geometric optical reflectance model used to produce spectral trajectories for land cover classification and biophysical estimation. One set of reflectance factors was used for the shadow component instead of using separate canopy and background spectra. This was done for three reasons: (i) the spectra of individual shadowed components were very similar; (ii) in the physical interpretation of shadow fraction in this research, it is not important whether the shadow falls on trees or background, instead, only the overall fraction of shadow present is of interest (i.e. the degree of shadowing present, not the location of the shadows); and (iii) results from the NASA COVER experiment at Superior National Forest (Chapter IV) used one overall shadow fraction component to successfully predict biophysical parameters of interest. Therefore, in this research, apparent reflectance

factors from individual shadow components were averaged to produce one set of integrated shadow component values per site. The reflectance spectra used at each site are presented next.

5.4.6.2 TF Site Species End-member Reflectance

The dominant mature species of old black spruce, old jack pine and old aspen were used as input to the reflectance model. Reflectance spectra were acquired at each of these sites, however, old aspen spectra were not used in this research due to the discrepancy in dates of field spectra acquisition (12 September) and Landsat TM satellite overpass (2 September). At the start of September the aspen foliage was still green, however 10 days later the senescence of deciduous foliage had progressed to a point where many of the leaves had begun to turn yellow. The author and associated field crew were located at the northern study area in Manitoba on 2 September so that ground data collection would be coordinated with the location of BOREAS remote sensing aircraft (including the RSS-19 CASI). Field spectra were collected at SSA-OA at the same time as CASI overflights, and these will be useful inputs to future BOREAS research, however these OA spectra are not used here. An alternate set of end-member factors were acquired from other sources in BOREAS for the OA site, as described in §5.5. The end-member spectra acquired for OBS and OJP components are presented next.

Figures 5.17, 5.18 and 5.19 show the Old Black Spruce (OBS) end-member spectra for sunlit canopy, sunlit background and shadow, respectively. The sunlit canopy reflectance spectra (Figure 5.17) exhibit the optical spectral properties which characterise green vegetation, as reviewed in §2.3.3. Reflectance throughout most of the visible portion of the spectrum is relatively low (<0.1), with the notable green peak near 552nm

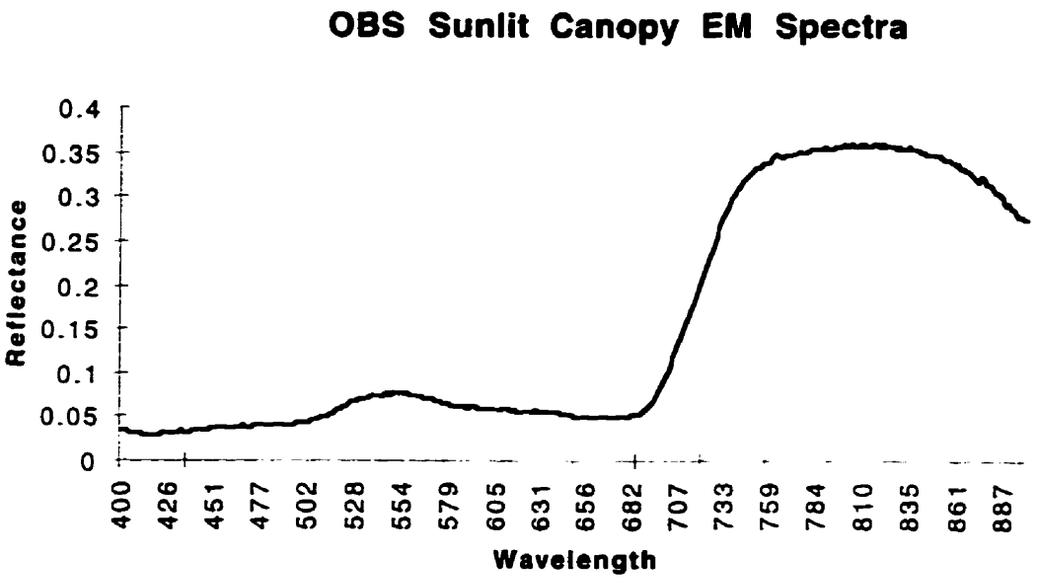


Figure 5.17. Sunlit canopy end-member (EM) reflectance spectra derived from field spectrometer data at SSA old black spruce (OBS) site.

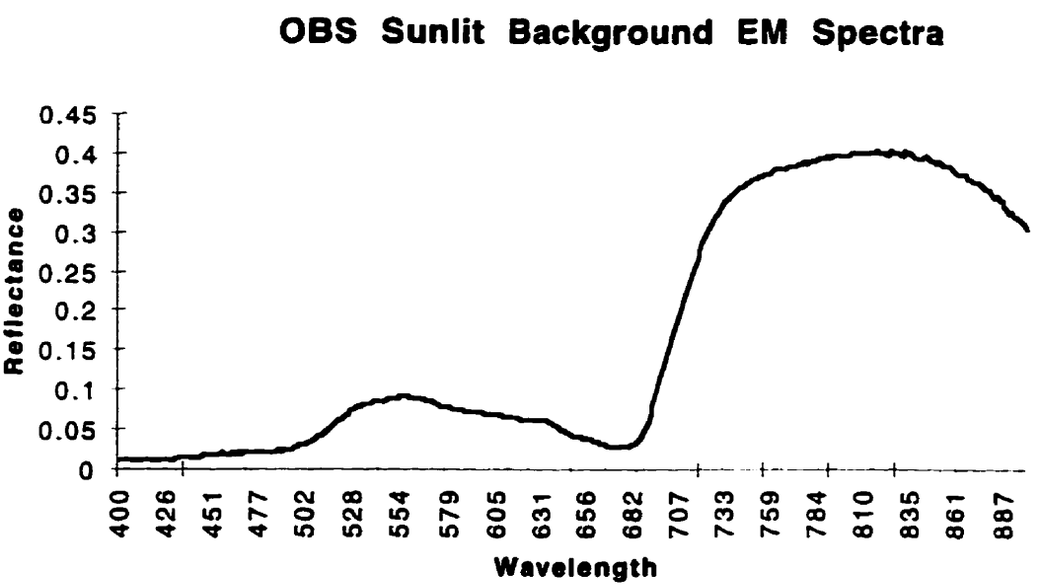


Figure 5.18. Sunlit background end-member reflectance spectra derived from field spectrometer data at SSA old black spruce site.

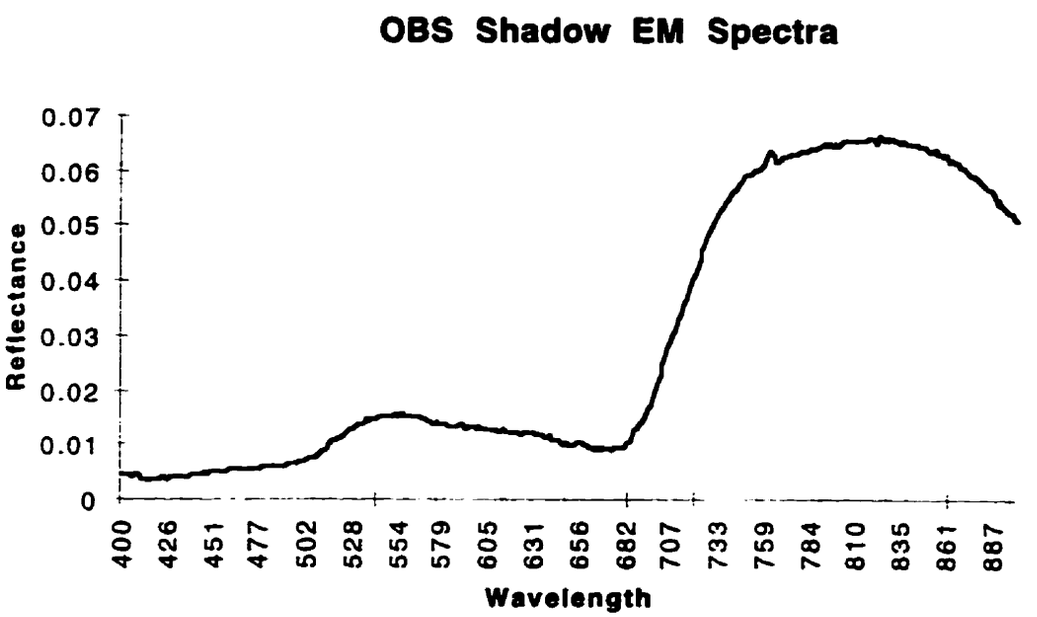


Figure 5.19. Shadow end-member apparent reflectance spectra referenced to the total direct plus diffuse incident irradiance derived from field spectrometer data at SSA old black spruce site. Spectra shown are the average of the shadowed background and canopy sample measurements.

apparent. The pronounced red-edge is seen from 680nm to 740nm marking the transition from chlorophyll absorption to leaf scattering. Reflectance remains near the maximum of about 0.37 throughout much of the NIR. The sunlit background component reflectance spectra for sphagnum moss (Figure 5.18) exhibits a similar overall shape, but with different absolute reflectance values. The green peak is slightly higher, and the reflectance values in the NIR are also greater (0.41). For the shadow apparent reflectance end-member spectra (Figure 5.19), the original shadowed canopy and shadowed background spectra were averaged, as discussed earlier. Here, the shape of the curve is similar to the sunlit spectral reflectance curve, however the overall magnitude of apparent reflectance is much

lower, with a maximum value of only about 0.065. As explained earlier, the shadow spectra used the total direct plus diffuse irradiance as the reference together with shadowed radiance measurements in the computation of apparent reflectance values. To obtain the actual reflectance of the target itself would require normalizing the reflected radiance to the actual irradiance reaching the shadowed target. In this case, a shadow reflectance curve similar to the sunlit spectrum of the same targets would result.

For Old Jack Pine (OJP), the component reflectance spectra are shown in Figures 5.20, 5.21, and 5.22, for sunlit canopy, sunlit background and shadow, respectively. Again, the characteristic spectral shape of green vegetation is evident, and as with OBS, the absolute reflectance values differ by species and component. Sunlit canopy (Figure 5.20) has lower reflectance values in the visible portion with the green peak ranging to 0.10. Beyond the red edge, the largest reflectance factors in the NIR are about 0.46. In both cases, these are larger than the OBS sunlit canopy reflectance factors. The OJP sunlit background component spectra (Figure 5.21) is taken from field measurements of cladina lichen material, which has a brighter appearance in the field and higher reflectance values throughout the visible portion of the electromagnetic spectrum compared to the OBS sphagnum background cover. A red edge is evident but less pronounced owing to the higher reflectance in the adjacent green portion of the spectrum. Maximum reflectance values range to 0.40. The shadowed component spectra (Figure 5.22) have a slight green peak and a noticeable red edge, but again the overall apparent reflectance values are much lower as the greatest value, found in the NIR, is only about 0.08.

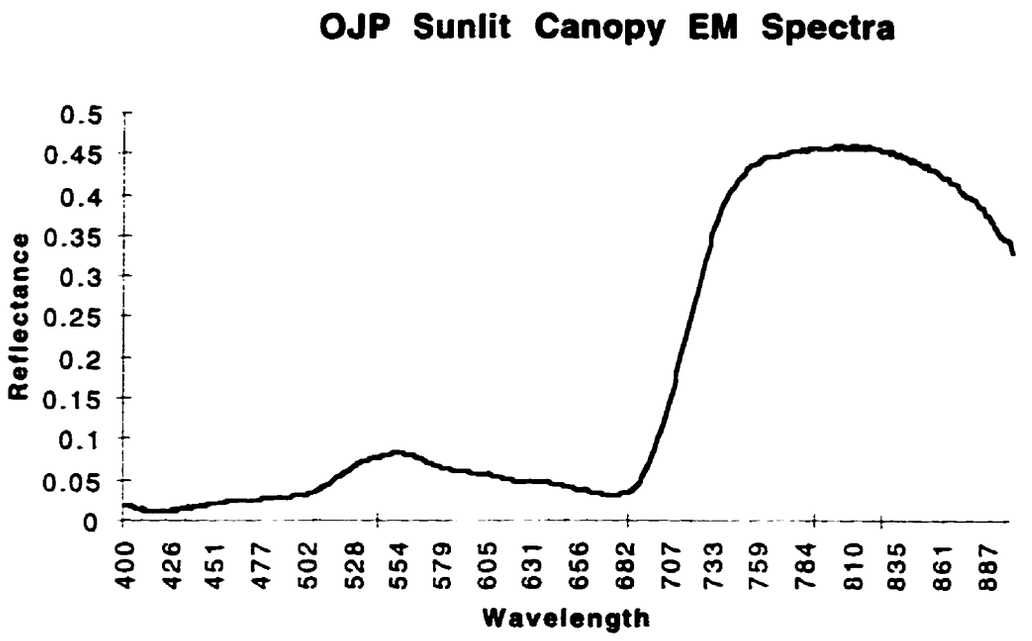


Figure 5.20. Sunlit canopy end-member reflectance spectra for OJP site.

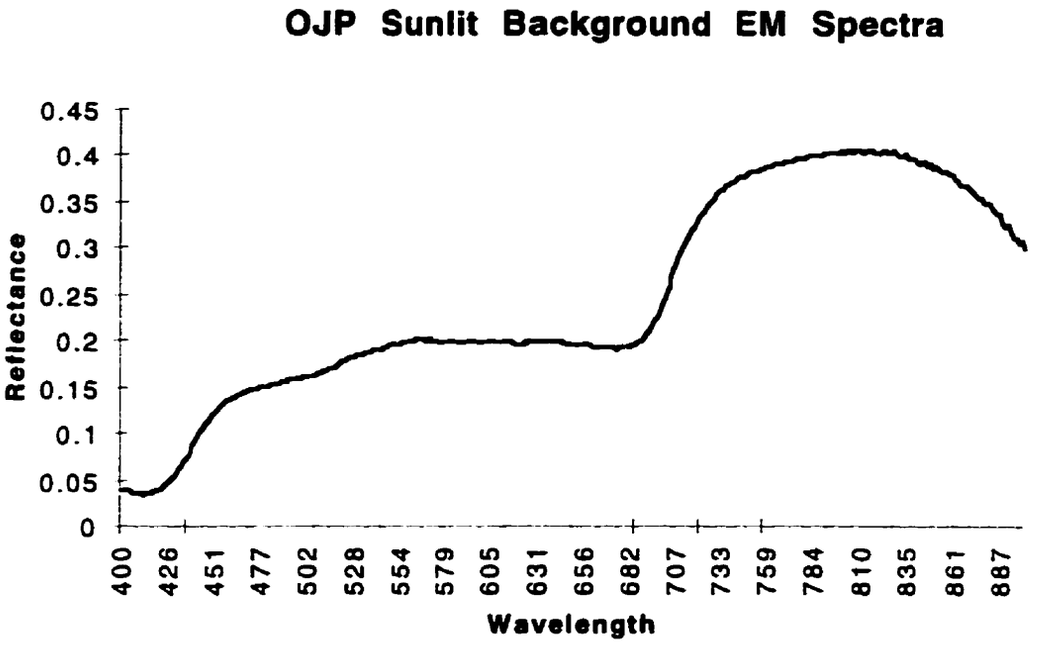


Figure 5.21. Sunlit background end-member reflectance spectra for OJP site.

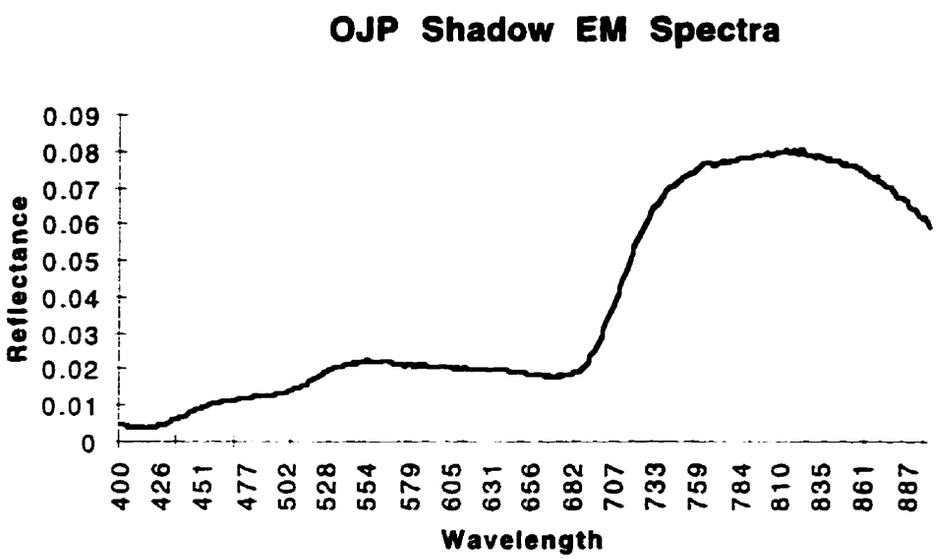


Figure 5.22. Shadow end-member apparent reflectance spectra referenced to the total direct plus diffuse incident irradiance derived from field spectrometer data at SSA old jack pine site. Spectra shown are the average of the shadowed background and canopy sample measurements.

Although the shapes of these reflectance curves are somewhat similar, as would be expected for green vegetation, the differences in absolute magnitude of reflectance values by component and also by species are evident. These spectra form one of the important sets of input to the geometric optical reflectance model used to generate spectral trajectories for input to the image classification and biophysical estimation algorithm. Methods used to generate these spectral trajectories are described next.

## 5.5 SPECTRAL TRAJECTORY GENERATION

### 5.5.1. Model Inputs

The Geometric-Optical Mutual Shadowing (GOMS) model of Li and Strahler (1992) was run in forward mode to compute spectral trajectories for the major boreal forest classes used in this study. The GOMS model has three fundamental types of input requirements: (i) spectral component end-member reflectance values for the tree species under consideration, (ii) physical descriptions of the dimensions and geometric form of these tree species, and (iii) the viewing and illumination angles of the remote sensing instrument and light source, respectively. Given these inputs, the model produces as output the component fractions and the overall reflectance values for the spectral bands and tree stand densities specified. Prior to presenting those results, a description of how the inputs to the model were determined and the interface methods developed for the GOMS modelling software are presented in the following sections.

#### 5.5.1.1 Component End-member Spectra

Component end-member reflectance values for Old Black Spruce and Old Jack Pine were obtained from the ASD field spectrometer data set as described in the previous section. Moss and lichen end-member spectra obtained from samples measured using the Portable Field Laboratory were used for the sunlit background end-member spectra for OBS and OJP, respectively. Sunlit canopy spectra were obtained from optically thick stacks using the PFL set-up for each species. For both OJP and OBS, the shadow reflectance measures were computed as a function of understorey and canopy reflectance

values obtained under shadowed conditions created with the PFL. The use of only one shadow component for GOMS model input necessitated this extra computation since individual shadowed component spectra were measured in the field. In each case, the high spectral resolution ASD reflectance output was synthesized for use with the Landsat TM bandwidths using a first order spectral response curve for TM bands 3 and 4 applied to each set of reflectance spectra. However, for the Aspen class, reliable field spectral measurement was not possible using these techniques, as explained earlier. Instead, a set of end-member spectra were obtained from BOREAS Staff members for Aspen sunlit background and shadowed understorey, while sunlit canopy end-member spectra was obtained from the BOREAS RSS-8 and TE-21 Science Teams (P.I. Dr. Steven Running, University of Montana) who made detailed measurements from the OA tower. The resulting set of spectra input to the GOMS modeling work is contained in Table 5.3

| Class | Band | Sunlit Background | Sunlit Canopy | Shadow |
|---|---|---|---|---|
| OBS | Red | 0.043 | 0.053 | 0.011 |
| | NIR | 0.383 | 0.341 | 0.063 |
| OJP | Red | 0.198 | 0.040 | 0.019 |
| | NIR | 0.384 | 0.433 | 0.075 |
| OA | Red | 0.083 | 0.051 | .0005 |
| | NIR | 0.160 | 0.410 | 0.021 |

Table 5.3. End-member reflectance values used as input to GOMS modeling of spectral trajectories for Old Black Spruce (OBS), Old Jack Pine (OJP) and Old Aspen (OA).

5.5.1.2 Physical Specification of Tree Dimensions and Geometric Form

The GOMS model requires the specification of four tree factors of geometric form which are scaled from five physical parameters. These physical parameters are listed in Table 5.4 and illustrated in Figure 2.2. These variables define the dimensions and spatial distribution of spheroids in the model. Of particular interest to this research is the tree density value ($\lambda$) as this parameter is not measured in the field but instead is used to produce spectral trajectories over the full range of tree densities from low density forest stands (i.e. areas with a sparse occurrence of trees) to high density stands (many trees spaced very closely together). Tree density represents the number of trees per given area and is expressed as a percentage in the reflectance model, where maximum density is defined by the largest number of spheroids that can exist without any overlap, computed as a function of horizontal crown radius (r) and tree height distribution (dh).

| Symbol | Physical Meaning |
|---|---|
| $\lambda$ | tree density (count/area) |
| r | horizontal radius of tree crown |
| b | vertical radius of tree crown (crown height/2) |
| h | height from ground to center of crown |
| dh | height distribution of trees (4 × standard deviation of height) |

Table 5.4. GOMS model inputs for physical tree dimensions and geometric form.

Table 5.5 contains the values of those parameters which were derived for each species. In some cases, direct measurements of these parameters were available through the BOREAS Information System (BORIS), while in other cases individual scientists or project groups within BOREAS were contacted directly to obtain the necessary measures or to obtain related terms from which the parameters could be derived. In time, all of these data will be resident on BORIS and available in one place - however when this part of the research was being performed, the process of placing these data on BORIS was in progress for most of the BOREAS project teams. In all cases, however, the contact individuals assured that all information provided had been quality checked and was suitable for investigator use throughout the BOREAS project. Although the task of assembling this data set was somewhat time consuming, it was quite beneficial since access to additional data (not scheduled for BORIS distribution) was made possible through contacts established with other BOREAS scientists which otherwise would not have occurred had all the data been downloaded anonymously from the online BORIS database.

A primary source of information was BOREAS project TE-23 (PI: Dr. Paul Rich, Kansas University; contact individual: Dr. Richard Fournier, RSS-19 and TE-9) whose team performed an extensive site characterisation of forest canopy architecture in BOREAS at tree and forest stand levels. A series of 300 $m^2$ map plots and grids were established at each BOREAS TF site within which sampling occurred at 10m intervals. A large number of canopy architecture measurements were acquired; only those relevant to this research are summarised here. Measurements of tree height were obtained based on trigonometric functions applied to measurements of the horizontal distance from the observer to the target (using a sonic rangefinder) and measurements of the angle from the observer to the top and base of the target (using a standard clinometer). Crown radius measurements were taken

by locating points directly underneath the observed outermost extent of the tree crown, and measuring the distance from that point to the center of the tree trunk. For certain sites, 'height to lowest green foliage' measurements were also available and were included in several computations here. These measurements were obtained either by direct tape measurement or by using the height measurement method described earlier, depending on accessibility to the tree and the field scientist's height.

| Parameter | OBS | OJP | OA |
|---|---|---|---|
| r | 0.84 | 1.2 | 1.7 |
| b | 2.53 | 3.5 | 3.03 |
| h | 7.72 | 11.06 | 20.13 |
| dh | 18.4 | 8.96 | 16.12 |

Table 5.5. Physical tree dimensions and geometric form parameters input to GOMS model for OBS, OJP and OA species. All parameters specified in metres. Symbols defined in Table 5.4; explanation of computations and sources of information contained in text.

For OBS, the 'r' value was obtained through BORIS from BOREAS project TE-23, with the 'b' value obtained from data acquired from BOREAS Staff. The value for 'h' was derived as a function of average tree height (Havg) obtained from TE-23 and the 'b' value using equation 5.2:

$$h = Havg - b \tag{5.2}$$

The standard deviation of tree heights was obtained from the same sample of tree heights used to compute Havg (TE-23), from which a value for 'dh' was derived.

For OJP, the values of 'r' and 'b' were obtained through BOREAS project HYD-3 (PI: Dr. Bert Davis, contact person: Dr. Janet Hardy) in collaboration with members of Dr. Alan Strahler's group at Boston University (Dr. Curtis Woodcock and Dr. Wenge Ni). The 'h' value for OJP was derived using equation 5.2 with Havg obtained from TE-23. Similarly, 'dh' was derived from the same sample of OJP tree height measurements from TE-23, in the same way as with OBS.

The Old Aspen tree measures were obtained from TE-23 BORIS data. The 'r' value was computed from the sample of available crown radii, with the 'b' value obtained as a function of average tree height (Havg) and height to lowest green foliage (HT_GR) measures acquired from the same sample, using equation 5.3.

$$b = \frac{Havg+HT\_GR}{2} \tag{5.3}$$

Similar to OBS and OJP, the value for 'h' was obtained using the Havg sample value and equation 5.2, with 'dh' also computed from the sample of tree heights.

The parameters listed in Tables 5.4 and 5.5 are actually entered into the GOMS model as 4 factors and not as individual tree parameters. These factors are listed in Table

5.6. The reason for this input specification is that, in the model, these factors only occur in these four combinations, and are never isolated (e.g. 'r' is not used on its own). This results in the model being less sensitive to individual parameter measurements which provides for a more robust representation of canopy geometry since the problem scales according to the proportions derived. Further, this provides flexibility on input for cases where actual tree parameter measurements are not available but instead relationships among key parameters are known. In Tables 5.5 and 5.6, the $\lambda$ parameter is not specified as this is varied in the spectral trajectory generation process for the range of tree densities. This computation is one of the functions of the GOMS interface software, described next.

| Input Parameter | OBS | OJP | OA |
|---|---|---|---|
| $\lambda \cdot r^2$ | $0.71\lambda$ | $1.44\lambda$ | $2.89\lambda$ |
| $\frac{b}{r}$ | 3.01 | 2.92 | 1.78 |
| $\frac{h}{b}$ | 3.05 | 3.16 | 6.64 |
| $\frac{dh}{b}$ | 7.27 | 2.56 | 5.32 |

Table 5.6. Actual GOMS model input parameters for OBS, OJP and OA derived according to input parameter formulae listed, using values contained in Table 5.5.

5.5.1.3 Sun-Sensor Orientation Angles

For each model run, the view angle and azimuth of the sensor must be specified, as well as the illumination zenith angle and azimuth. These parameters are listed in Table 5.7. The illumination angles correspond to the solar position at the time of Landsat TM image acquisition on 2 September 1994.

| | Zenith | Azimuth |
|---|---|---|
| View | 0.0 | 0.0 |
| Illumination | 50.71 | 146.0 |

Table 5.7. Landsat TM satellite view angles and solar illumination positions for TM scene acquired 2 September 1994 over BOREAS SSA. Each parameter is input to the GOMS model to specify sun-sensor orientation.

### 5.5.2 Geometric Optical Model Software Interface

The information described in the previous section must be organised into separate files for input to the GOMS model. For a small number of model runs, it is feasible to simply create these input files using a standard word processor and run the GOMS model interactively. However, when using the reflectance model to compute spectral trajectories and component fractions, a large number of model runs are required and therefore both the manual creation of large numbers of input files as well as the interactive execution of the

modeling software itself is prohibitive. Therefore, these tasks were automated through the creation of a software interface to acquire these inputs and produce the necessary set of input files and operating system command files to direct batch mode execution of the large set of model runs needed to produce each spectral trajectory. In this research, trajectories were created for tree densities ranging from 0.01 to 1.00 (the $\lambda$ value in Tab'e 5.4) at an increment of 0.01. Appendix B contains a description of this program and a listing of the source code (BAT_GOMS.C) together with the input files and operating system command files necessary to use the software. Example output files are also contained in Appendix B, with the spectral trajectories produced from this process presented in the next section.

### 5.5.3 Model Output: Component Fractions and Spectral Trajectories

For each BOREAS TF site tree species class considered (OBS, OJP, OA), the output from the GOMS model runs consists of a set of component fractions and the overall reflectance value computed at each tree density value specified. In all cases, these values were computed for stand densities ranging from 0.01 to 1.00 at an increment of 0.01. The full set of computed reflectance values and their associated component fractions produced over this range of tree densities constitute the modelled spectral trajectory for each species being considered. In this section, these species class trajectories are presented, as well as the method used to derive trajectories for the mixed forest class. In each case, the full reflectance and component fraction trajectories are presented and discussed for each class, and an intercomparison of trajectories by species is also presented. These trajectories are also discussed in more detail later in this Chapter when they are compared to training data produced for these same classes.

5.5.3.1 Coniferous and Deciduous Trajectories

For each class, illustrations have been generated to show (i) the overall reflectance values produced over the full range of stand densities in both red and NIR bands, and (ii) the set of component fractions (C,B,S) associated with each reflectance value over the range of densities. In interpreting these trajectories, there exists an intimate relationship between component fraction magnitude and modelled reflectance at any given tree density value. As we shall see, there are characteristic shapes to these trajectories which vary as a function of stand density and canopy cover. The magnitude of the fractions and actual reflectance values produced vary by species as a function of the component end-member reflectance values and the physical descriptions of geometric form and dimension for individual tree types as input to the model. For each species considered, a physical understanding and explanation of patterns observed in modelled component fraction and reflectance trajectories is provided with respect to actual canopy morphology and solar interactions with the forested medium.

Figure 5.23 shows the component fractions for sunlit canopy (C), sunlit background (B) and shadow (S) over the full range of tree densities. The modelled red and NIR reflectance for OBS are shown in Figure 5.24. In the case of OBS, at very low density values where there are few trees, the sunlit background fraction is high and this component comprises most of the overall reflectance signal. Accordingly, the red and NIR reflectance values in Figure 5.24 are close to the end-member sunlit background reflectance values (Table 5.3). As tree density is increased in the model, the sunlit canopy fraction begins to increase, because there are more trees, while the sunlit background fraction decreases as the understorey becomes more obscured. With more trees, there will be more

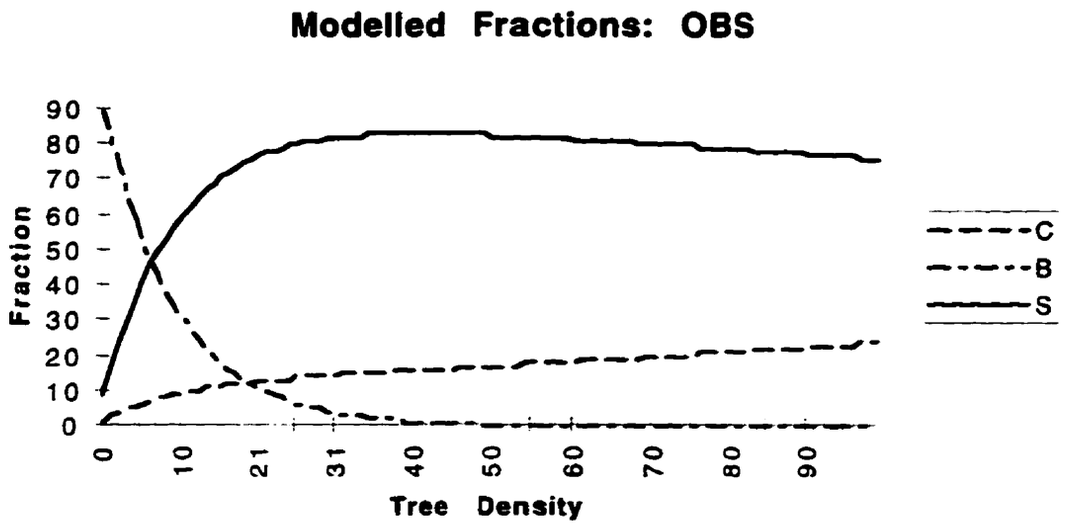


Figure 5.23. Variation of component fractions generated by GOMS model for sunlit canopy (C), sunlit background (B) and shadow (S) as a function of tree density for Old Black Spruce (OBS).

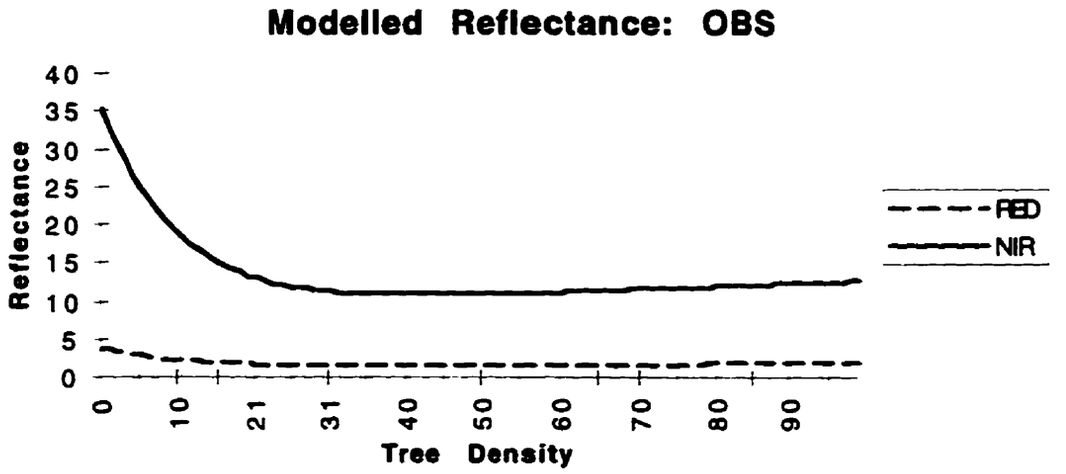


Figure 5.24. GOMS modelled red and NIR reflectance for OBS TF site over a full range of tree densities.

shadows cast, and therefore the shadow fraction increases. Accordingly, as shadows increase. reflectance values would be expected to decrease. This is the case, as depicted in Figure 5.24, where both red and NIR reflectance values decrease with increasing tree density. For OBS, as tree density increases to the maximum, sunlit canopy fraction continues to show a rather small, linear increase while shadow fraction shows a small decrease, with sunlit background fraction going to zero. Consistent with this trend, the modelled red and NIR reflectance values are mostly flat, with a slight increase with tree density noted.

The modelled fractions and reflectance values for Old Jack Pine are shown in Figures 5.25 and 5.26, respectively. Similar to OBS, the initial values for sunlit background fraction are high for low stand densities, with the corresponding red and NIR reflectance values approaching the sunlit background end-member reflectance values. However, as tree density increases, sunlit background fraction decreases more quickly for OJP than for OBS, with sunlit canopy fraction and shadow fractions increasing at a higher rate. This difference is due in part to the larger horizontal and vertical crown radii values ('r' and 'b', respectively) specified in the physical description of OJP trees (see Table 5.5). For an incremental increase in stand density, the corresponding increase in tree size at the stand level is greater for OJP than for OBS since the individual trees being added are larger. Also, OJP has a smaller degree of height variability (dh) compared to OBS, and has taller trees (interpreted through 'h'). With this more rapid increase in C and S, the sunlit background fraction decreases at a higher rate and goes to zero at a lower tree density than OBS. Again, this is due to the different physical specification of canopy morphology for these species.

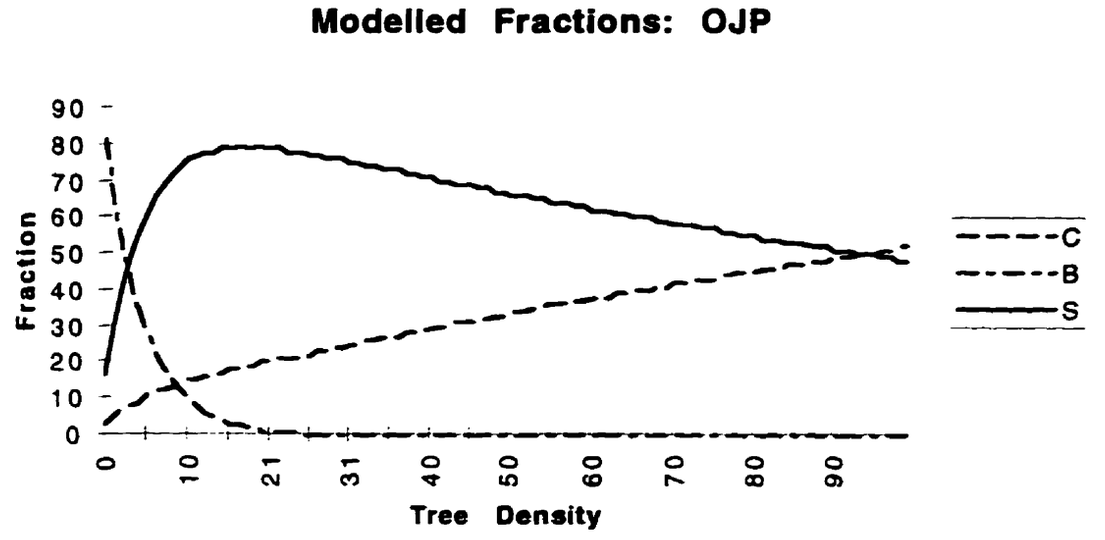


Figure 5.25. Variation of component fractions generated by GOMS model for sunlit canopy (C), sunlit background (B) and shadow (S) as a function of tree density for Old Jack Pine (OJP).

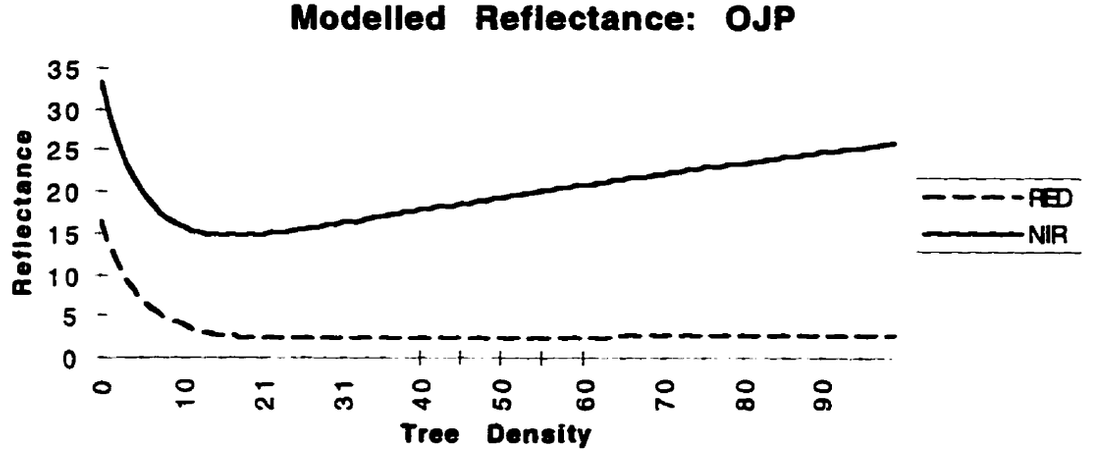


Figure 5.26. GOMS modelled red and NIR reflectance for OJP TF site over a full range of tree densities.

With OJP, an interesting pattern is observed in the evolution of component fractions and reflectance as stand density is increased. As mentioned above, as tree density increases from the minimum, sunlit canopy fraction and shadow fraction also increase. However, as is evident in Figure 5.25, shadow fraction reaches a maximum and then starts to decrease beyond a certain value of increasing tree density. At this point, termed the critical density (Hall *et al.* 1995), the sunlit crowns are sufficiently dense that they begin to obscure the shadows produced by nearby trees. Beyond this point, as tree density increases further, the additional crowns continue to increasingly obscure shadow and hence the shadow fraction continues to decrease, while sunlit canopy fraction continues to increase steadily, with sunlit background fraction remaining at zero as this component is completely obscured by either sunlit canopy, shadow, or both.

In terms of reflectance (Figure 5.26), the red and NIR reflectance values decrease initially from near the sunlit background end-member reflectance value as the fraction of sunlit tree canopy and the associated shadow fractions increase. Here, it is primarily the increase in shadow fraction which results in overall reflectance values being reduced. This trend of decreasing red and NIR reflectance continues until the critical density point is reached. At that point, modelled reflectance values start to increase, particularly in the NIR, since the amount of shadow is decreasing, as explained above. The physical explanation of the larger increase in NIR reflectance is that at higher tree densities where there is more sunlit canopy, there will be a greater incidence of multiple scattering. Since the amount of scattering from cell walls governs light reflectance in the NIR, a more pronounced increase in NIR would be expected as tree density increases, and this is the case.

The component fraction and reflectance trajectories for Old Aspen (OA) are shown in Figures 5.27 and 5.28, respectively. As might be expected for these deciduous trees, the modelled trajectories are rather different when compared to the coniferous OBS and OJP trajectories. This is due to the substantial differences in both the end-member spectral values for each deciduous component, and also in the physical geometric form and dimension parameters associated with this species. These trees had the largest horizontal crown radius (r) and also the greatest tree heights (interpreted from 'h') and degree of variability of tree heights (dh), as listed in Table 5.5. In particular, aspen trees contain much of their foliage in the upper half and near the top of the trees, in contrast to both OBS and OJP whose live branches tend to begin lower to the ground with a more tapered shape near the crown apex. In terms of the model inputs, this difference is evident with the OA h/b ratio (see Table 5.6), which is twice that of both OBS and OJP. The OA canopies are represented by spheroids that are more oblong in the horizontal dimension (largest r; smallest b/r ratio) and which rest on a considerably longer trunk (h/b).

The fractions produced by the model follow a somewhat similar shape as with OBS and OJP as tree density increases, but with several notable exceptions. As before, at low densities a high sunlit background fraction is observed, and this decreases rapidly as density increases. The critical density value is prominent and occurs at lower densities than with OJP. However, sunlit canopy fraction shows a more rapid increase as stand density is increased, and this trend continues to maximum density. This steeper slope of the curve of sunlit canopy fraction increase is likely due to the larger horizontal crown radii and the more flat shape of the spheroid in the horizontal dimension. This would also explain the steep rise in shadow fraction as tree density is increased from minimum to low densities. Each modelled crown is larger in the horizontal dimension and therefore presents a larger

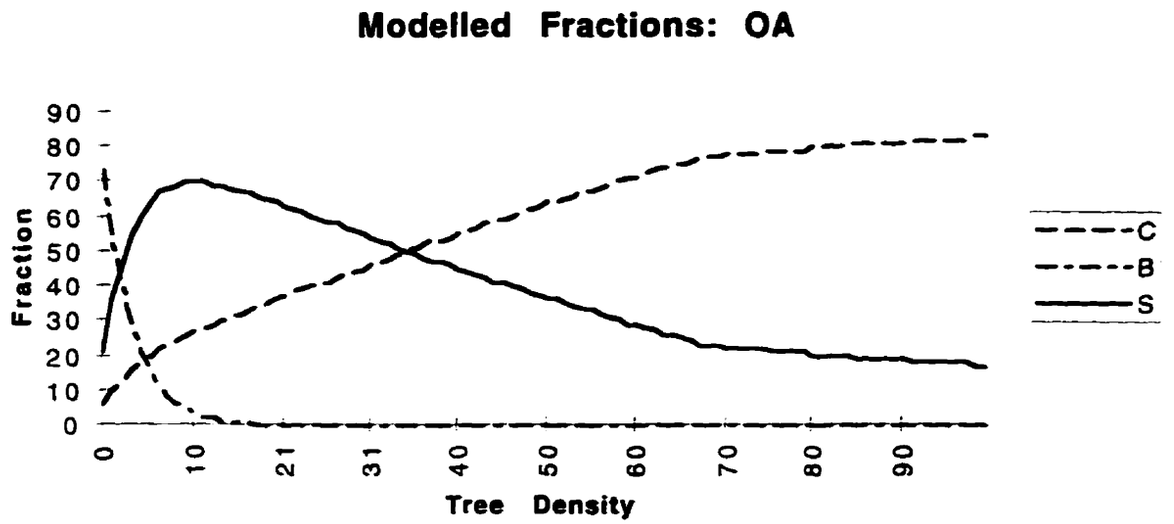


Figure 5.27. Variation of component fractions generated by GOMS model for sunlit canopy (C), sunlit background (B) and shadow (S) as a function of tree density for Old Aspen (OA).

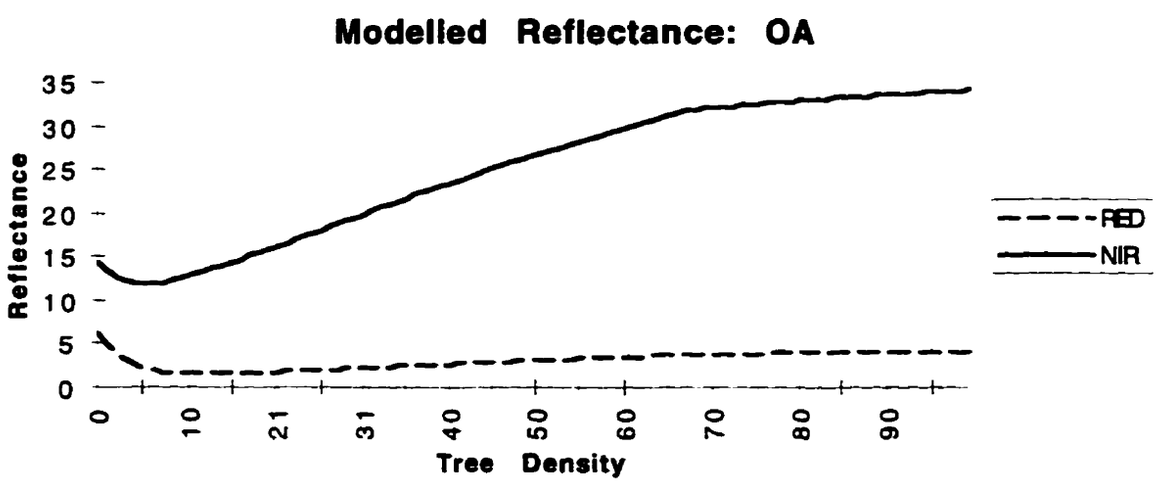


Figure 5.28. GOMS modelled red and NIR reflectance for OA TF site over a full range of tree densities.

canopy surface area for observation, while quickly producing larger shadows. This effect is such that as tree density is further increased the sunlit canopy fraction exceeds the shadow fraction at mid-range densities. Here, the larger, more flat shape of the spheroid results in greater sunlit canopy fractions, and as the density of these spheroids is increased the sunlit canopy is less likely to be shadowed due to this flatness, resulting in the consistent and corresponding decrease in the shadow fraction. In contrast to this, the longer, more peaked spheroids used to represent OBS and OJP do not provide as much new surface area at the nadir view angle when their tree densities are increased.

Similar to OJP and OBS, the modelled reflectance values for OA (Figure 5.28) exhibit the initial decrease in reflectance as the more highly reflective sunlit background becomes quickly obscured. This decrease is not as large as with OJP or OBS as the critical density is reached at a considerably lower tree density. The marked increase in sunlit canopy and decrease in shadow fraction as tree densities are further increased results in the corresponding increase in reflectance. This increase in reflectance is larger for OA compared to both OJP and OBS. This is due to the larger rates of change of C and S with OA, as explained above in terms of the characteristic physical geometry of these deciduous trees.

In addition to the different geometric form parameters used, the rapid increase in shadow fraction at lower densities for all species concerned is also accentuated by the time of year, the time of day for satellite image acquisition, and latitude. All of these factors contribute to the higher solar zenith angles encountered in this study. Therefore, as tree density increases from a minimum, individual shadows cast by trees will be larger in a sparse, low density forest. As tree density increases, the differences in shadow fraction

would be less. This trend of rapidly increasing shadow fraction would be more subdued at earlier times of the summer, such as near the summer solstice, at daily observation times closer to solar noon, or at lower latitudes.

5.5.3.2 Mixed Forest Trajectories

The previous model outputs were generated for pure stands of each species, with end-member spectra and physical dimension and form measured for each directly in the field. However, for the mixed forest class, direct measures of such parameters were not possible since firstly it would be difficult to identify an appropriate mixed forest candidate site for this type of procedure, and secondly, homogeneous samples of each forest component are required in the field but mixed samples do not occur in nature at the scales required for measurement. Various methods of combining samples in different proportions could be proposed for field measurement, however this was not considered as it would be fraught with experimental errors and inconsistencies, as well as logistical impracticalities. Instead, the approach taken here was to combine the spectral trajectories generated from each species which occur in the mixed forest class. The underlying rationale for generating spectral trajectories lends itself well to identifying a mixed forest trajectory as function of the component species which comprise the mixed forest class.

To produce modelled spectral trajectories, the composition of the theoretical mixed forest class is defined to contain an equal abundance of coniferous and deciduous trees (i.e. 50% each). Further, since the former class contains two species (OBS and OJP), their contribution must also be quantified. Again, an even division was used in terms of the

contribution of each coniferous species to the resulting mixed class trajectory. The final mixed forest class trajectory values ($M_{TV}$) for component fractions and reflectance values were computed using a weighted average function applied to the OBS, OJP and OA trajectory values ($OBS_{TV}$, $OJP_{TV}$, $OA_{TV}$, respectively) at each point along the trajectory defined by the range of tree densities, using the following equation:

$$M_{TV} = 0.50\ OA_{TV} + 0.25\ OBS_{TV} + 0.25\ OJP_{TV} \qquad (5.4)$$

The resulting component fraction and reflectance trajectories produced are illustrated in Figures 5.29 and 5.30, respectively. Since, in general, all three species trajectories have somewhat similar shapes, the shape of the mixed trajectories does not differ greatly from the others. Of course, the magnitude of reflectance values and the positioning of fractional variations are quite different, as is the case with each of the three species trajectories. As the mixed forest class is likely to contain substantially more internal variability compared to the other classes, the definition of an optimal method of representing such a class is not straight forward regardless of the method of analysis. Further, it is difficult, if not impossible, to perform a rigorous evaluation of the class representation. Therefore, the method used in this research to generate a mixed forest trajectory is deemed to be a reasonable approach, although from a theoretical standpoint it is difficult to know if this approach is optimal.

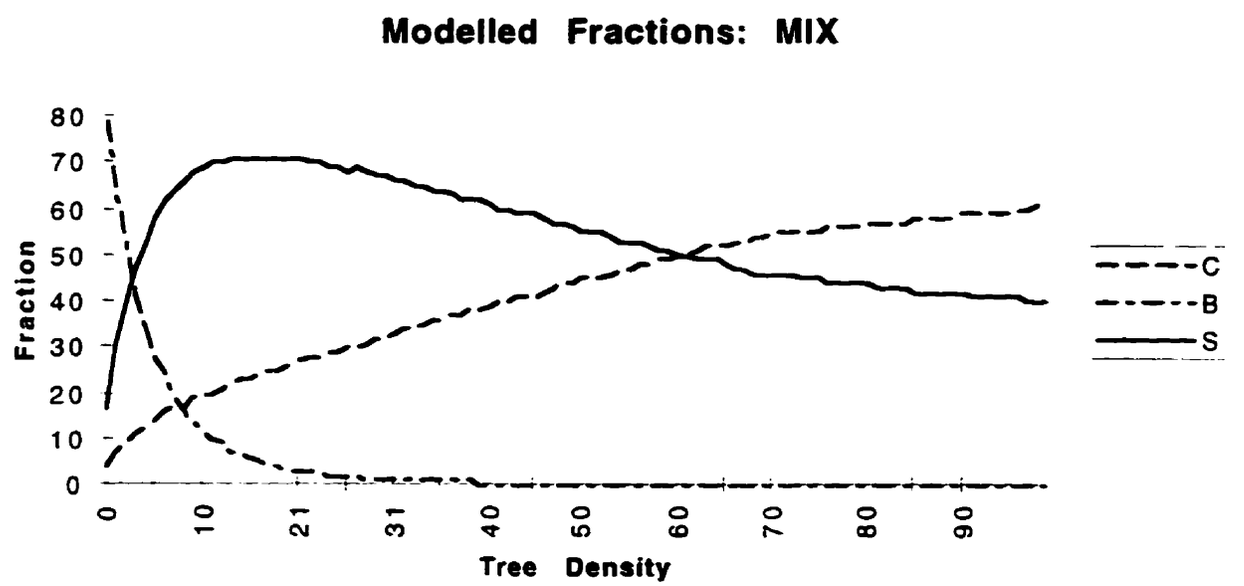


Figure 5.29. Variation of component fractions for sunlit canopy (C), sunlit background (B) and shadow (S) as a function of tree density for mixed forest (MIX).

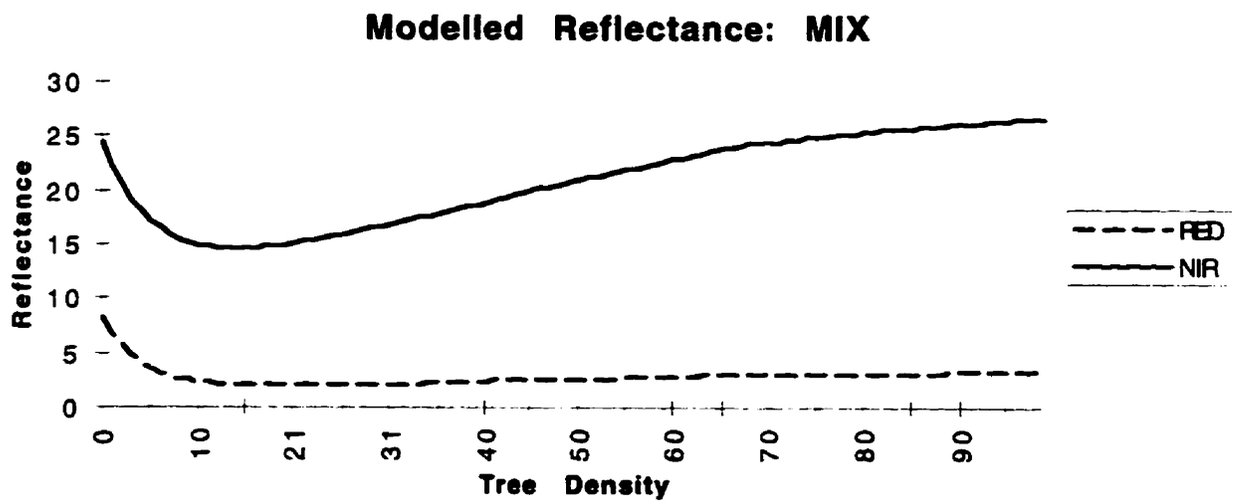


Figure 5.30. Mixed forest trajectory produced by integrating modelled reflectance trajectories from OBS, OJP and OA over a full range of tree densities.

5.5.3.3 Comparison and Evaluation of Class Trajectories

In the previous sections, the trajectories produced for each class were presented and evaluated individually. However, as the goal of these trajectories is to, in the first instance, provide useful information for land cover classification (with subsequent biophysical parameter estimation), it is important to evaluate the spectral trajectories as a group with respect to their ability to provide discrimination of forest classes of interest based on input satellite spectral response. Therefore, for each spectral band, the four spectral reflectance trajectories are displayed together over the full range of tree densities used. The resulting plots are shown in Figures 5.31 and 5.32 for the red and NIR bands, respectively.

As is evident in both the red and NIR plots, each class occupies different positions through spectral space with respect to tree density. This is desirable since excessive overlap of spectral class trajectories can lead to landcover misclassification and error in biophysical parameter estimation. In the red band, there is reasonable separation of class trajectories, particularly at low densities (<10%) and also above 25%. Between 10% and 25%, there is some overlap with the OBS and MIX trajectory, and also this is where the deciduous OA trajectory crosses the coniferous (OBS and OJP) trajectories, owing to the different physical and spectral properties of the deciduous trees being modelled, as explained earlier. For the mixed class, some areas of overlap or modelled spectral similarity would be expected, owing to the method used to derive the MIX trajectory as a function of the OBS, OJP and OA trajectories (equation 5.4). Fortunately, these areas of direct overlap are minimal and are limited only to individual intersection points. As the dynamic range of variation among spectral response of these species is not as great as in the NIR, the

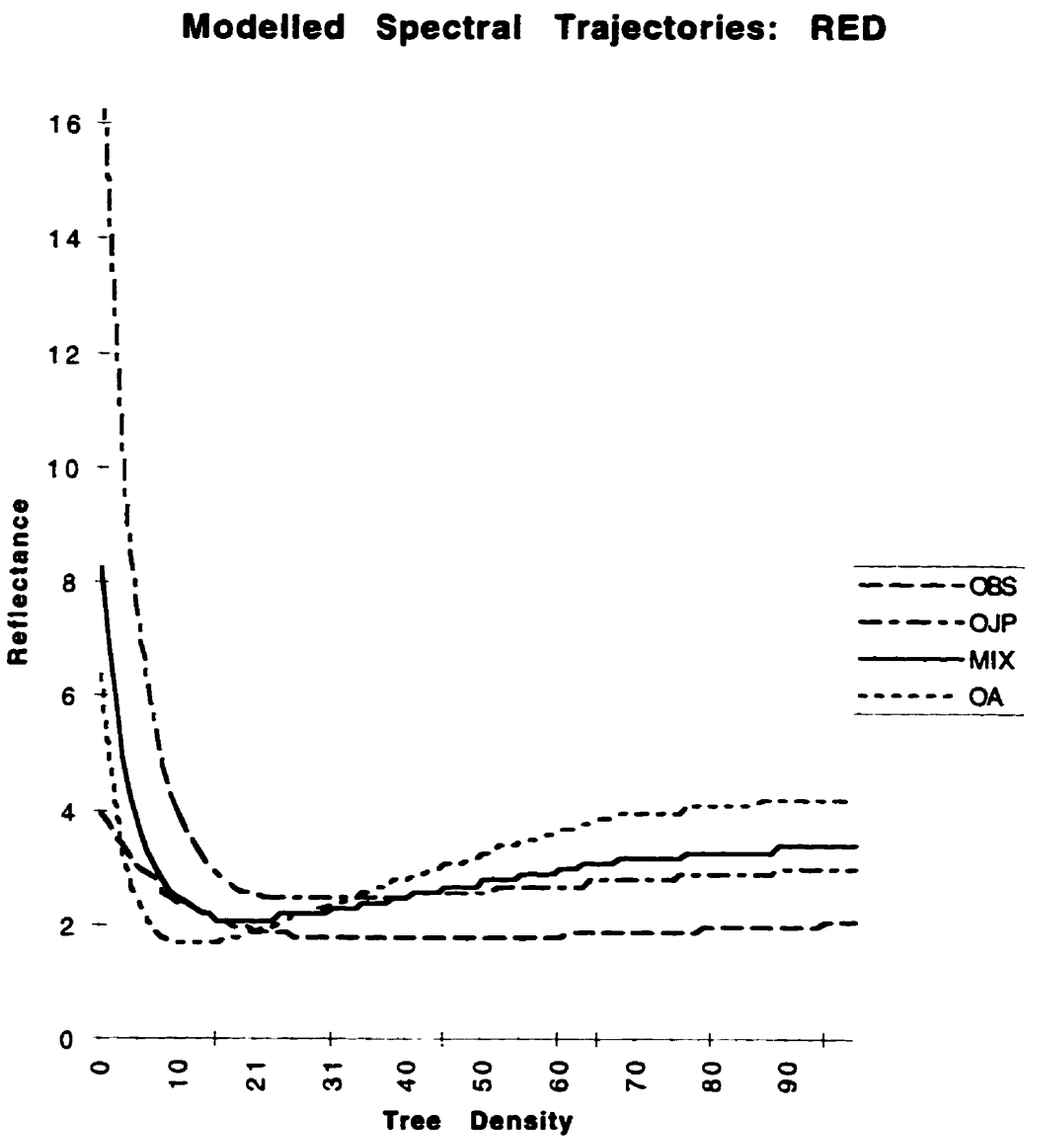


Figure 5.31. GOMS modelled red reflectance trajectories for each of the major BOREAS forest cover classes over a full range of tree densities.

differences in absolute reflectance values of the modelled trajectories would also be expected to correspond to this trend, and this is indeed the case. It is more important to minimise overlap than to have larger differences in absolute reflectance values, since it is the proximity to the trajectories that defines the land cover class and biophysical estimates. Given this, the differences observed among class trajectories would be expected to provide good discrimination in this band.

In the NIR band (Figure 5.32), there is also good separation between class trajectories. There is no direct overlap of spectral trajectory regions for any of the four classes modelled. In terms of intersection points, there is only one, however all four classes intersect at that point, which is located at 17% tree density. When classifying stands at that density, the NIR band would provide no discrimination among any of the classes. Fortunately, this only occurs at one point, and as noted the discrimination for virtually the entire range of tree densities is quite good. For stand densities at or near 17%, discrimination would rely on differences in the red band. The modelled red trajectory near 17% shows reasonable discrimination among all classes, except OBS and MIX, where the trajectories are rather similar. Therefore at stand densities near 17% where the NIR would be less effective, the red band should be able to provide adequate discrimination. As the dynamic range of spectral response is greater in the NIR, there are also larger differences in absolute reflectance by class. The greatest amount of spectral separation is found at higher densities in the NIR, between densities of 20% and 100%. The three major forest classes are well separated, while the MIX class is located in the middle and closer to the OJP trajectory at these densities. The difference between low density and high density spectral separation is greater in the NIR compared to the red, where the degree of separation is reasonably consistent except at densities between 10% and 25% where OBS and MIX

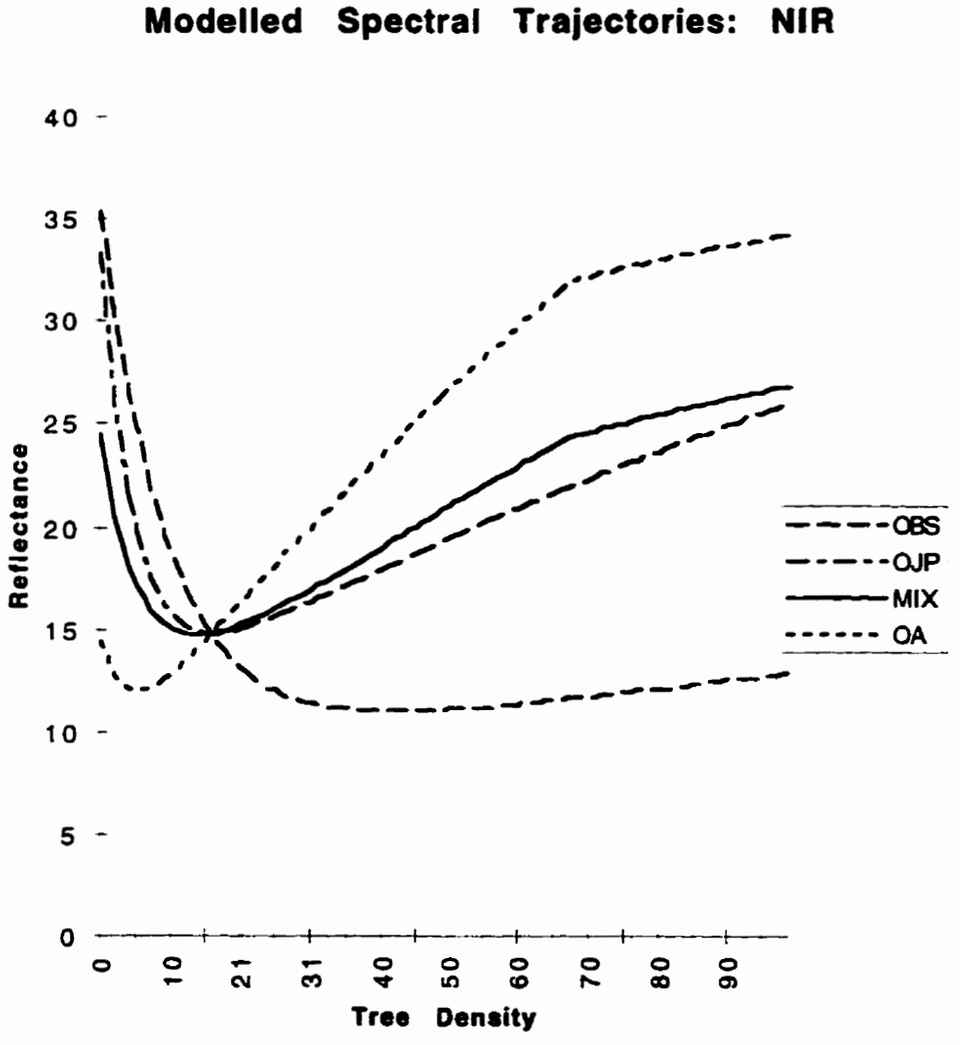


Figure 5.32. GOMS modelled near infrared (NIR) reflectance trajectories for each of the major BOREAS forest cover classes over a full range of tree densities.

overlap, as discussed earlier. Overall, it is concluded that there appears to be good spectral separation provided by these red and NIR trajectories with respect to the full range of tree densities considered. In the next section, we examine the sensitivity of model inputs with respect to the trajectories created using this approach.

#### 5.5.3.4 Sensitivity of Trajectories to Model Inputs

In the previous sections, class trajectories were presented and plotted as a function of the tree density parameter which was varied on model input to produce a full trajectory in each case. In this section, we are interested to examine the sensitivity of trajectory outputs as a function of variability of model inputs to gain insight into model performance as well as field data requirements. As we have seen, there are three general categories of inputs to the GOMS model when run in forward mode: (i) end-member spectra for each forest component (§5.5.1.1); (ii) specifications of tree dimension and geometric form (§5.5.1.2); and, (iii) sun-sensor orientation angles (§5.5.1.3). In the case of end-member spectra, these were obtained by direct measurement of individual component samples and therefore, in this study, this set of model inputs was not derived from a sample that had an associated variability measure. Although it is possible to derive end-member spectra from a sample and hence provide an indication of sample variance, such an indicator may not be appropriate for modifying this particular model input due to the nature and fundamental definition of end-member spectra and the need to identify and measure components with minimum heterogeneity, or ideally, one which is homogeneous. In the case of the third set of model inputs, these are constant parameters which define the absolute position of the sun and the remote sensing instrument with respect to the target surface, and again, these parameters do not have an associated measure of variability.

In contrast to both of these types of model inputs, the set of tree dimension and geometric form parameters (see Figure 2.2 and Table 5.4) may be derived as average values from a sample of individual tree measurements, and therefore it would be appropriate to evaluate trajectory outputs as a function of input parameter variability. In this study, however, several approaches and sources of data were used to obtain these model inputs due to the varying availability of data in BOREAS at the time when these trajectory inputs were required, as explained in §5.5.1.2. In many cases, a single value was obtained for a particular parameter from another BOREAS scientist, with no opportunity to derive measures of sample variance associated with that value. This was true for the horizontal tree crown parameter (r) and the vertical radius of tree crown (b) parameter for OBS and OJP. The parameter which specifies the height distribution of trees (dh) is calculated as a function of sample variance and is therefore not appropriate to be modified upon model input, since to alter this parameter would violate the original definition of how this parameter is computed. The only other remaining input tree dimension parameter is height from ground to center of crown (h). Although it is possible to measure this parameter in the field, in this study it was derived from a sample of tree measurements from BOREAS project TE-23 as a function of the average tree height from a sample, and a single value for vertical radius of tree crown (b), using equation 5.2. Therefore, the only variable from which sample variance could be computed in that equation is the tree height parameter, but since this is functionally equivalent to the dh parameter, we find that it is not plausible to vary this parameter for the purpose of the sensitivity analysis objective. As a result, it was not possible to perform a class specific sensitivity analysis with the available data.

Instead, an empirically-based simulation of model sensitivity was performed with respect to the Old Aspen tree dimension and form parameters for which appropriate sample data existed. This approach takes advantage of the fact that the actual model inputs are entered as ratios of individual parameters (see Table 5.6), and therefore these inputs are less sensitive to variability among individual measurements since, in physical terms, these parameters scale in nature within the range of possible tree forms and dimensional relationships inherent to a given tree species. As with the OBS and OJP data, samples for each input parameter did not exist for OA and this prevented a direct sensitivity analysis. However, unlike the conifer classes, samples of OA tree measurements were available from which input parameters could be calculated. Specifically, the $\frac{b}{r}$ and $\frac{h}{b}$ ratios could be derived from sample data using equations 5.2 and 5.3. Analysis of these derived samples revealed that these ratios did not vary by more than 10% for Old Aspen. This figure was taken to be a reasonable estimate of the magnitude of variability which we may expect from other model input ratios from different classes. Accordingly, based on this assumption, error bands of $\pm 5\%$ were computed for each class spectral trajectory, and these were plotted in Red-NIR spectral space for each major forest class together with the original spectral trajectory output by the model. The results of this process are shown in Figures 5.33 - 5.36 and discussed next. We note, however, that these results should be interpreted with caution since there are insufficient data available in the present analysis to test the assumptions regarding the absolute magnitude of error bands shown. As additional tree data become accessible through BORIS it may be possible to devise a more rigorous sensitivity analysis based on direct model inputs. In lieu of that, the present approach is appropriate for the purposes of creating an initial way of estimating the sensitivity to GOMS input factors and model output variability.

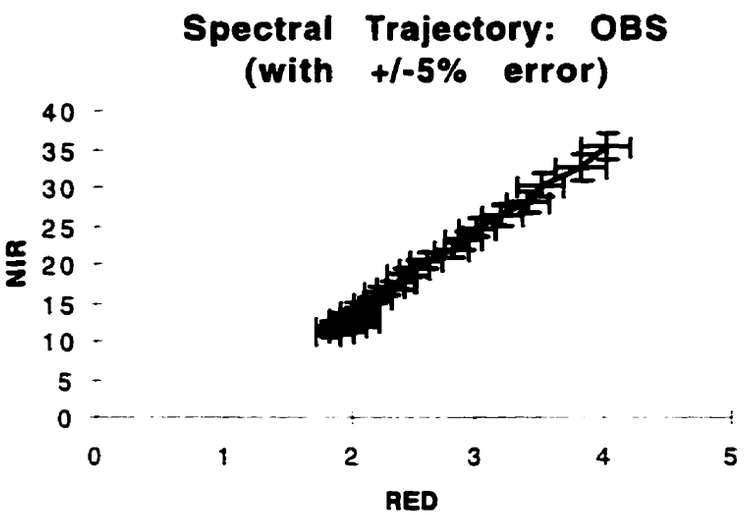


Figure 5.33. Spectral trajectory of Old Black Spruce showing ±5% error bands computed as an estimate of GOMS model sensitivity to tree dimension and form parameter inputs.

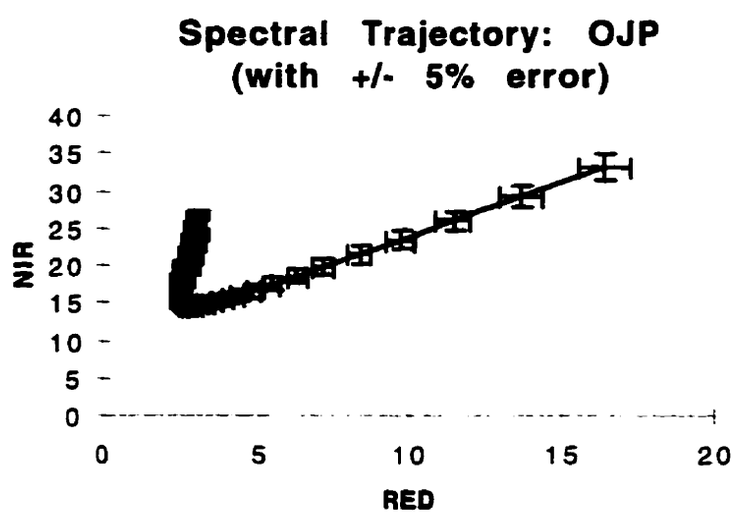


Figure 5.34. Spectral trajectory of Old Jack Pine showing ±5% error bands computed as an estimate of GOMS model sensitivity to tree dimension and form parameter inputs.

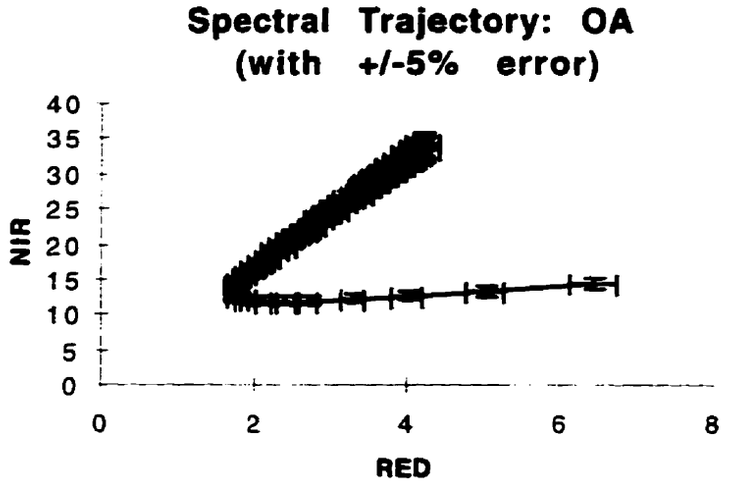


Figure 5.35. Spectral trajectory of Old Aspen showing ±5% error bands computed as an estimate of GOMS model sensitivity to tree dimension and form parameter inputs.

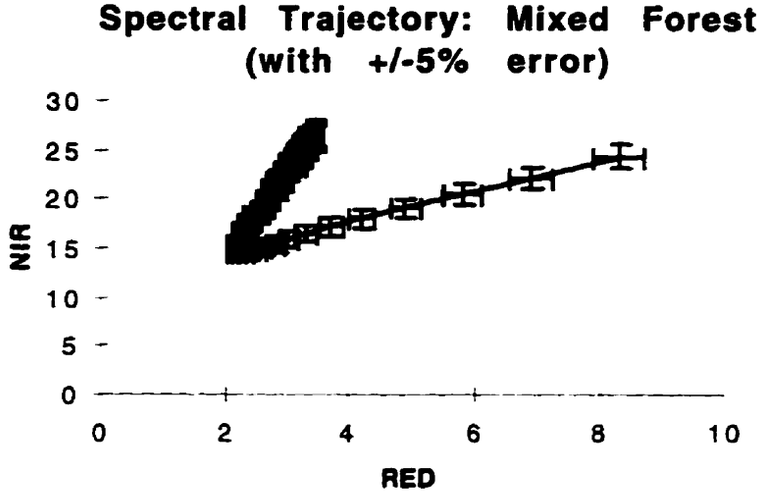


Figure 5.36. Spectral trajectory of the Mixed Forest class showing ±5% error bands computed as an estimate of GOMS model sensitivity to tree dimension and form parameter inputs.

The OBS Red-NIR spectral plot, shown in Figure 5.33, depicts a primarily linear distribution of values, although a small hook is noticeable near the bottom of the trajectory corresponding to lower pixel values in the red and NIR which occur at very high tree densities. This small hook-shape at the end of the trajectory is indicative of the spectral position of the critical density value. This is where tree density becomes sufficiently high such that the shadow fraction begins to decrease as the canopy closes and adjacent crowns become preferentially illuminated. In terms of the error bands shown, there appears to be little overlap except near the bottom part of the trajectory where the maxima of computed pixel variance overlaps with nearby values in spectral space where the trajectory positions are directly affected by the critical density value. For OJP, shown in Figure 5.34, we see a much more pronounced change in the shape of the spectral trajectory as the critical density value is encountered. Below the critical density value, red and NIR spectral response decreases from a maximum of about 16% and 34%, respectively, until red reflectance values of 3% and NIR reflectance of 13% are reached. Beyond this critical density point, as tree density continues to increase, we see increasing NIR reflectance values. The resultant trajectory has a highly non-linear shape through spectral space. In terms of the error bands shown, there appears to be minimal overlap in this trajectory, even at the critical density point which, for OJP, is clearly defined by a sharp transition from decreasing to increasing reflectance, particularly in the NIR. For OA, shown in Figure 5.35, we again see a distinct non-linear shape of the trajectory. However, in contrast to both OBS and OJP, we only see shifts in red reflectance below the critical density point. At low tree densities, red reflectance is at its maximum value of 7%, which decreases to less than 2% as tree density increases to the critical value. Up to this point, NIR reflectance is relatively stable, however, beyond the critical density point we see a steady increase in both red and NIR modelled reflectance, with the highest NIR reflectance corresponding to the position of

greatest tree density. Again, there is little overlap amongst trajectory points with respect to the error bars generated from the sensitivity analysis, except for a small degree of convergence at the critical value point. The mixed forest trajectory, depicted in Figure 5.36, appears to have an intermediate trajectory position through spectral space, which is not unexpected given the method used to compute it as a weighted average of the other three class trajectories. This trajectory is highly non-linear, has a distinct critical density point, and shows only minor overlap of error bands near that point.

Additional insight into the spectral discriminatory power of these trajectories is possible by plotting all class trajectories together in Red-NIR space. This is illustrated in Figure 5.37. Here, we see the characteristic non-linear shape of the individual class trajectories and the positions of the respective critical density points. At low tree densities, well below any of the critical density points, good separation is found among all classes. The end-point and the slope of each trajectory curve are all different and distinct. Further, the error bars for each trajectory do not overlap. At these densities, sunlit background fractions will be higher, which is significant since this component is reasonably distinct among classes. As a result, we would expect very good discrimination among all classes in situations of low to medium density stands, both of which are common in the boreal forest. As tree density increases and the trajectories approach their respective critical density points, we begin to see increased proximity of trajectory positions, although the critical density points do not appear to overlap, except perhaps OJP and the mixed forest class. Beyond the critical density point, however, as tree density becomes quite high, increasing overlap of the error bars surrounding each spectral trajectory is noticeable. This observation may be attributed, in part, to the decreasing sunlit background fraction and the corresponding reduction in the discrimination provided by that component to the overall

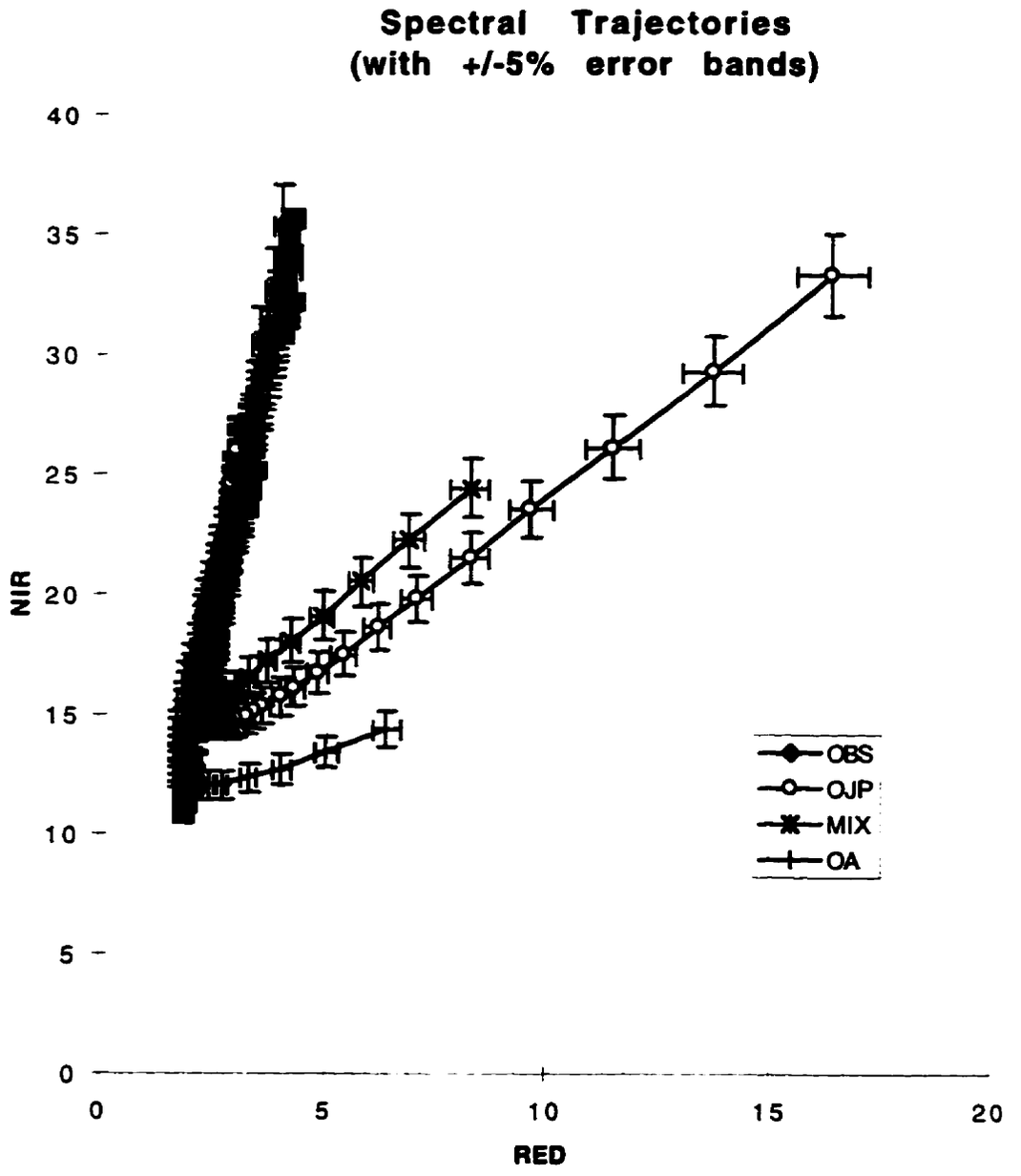


Figure 5.37. Spectral trajectories of the four major forest classes showing ±5% error bands computed as an estimate of GOMS model sensitivity to tree dimension and form parameter inputs.

pixel level reflectance among classes. Conversely, as tree density increases we see increasing sunlit canopy fraction. This component has greater spectral similarity among classes and this may explain the greater proximity of trajectories at these higher tree densities. As a result, we may expect some classification error to result at these higher tree densities.

This proximity of spectral values at this part of the trajectory highlights the need for careful field measurement of component spectra, as well as the importance of measuring or obtaining quality tree geometry and form parameters. It would appear, from this initial sensitivity analysis, that the analysis could be affected by smaller changes in the shape of a given trajectory in these areas of high tree density. Other factors such as variability and specification of other model inputs and a more rigorous sensitivity analysis may also provide better insight into the spectral discrimination. In terms of biophysical analyses, it is possible that tree density determination may be as or more important than class differentiation, particularly in cases where different classes have similar physical and structural properties at a given tree density. It is difficult to comment on this based on the spectral plots and sensitivity analyses presented in these sections. A better indicator of these capabilities will be provided later in the thesis when this approach is tested in terms of actual classification accuracy and for predicting biophysical variables.

Based on the analysis of spectral trajectories with respect to tree density (§5.5.3.3), as well as the sensitivity analysis presented here, it is concluded that these trajectories are appropriate for input to the landcover classification and biophysical parameter estimation procedures, but that some misclassification may be expected at high tree densities. In the next section, the software designed to process these trajectories for this task is described.

## 5.6 PHYSICALLY BASED EVIDENTIAL REASONING SOFTWARE

### 5.6.1 Rationale for Evidential Reasoning Algorithm

Having generated a set of spectral trajectories from field data and geometric optical reflectance models, a way is needed to use these trajectories to perform land cover classification and produce information for terrain biophysical estimates. Normally, with an image classification algorithm, the goal is to classify input pixels into land cover classes, and this is typically done by identifying representative class training areas from which spectral signatures are generated and used to classify the image. A variety of image classification algorithms for achieving this task have become a standard software component of commercial image analysis systems. However, these commercially available programs do not provide any additional information beyond land cover information. They are not set up for processing the additional information contained in the spectral trajectories presented here. Therefore, in this research, the goal extends beyond that of land cover classification to also include the output of sub-pixel scale scene component information together with other scene specific information to provide the additional required information for more complex analyses. Here, the additional application is estimating forest biophysical parameters, however, this need could be generalised to other applications where further information is required beyond that provided by land cover classification output alone.

Limitations of commercial image analysis system classification algorithms for addressing more complex applications have been addressed in previous and ongoing work by the author (Peddle, 1993, 1995a,b). Problems have been encountered with commercial image classification software programs for processing diverse, multi-source data inputs for

complex applications of environmental change. To address those problems, a software package was implemented by the author based on the evidential reasoning approach to integrating and classifying larger, complex digital data sets. This software enabled new applications of remote sensing multi-source image analysis to be explored (Peddle and Franklin, 1993), and has since been shown to provide more accurate land cover classification accuracies in comparison to a variety of commercially available image classification algorithms (Peddle, 1993, 1995b; Duguay and Peddle, 1996). As a result of this, and the fact that the full computer source code was written by the author and therefore was available to this research (usually not the case with commercial software), the evidential reasoning software package was appropriate to be modified and improved for processing the new spectral trajectory inputs in this research. As these upgrades were extensive, involving both modification to existing code and the writing of new software modules interfaced into the package, a description of this aspect of the research is contained in this section. However, in order to understand this component of the thesis, the reader should be familiar with the evidential reasoning approach and its previous implementation in software to provide an appropriate context for the current work. Accordingly, a review of evidential reasoning theory has been included in Appendix C, with pertinent information on related applications presented in the next section and followed by a description of the new software and code enhancements implemented as part of this thesis research.

### 5.6.2 Previous Research and M⊕P Software Context

Previous work by others in the field have used the Dempster-Shafer evidential reasoning approach for a number of remote sensing applications, such as image

classification (Lee *et al.* 1987; Srinivasan and Richards, 1990), geology (Moon, 1990, 1993), water resources (Caselton and Luo, 1992), detecting ship wakes on SAR imagery (Rey *et al.* 1993), route selection (Garvey, 1987), and as an interface to expert systems to measure the level of uncertainties in hypothesis testing (Goldberg *et al.*, 1985; Wilkinson and Mégier, 1990). As a result of this work, there has been an increasing recognition of the power of evidential reasoning for classifying higher dimensional multi-source data sets with diverse statistical properties, and for handling the inherent information uncertainty and conflicting knowledge typical of divergent data sources. However, in these studies the methods used to derive evidence from remote sensing data for input to the Dempster-Shafer theory have been subjective, informal, data specific, and ad hoc in nature (see the review in Peddle, 1995a). As a first step towards overcoming these issues, a formal, more objective algorithm to derive evidence directly from supervised classification training data has been presented by Peddle (1995a,b) as part of a larger implementation of the Dempster-Shafer theory of evidential reasoning. This software package has been written in the C programming language and is known as the MERCURY⊕ classifier (Multi-source Evidential Reasoning Classification by Orthogonal Summation (⊕)). This software has been used in a variety of studies involving complex terrain and detailed class structures. For example, in a study of mountainous terrain in south west Yukon Territory, this non-parametric classifier was shown to provide the highest land cover classification accuracies in a detailed comparison with maximum likelihood and linear discriminant analysis algorithms (Peddle, 1993). These accuracies were attributed to the fact that the MERCURY⊕ evidential reasoning classifier was able to take advantage of the additional information content provided by spectral, geomorphometric, and textural data sets which were required for this complex environment. In a further study of alpine permafrost in that area, Peddle and Franklin (1993) used the evidential reasoning software to provide estimates of permafrost

occurrence and four active layer depth classes using a multi-source data set. Accuracies of 80% were obtained from field and remotely sensed data sets derived from disparate information sources and different data levels which together could not be analysed by the other classification algorithms available to the study. More recently, Duguay and Peddle (1996) compared the MERCURY⊕ software to a neural network classifier in a detailed comparison of alpine vegetation classification in the Colorado Rocky Mountains using a multi-source spectral, topographic, and climatological data set derived using Geographical Information Systems (GIS). In that study, the evidential reasoning software provided higher accuracies than the commercial neural network program, and also had substantially faster computer run times by several orders of magnitude. It was also shown that the MERCURY⊕ software can provide new functionality not available in GIS. The GIS used in that study was not capable of processing the range of data levels required for the analysis. Although the MERCURY⊕ program was originally written in the context of image analysis systems, it has also been used directly in a GIS processing environment and is fully compatible with either.

The basis for these improved results using the MERCURY⊕ evidential reasoning algorithm is that it provides a number of advantages over conventional, commercially available programs. The software has been implemented such that it can process data at all four levels of measurement, and without any restrictions on the number of input variables. Further, the classifier uses a supervised, non-parametric approach and therefore does not require the data being classified to adhere to any particular statistical model (e.g. Gaussian distribution). It also has an explicit method for dealing with information uncertainty, together with a more general representation of probabilities which provides a more realistic representation of input data interpreted as evidence.

In this research, an important consideration is the need for accurate land cover classification information as one of several required variables for biophysical parameter estimation. As a result of the advantages of the MERCURY⊕ evidential reasoning software and its demonstrated classification abilities compared to a variety of other algorithms, this software package provided a favourable processing environment within which to focus the software development component of this research. Direct access to the MERCURY⊕ source code meant that new functionality could be implemented and coupled directly with a powerful image classifier. This was done. A significant upgrade of the MERCURY⊕ software was performed to incorporate processing of spectral trajectories and to provide the necessary output at sub-pixel scales for use in this forestry application. As with any larger set of programs, it can be convenient to provide an acronym or name for the software for ease of reference. The name of this new software package is M⊕P, which in the present context is an acronym for the MERCURY⊕ Physically-based software system. The major additions to MERCURY⊕ which constitute the new M⊕P evidential reasoning software package are described in the next section.

### 5.6.3 M⊕P Software Implementation

#### 5.6.3.1 Organisation of Software

Using the MERCURY⊕ system as a starting point for the software development component of this research, a number of revisions and upgrades involving new code were implemented to permit the input and analysis of spectral trajectories for land cover classification as well as sub-pixel component outputs. The earlier MERCURY⊕ software

system was designed to analyse training data inputs only. In this research, two new processing modes have been implemented and added to the software, while still preserving the full functionality of the original MERCURY⊕ program. The new M⊕P software now provides the user with three processing modes, as follows:

1. Full Training Mode
2. Full Spectral Trajectory Mode
3. Hybrid Trajectory-Training Mode

Option 1 is essentially the original MERCURY⊕ program which processes training data. The two new options added to the software systems are, Option 2: a "Full Trajectory Mode" where a complete set of spectral trajectories are input to the software and used for classification and component fraction output based on physical properties of the scene, and, Option 3: a "Hybrid Trajectory-Training Mode" in which the user may combine inputs from both training data and from spectral trajectories according to the nature of available inputs and individual classes. The hybrid mode provides a particularly powerful and attractive option for the user since the advantages of the trajectory method can be combined with other class data for which trajectory inputs may not exist or be possible to derive. From an operational standpoint, although the creation of the hybrid mode was not essential to testing and evaluating this methodology in the current research, it is likely that in most cases one may not have a full trajectory model characterisation of all classes of interest. This provides the necessary flexibility to the user such that the advantages of trajectory inputs can be realised, but without the restrictive need of trajectories being generated for all classes. As we shall see in the following chapter, after a series of initial tests of full trajectory mode, the hybrid mode was used extensively in this research to analyse the full set of BOREAS

land cover classes, which included a number of forested and non-forested classes for which spectral trajectories were not available or not possible to create. This hybrid option can be extended to the general case where partial model outputs which produce spectral trajectories could be used together with other, more conventional, supervised training inputs. Further information on program modules are provided in Appendix C.

5.6.3.2 Knowledge Representation and Spectral Trajectory Volumes

A key component of the M⊕P software is the interface between the input supervised training and trajectory data and the specification of support values for processing using the mathematical theory of evidence. The method implemented uses an automatic, frequency-based approach to building a knowledge look-up table (K-LUT) from which evidential support values are derived for input to the Dempster-Shafer orthogonal combination formulae (see equations in Appendix C). Evidential support is computed for a given input pixel value based on its frequency of occurrence in training or trajectory data. For quantitative data (i.e. at interval or ratio scales of measure) as well as with trajectories, a bin structure can be placed over an input distribution to extend knowledge over a greater dynamic range of the data source and to reduce any bias associated with individual frequency counts. This approach permits evidence to be gathered consistently and objectively from multi-source data of varying type, format, and scale of measurement (e.g. nominal level thematic GIS data, ordinal level forest information, directional aspect data, ratio level remote sensing imagery). For the trajectory mode, the specification of the bin structure as part of the K-LUT is essential. This is because the spectral trajectories that are input to the program represents a line through spectral space (e.g. Figures 5.31 and 5.32). However, in terms of evidential classification, in which a given pixel being considered

must be evaluated to determine the class trajectory for which the greatest amount of evidence exists to grant membership to that class, the K-LUT representing each trajectory must be structured such that the area surrounding each spectral curve must be provided with appropriate evidential support values such that the points not falling exactly on the spectral curve will be characterised. The result of this process is that each spectral curve is expanded into a three dimensional volume in spectral space. The radius of the volume is defined by the evidential bin size specified. Pixels falling outside a spectral trajectory volume for a given class will have no evidential support assigned in support of membership into that class. If a pixel intersects a given class trajectory volume, the evidence assigned to that pixel in terms of class membership is a function of the position in the volume where the intersection occurs and the proximity to the axis of the volume defined by the spectral trajectory. Essentially, through the bin process, a weighted distance decay function defines evidential support values as one moves progressively though a plane of the volume perpendicular to the spectral trajectory.

#### 5.6.3.3 Integrated Classification and Trajectory Analysis

Once the interface between the input trajectory or training data and the evidential reasoning framework has been achieved through the construction of the knowledge look-up table, the next phase of the M⊕P process is to use this evidence to analyse image pixels to assign them to one of the land cover classes (classification), and, when in trajectory mode or hybrid trajectory-training mode, perform the additional processing required to compute the spectral components associated with that pixel and its class assignment. The main program of the M⊕P software package, M⊕P.C, is used to do this. The classification process is achieved using the orthogonal summation process from the mathematical theory

of evidence. This is embedded in the original MERCURY⊕ software and was described briefly in §5.6.2. The second part, that of computing the spectral component outputs from the trajectories, forms the new work implemented in this part of the software and the topic for this section, with relevant source code contained in Appendix C. In terms of trajectory inputs, the first task is to input the reflectance values along the trajectory into the K-LUT for use in the land cover classification (functions 'read_klut' and 'get_data' in Appendix C), and then calculate the set of trajectory volumes for each spectral curve (functions 'bin_klut' and 'normalise_klut' in Appendix C). This is also where any user specified *a priori* weights are applied. These trajectory volumes (together with processed training data if in hybrid mode) are then used to identify the land cover class both for disk output and also to direct the trajectory processing to determine spectral component outputs. To facilitate trajectory processing, two functions are utilised in M⊕P.C. The first function, 'load_trajectory_LUT', reads in the spectral component information associated with each point along the trajectory (in this case, tree density, sunlit canopy fraction, sunlit background fraction, shadow fraction) and stores these in a separate trajectory look-up table (T-LUT). This was implemented as a multi-dimensional array data structure since it is known that with these spectral trajectories the input values have a known and consistent numerical range. This is in contrast to the intricate multi-level circularly linked list data and hash table data structure used to store training data. These values were also kept separate from the K-LUT since no modification of these values are required, as is the case with the K-LUT where the information must be converted into evidential support and plausibility measures. For the T-LUT, the spectral reflectance values are stored in the array 'TLUT_spv' with the component fractions stored in the array 'TLUT_fr' (Appendix C). The entire set of values associated with all class spectral trajectories are read into these arrays (function 'load_trajectory_LUT') prior to commencing classification. Then,

classification begins using the evidential reasoning method with reference to the knowledge look-up table of trajectory and/or training data evidence.

Once class membership has been determined, this is used to identify which spectral trajectory is to be used for further class-specific trajectory processing. In either of the two trajectory modes (full trajectory mode or hybrid mode), the function 'analyse_trajectory_LUT' is invoked to do this processing. This function is given as input two sets of values. One is the set of pixel level reflectance values that have just been classified, and the second value is the class number those pixels have been assigned to. The function accesses the spectral trajectory for that class, and then determines the point along the trajectory which has the greatest proximity to the reflectance values being considered. This is done by traversing the trajectory and, for each point, finding the distance between the input reflectance values and each trajectory point. Specifically, the Euclidean distance ($\delta$) in spectral space is calculated from the input reflectance value ($\rho$) being analysed in the red (r) and NIR (n) bands to each spectral trajectory value ($\sigma$) in each band, using the following equation:

$$\delta = \sqrt{( \rho_r - \sigma_r )^2 + ( \rho_n - \sigma_n )^2} \qquad (5.5)$$

Equation 5.5 is expressed for the two-dimensional (red, NIR) case, however, in the M⊕P software this equation has been implemented for the n-dimensional case to allow for any number of spectral bands and trajectories to be processed, using the general equation (modified from Swain and Davis, 1978):

$$\delta = \sqrt{\sum ( \rho_i - \sigma_i )^2} \qquad (5.6)$$

The point along the trajectory which minimises $\delta$ is determined as the trajectory point for the pixel. The associated trajectory information for that point is then output to disk, together with the previously generated land cover class. In the present forestry application of the M⊕P software, the tree density value (defined from the trajectory position) and the three mixture fractions (C,B,S) are output.

In this research, these output values are used for biophysical parameter estimation, in which the land cover class is used to stratify mixture fraction outputs which, in turn, are used for predicting a variety of forest attributes. However, it is noted that, from a software standpoint, the M⊕P upgrade has been implemented in a general form such that any model input with any number of associated attributes could be input to the program and analysed in the same way as the land cover classes and mixture fraction components have been used in this forestry application. The software, therefore, could be used in a variety of other fields in which sub-pixel component fractions associated with land cover classification is of interest. This issue is taken up in more detail in the concluding chapter of the thesis. In the next chapter, the application of the M⊕P software is presented for land cover classification and biophysical parameter estimation in BOREAS.

## 5.7 CHAPTER SUMMARY

In this Chapter, a full account of the methodology implemented has been provided for a regional scale analysis as part of the BOREAS project. The method involves significant field spectral data input, reflectance processing, generating spectral trajectories using reflectance models, and the use of new computer programs which provide a coupled land cover and biophysical estimation algorithm. Each step required software developments implemented in several platforms and computing environments. The end result is a flexible analysis software system which permits full training mode classification, trajectory mode processing, or a hybrid approach in which both training and trajectory inputs are accepted. In the next Chapter, this method and the software developed to implement these ideas are tested for a large sample of different forest types that comprise the boreal forest landscape defined by the BOREAS region.

# CHAPTER VI

## REGIONAL SCALE ANALYSIS OF THE BOREAS SOUTHERN STUDY AREA

### 6.1 INTRODUCTION

In this Chapter, the methods developed in Chapter V are tested for a sample of pixels which represent the major forest types found throughout the BOREAS Southern Study Area (SSA). This Chapter has two main sections. In the next section, the focus is land cover stratification. A comparison of the M⊕P full training and full trajectory modes is first performed for the four mature dominant boreal forest classes. Following this, the full set of 12 land cover classes is classified using both the M⊕P full training mode and the hybrid trajectory training mode, with results compared and evaluated. Once a land cover classification is established, trajectory mode outputs are applied in §6.3 for the task of biophysical parameter estimation. Four biophysical parameters are tested. The need for *a priori* land cover information is determined, and the effect of misclassification error on biophysical estimates is assessed. Results obtained using these methods are compared to NDVI results obtained with and without the land cover stratification.

## 6.2 LAND COVER CLASSIFICATION

### 6.2.1 Experimental Design

#### 6.2.1.1 Classification Algorithms

In this section, the physically based M⊕P classification trajectory software developed in §5.6 is tested for the BOREAS data set. A central advantage to the M⊕P approach is that, for a given land cover classification label assigned to a pixel, a full set of forest component mixture fractions is also provided for purposes such as biophysical parameter estimation. In this application, the accuracy of land cover classification is important for biophysical parameter estimation since a misclassified pixel in trajectory mode (incorrect trajectory identified) will result in the wrong set of mixture fractions being output for follow-on analysis. Therefore, in this section, an in-depth evaluation of land cover classification accuracy provided by the new M⊕P software is presented. The desired minimum level of accuracy for the M⊕P software would be to provide equivalent accuracies to conventional supervised training based methods. As the consideration of sub-pixel scale phenomena has the possibility of improving land cover classification accuracy, it would be useful to test this using real data and compare the M⊕P algorithm to the conventional training approach to see if increased accuracies can be achieved using the physically based trajectory method. If so, this new approach would provide an improved input for the biophysical estimation process where errors in the prior stratification of land cover must be minimised.

In a variety of studies conducted in different environments, the MERCURY⊕ evidential reasoning classifier has been shown to provide increased land cover classification accuracy compared to maximum likelihood and linear discriminant analysis (Peddle, 1993, 1995a,b), and more recently, neural network classifiers (Duguay and Peddle, 1996). That work used the earlier version of the software which provided the supervised training approach only. As the central objective of the present comparison is to evaluate the new physically based classifier run in trajectory mode and compare it with the more conventional supervised training approach, in this work the land cover classification comparisons will focus on comparing the M⊕P classifier run in training mode with the results obtained from running it in full trajectory mode. This strategy provides maximum experimental control for this focused objective since the internal algorithm (evidential reasoning) used to produce the land cover classification is the same in each case. As a result, the trajectory inputs can be compared to training data inputs with confidence, without the possible bias introduced by using a different algorithm in each case.

In this section, an extensive comparison of the trajectory mode and the training mode is performed for two sets of land cover classes. The first comparison involves the set of classes for which spectral trajectories have been generated (OBS, OJP, MIX, OA). In this comparison, the M⊕P classifier is run in full training mode and then in full trajectory mode. The second comparison is based on the complete set of land cover classes defined for the BOREAS SSA. In that comparison, the M⊕P classifier is run in full training mode with the spectral trajectories analysed in hybrid training-trajectory mode. In the next section, the classes used in these experiments are described.

### 6.2.1.2 Class Structure

A class structure of 13 land cover classes has been identified for the SSA by BOREAS Staff for use by investigators in the BOREAS project. These are listed in Table 6.1, together with the corresponding class identifier used in this work. This particular set of classes has evolved somewhat within the BOREAS project, however, the current version and all predecessors recognise the same general set of land cover patterns to be discriminated. These include the dominant mature forest species of black spruce, jack pine, and aspen, a mixed forest class, as well as several forest regeneration classes (BOREAS, 1994). Other classes which have little or no occurrences of living trees include fen, water, areas recently burned or logged, grass lands, and man-made features (airports, roads etc.). Previous versions of land cover classes varied somewhat in how the regeneration classes were defined while other class structures have had a greater emphasis on moisture status. The classes defined for use here represent a rather detailed and ambitious set of land cover types. This provides a good challenge to the research objective of obtaining accurate land cover classification accuracies, given that 8 of the 12 classes contain forest stands, with four classes defined for coniferous areas, three for deciduous, as well as a mixed forest class. In the following paragraphs, these individual classes are described.

| Class Number | Class Name |
|---|---|
| 1 | Old Black Spruce (OBS) |
| 2 | Old Jack Pine (OJP) |
| 3 | Mixed Deciduous and Conifer (MIX) |
| 4 | Old Aspen (OA) |
| 5 | Fen |
| 6 | Water |
| 7 | Disturbed |
| 8 | Recently Burned |
| 9 | New Regeneration Conifier |
| 10 | Medium Age Regeneration Conifier |
| 11 | New Regeneration Deciduous |
| 12 | Medium Age Regeneration Deciduous |
| 13 | Grassland |

Table 6.1. Class structure used for BOREAS SSA. Details of class composition contained in text with reference to BOREAS (1994).

Class 1 consists of Old Black Spruce stands which are typically found in areas of poor drainage with an understorey of sphagnum moss on clay which sometimes also includes embedded plants such as Labrador tea and occurrences of feather moss found in

areas of moderate drainage. Low density occurrences of this class are sometimes found in fens. This class has a good correspondence with the wet conifer class used in other BOREAS class structures.

Class 2 consists of Old Jack Pine stands with an understorey of lichen (cladina) on well drained, sandy soils. In some areas, bearberry plants are also present in the lichen understorey. This class has a good correspondence with the dry conifer class used in other BOREAS class structures.

Class 3 is the mixed forest class which consists of a mixture of coniferous and deciduous trees such as black spruce, jack pine, and aspen, with other occurrences such as birch, tamarack, balsam poplar and white spruce also found in lower abundances. The composition of this class typically contains less than 80% of the dominant tree species present. The understorey varies by site and includes mosses, lichen, grasses, and other small plants.

Class 4 is the old aspen class. This deciduous class is dominated by mature aspen trees but can include smaller occurrences of birch. The understorey is characterised by hazelnut with a ground cover consisting of leaf litter and a variety of herbs and grasses on soils which are usually well drained.

Class 5 contains fens that have a water table at or near the surface where lateral and vertical transport of water occurs. These areas typically contain a variety of sedges, mosses and other low plants, as well as low density occurrences of trees such as tamarack and

black spruce. This class also includes bogs which are enclosed landforms with only vertical transport of water and which are usually treeless.

Class 6 is water found in lakes, ponds, rivers and streams.

Class 7 is the disturbed class which contains areas of bare soil, rock outcrops, recent logging activity, as well as man-made features such as roads, airports, urban areas, or small towns.

Class 8 contains areas that have been recently burned, generally within a period of 5 or 6 years prior to image acquisition. These fire blackened areas are characterised by a distinct charred background from high intensity burns where little or no vegetation survives.

Class 9 is the first of four regeneration classes defined in this class structure. The new regeneration conifer class is generally comprised of young conifer trees regrowing after a forest fire or after being cleared. This may include areas where regeneration is occurring after a low to medium intensity burn in which some trees still remain standing.

Class 10, the medium age regeneration conifer class, consists of coniferous trees which are about 10 years old that are growing back after being cleared or burnt. Usually, the regenerating species is either young black spruce trees or young jack pine, depending on drainage and other factors.

Class 11 consists of new regeneration deciduous trees that are regrowing after a recent clearing or fire event. The regenerating species is usually aspen which can be accompanied by early successional vegetation such as grasses and other herbaceous plants.

Class 12 is medium age regeneration deciduous trees that are approximately 10 years of age and which are typically growing back as aspen following a clearing or forest fire event. At this age, thinning has yet to begin, however, understorey development is sufficiently well advanced such that background soils are typically obscured.

Class 13 is grass. This class also includes small shrub communities as well as agricultural fields and other low vegetation that has been planted.

6.2.1.3 Sampling Design

As the goal of this section is to compare the training and trajectory modes of the M⊕P classifier, a set of input training data of pixel values with known land cover types was required to run the supervised training mode experiments. In addition to this, a separate set of independent, mutually exclusive test pixels was required, again with known land cover, to perform a rigorous accuracy assessment. Reference data with known co-ordinates and land cover classes were acquired from BOREAS Staff, and consisted of the pixel locations of all Tower Flux sites as well as a number of Auxiliary (AUX) Sites, for a total of 36 sites for classes 1-4, as well as a number of additional validation sites of known land cover composition for classes 5 through 13. This small number of TF and AUX sites, on their own, did not provide an adequate sample size for classification training and testing for the four main classes of interest. However, since one of the criterion for TF

and AUX site selection included land cover homogeneity in the area of the site (BOREAS, 1994), additional reference pixel locations could be created for these classes. TF sites are located within a homogenous area of 1 × 1 km, with AUX sites containing a minimum 100 × 100m area of homogeneous land cover, which in many cases ranged to areas of 250 × 250m or more. To create an adequate sample size, a 5 × 5 window of pixels was first extracted around each site. This was well within the TF area of homogeneity, and also was suitable for most AUX sites. However, to ensure the sample was not contaminated, air photos were consulted for these sites to exclude any neighbouring pixels which had a different or questionable land cover than the center site pixel. Of the 900 candidate pixel values, a total of 765 were retained for classes 1-4 for the purposes of classification training and testing. The full sample (including pixels for classes 5-13) consisted of 2,639 pixels. This full set of samples was divided randomly into separate training and test data files consisting of 1647 training pixels and 992 test pixels.

A plot of the full training data set is contained in Figure 6.1. There appears to be two main clusters of spectral response, one which contains grasslands and the medium age and mature deciduous classes, with the other grouping containing the remaining classes which have lower reflectance values. However, the large number of classes makes this plot more difficult to interpret due to the overlap evident among some classes. Therefore, to provide further insight, three sets of classes were plotted separately for interpretation. These three sets include the four mature classes (1-4), the four regeneration classes (9-12), and the other four classes (5,7,8,13).

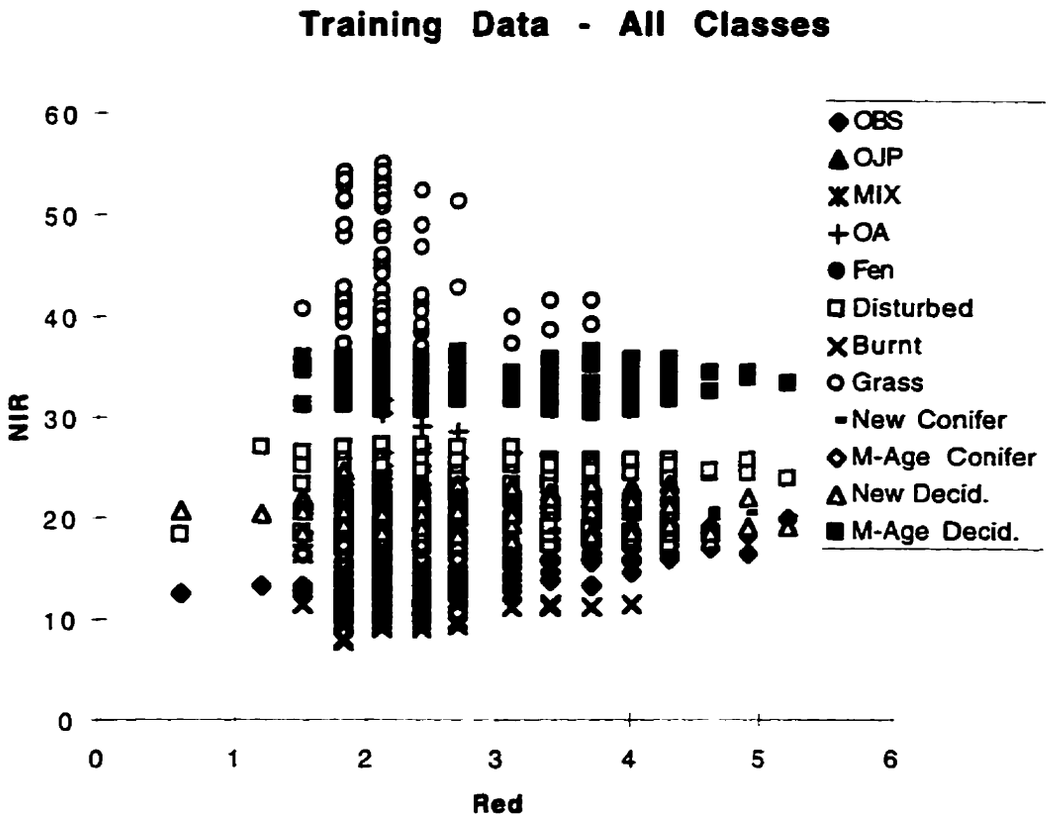


Figure 6.1. Training data reflectance values for all 12 classes.

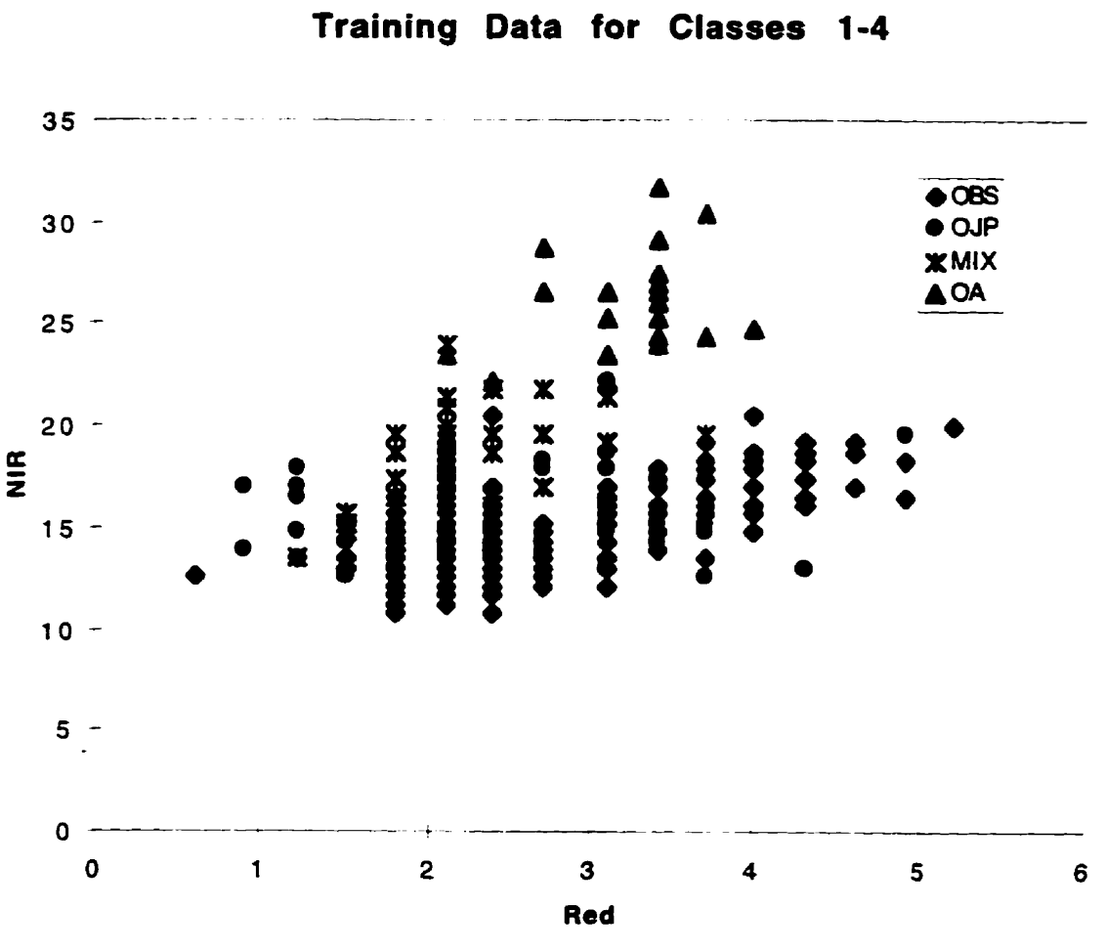


Figure 6.2. Training data reflectance values for the mature forested classes (OBS,OJP,MIX and OA).

For the four mature forested classes (1-4) shown in Figure 6.2, the OA reflectance values appear to be spectrally distinct from the other classes, particularly in the NIR. However, the OBS and OJP values appear to have some degree of spectral overlap. The mixed forest class lies between the conifer and deciduous clusters and has some overlap with each of the other classes, as would be expected. From this training plot alone, classification accuracy would be expected to be higher for OA than the other classes. It is

difficult to hypothesize on the potential accuracies possible for the other classes as the degree of discrimination among these classes is less obvious. This issue is taken up in the next section when classification results for these four classes alone are evaluated and compared to results from the spectral trajectories.

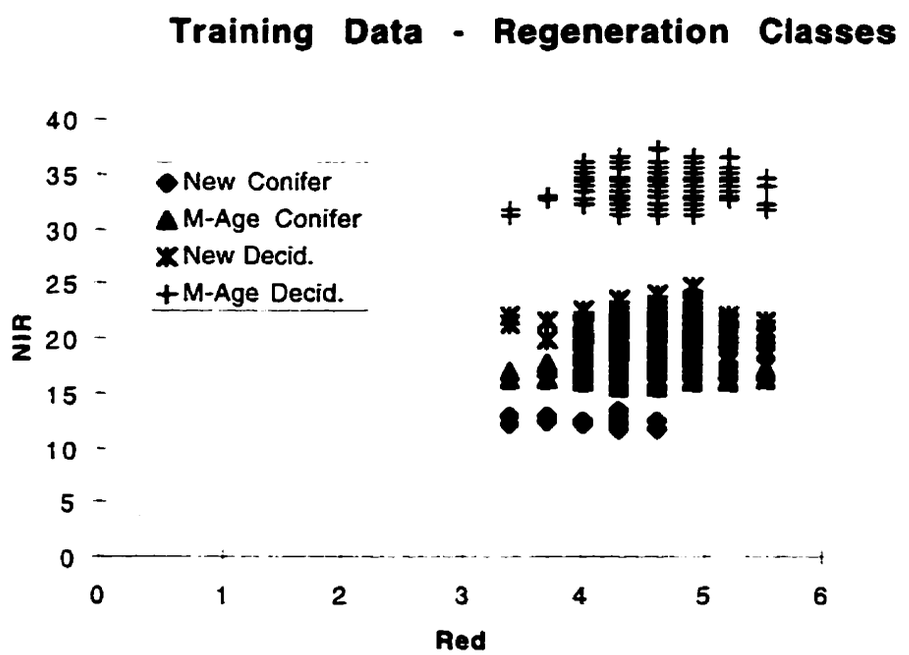


Figure 6.3. Training data reflectance values for the regeneration forested classes (new and medium age deciduous, new and medium age conifer).

For the regeneration classes, shown in Figure 6.3, the medium age deciduous training data reflectance values are spectrally distinct from the other classes. This is likely due to the increased tree density for stands of this age, as well as the fact that the background is almost completely obscured. The new regeneration deciduous class shows some spectral differences, though this class is not as distinct as the medium age regeneration deciduous class. The lower reflectance values also resulted in some spectral

overlap with the coniferous regeneration classes, particularly the medium age conifer class. The two regeneration conifer classes appear to have greater overlap than the deciduous regeneration classes. This may be attributed to the smaller degree of change in the canopy as conifers grow compared to deciduous trees. As a result, the degree to which the understorey is obscured over time will not vary as greatly as with growing deciduous trees. Similar to the deciduous regeneration classes, the medium age conifer class appears to have higher reflectance values than the new conifer class, although this pattern is less distinct.

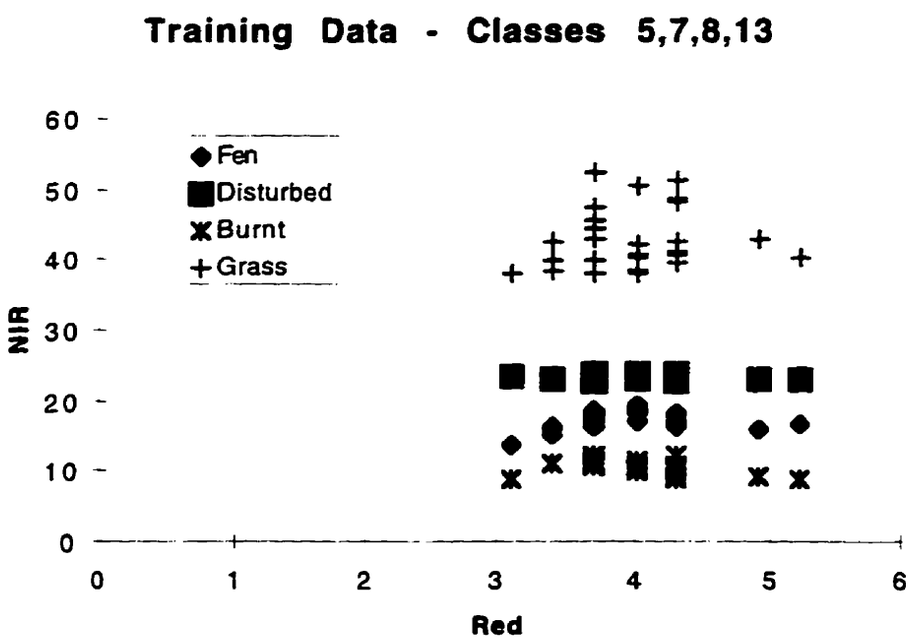


Figure 6.4. Training data reflectance values for the fen, disturbed, burnt, and grassland classes.

For the other classes (5, 7, 8, 13), shown in Figure 6.4, good separation is apparent. Each of these classes (fen, disturbed, burnt, grass) are very different on the ground and therefore they should have different spectral properties.

The training data (or trajectories, as appropriate) were input to the M⊕P software package and used to generate evidential vectors for the creation of the knowledge look-up table. The test pixels were then classified based on this evidence and output to a disk file. The M⊕P output was compared to the test pixel reference data using a classification accuracy assessment program written by the author. That program provides tabular output of classification accuracy based on overall and individual class percent accuracy as well as individual class and overall kappa co-efficients of agreement. The kappa co-efficient compensates for change agreement of pixels and therefore is a more rigorous assessment of agreement between reference data and classification output. Despite this, percent accuracy remains the more common statistic used, partly because of its simplicity and ease of interpretation. Both measures of agreement are reported here. The program produces as output a tabulated set of results for each classification from which a full analysis of classification accuracy and error is possible for individual classes as well as the overall result.

6.2.1.4 Classification Procedures

Spectral trajectories were generated for classes 1 - 4. Classes 5 - 8 and 13 were not suitable for generating spectral trajectories from the reflectance model based on a varying tree density parameter, since these classes do not have trees. No trajectories were produced in this research for the 4 regeneration classes (classes 9 - 12). There were several reasons for this. Firstly, these areas occupy a considerably smaller area compared to the dominant mature classes (1-4), and further, they contain smaller trees. Therefore, these classes have a significantly smaller contribution to the overall amount of biomass at the regional scale. This may explain why there is only one regeneration tower flux site in SSA,

which is the Young Jack Pine (YJP) site. The YJP site would fall into the medium age regeneration conifer class, however, no other TF sites exist for the other 3 regeneration classes used in this study. A full suite of end-member field spectra data were collected at the YJP TF site during IFC-3, however these were not used in the present research. Secondly, with four regeneration classes defined, additional field work would have been required. Although not prohibitive, field sampling in these classes would be less straight forward due to increased variability of the developing understorey for these transitional, succession classes. This was the case for the measurements obtained at the YJP site. Thirdly, tree dimension and form measurements were only available for the YJP site, but not for the other three regeneration classes. Again, while not prohibitive, additional and in this case different field measurements would be required. In the present research, the four regeneration classes were classified using training data available from BOREAS, with the generation of trajectories for these classes deemed to be beyond the scope of the present work.

In this investigation, two sets of classifications were performed. This was done to satisfy two objectives: (i) to compare the trajectory and training modes of classification, and (ii) to assess the ability to classify the full set of land cover classes. For the first objective, because spectral trajectories were produced only for classes 1 - 4, the first set of classifications was limited to those 4 classes to allow a direct comparison of the training and trajectory approaches. This approach excluded classes 5-13, for which only training data were available. In each mode evaluated, the same set of test pixels was used to determine classification accuracy, with the set of test pixels restricted to the 4 classes being considered.

The second set of tests involved all 13 classes. The training data were classified in full training mode. The hybrid trajectory-training mode was used to include the 4 spectral trajectories for classes 1 - 4, with the training data for classes 5 - 13 used for the remaining classes for which no trajectories exist. Here, the ability to include a full set of classes can be assessed in terms of overall classification accuracy as well as the performance of the spectral trajectories versus the training data for classes 1 - 4. However, the fact that the same training data sets are used for classes 5 - 13 must be taken into account when comparing overall and individual class accuracies obtained from each classification method. The use of two separate sets of experiments allows all three modes of the M⊕P software to be tested (training, trajectory, and hybrid training-trajectory modes).

As the objective of the present research is to evaluate these methods for the application of forest land cover classification and biophysical parameter estimation, only the land based classes are of interest. Since water is spectrally distinct from land, it is typically classified with very high accuracies. For this land based evaluation, the inclusion of a water class would serve to inflate the overall accuracies above that which could be expected for the land cover classes of interest in this research. Therefore, the water class was excluded from the analysis. For a mapping application, however, a water class would be added. In the next two sections, the full set of results generated for the trajectory class comparisons and the full land cover class sets are presented.

### 6.2.2 Comparison of Training and Trajectory Modes

#### 6.2.2.1 Full Training Mode Results

Training data and spectral trajectories exist for classes 1 - 4. Table 6.2 contains the results of the training mode classification of classes 1-4, with the results from the full trajectory mode classification of these same classes found in Table 6.3. As the goal of this test is to compare the two methods for generating evidence in the M⊕P classifier, the *a priori* weighting options available in the software were not used here. Assigning weights to the input data would make a rigorous comparison more difficult since a given set of weights could affect each set of inputs in a different way, even if identical weights were used for each class. In the second experiment, when all classes are classified, the absolute classification accuracy is of greater interest and therefore weights are applied in that experiment.

TRAINING MODE: CLASSES 1-4

| Classification Label --> | 1 | 2 | 3 | 4 | Total | % | K |
|---|---|---|---|---|---|---|---|
| Class 1: | 88 | 10 | 0 | 0 | 98 | 89.80 | 0.85 |
| Class 2: | 23 | 45 | 21 | 0 | 89 | 50.56 | 0.41 |
| Class 3: | 0 | 2 | 10 | 33 | 45 | 22.22 | 0.14 |
| Class 4: | 0 | 0 | 2 | 120 | 122 | 98.36 | 0.97 |
| Total: | 111 | 57 | 33 | 153 | 354 | **74.29** | **0.64** |

Table 6.2. M⊕P training mode classification output for classes OBS, OJP, MIX and OA.

Using the training data, an overall accuracy of 74% (K=.64) was obtained. Individual class accuracies ranged from a low of 22% for the mixed class to 98% for OA. The OBS class had an accuracy of 89%, with OJP at 50%. In terms of classification error for OBS, the 10 errors of omission (that is, pixels that should have been classified as old black spruce but instead were omitted from that class and included in a different class) all occur in the OJP class. As discussed and illustrated earlier, the spectral training areas of these classes had some overlap. Classification errors of omission for OJP are found in both OBS and the mixed forest class, likely due to the increased proximity of OJP to the MIX training data in spectral space as well as overlap with OBS. The MIX class contained many errors of omission, and these occurred primarily in the OA class, with two site errors into OJP, however, there were no errors of omission into the OBS class. As illustrated earlier, the MIX class is located mid-way between the conifer and deciduous classes in training data spectral space, but is further from OBS than the higher reflectance values for OJP. The only errors of omission for OA were into the mixed class, for two sites. This is not unexpected, since lower density occurrences of OA will fall closer to the cluster of mixed forest training data. The overall accuracy of 74% is reasonable, however, the individual class accuracies of 22% and 50% for OJP and MIX are not satisfactory.

#### 6.2.2.2 Full Trajectory Mode Results

The trajectory mode results are shown in Table 6.3. Using the spectral trajectories alone, an overall classification accuracy of 83% (K=0.77) was achieved. This was higher than the overall accuracy from the training mode result. In terms of individual class accuracies, three of the four classes showed improvement using the trajectory mode, with substantial increases of over 30% noted for two of the four classes. The OBS was slightly

higher (by 1%), class 2 (OJP) improved by 30% from 50% in training mode to 80% in trajectory mode, and a 30% increase in accuracy was also found for the MIX class, from 22% in training mode to 53% in trajectory mode. Despite this increase in the MIX class, the largest accuracy of 53% obtained by either method is still less than desired. The OA accuracy of 90% in trajectory mode was less than the 98% achieved in training mode, however both modes provided acceptable levels of accuracy for this class.

TRAJECTORY MODE: Classes 1-4

| Classification Label --> | 1 | 2 | 3 | 4 | Total | % | K |
|---|---|---|---|---|---|---|---|
| Class 1: | 89 | 9 | 0 | 0 | 98 | 90.82 | 0.87 |
| Class 2: | 16 | 72 | 1 | 0 | 89 | 80.90 | 0.74 |
| Class 3: | 0 | 9 | 24 | 12 | 45 | 53.33 | 0.48 |
| Class 4: | 0 | 0 | 11 | 111 | 122 | 90.98 | 0.86 |
| Total: | 105 | 90 | 36 | 123 | 354 | **83.62** | **0.77** |

Table 6.3. M⊕P trajectory mode classification output for classes OBS, OJP, MIX and OA.

The errors of omission found in trajectory mode were similar to those found with the training mode, with the exception that they were less frequent. In general, for the two conifer classes, errors of omission were restricted to only within those classes, with omission errors in the MIX class found with OA and OJP. OA omission errors were limited to the MIX class. These trends show that the nature of classification error did not involve errors between deciduous and coniferous classes, with the exception of the MIX class where such errors would not be unexpected.

From this first set of results, it is concluded that the new trajectory mode of evidential classification implemented in this research has been shown to provide good overall and individual levels of classification accuracy, and that this method has provided increased levels of accuracy in comparison to the more traditional training data method. This is a positive first result, particularly since the trajectory method also provides additional information on forest component fractions for biophysical parameter estimation together with the land cover classification output.

### 6.2.3 Analysis of all BOREAS SSA Classes

In this section, the full set of 12 land cover classes for the BOREAS southern study area are classified using the new M⊕P software developed here. Trajectories exist for classes 1 - 4; to this is added training data for the remaining classes for which the full set of classes is analysed both in full training mode, and also in hybrid trajectory-training mode. In hybrid mode, the spectral trajectories from class 1 - 4 are used together with the training sets for classes 5-13. In contrast to the previous section, where a rigorous comparison of the training and trajectory methods was the main objective, the goal here is to determine the highest overall classification accuracies possible for these classes using this new software. Implicit to this objective is a comparison of the training and trajectory methods, however, this is of secondary importance. Given the current emphasis, the *a priori* class weighting options available in the M⊕P software package are used to attempt to increase individual and overall class accuracies. As noted in §6.2.2.1, a given set of weights could affect trajectory and training inputs in different ways, and so this is kept in mind when comparing

methods. Further, the combined use of training data for classes 5-13 with the two methods used to characterise classes 1-4 makes it more difficult to make direct comparisons of the training and trajectory methods. With this understanding, the use of weights to improve individual classification accuracies is presented as a valid strategy for assessing the potential of each approach in terms of overall classification accuracies. In the next two sections, results obtained from the M⊕P software run in full training mode and hybrid trajectory-training mode are presented.

#### 6.2.3.1 Training Mode Results

Having evaluated classes 1-4 separately in the previous section, the first classification done in this section was to isolate and evaluate the new classes necessary to produce the full classification. Accordingly, classes 5-13 were first processed separately to gain a sense of the classification accuracies possible within this subset of classes. The result of classifying these 8 classes is shown in Table 6.4. The overall accuracy for this set of classes was 88% (K=0.86). Individual class accuracies in excess of 80% were obtained for all classes except fen (64%) and the new regeneration conifer class (66%), with a

TRAINING MODE: Classes 5-13 ONLY

| Classification Label --> | 5 | 6 | 7 | 8 | 9 | 10 | 11 | 12 | 13 | Total | % | K |
|---|---|---|---|---|---|---|---|---|---|---|---|---|
| Class 5: | 16 | 0 | 0 | 2 | 0 | 7 | 0 | 0 | 0 | 25 | 64.00 | 0.61 |
| Class 6: | 0 | 0 | 0 | 0 | 0 | 0 | 0 | 0 | 0 | 0 | | |
| Class 7: | 18 | 0 | 123 | 0 | 0 | 8 | 1 | 0 | 0 | 150 | 82.00 | 0.78 |
| Class 8: | 0 | 0 | 0 | 57 | 0 | 0 | 0 | 0 | 0 | 57 | 100.00 | 1.00 |
| Class 9: | 9 | 0 | 0 | 6 | 44 | 0 | 7 | 0 | 0 | 66 | 66.67 | 0.64 |
| Class 10: | 6 | 0 | 0 | 0 | 0 | 45 | 0 | 0 | 0 | 51 | 88.24 | 0.87 |
| Class 11: | 3 | 0 | 3 | 0 | 1 | 1 | 126 | 0 | 0 | 134 | 94.03 | 0.92 |
| Class 12: | 0 | 0 | 0 | 0 | 0 | 0 | 0 | 119 | 1 | 120 | 99.17 | 0.99 |
| Class 13: | 0 | 0 | 0 | 0 | 0 | 0 | 0 | 0 | 35 | 35 | 100.00 | 1.00 |
| Total: | 52 | 0 | 126 | 65 | 45 | 61 | 134 | 119 | 36 | 638 | **88.56** | **0.86** |

Table 6.4. M⊕P training mode classification output for fen, disturbed, burnt, grassland, and the four regeneration classes..

number of classes having accuracies above 90%. Classification omission error in the fen class was primarily with the medium age regeneration conifer class. This may be due to some similarities of the regeneration class understorey with the variable fen surface, which can also include some occurrences of trees. Similarly, for class 9, the new regeneration conifer class, the largest source of omission error was also with the fen class, with omission error also noted for the new regeneration deciduous class. The latter error could be due to similarities which may exist in the early development of forest understories in lower density, young stands where the surface cover can be rather variable. In general, this set of class accuracies is good, as would be expected given the diverse nature of classes such as burnt, disturbed areas, and grassland. The regeneration classes were also classified

well, with the exception of class 9. These results are consistent with observations of the training data plots made in §6.2.1.3 from Figures 6.3 and 6.4.

Table 6.5 shows the results of classifying all 12 classes using training data for each class input to the M⊕P classifier run in full training mode with no weights used. The overall accuracy achieved was 69% (K=0.67). The class accuracies for classes 5 - 13 were similar to those obtained in Table 6.4, where classes 1 - 4 were excluded. However, in this classification of all 12 classes, the accuracies for classes 1 - 4 were considerably lower than the earlier classification which considered these four classes on their own (Table 6.2).

TRAINING MODE: Classes 1 - 13

Classification Label:

| Cls | 1 | 2 | 3 | 4 | 5 | 6 | 7 | 8 | 9 | 10 | 11 | 12 | 13 | Total | % | K |
|---|---|---|---|---|---|---|---|---|---|---|---|---|---|---|---|---|
| 1: | 73 | 9 | 0 | 0 | 0 | 0 | 0 | 15 | 0 | 1 | 0 | 0 | 0 | 98 | 74.49 | 0.72 |
| 2: | 10 | 19 | 5 | 0 | 19 | 0 | 0 | 13 | 2 | 20 | 1 | 0 | 0 | 89 | 21.35 | 0.19 |
| 3: | 0 | 1 | 5 | 28 | 0 | 0 | 0 | 0 | 0 | 3 | 3 | 5 | 0 | 45 | 11.11 | 0.10 |
| 4: | 0 | 0 | 0 | 32 | 0 | 0 | 0 | 0 | 0 | 0 | 0 | 90 | 0 | 122 | 26.23 | 0.21 |
| 5: | 1 | 0 | 0 | 0 | 16 | 0 | 0 | 1 | 0 | 7 | 0 | 0 | 0 | 25 | 64.00 | 0.61 |
| 6: | 0 | 0 | 0 | 0 | 0 | 0 | 0 | 0 | 0 | 0 | 0 | 0 | 0 | 0 | | |
| 7: | 0 | 0 | 0 | 0 | 18 | 0 | 123 | 0 | 1 | 8 | 0 | 0 | 0 | 150 | 82.00 | 0.79 |
| 8: | 0 | 0 | 0 | 0 | 0 | 0 | 0 | 57 | 0 | 0 | 0 | 0 | 0 | 57 | 100.00 | 1.00 |
| 9: | 0 | 0 | 0 | 0 | 9 | 0 | 0 | 6 | 44 | 0 | 7 | 0 | 0 | 66 | 66.67 | 0.65 |
| 10: | 0 | 0 | 0 | 0 | 6 | 0 | 0 | 0 | 0 | 45 | 0 | 0 | 0 | 51 | 88.24 | 0.87 |
| 11: | 0 | 0 | 0 | 0 | 3 | 0 | 3 | 0 | 1 | 1 | 126 | 0 | 0 | 134 | 94.03 | 0.93 |
| 12: | 0 | 0 | 0 | 0 | 0 | 0 | 0 | 0 | 0 | 0 | 0 | 119 | 1 | 120 | 99.17 | 0.99 |
| 13: | 0 | 0 | 1 | 0 | 0 | 0 | 0 | 0 | 0 | 0 | 0 | 0 | 34 | 35 | 97.14 | 0.97 |
| Σ: | 84 | 29 | 11 | 60 | 71 | 0 | 126 | 92 | 48 | 85 | 137 | 214 | 35 | 992 | **69.86** | **.67** |

Table 6.5. M⊕P training mode classification output for all 12 classes for the BOREAS SSA.

Here, three of the four classes have accuracies less than 30%, with the fourth at 74%. Class 2 (OJP) had an accuracy of 21%, with the highest commission error found with the medium age regeneration conifer class (10). The main difference between these two classes is their age and understorey development. Low density OJP stands could be confused with medium age regeneration conifer. Here, the incorporation of tree density could be useful, as provided by the M⊕P trajectory mode. There was also some error noted with OJP and the fen and disturbed classes. The new regeneration conifer class (9) also showed a similar trend, as well as omission errors with the new regeneration deciduous class (11), which is most likely due to the similar age of both classes and that both have an early successional understorey. The fen class contains some trees, and this may have caused confusion with the OJP and new regeneration conifer classes. The mixed class (4) had an accuracy of 11% in full training mode, with most of it's omission error falling into the old aspen class. Similar to OJP, the OA class had a low classification accuracy (26%), and a high rate of omission error with the medium age regeneration deciduous class. Again, low density, mature OA stands could be similar to medium age regeneration deciduous stands. Following this analysis of errors, the main finding which emerges from this full training mode classification is that, for the dominant mature boreal forest species (OBS, OJP, OA and MIX), there was considerable error, but that these errors were often restricted to related classes such as medium age regeneration stands. This would suggest that with some adjustment to the way the training data are processed, a higher accuracy could be attained for these important classes. This is pursued and evaluated next using the M⊕P *a priori* weighting option.

WEIGHTED TRAINING MODE: Classes 1-13

Classification Label:

| Cls | 1 | 2 | 3 | 4 | 5 | 6 | 7 | 8 | 9 | 10 | 11 | 12 | 13 | Total | % | K |
|---|---|---|---|---|---|---|---|---|---|---|---|---|---|---|---|---|
| 1: | 87 | 10 | 0 | 0 | 0 | 0 | 0 | 1 | 0 | 0 | 0 | 0 | 0 | 98 | 88.78 | 0.87 |
| 2: | 23 | 41 | 11 | 0 | 0 | 0 | 0 | 0 | 5 | 8 | 1 | 0 | 0 | 89 | 46.07 | 0.43 |
| 3: | 0 | 1 | 7 | 33 | 0 | 0 | 0 | 0 | 0 | 1 | 3 | 0 | 0 | 45 | 15.56 | 0.14 |
| 4: | 0 | 0 | 0 | 92 | 0 | 0 | 0 | 0 | 0 | 0 | 0 | 30 | 0 | 122 | 75.41 | 0.71 |
| 5: | 2 | 1 | 0 | 0 | 0 | 0 | 0 | 0 | 9 | 13 | 0 | 0 | 0 | 25 | 0.00 | 0.00 |
| 6: | 0 | 0 | 0 | 0 | 0 | 0 | 0 | 0 | 0 | 0 | 0 | 0 | 0 | 0 | | |
| 7: | 0 | 0 | 0 | 0 | 0 | 0 | 130 | 0 | 9 | 11 | 0 | 0 | 0 | 150 | 86.67 | 0.85 |
| 8: | 1 | 0 | 0 | 0 | 0 | 0 | 0 | 56 | 0 | 0 | 0 | 0 | 0 | 57 | 98.25 | 0.98 |
| 9: | 1 | 0 | 0 | 0 | 0 | 0 | 0 | 5 | 53 | 0 | 7 | 0 | 0 | 66 | 80.30 | 0.79 |
| 10: | 0 | 6 | 0 | 0 | 0 | 0 | 0 | 0 | 2 | 43 | 0 | 0 | 0 | 51 | 84.31 | 0.83 |
| 11: | 0 | 0 | 0 | 0 | 0 | 0 | 5 | 0 | 1 | 2 | 126 | 0 | 0 | 134 | 94.03 | 0.93 |
| 12: | 0 | 0 | 0 | 18 | 0 | 0 | 0 | 0 | 0 | 0 | 0 | 91 | 11 | 120 | 75.83 | 0.72 |
| 13: | 0 | 0 | 0 | 0 | 0 | 0 | 0 | 0 | 0 | 0 | 0 | 0 | 35 | 35 | 100.00 | 1.00 |
| ∑: | 114 | 59 | 18 | 143 | 0 | 0 | 135 | 62 | 79 | 78 | 137 | 121 | 46 | 992 | **76.71** | **.74** |

Table 6.6. M⊕P training mode classification output for all 12 classes, with variable weights assigned to classes 5, 8, 10 and 12.

Table 6.6 shows the results of classifying the 12 classes using a set of weights as follows: class 5 = 0.80; class 8 = 0.85; class 10 = 0.90, and class 12 = 0.70. All other class weights were set to 1.0. These weights were chosen to reduce the allocation of pixels to these classes, since, as was seen in the previous classification (Table 6.5), the 4 dominant classes (1-4) had varying amounts of omission errors with classes 5, 8, 10 and 12. Using these weights, overall classification accuracy was improved from 69% (K=0.66) without weights to 76% (K=0.74). Most of the individual class improvements were found in classes 1 - 4. The OBS class accuracy was increased from 74% to 88%, OJP was

improved from 21% to 46%, with OA accuracy increased from 26% to 75%. This set of weights successfully eliminated omission errors with the new regeneration conifer and deciduous classes (10 and 12) for OJP and OA, respectively. In doing so, however, the class 10 and 12 accuracies decreased somewhat, from 88% to 84% for class 10, and from 99% to 75% for class 12. Also, omission errors into the fen and disturbed classes were reduced, but again not without some decreases in accuracy for these classes. The fen class accuracy dropped to 0%, with large errors of omission into the two regeneration conifer classes, while the disturbed class accuracy went from 100% to 98%.

Some interesting trends have emerged from this first attempt at classifying the full set of BOREAS SSA classes. Firstly, by using *a priori* class weights for selected classes, reasonable levels of accuracy were obtained for certain classes as well as for the overall result. Despite these efforts, however, two of the dominant mature forest class accuracies remain below the 50% level (OJP and MIX). These results were lower than the accuracies obtained when only the four dominant classes were considered alone (Table 6.2). The patterns of error are interesting and can be explained in terms of ecological similarities amongst classes. There were few occurrences of error that could not be readily understood (e.g. a mature black spruce area classified as grassland). Considering the detail and complexity of the class structure being used, these results show some merit and potential. Classification error would not be unexpected given that 8 of the 12 classes comprise healthy stands of trees (4 coniferous classes, 3 deciduous, and one mixed forest class), with two further classes also containing minor occurrences of trees (fen and burnt). One can begin to realise the complexities in the task as well as understand the varying levels of accuracy produced. However, regardless of this, it is clear that improved land cover classification accuracies are needed, particularly for the dominant mature classes (1-4). For

example, the class accuracies for these major boreal forest classes would not provide a satisfactory land cover stratification for the purpose of obtaining subsequent biophysical estimates. In the next section, the spectral trajectories for classes 1 - 4 are tested together with the training data for the remaining classes to explore the potential of the hybrid mode approach to the problem.

6.2.3.2 Hybrid Trajectory-Training Mode Results

In this section, the hybrid trajectory-training mode of the M⊕P software was used to provide an integrated processing environment for land cover classification using the spectral trajectories generated for classes 1 - 4 together with the supervised training data for classes 5 - 13. As with the full training mode, the first test did not use the *a priori* weighting option of the M⊕P software. The results of the hybrid mode classification of the full set of classes is provided in Table 6.7. An overall classification accuracy of 71% (K=0.68) was found, which was slightly higher than the 69% (K=0.66) overall accuracy obtained in full training data mode. The individual class results varied for the dominant forest classes (1 - 4). For example, OBS was classified with an accuracy of 87% in hybrid mode compared to 74% in training mode. Similar to training mode, the OJP class accuracy without weights was low, at 14% in hybrid mode compared to 21% in training mode. In hybrid mode, the most omission errors with OJP were with the fen and medium age regeneration conifer class, with a number of errors also found with the disturbed class. Similar to the results obtained using the training mode without weights, the OA class accuracy was also low in hybrid mode, with an individual class accuracy of only 20% compared to 26% in training mode. Again, almost all of the omission errors were with the medium age deciduous regeneration class. The MIX class was classified considerably

better in hybrid mode than full training mode, with a 37% increase in accuracy realised. In terms of the remaining 8 classes, the individual class accuracies were similar in all cases. This would be expected since the same training data sets were used for these classes in both the full training mode as well as in the hybrid trajectory-training mode. In terms of the four major boreal forest classes, the average accuracy of the four classes was increased by 10% in hybrid mode compared to full training mode. However, improvements in the individual class accuracies for these dominant classes is still required.

HYBRID MODE TRAJECTORY: Classes 1-4
TRAINING: Classes 5-13

Classification Label:

| Cls | 1 | 2 | 3 | 4 | 5 | 6 | 7 | 8 | 9 | 10 | 11 | 12 | 13 | Total | % | K |
|---|---|---|---|---|---|---|---|---|---|---|---|---|---|---|---|---|
| 1: | 86 | 9 | 0 | 0 | 0 | 0 | 0 | 3 | 0 | 0 | 0 | 0 | 0 | 98 | 87.76 | 0.87 |
| 2: | 1 | 13 | 1 | 0 | 28 | 0 | 0 | 20 | 2 | 24 | 0 | 0 | 0 | 89 | 14.61 | 0.12 |
| 3: | 0 | 7 | 22 | 9 | 0 | 0 | 0 | 0 | 0 | 2 | 2 | 3 | 0 | 45 | 48.89 | 0.47 |
| 4: | 0 | 0 | 11 | 25 | 0 | 0 | 0 | 0 | 0 | 0 | 0 | 86 | 0 | 122 | 20.49 | 0.18 |
| 5: | 1 | 0 | 0 | 0 | 16 | 0 | 0 | 1 | 0 | 7 | 0 | 0 | 0 | 25 | 64.00 | 0.61 |
| 6: | 0 | 0 | 0 | 0 | 0 | 0 | 0 | 0 | 0 | 0 | 0 | 0 | 0 | 0 | | |
| 7: | 0 | 0 | 0 | 0 | 18 | 0 | 123 | 0 | 1 | 8 | 0 | 0 | 0 | 150 | 82.00 | 0.79 |
| 8: | 0 | 0 | 0 | 0 | 0 | 0 | 0 | 57 | 0 | 0 | 0 | 0 | 0 | 57 | 100.00 | 1.00 |
| 9: | 0 | 0 | 0 | 0 | 9 | 0 | 0 | 6 | 44 | 0 | 7 | 0 | 0 | 66 | 66.67 | 0.65 |
| 10: | 0 | 1 | 0 | 0 | 6 | 0 | 0 | 0 | 0 | 44 | 0 | 0 | 0 | 51 | 86.27 | 0.85 |
| 11: | 0 | 0 | 0 | 0 | 3 | 0 | 3 | 0 | 1 | 1 | 126 | 0 | 0 | 134 | 94.03 | 0.93 |
| 12: | 0 | 0 | 0 | 0 | 0 | 0 | 0 | 0 | 0 | 0 | 0 | 119 | 1 | 120 | 99.17 | 0.99 |
| 13: | 0 | 3 | 0 | 0 | 0 | 0 | 0 | 0 | 0 | 0 | 0 | 0 | 32 | 35 | 91.43 | 0.91 |
| Σ : | 88 | 33 | 34 | 34 | 80 | 0 | 126 | 87 | 48 | 86 | 135 | 208 | 33 | 992 | **71.27** | **.68** |

Table 6.7. M⊕P hybrid trajectory-training mode classification output for all 12 classes.

This first hybrid mode result suggests the need for adjustment of class weights to overcome some of the class omission errors found between the dominant mature classes and the regeneration classes and other classes. To address this, the *a priori* weighting option available in the hybrid trajectory-training mode of the M⊕P software package was used. The following weights were used to compensate for class allocation errors determined from the previous classification test: class 5 = 0.85; class 8 = 0.80; class 9 = 0.95; class 10 = 0.90; and class 12 = 0.90. The resulting classification accuracies are shown in Table 6.8. The overall accuracy is increased by a small amount to 72% (K=0.69), however considerable improvements were obtained for the major dominant

WEIGHTED HYBRID MODE — TRAJECTORY: Classes 1-4; TRAINING: Classes 5-13

Classification Label:

| Cls | 1 | 2 | 3 | 4 | 5 | 6 | 7 | 8 | 9 | 10 | 11 | 12 | 13 | Total | % | K |
|---|---|---|---|---|---|---|---|---|---|---|---|---|---|---|---|---|
| 1: | 89 | 9 | 0 | 0 | 0 | 0 | 0 | 0 | 0 | 0 | 0 | 0 | 0 | 98 | 90.82 | 0.90 |
| 2: | 12 | 59 | 1 | 0 | 0 | 0 | 0 | 4 | 9 | 4 | 0 | 0 | 0 | 89 | 66.29 | 0.62 |
| 3: | 0 | 9 | 22 | 12 | 0 | 0 | 0 | 0 | 0 | 0 | 2 | 0 | 0 | 45 | 48.89 | 0.47 |
| 4: | 0 | 0 | 11 | 84 | 0 | 0 | 0 | 0 | 0 | 0 | 0 | 27 | 0 | 122 | 68.85 | 0.64 |
| 5: | 2 | 4 | 0 | 0 | 3 | 0 | 0 | 0 | 3 | 13 | 0 | 0 | 0 | 25 | 12.00 | 0.12 |
| 6: | 0 | 0 | 0 | 0 | 0 | 0 | 0 | 0 | 0 | 0 | 0 | 0 | 0 | 0 | | |
| 7: | 0 | 2 | 0 | 0 | 1 | 0 | 131 | 0 | 3 | 12 | 1 | 0 | 0 | 150 | 87.33 | 0.85 |
| 8: | 8 | 0 | 0 | 0 | 0 | 0 | 0 | 49 | 0 | 0 | 0 | 0 | 0 | 57 | 85.96 | 0.85 |
| 9: | 3 | 0 | 0 | 0 | 0 | 0 | 0 | 3 | 34 | 0 | 26 | 0 | 0 | 66 | 51.52 | 0.49 |
| 10: | 0 | 34 | 0 | 0 | 0 | 0 | 0 | 0 | 0 | 17 | 0 | 0 | 0 | 51 | 33.33 | 0.30 |
| 11: | 0 | 0 | 0 | 0 | 0 | 0 | 5 | 0 | 0 | 2 | 127 | 0 | 0 | 134 | 94.78 | 0.94 |
| 12: | 0 | 0 | 0 | 44 | 0 | 0 | 0 | 0 | 0 | 0 | 0 | 75 | 1 | 120 | 62.50 | 0.58 |
| 13: | 0 | 3 | 0 | 0 | 0 | 0 | 0 | 0 | 0 | 0 | 0 | 0 | 32 | 35 | 91.43 | 0.91 |
| Σ | 114 | 120 | 34 | 140 | 4 | 0 | 136 | 56 | 49 | 48 | 156 | 102 | 33 | 992 | **72.78** | **.70** |

Table 6.8. M⊕P hybrid trajectory-training mode classification output for all 12 classes, with variable weights assigned to classes 5, 8, 9, 10 and 12.

forest classes of interest (classes 1 - 4). A 20% increase in average accuracy for these four classes was realised. In terms of individual class accuracies, OJP class accuracy was increased to 66% using the weighted hybrid mode compared to 14% without weights. This was due to the substantial reduction in omission errors with the weighted classes 5, 8 and 10. Similarly, the old aspen class increased from 20% to 68% as the omission errors with the medium age regeneration deciduous class was reduced somewhat. The OBS class accuracy increased from 87% to 90% with the mixed forest accuracy unchanged at 48%. Individual accuracies for classes 1 - 4 were also higher in the weighted hybrid mode in 3 out of the 4 classes compared to the results from the training mode with weights. The OBS class increased marginally from 88% to 90%, with OJP increased by 20% to 66% and mixed forest improved by 33%. The OA accuracy, however, decreased from 75% to 68% using the hybrid weighted mode. Similar to the trend found with the training mode results when weights were introduced, individual class accuracies decreased for those classes which were assigned lower *a priori* weights. In terms of overall accuracy, the weighted hybrid mode achieved a higher average accuracy (+12%) of the four major classes of interest (1 - 4) compared to the weighted training mode, however, the overall accuracy for all classes decreased slightly (by 4%).

From this section, an ability to increase classification accuracy using *a priori* weights assigned to input training and trajectory data has been demonstrated. However, while the accuracies of individual classes of interest such as the dominant mature boreal forest classes have been increased, a consistent level of individual class accuracy and an acceptable level of overall classification accuracy has not been attained. Nonetheless, based on the analysis of trajectory and training data inputs, sufficient information content appears to be available from these two independent sources. This suggests that an improved result beyond that obtained in this section may be possible. In the next section, a method for

segregating evidence from independent classification inputs is proposed and tested for the purpose of maximising the available information content such that higher classification accuracies may be attained.

6.2.3.3 Hybrid Mode Two Pass Sequential Weighting

In the previous section, it became apparent that shifting the weighting criteria for one set of classes (e.g. the mature, dominant forest classes 1 - 4) would invariably result in other class accuracies being significantly reduced (e.g. the regeneration classes). Experience with the weighting factors specified suggested that individual class accuracies were rather sensitive to small changes in individual weighting factors applied. This is particularly true for larger numbers of classes where the evidential vector, or mass, can be distributed over a larger number of candidate propositions. When considering all 12 classes in the BOREAS SSA, in this research two distinct groups of spectral inputs were used in hybrid mode, namely, the spectral trajectories for classes 1 - 4, and the training data for the remaining classes. Further, in each case the class inputs were shown to have good discriminatory power within each sub-set of classes. Good accuracies were obtained within classes 1 - 4 in full trajectory mode, as well as for classes 5 - 13 in full training mode. However, when used together, the results were less than optimal, even when the weighting options were applied in hybrid trajectory-training mode. It was difficult to determine one set of weights that would provide adequate discrimination for all classes being considered. Therefore, an alternative method was sought to more effectively pool this evidence.

Given that there were two distinct set of spectral inputs, a two stage approach to classification was implemented which uses the *a priori* weighting option in a different way

to produce intermediate classification results which are then merged to create a final product. No modification to the M⊕P software was required for this, instead, the program was run two separate times with different inputs, effectively creating a two-pass, sequential approach. In each pass, all 12 classes are classified, however, the weights are specified such that in the first pass, the trajectory class inputs (1 - 4) are given priority by reducing the weights for all other classes (5 - 13), while in the second pass, the training mode input data are given priority by reducing the weights assigned for the trajectory mode inputs. In reducing class weights, it is essential that the same weighting factor be used for all non-priority classes in a classification, and also that this same weighting factor be used in both passes. The set of weights used for these classes is termed the non-priority weighting factor. For each intermediate classification, the absolute magnitude of evidence associated with the class designated for that pixel (as specified by the evidential reasoning decision rule of maximum support) is recorded. In the final pass, in which the two intermediate results are merged, the class labels generated from each pass are first compared. If they are the same, then consensus on the evidence already exists and the class label is output to disk. However, such consensus would not be expected to be common, given that the non-priority weighting factor used should be significantly less than 1.0 compared to the full weight used for the priority classes in a given pass. If the class labels differ from each intermediate product, then the degree of evidence associated with each classification decision is consulted, with the pixel being assigned to the class with the higher amount of evidence. Keeping the two groups separate at the intermediate stages permits the evidence to first be evaluated within each group instead of having evidence being directed towards other spectrally similar classes generated from the other set. Essentially, this method is analogous to first deciding whether a pixel falls into the mature dominant set of classes or if it belongs in the other set of classes (regeneration classes, plus the others), and then, once

the appropriate group has been determined, focusing in on that group to make the final class allocation. This is an effective way of dealing with larger number of classes, particularly when a number of classes are somewhat similar, as is the case here with the 8 forested classes. For a pixel which does not belong to a given group, the degree of consensus for the class label determined within that group should not be great. The supporting evidence within the other group (within which the pixel actually belongs) ought to be substantially higher.

This hybrid mode two-pass sequential weighting method was tested in this research using the trajectory (classes 1 - 4) and training (class 5 - 13) inputs. Several trial runs of this method were conducted to experiment with different non-priority weighting factors. In this research, a non-priority weighting factor of 0.75 was used for both intermediate passes. Use of a non-priority weighting factor greater than this resulted in overall classification accuracy being reduced. Table 6.9 shows the results obtained from the first intermediate pass in which the trajectory classes (1-4) were given preference (weights = unity) with the training based classes (5 - 13) each assigned the non-priority weighting factor. As would be expected, the trajectory classes yielded higher accuracies than the training based classes as a direct result of the weights used. The individual accuracies of classes 1 - 4 are very similar to the accuracies obtained when only 4 classes were used and without any weighting applied (Table 6.3). Class 2 (OJP) had a lower classification accuracy in this intermediate pass as a result of omission error with the new regeneration conifer class (9) being introduced.

WEIGHTED HYBRID MODE  TRAJECTORY: Classes 1-4
TRAINING: Classes 5-13

TWO PASS SEQUENTIAL WEIGHTING: TRAJECTORY PASS (1)
NON-PRIORITY WEIGHTING FACTOR: 0.75

Classification Label:

| Cls | 1 | 2 | 3 | 4 | 5 | 6 | 7 | 8 | 9 | 10 | 11 | 12 | 13 | Total | % | K |
|---|---|---|---|---|---|---|---|---|---|---|---|---|---|---|---|---|
| 1: | 89 | 9 | 0 | 0 | 0 | 0 | 0 | 0 | 0 | 0 | 0 | 0 | 0 | 98 | 90.82 | 0.89 |
| 2: | 16 | 71 | 1 | 0 | 0 | 0 | 0 | 0 | 1 | 0 | 0 | 0 | 0 | 89 | 79.78 | 0.73 |
| 3: | 0 | 9 | 24 | 12 | 0 | 0 | 0 | 0 | 0 | 0 | 0 | 0 | 0 | 45 | 53.33 | 0.48 |
| 4: | 0 | 0 | 11 | 111 | 0 | 0 | 0 | 0 | 0 | 0 | 0 | 0 | 0 | 122 | 90.98 | 0.88 |
| 5: | 2 | 23 | 0 | 0 | 0 | 0 | 0 | 0 | 0 | 0 | 0 | 0 | 0 | 25 | 0.00 | 0.00 |
| 6: | 0 | 0 | 0 | 0 | 0 | 0 | 0 | 0 | 0 | 0 | 0 | 0 | 0 | 0 | | |
| 7: | 0 | 36 | 0 | 0 | 1 | 0 | 113 | 0 | 0 | 0 | 0 | 0 | 0 | 150 | 75.33 | 0.72 |
| 8: | 33 | 0 | 0 | 0 | 0 | 0 | 0 | 24 | 0 | 0 | 0 | 0 | 0 | 57 | 42.11 | 0.41 |
| 9: | 6 | 41 | 1 | 0 | 0 | 0 | 0 | 0 | 12 | 0 | 6 | 0 | 0 | 66 | 18.18 | 0.17 |
| 10: | 0 | 51 | 0 | 0 | 0 | 0 | 0 | 0 | 0 | 0 | 0 | 0 | 0 | 51 | 0.00 | 0.00 |
| 11: | 0 | 6 | 60 | 0 | 0 | 0 | 1 | 0 | 1 | 0 | 66 | 0 | 0 | 134 | 49.25 | 0.45 |
| 12: | 0 | 0 | 0 | 120 | 0 | 0 | 0 | 0 | 0 | 0 | 0 | 0 | 0 | 120 | 0.00 | 0.00 |
| 13: | 0 | 4 | 5 | 8 | 0 | 0 | 0 | 0 | 0 | 0 | 0 | 0 | 18 | 35 | 51.43 | 0.51 |
| Σ | 146 | 250 | 102 | 251 | 1 | 0 | 114 | 24 | 14 | 0 | 72 | 0 | 18 | 992 | **53.23** | **.48** |

Table 6.9. Results of the first intermediate pass of the two-pass sequential weighting hybrid trajectory-training mode classification. Priority weights are assigned to spectral trajectory inputs in this pass.

A similar result was found with the second intermediate pass (Table 6.10) in which priority weights were assigned to the training data classes (5-13). The accuracies for classes 5 - 13 were almost as high as the non-weighted training mode classification which considered the 8 non-trajectory classes only (Table 6.4). Class accuracies for the non-priority classes in pass 2 (classes 1 - 4) were considerably lower, as would be expected. The grass class experienced some reduction in accuracy as a result of omission into class 2.

WEIGHTED HYBRID MODE — TRAJECTORY: Classes 1-4; TRAINING: Classes 5-13

TWO PASS SEQUENTIAL WEIGHTING: TRAINING PASS (2)
NON-PRIORITY WEIGHTING FACTOR: 0.75

Classification Label:

| Cls | 1 | 2 | 3 | 4 | 5 | 6 | 7 | 8 | 9 | 10 | 11 | 12 | 13 | Total | % | K |
|---|---|---|---|---|---|---|---|---|---|---|---|---|---|---|---|---|
| 1: | 86 | 8 | 0 | 0 | 0 | 0 | 0 | 3 | 0 | 1 | 0 | 0 | 0 | 98 | 87.76 | 0.87 |
| 2: | 0 | 12 | 1 | 0 | 28 | 0 | 0 | 21 | 2 | 25 | 0 | 0 | 0 | 89 | 13.48 | 0.11 |
| 3: | 0 | 7 | 22 | 9 | 0 | 0 | 0 | 0 | 0 | 2 | 2 | 3 | 0 | 45 | 48.89 | 0.47 |
| 4: | 0 | 0 | 11 | 24 | 0 | 0 | 0 | 0 | 0 | 0 | 0 | 87 | 0 | 122 | 19.67 | 0.17 |
| 5: | 1 | 0 | 0 | 0 | 16 | 0 | 0 | 1 | 0 | 7 | 0 | 0 | 0 | 25 | 64.00 | 0.61 |
| 6: | 0 | 0 | 0 | 0 | 0 | 0 | 0 | 0 | 0 | 0 | 0 | 0 | 0 | 0 | | |
| 7: | 0 | 0 | 0 | 0 | 18 | 0 | 123 | 0 | 1 | 8 | 0 | 0 | 0 | 150 | 82.00 | 0.79 |
| 8: | 0 | 0 | 0 | 0 | 0 | 0 | 0 | 57 | 0 | 0 | 0 | 0 | 0 | 57 | 100.00 | 1.00 |
| 9: | 0 | 0 | 0 | 0 | 9 | 0 | 0 | 6 | 44 | 0 | 7 | 0 | 0 | 66 | 66.67 | 0.65 |
| 10: | 0 | 0 | 0 | 0 | 6 | 0 | 0 | 0 | 0 | 45 | 0 | 0 | 0 | 51 | 88.24 | 0.87 |
| 11: | 0 | 0 | 0 | 0 | 3 | 0 | 3 | 0 | 1 | 1 | 126 | 0 | 0 | 134 | 94.03 | 0.93 |
| 12: | 0 | 0 | 0 | 0 | 0 | 0 | 0 | 0 | 0 | 0 | 0 | 119 | 1 | 120 | 99.17 | 0.99 |
| 13: | 0 | 3 | 0 | 0 | 0 | 0 | 0 | 0 | 0 | 0 | 0 | 0 | 32 | 35 | 91.43 | 0.91 |
| Σ | 87 | 30 | 34 | 33 | 80 | 0 | 126 | 88 | 48 | 89 | 135 | 209 | 33 | 992 | **71.17** | **.68** |

Table 6.10. Results of intermediate pass #2 of the two-pass sequential weighting hybrid trajectory-training mode classification. Priority weights were assigned to training data class inputs in this pass.

Once the sequential two pass stage had been completed, the evidential output from the two intermediate classifications was merged to produce the final classification output. The result is shown in Table 6.11. An overall classification accuracy of 85% (K=0.83) was achieved, with good individual class accuracies obtained. This is the best result found of any of the methods tested, including both the weighted full training mode and the hybrid trajectory-training mode results.

WEIGHTED HYBRID MODE  TRAJECTORY: Classes 1-4
TRAINING: Classes 5-13

TWO PASS SEQUENTIAL WEIGHTING: FINAL CLASSIFICATION

Classification Label:

| Cls | 1 | 2 | 3 | 4 | 5 | 6 | 7 | 8 | 9 | 10 | 11 | 12 | 13 | Total | % | K |
|---|---|---|---|---|---|---|---|---|---|---|---|---|---|---|---|---|
| 1: | 87 | 9 | 0 | 0 | 0 | 0 | 0 | 1 | 0 | 1 | 0 | 0 | 0 | 98 | 88.78 | 0.87 |
| 2: | 16 | 71 | 1 | 0 | 0 | 0 | 0 | 0 | 1 | 0 | 0 | 0 | 0 | 89 | 79.78 | 0.76 |
| 3: | 0 | 9 | 24 | 12 | 0 | 0 | 0 | 0 | 0 | 0 | 0 | 0 | 0 | 45 | 53.33 | 0.51 |
| 4: | 0 | 0 | 11 | 109 | 0 | 0 | 0 | 0 | 0 | 0 | 0 | 2 | 0 | 122 | 89.34 | 0.88 |
| 5: | 2 | 8 | 0 | 0 | 15 | 0 | 0 | 0 | 0 | 0 | 0 | 0 | 0 | 25 | 60.00 | 0.59 |
| 6: | 0 | 0 | 0 | 0 | 0 | 0 | 0 | 0 | 0 | 0 | 0 | 0 | 0 | 0 | | |
| 7: | 0 | 27 | 0 | 0 | 1 | 0 | 122 | 0 | 0 | 0 | 0 | 0 | 0 | 150 | 81.33 | 0.79 |
| 8: | 0 | 0 | 0 | 0 | 0 | 0 | 0 | 57 | 0 | 0 | 0 | 0 | 0 | 57 | 100.00 | 1.00 |
| 9: | 6 | 9 | 1 | 0 | 0 | 0 | 0 | 0 | 44 | 0 | 6 | 0 | 0 | 66 | 66.67 | 0.65 |
| 10: | 0 | 7 | 0 | 0 | 0 | 0 | 0 | 0 | 0 | 44 | 0 | 0 | 0 | 51 | 86.27 | 0.86 |
| 11: | 0 | 6 | 1 | 0 | 0 | 0 | 1 | 0 | 1 | 0 | 125 | 0 | 0 | 134 | 93.28 | 0.92 |
| 12: | 0 | 0 | 0 | 6 | 0 | 0 | 0 | 0 | 0 | 0 | 0 | 114 | 0 | 120 | 95.00 | 0.94 |
| 13: | 0 | 3 | 0 | 0 | 0 | 0 | 0 | 0 | 0 | 0 | 0 | 0 | 32 | 35 | 91.43 | 0.91 |
| ∑ | 111 | 149 | 38 | 127 | 16 | 0 | 123 | 58 | 46 | 45 | 131 | 116 | 32 | 992 | **85.08** | **.83** |

Table 6.11. Final result from merging intermediate M⊕P outputs produced using the two-pass sequential weighting approach in hybrid trajectory-training mode.

In terms of the 4 mature dominant boreal forest classes, OBS had an accuracy of 88%, OJP was 79%, and OA was 89%. However, the mixed forest class accuracy was considerably lower, at 53%. For classes 5 - 13, the accuracies exceeded 80% for all but two classes, with four of the eight classes over 90%. The four regeneration classes (9-12) had good accuracies, with the exception of the new regeneration conifer class (9), which had omission errors with OBS, OJP and the new regeneration deciduous classes. Using the two pass sequential weighting method, the individual class accuracies approached the classification accuracies obtained for the priority classes in each pass, and in some cases the same level of accuracy was achieved.

In terms of classification error, there were a number of differences in the distribution and allocation of omission error for misclassified pixels in the final result compared to each intermediate pass for which that class was assigned priority. For example, the omission errors for class 5 (fen) in the intermediate pass #2 (training data priority) were primarily with the medium age regeneration conifer class, whereas in the final classification these errors were with OBS and OJP. Similarly, the omission errors for class 7 (disturbed) shifted from classes 5 and 10 in pass 2 to class 2 in the final product. Class 9 (new regeneration conifer) omission errors were also displaced from classes 5 and 8 to classes 1 and 2, with the omission errors for class 10 (medium age regeneration conifer) shifted from the fen class to OJP. Of the 4 mature forest classes, OJP had the largest errors of commission. Such errors of commission into the mature dominant classes is not unexpected for the final product, however these errors are less than the degree of misclassification found when applying sets of weights to all classes without the 2 pass approach.

The two-pass sequential weighting method used here has successfully provided a good classification output product, and it represents the best land cover classification accuracy obtained from the various methods tested here. This suggests that the additional computation and processing time required to perform the two-passes of intermediate classifications together with the final merging process is worthwhile. In the next section, the results obtained from the trajectory classes are used for estimating biophysical parameters using the associated forest component outputs which accompany each pixel label in the spectral trajectory mode output.

## 6.3 BIOPHYSICAL PARAMETER ESTIMATION

### 6.3.1 Biophysical Data

The land cover classification results produced in the previous section were based on the network of BOREAS Tower Flux (TF) and Auxiliary (AUX) Sites. At these sites, an extensive set of biophysical data was collected by several other science teams in BOREAS and made available to BOREAS investigators. The primary source of biophysical information used here was derived from a data set placed on the BOREAS information system (BORIS) by Terrestrial Ecology project #6 (TE-06, P.I.: Dr. Tom Gower, University of Wisconsin-Madison). Additional sources of information included biometry and auxiliary site data from project TE-13 (P.I.: Dr. Mike Apps, Northern Forestry Centre, Canadian Forestry Service, Edmonton) as published in Halliwell and Apps (1995, 1996), as well as canopy architecture information from project TE-23, as discussed in §5.5.1, and

the BOREAS Experiment Plan Document (BOREAS, 1994). The following biophysical parameters were available and used in this study: biomass (BIO), leaf area index (LAI), tree height (HGT), and tree diameter at breast height (DBH). Unfortunately, there were gaps in the data for net primary productivity for the set of sites used in this research, and therefore this variable was not analysed in the present study. A brief synopsis of how the biophysical data used in this study were collected is presented in the following paragraphs, together with a description of additional processing required by the author to place these data in final form for the analysis.

The biomass, LAI, DBH and height data were collected by TE-06 personnel at all TF sites and at a variety of AUX sites. This effort was coordinated with measurements taken by Canadian Forestry Service personnel which are published in Halliwell and Apps (1996). According to documentation which accompanies the TE-06 data set on BORIS, site-specific allometric equations were developed for the dominant overstorey species at each TF site and for selected AUX sites based on a harvest completed in August 1994. Using these equations, biomass and leaf area were estimated for trees sampled using a system of plots established at each site. Four plots spaced 10m apart were identified in the four cardinal directions from an established site center point to guide sampling. Measurements of tree height and DBH were taken within these samples, with the latter determined at standard heights of 1.37m from the base of live trees. In cases where site-specific allometric equations were not available for a given site, equations developed from harvests conducted in August 1994 and August 1995 were matched to the AUX site under consideration based on the study area, range of tree diameters and site characteristics.

The leaf area data extracted from the data set was the total foliage leaf area expressed in units of $m^2/m^2$. The biomass variable used was total biomass of live trees expressed in kg carbon/hectare (kgC/ha). In this study, biomass and leaf area data for each site were subsequently averaged from the four plot directions to produce one measure each per site. The biomass variable was then converted from kgC/ha to kgC/m (using the conversion factor 1 ha = 10117.361 $m^2$). The DBH and tree height variables were taken directly from the data set as site average DBH and site average tree height, respectively, as determined from the plot sampling scheme. Data for each of the four variables (BIO, LAI, DBH, HGT) were available for the TF and AUX sites from BORIS TE-06, with the exception of HGT which was not yet available for TF sites. These measures were obtained from the TE-23 canopy architecture data set (described in §5.5.1) in consultation with the TE-13 data (Halliwell and Apps, 1996) and the BOREAS Explan (BOREAS, 1994).

### 6.3.2 Experimental Design

The biophysical data described in the previous section were compiled and synthesized into one data file, organised by site land cover class, and sub-sampled to correspond with the BOREAS TF and AUX sites used in the land cover classification experiments presented in §6.2. Sites analysed in the land cover experiments for which there were no biophysical data were excluded from the biophysical estimation analysis in this section. Further, the analysis was restricted to the four mature, dominant classes (OBS, OJP, MIX and OA) for which trajectory information with forest components were available. There was a good representation of each of these classes from the available 26 sites of biophysical data for these classes, with the exception of the mixed class, for which

there were only three ground validation sites. The final set of biophysical data used in this analysis is listed in Appendix D.

Although there were a number of land cover classifications available for input to this biophysical estimation process, only one set of classification results was used here. As pointed out in §6.2, the training data method provided no associated information for follow-on biophysical parameter estimation. Therefore, only those land cover results generated using one of the M⊕P trajectory modes were appropriate for the biophysical analysis. These classifications contain land cover information together with sunlit canopy fraction, sunlit background fraction, shadow fraction, and tree density. In this experiment, the land cover classification results generated using the two pass sequential weighted hybrid trajectory training mode were used as input to this biophysical data analysis, as these results were obtained in conjunction with the full set of 12 land cover classes. Although more accurate trajectory mode land cover classification results existed for classes 1 - 4 from the classifications presented in §6.2.2.2, these were not used since they were not produced in the context of the full set of classes present in the BOREAS SSA.

Results from the two pass sequential weighted hybrid trajectory training mode classification (Table 6.11) were extracted and sampled to correspond to the available biophysical data, as described above. For a given site, the same $5 \times 5$ pixel window neighbourhood of satellite reflectance values was used, with the exception of any pixels that were determined to be a member of a different land cover class (these pixels were excluded prior to the land cover classification experiments). Since for each site there is one set of biophysical parameters, the same value for each parameter is used for all pixels in the $5 \times 5$ window. For each pixel, the available information from the trajectory based land

cover classification consisted of the land cover class identifier and the set of forest component fractions associated with the tree density value. The full set of information from the classification output and the biophysical data set available for a given pixel is listed in Table 6.12. The tree density value was determined as the position along the spectral trajectory to which the satellite TM pixel reflectance values had the closest proximity. As explained in §5.6, this is how the M⊕P classifier works when run in trajectory mode. The component fractions output were the set of fractions associated with that tree density point along the trajectory, as generated by the canopy geometrical optical reflectance model.

The information for each pixel, as listed in Table 6.12, provides an opportunity to assess the correspondence between the various trajectory outputs (component fractions, tree density, land cover class) and the biophysical parameters. This was tested by linear regression analysis using the SPSS statistical package REGRESSION procedures (SPSS, 1988). In these analyses, the biophysical parameters are being predicted and therefore these are set as the dependent (Y) variable (BIO, LAI, DBH, HGT). The trajectory outputs (C,B,S,Td) are used to obtain the predictions and therefore these are the independent (X) variables. A series of regressions were run in which each trajectory output variable was tested separately for each biophysical parameter. As in Chapter IV, the ability of the trajectory outputs to predict the biophysical parameters is assessed according to the magnitude of the coefficient of determination ($r^2$). A level of significance of $\alpha = 0.05$ was used for all regressions reported in this Chapter.

| Variable Name | Description |
|---|---|
| ID | BOREAS Site Identifier of pixel |
| LIN | Image line co-ordinate of sample |
| PIX | Image pixel co-ordinate of sample |
| RED | Landsat TM Red (band 3) reflectance value |
| NIR | Landsat TM near infrared (band 4) reflectance value |
| CLS | Land cover class from ground data |
| MCLS | Land cover class from M⊕P trajectory classification |
| C | Sunlit canopy fraction from M⊕P trajectory |
| B | Sunlit background fraction from M⊕P trajectory |
| S | Shadow fraction from M⊕P trajectory |
| Td | Tree Density value from M⊕P trajectory |
| BIO | Biomass from ground data |
| LAI | Leaf area index from ground data |
| DBH | Tree diameter at breast height from ground data |
| HGT | Tree height from ground data |

Table 6.12. Land cover classification and biophysical ground data for each pixel site in the sample.

In the next section, the relationships between the M⊕P trajectory outputs and boreal forest biophysical parameters are explored. A fundamental aspect of this work at the regional scale is the hypothesized importance of stratifying the biophysical analysis by land cover class. This hypothesis is explored through several sets of results. In the first set (§6.3.3.1), land cover classes are not used, and instead all sites are pooled together to explore the ability to predict biophysical parameters without a prior land cover stratification. Then, the analysis is stratified by land cover class and the results compared to evaluate the importance and need for land cover classification (§6.3.3.2). The third set of results (§6.3.3.3) is used to evaluate the impact of land cover misclassification and to gain an understanding of how classification error affects biophysical parameter estimation. In the final section (§6.3.3.4), the M⊕P trajectory results are summarised and compared to results obtained using a vegetation index.

### 6.3.3 Biophysical Parameter Estimation Results

#### 6.3.3.1 Predictions Without Land Cover Stratification

To evaluate the importance of land cover stratification in biophysical parameter estimation, it is useful to first do the analysis without land cover classes to determine (i) if land cover classification is indeed necessary, and (ii) to establish a baseline set of results for comparing stratified and non-stratified estimates. Accordingly, the full set of M⊕P hybrid trajectory training mode outputs were input to a regression analysis with each of the four biophysical parameters. The results are shown in Table 6.13. In all cases, the results were poor as evidenced by the very low $r^2$ values. The highest overall $r^2$ value between

any trajectory and biophysical variable was only 0.16. This, and the other results in the table suggest a very weak relationship between these variables, and in some cases, the $r^2$ values were not significant. Clearly, improved results are required. Given that site land cover classes were excluded from these regressions, it would appear that an improved predictive capability might be realised if the analysis were stratified by land cover. This is tested in the next section.

| | M⊕P Trajectory Outputs | | | | Veg. Index |
|---|---|---|---|---|---|
| | Td | C | B | S | NDVI |
| **BIO** | .07 | **.09** | .** | **.09** | .07 |
| **LAI** | .** | .** | **.04** | .** | **.04** |
| **DBH** | .** | **.05** | .04 | .04 | .** |
| **HGT** | .09 | .15 | .** | **.16** | .05 |

Table 6.13. Predicting biophysical parameters without land cover stratification. Linear regression coefficients of determination ($r^2$) among the biophysical parameters biomass, LAI, DBH, tree height, and the trajectory outputs of tree density (Td) and component fractions sunlit canopy (C) sunlit background (B) and shadow (S). Results with NDVI also shown. Best overall results for each parameter shown in bold. Results not significant at $\alpha = 0.05$ shown as **.

6.3.3.2 Predictions With Land Cover Stratification

In this section, each linear regression analysis between a M⊕P remote sensing variable and a biophysical parameter was performed separately for each land cover class for which trajectory outputs were available. These classes were OBS, OJP, MIX and OA which are the mature, dominant forest cover classes defined for the BOREAS SSA. In this section, M⊕P trajectory output for pixels assigned to their correct land cover classes were used in the biophysical analysis. This was done for three reasons. Firstly, it was desirable to determine the potential for the method given correct land cover information. If a potential for predicting biophysical parameters is demonstrated using an accurate land cover stratification, then additional work can be directed towards improving land cover classification methods as required. Secondly, biophysical estimates generated using a correct land cover classification provides a basis for comparison to assess the impact of classification error. This is done in the next section. Thirdly, if good correspondence exists between class specific trajectory outputs and biophysical estimates, then it will be desirable to derive predictive equations which quantify these relationships. Pixels assigned to incorrect land cover classes must be excluded from this process since otherwise the wrong trajectory outputs would be included in the derived equations. Related to this, although the biophysical estimations based on land cover could also be based on the full set of ground sites (essentially replacing any digital land cover misclassifications with the ground observed class), this was not done so that the comparison, and also the derived equations, would be based upon the sites which the digital classification algorithm actually classified properly, instead of including additional pixel sites for which it is not clear that a correct classification is possible given existing algorithms. However, since good accuracies were obtained for all but one of the mature forest classes from the M⊕P hybrid mode

classification (Table 6.11), this factor is not deemed significant. For the mixed class, which had a lower class accuracy, it is best not to assume that all sites can be classified correctly given its complex and, on times, highly variable class composition.

The results of using M⊕P trajectory output for predicting each biophysical parameter are presented in Table 6.14. In all cases, considerable improvements were found when the analysis was stratified by correct land cover classes, compared to the results obtained without land cover information (Table 6.13). Regression $r^2$ values within each class are larger than those obtained when samples from all classes were merged. Results from individual biophysical parameters are discussed next.

For biomass, $r^2$ values in the range of 0.70 were obtained for OBS and OJP, suggesting a strong relationship between the mixture fractions and the biophysical parameter, with moderately strong $r^2$ values found within the mixed and OA classes. Without the land cover stratification, the $r^2$ values were all $< 0.10$ for biomass. The same pattern was found for LAI, although the strength of the relationship was greater (0.74) for OBS and OJP. In both cases, interesting trends are found in terms of the utility of individual trajectory component outputs. For both biomass and LAI, the shadow fraction produced the highest $r^2$ values in most classes, such as in the OBS and OA classes for both parameters, as well as showing the strongest relationship with LAI in the OJP class. In cases where shadow fraction did not provide the strongest relationship, it usually had a $r^2$ value that was only slightly lower (e.g. 0.70 for OJP when the highest $r^2$ was 0.72), while not having any instances of a weak relationship. Tree density and sunlit canopy fractions also produced good results, though not at the same level of consistency as with

| Biophy. Parameter | Land Cover Class | M⊕P Trajectory Output | | | |
|---|---|---|---|---|---|
| | | Td | C | B | S |
| **BIOMASS** | OBS | .14 | .12 | .31 | **.69** |
| | OJP | **.72** | **.72** | .60 | .70 |
| | MIX | **.68** | .55 | .19 | .50 |
| | OA | .46 | **.51** | .** | **.51** |
| **LAI** | OBS | .14 | .12 | .33 | **.74** |
| | OJP | **.74** | .73 | .61 | **.74** |
| | MIX | **.67** | .54 | .18 | .50 |
| | OA | .48 | .55 | .** | **.55** |
| **DBH** | OBS | .05 | .06 | .17 | **.42** |
| | OJP | **.65** | **.65** | .50 | **.65** |
| | MIX | **.66** | .53 | .19 | .50 |
| | OA | .31 | .38 | .** | **.38** |
| **HEIGHT** | OBS | .** | .04 | .13 | **.38** |
| | OJP | **.83** | **.83** | .71 | .82 |
| | MIX | **.68** | .54 | .18 | .51 |
| | OA | .25 | .35 | .** | **.36** |

Table 6.14. Predicting biophysical parameters with land cover stratification. Linear regression $r^2$ values among the biophysical parameters biomass, LAI, DBH, tree height and the trajectory outputs of tree density (Td), and component fractions (C, B, S). Best results within each land cover class for each parameter shown in bold. Results not significant at $\alpha = 0.05$ shown as **.

shadow fraction. This first set of results is consistent with those found in the earlier analysis conducted in the Superior National Forest (Chapter IV). In that analysis, shadow fraction also produced the best results. The physical basis for shadow fraction being optimal in both studies for predicting biophysical variables is the increased sensitivity to tree size and morphology, as explained in §4.5.1. In terms of class differences, biomass and LAI were more strongly related to M⊕P trajectory outputs in the conifer classes than the mixed or deciduous class. For the mixed class, the greater variability of site characteristics at a given stand density is likely a confounding issue, as well as the variety of canopy geometries and understorey composition which occurs. The way the spectral trajectories were combined to depict this class in spectral space may be less appropriate in some cases. For OA, the different canopy geometry of these stands may not be represented as well in the spheroid model used. Also, the use of spectral end-member reflectance values from outside sources may have introduced some inconsistencies in this class compared to the field based measurements of the coniferous end-members. Overall, a strong predictive capability was found between the trajectory outputs and biomass and LAI.

Having found strong relationships between the M⊕P outputs and these biophysical parameters, it is useful to quantify these relationships through deriving equations from the regression analysis. This was done for biomass and LAI, with the shadow fraction selected from the group of independent variables as being the best predictor for these parameters, as explained above. Equations linking shadow fraction and biomass and LAI were derived from the statistical output of the regression analysis which computed the regression co-efficients. The general form of the regression equation describing the line fit through a set of values is:

$$Y_i = \beta_0 + \beta_1 X_i \quad (6.1)$$

where $Y_i$ is the dependent variable (the biophysical parameter being predicted), $X_i$ is the independent variable (the trajectory output) and $\beta_1$ and $\beta_0$ are the regression co-efficients (slope, intercept). In this analysis, equations were derived for each class for both biomass and LAI. Each set of equations is listed in Tables 6.15 and 6.16. Using these equations, estimates of biomass and LAI could be derived as a function of shadow fraction for other parts of the study area, using the appropriate equation defined for each land cover class.

For DBH and tree height, similar patterns of relationships were found as with biomass and LAI, however, the strength of the relationships between the trajectory outputs and these biophysical parameters was considerably lower. For example, the maximum values for any of the classes with DBH was $r^2 = 0.66$, with considerably lower $r^2$ values found for tree height, with the exception of OJP, which had a value of $r^2 = 0.83$. This may, in part, be due to the smaller variability of tree heights in the OJP class, as evident in Appendix D. Again, shadow fraction produced the best results for five of the eight class cases evaluated (4 classes for each of DBH and tree height). As with biomass and LAI, when shadow fraction did not produce the highest $r^2$ value, it was not far from it. The weaker relationships between the trajectory outputs and DBH and tree height may be due to the greater structural complexity of these parameters in terms of their remote estimation. Biomass and LAI both have a larger overall canopy component than does DBH or tree height. As a result, DBH and tree height involve greater inference between component fractions and these measures. This may explain the lower $r^2$ values found with these parameters. However, given this complexity, these results are promising and suggest a

potential for this method to be further refined such that DBH and tree height estimates could be improved.

| BIOMASS | |
|---|---|
| **Class** | **Equation** |
| OBS | BIO = 0.54 S - 36.32 |
| OJP | BIO = 0.35 S - 22.90 |
| MIX | BIO = 0.48 S - 12.58 |
| OA | BIO = 0.51 S - 7.52 |

Table 6.15. Regression equations for biomass (BIO) as a function of shadow fraction (S) for the four dominant, mature forest cover classes in the BOREAS SSA.

| LEAF AREA INDEX | |
|---|---|
| **Class** | **Equation** |
| OBS | LAI = 0.93 S - 65.33 |
| OJP | LAI = 0.13 S - 8.73 |
| MIX | LAI = 0.71 S - 23.30 |
| OA | LAI = 0.21 S - 3.50 |

Table 6.16. Regression equations for leaf area index (LAI) as a function of shadow fraction (S) for the four dominant, mature forest land cover classes in the BOREAS SSA.

The main result from this section is that land cover classification has been shown to be very important for providing improved biophysical estimates, owing to the much stronger relationships found between trajectory outputs and biophysical parameters when *a priori* land cover stratification was performed. Given this, it is useful to gain insight into how classification error may affect the estimation of biophysical parameters. This is explored in the next section.

6.3.3.3 Assessing the Impact of Land Cover Misclassification

Results in the previous section were based on pixel sites that were classified into the correct land cover class by the M⊕P algorithm. In this section, both correct and incorrect land cover pixels are evaluated to gain an indication of how classification error contributes to biophysical estimation error. This propagation of error results from the fact that whatever land cover class a pixel is assigned to, the trajectory associated with that class is used in the biophysical parameter estimation process. If a pixel is misclassified, then the component fractions and tree density estimates would be obtained from the wrong trajectory. As it has been shown that land cover stratification is important to successful biophysical parameter estimation, it would seem to follow that incorrect land cover information would have a negative effect. This would be evidenced by decreases in the strength of relationships between the trajectory outputs and the biophysical parameters when such misclassification errors are included.

Table 6.17 contains the results of predicting biophysical parameters using the full set of site pixels classified by the M⊕P software as being in one of the four mature dominant classes (OBS, OJP, MIX, OA). As shown in Table 6.11, there was some

| Biophy. Parameter | Land Cover Class | M⊕P Trajectory Output | | | |
|---|---|---|---|---|---|
| | | Td | C | B | S |
| **BIOMASS** | OBS | .07 | .06 | .21 | **.66** |
| | OJP | .59 | .58 | .40 | **.61** |
| | MIX | **.36** | .27 | .19 | .24 |
| | OA | .39 | .42 | .04 | **.43** |
| **LAI** | OBS | .** | .09 | .08 | **.44** |
| | OJP | .17 | .16 | **.58** | .21 |
| | MIX | **.43** | .34 | .22 | .31 |
| | OA | .47 | .53 | .** | **.54** |
| **DBH** | OBS | .08 | .09 | .20 | **.42** |
| | OJP | **.61** | **.61** | .47 | **.61** |
| | MIX | **.29** | .20 | .16 | .18 |
| | OA | .30 | .35 | .** | **.36** |
| **HEIGHT** | OBS | .05 | .06 | .16 | **.37** |
| | OJP | **.80** | **.80** | .65 | .79 |
| | MIX | .** | .** | **.03** | .** |
| | OA | .25 | **.36** | .** | **.36** |

Table 6.17. Predicting biophysical parameters with land cover stratification, including errors of misclassification. Linear regression $r^2$ values among the biophysical parameters biomass, LAI, DBH, tree height and the trajectory outputs of tree density (Td), and component fractions (C, B, S). Best results within each land cover class for each parameter shown in bold. Results not significant at $\alpha = 0.05$ shown as **.

misclassification of site pixels, and these cases were included in this regression analysis together with the correctly classified pixels. In terms of the accuracy of land cover classification information used to stratify the regression analysis, OBS had an accuracy of 89%, OJP 79%, MIX 53% and OA 89%. This provides a useful range to explore how different levels of stratification accuracy affect biophysical parameter estimation. This is achieved by evaluating the magnitude of change in the strength of biophysical predictive relationships for individual classes obtained from the correctly classified sample of trajectory outputs, and the sample which also included misclassification. However, since each class sample is different, comparisons among classes are made with some caution. Accordingly, the focus of the evaluation is on the degree of change as a function of the level of error, with less emphasis placed on comparing actual $r^2$ values. Further, as shadow fraction has been shown in the previous section to be best suited for biophysical estimation, this component will form the basis for the comparison. All components are considered in a direct comparison of overall results, presented later in this section.

The first observation of interest from the set of results is that the strength of the relationships between the trajectory outputs and the biophysical parameters is not as strong when misclassified pixels are included. Using shadow fraction as a predictor for biomass, $r^2$ values decrease between 0.03 to 0.09 in magnitude for OBS, OJP and OA. This decrease is relatively small, and corresponds to the high overall land cover classification accuracies produced by the M⊕P classifier for these classes. The MIX class, however, had a decrease in $r^2$ of 0.26 when misclassification errors were included. This was because there were more classification errors with this class (land cover accuracy for MIX = 53%). This class also had the lowest overall $r^2$ values of any of the classes, both for the correctly classified sample as well as the sample containing misclassified pixels. This is consistent

with the lower land cover classification accuracies for MIX, further supporting both the complexities and increased difficulties in defining and discriminating this class. For LAI, similar results were found as with biomass, although there appeared to be a greater sensitivity to misclassification in terms of biophysical parameter estimation for the OBS and OJP classes. The OA class, with the highest classification accuracy of the four classes considered, had a decrease in $r^2$ of only 0.01. OBS and OJP, however, decreased by 0.30 and 0.53, respectively. For OJP, this larger change was possibly due to the fact that when misclassification is included, the sunlit background fraction had a stronger relationship with LAI than shadow fraction. For that component, the reduction in $r^2$ was only 0.03, which is more consistent with the fact that the level of misclassification is not large (79% accuracy for OJP). These reductions in $r^2$ could also be explained by the nature of errors of commission with these classes. A large degree of the misclassification in these classes occurs between OBS and OJP, suggesting that the trajectories applied erroneously in generating the M⊕P output for those cases of misclassification created significant outliers in the analysis which resulted in the reduction in the strength of the relationships with LAI.

For DBH and tree height, again, the level of misclassification controls the strength of the relationship for predicting the biophysical parameters. For DBH, shadow fraction $r^2$ values decrease by only 0.04 for the three classes with highest classification accuracies (OA, OBS, OJP), whereas with MIX, the $r^2$ value decreased by 0.32 when misclassified pixels were included from the overall land cover class accuracy result of 53%. The same was true for tree height. The $r^2$ values remained the same for OA, and decreased by 0.01, and 0.03 with shadow fraction predictions in the OBS and OJP classes, respectively, whereas the MIX $r^2$ value went from $r^2$=0.51 to being not significant. These results suggest the need to perform *a priori* land cover classification, and that when good levels

of classification accuracy are obtained, reasonable estimates of biophysical parameters are possible.

The overall magnitude of error found in estimating biophysical parameters has been summarised in Table 6.18. In this table, the results for each biophysical parameter have been averaged over the four classes for both the correct land cover classification sample, and the ones with errors of land cover misclassification (listed in brackets in the table). The standard errors (S.E.) of the estimate are also reported to gain additional insight into the degree of error associated with estimating each parameter. For all four biophysical parameters, the shadow fraction had the best overall results of the trajectory outputs (shown in bold in the table). For biomass, an overall $r^2 = 0.60$ was obtained with an S.E. of 2.39, compared to 0.49 and 2.98 when misclassified pixels were included. These results are good, with the capability to estimate biomass within 2.39 kgC/m representing a positive result given an appropriate land cover classification. For LAI, the best overall averaged result was obtained from shadow fraction, with a $r^2 = 0.63$ and S.E. = 0.76 $m^2/m^2$. However, there was a greater discrepancy between shadow fraction averaged results from all four classes when misclassified pixels were included compared to when they were not ($r^2$ =0.38, S.E.=1.27 $m^2/m^2$). As explained above, this discrepancy is more a function of the fact that tree density and sunlit background fraction showed a stronger relationship with LAI than shadow fraction for the mixed forest and OJP classes. It is interesting that the tree density trajectory position was optimal for predicting LAI in both the correct classification and the one which included misclassification. This could suggest that, due to the greater natural variability within this class, the stand density as depicted by the trajectory position provides a better estimate for LAI compared to any of the component fractions. This is likely due to the weighted averaging method used to construct the mixed forest trajectory as

| | Td | | C | | B | | S | |
|---|---|---|---|---|---|---|---|---|
| | $r^2$ | S.E. | $r^2$ | S.E. | $r^2$ | S.E. | $r^2$ | S.E. |
| **BIO** | .50 | 2.87 | .48 | 2.99 | .28 | 5.12 | **.60** | **2.39** |
| | (.35 | 4.20) | (.34 | 4.22) | (.21 | 6.84) | (.49 | 2.98) |
| **LAI** | .51 | 0.94 | .49 | 0.98 | .29 | 1.66 | **.63** | **0.76** |
| | (.27 | 1.69) | (.28 | 1.68) | (.23 | 2.09) | (.38 | 1.27) |
| **DBH** | .42 | 5.27 | .41 | 5.35 | .22 | 6.35 | **.49** | **5.15** |
| | (.32 | 6.08) | (.32 | 6.09) | (.21 | 6.74) | (.39 | 5.89) |
| **HGT** | .45 | 2.99 | .44 | 2.90 | .26 | 3.46 | **.52** | **2.79** |
| | (.28 | 4.01) | (.31 | 3.89) | (.21 | 4.43) | (.38 | 3.76) |

Table 6.18. Summary of average results for each biophysical parameter (biomass, LAI, DBH, tree height). Linear regression $r^2$ values and standard errors (S.E.) of predictions from trajectory outputs (tree density, component fractions of C,B,S) averaged from the four mature dominant land cover classes. Results including misclassification shown in brackets, best results for each parameter shown in bold. A level of significance of $\alpha = 0.05$ was used for all regressions shown.

a function of the OBS, OJP and OA trajectories. In that process, the trajectory fractions are averaged from each class at each trajectory position, and each position is defined by tree density. Therefore, tree density is invariant among each class, and so in the merging of the individual class trajectories, the tree density parameter is not changed, however, the

fractions are modified as per equation 5.4. For LAI, it is also interesting to note that, despite the fact that only two of the four individual class $r^2$ values were best for shadow fraction with misclassification, the overall shadow fraction average $r^2$ and S.E. values were still best, and by a considerable margin. This lends further support to the overall recommendation towards using shadow fraction for estimating this biophysical parameter.

For DBH and tree height, similar trends to biomass and LAI were also found. The overall average from shadow fraction from the four classes for DBH had a $r^2 = 0.49$ and S.E. of 5.15 cm, whereas with misclassified pixels included, the results decreased somewhat to $r^2 = 0.39$ and S.E. = 5.89 cm. Similar levels were found with tree height, with values ranging from $r^2 = 0.52$, S.E. = 2.79m with correct land cover information, which decreased to $r^2 = 0.38$, S.E. = 3.76m with misclassified pixels. Although with both DBH and tree height the $r^2$ values were not as high as with biomass and LAI, they do indicate an ability to predict these more complex biophysical parameters. This suggests potential for this technique to predict complex forest structural variables based on the ability to provide forest component fractions at sub-pixel scales when stratified by land cover class.

#### 6.3.3.4 Comparison with Vegetation Index Results

Having established the importance of land cover stratification in estimating biophysical parameters, it is desirable to apply this stratification to the computation of vegetation indices and compare their performance to those obtained from the trajectory outputs in terms of predicting biophysical parameters. Accordingly, band ratio estimates of

| Trajectory Outputs vs. NDVI | | | | |
|---|---|---|---|---|
| **Biophy. Parameter** | **Land Class** | **Best Indiv. Trajectory** | **Shadow Fraction** | **NDVI** |
| **BIOMASS** | OBS | .69 | .69 | .12 |
| | OJP | .72 | .70 | .54 |
| | MIX | .68 | .50 | .** |
| | OA | .51 | .51 | .** |
| | **AVG:** | **.65** | **.60** | **.17** |
| **LAI** | OBS | .74 | .74 | .07 |
| | OJP | .74 | .74 | .54 |
| | MIX | .67 | .50 | .** |
| | OA | .55 | .55 | .** |
| | **AVG:** | **.68** | **.63** | **.16** |
| **DBH** | OBS | .42 | .42 | .14 |
| | OJP | .65 | .65 | .45 |
| | MIX | .66 | .50 | .** |
| | OA | .38 | .38 | .14 |
| | **AVG:** | **.53** | **.49** | **.19** |
| **HEIGHT** | OBS | .38 | .38 | .20 |
| | OJP | .83 | .82 | .61 |
| | MIX | .68 | .51 | .10 |
| | OA | .36 | .36 | .08 |
| | **AVG:** | **.56** | **.52** | **.25** |

Table 6.19. Linear regression of NDVI values stratified by land cover class with the four biophysical parameters. Results from shadow fraction also shown, together with the best overall trajectory outputs per class. For each biophysical parameter, overall average values are summarised (shown in bold). Results not significant at $\alpha = 0.05$ shown as **.

NDVI were computed and input to the linear regression analysis for each correct land cover class defined by the M⊕P evidential reasoning classifier. The full set of NDVI results by class for all four biophysical parameters is shown in Table 6.19, together with a summary of the results obtained from the shadow fraction trajectory values. Also shown in the table is the best individual result obtained from the trajectory output for each class. This table serves two purposes. First, it allows a detailed comparison of NDVI results with the trajectory component of choice. As shown in the previous sections, shadow fraction is the overall component of choice since it provided the strongest predictive relationships for the biophysical parameters compared to the other components and tree density. However, as has been noted, it does not, in all cases provide the best result (e.g. the mixed forest class). Secondly, this analysis provides insight into the highest overall results possible if one could selectively choose specific components in different situations such that the strongest predictive relationship could be made available to a given pixel being analysed. These best results are shown in the table, together with overall averages computed for each biophysical variable. Nonetheless, unless it was possible to preferentially select certain components in certain situations, one must normally choose one of the trajectory outputs for regional scale use. Therefore, the NDVI results are intended to be compared only with those obtained from shadow fraction.

Overall, the NDVI had lower $r^2$ values than the shadow fraction trajectory outputs. For biomass, a difference of $r^2 = 0.43$ was found (shadow fraction, S: $r^2 = 0.60$; NDVI $r^2 = 0.17$). Individual results by class were also rather low for NDVI, with the exception of OJP which had a $r^2 = 0.54$ compared to a $r^2 = 0.70$ for shadow fraction. NDVI in the mixed forest and OA classes had no relationship to biomass. For LAI, the same patterns held for all classes as well as the overall case. The difference of averages was

$r^2 = 0.47$ (S: $r^2 = 0.63$; NDVI $r^2 = 0.16$), with low $r^2$ values found for OBS, MIX and OA. For DBH and tree height, the overall level of $r^2$ values for NDVI was consistent, and somewhat stronger, at $r^2 = 0.19$ for DBH and 0.25 for tree height. However, these values were lower compared to the shadow fraction results, which had $r^2$ values of 0.49 and 0.52 for DBH and tree height, respectively. Individual class results followed the same trends as with biomass and LAI. Although the NDVI results improved when stratified by land cover class (compare NDVI results here to those found in Table 6.13), the overall predictive ability of NDVI is weak, even when land cover stratification was applied. The physical basis for the poor performance of NDVI is that it does not account explicitly for background or shadows which make significant contributions to the overall pixel level reflectance, nor does it make explicit adjustments for changes in canopy geometry, stand density, or sun-sensor orientation.

In terms of the best possible results obtained from the trajectory outputs, two important observations are made. Firstly, the overall strengths of the best relationships between trajectory components and biophysical parameters was found to be quite good, particularly given the large number of land cover classes considered, and that this set of classes included a variety of regeneration classes in the initial stratification as well as a mixed forest class. On average, $r^2$ values between 0.65 and 0.70 were found for biomass and LAI, with average values approximately 0.55 for DBH and tree height. Given that these results were obtained using Landsat TM image data, considerably better results might be expected from sensors with higher spatial and spectral resolutions. Secondly, differences were small between the best overall results and those obtained exclusively from shadow fraction. Overall, the shadow fraction results were only $r^2 = 0.05$ less than the best results obtained selectively from all trajectory outputs. This is significant since

normally the analyst would have to choose one trajectory output variable for biophysical estimation. If the best results varied greatly among trajectory components in terms of class values and biophysical parameters, it would be difficult to recommend one trajectory output for use. However, the shadow fraction has been repeatedly shown in this research to be best suited for the task of biophysical parameter estimation.

## 6.4 CHAPTER SUMMARY

In this Chapter, the regional scale methodology implemented in the M⊕P software package has been evaluated in terms of land cover classification and biophysical parameter estimation. It was shown that the M⊕P trajectory mode provided higher classification accuracies than the training mode, while also providing additional information at sub-pixel scales for use in estimating biophysical parameters. A two pass sequential weighting method devised for hybrid mode processing was used to classify the full set of forest cover classes with greater accuracy than the full training mode. Trajectory outputs within land cover class stratifications were used to predict four biophysical parameters. Good results were obtained for biomass and LAI, with a potential shown for predicting tree height and DBH values. Land cover stratification was shown to be essential for biophysical analysis, with misclassification errors serving to reduce the overall predictive ability in terms of biophysical parameters. In all cases, the method implemented here was shown to provide significant improvements over results obtained using vegetation index methods. In the final Chapter, presented next, major conclusions are drawn from this thesis research, together with prospects for future research.

# CHAPTER VII

# CONCLUSIONS

## 7.1 SUMMARY

Understanding the cycling of carbon between the atmosphere and biosphere is of great scientific and cultural significance as a result of the potential risks to the Earth's environment associated with increased concentrations of atmospheric carbon dioxide and other greenhouse gases from natural and anthropogenic sources, which together are contributing to change in the physical climate system and possible global warming (Mitchell, 1989). This is of particular importance in the North American boreal forest, which is one of the largest biomes on Earth and a major storehouse of organic carbon within the global carbon cycle (Bonan, 1991a,b). Moreover, this biome occupies vast tracts of land in the high latitude (45°-65°N) continental interior where a number of climate models suggest the greatest warming will occur from increased levels of $CO_2$ (Pastor and Post, 1988), with the potential for profound long-term economic and ecological impacts on agricultural zones as well as boreal forest and Arctic Tundra ecosystems caused by shifts in major vegetation boundaries (Gates, 1990) driven by feedback mechanisms in the physical climate system.

Within these forests, photosynthesis is the key process in which carbon is sequestered from the atmosphere and accumulated over lengthy growth cycles as standing biomass and in root systems. Regional scale models of terrestrial carbon flux, ecosystem processes, biosphere-atmosphere interactions and photosynthetic activity within boreal forests all require biophysical structural parameters (Sellers and Schimel, 1993). Remote sensing imagery provides the only appropriate synoptic scale information for determining these variables such as leaf area index (LAI), net primary productivity (NPP) and biomass over vast forested areas for assessing and quantifying ecosystem evolution and change. However, traditional remote sensing processing techniques such as vegetation indices (e.g. NDVI) have been shown in this research, both theoretically and empirically, to be unreliable for extracting this information for vegetated canopies, primarily because of the large influence of background soil and forest floor effects which confound the spectral signal of vegetation, as well as the variability in canopy cover, geometry, and leaf optical properties at sub-pixel scales (Sellers, 1985; Curran and Williamson, 1987; Guyot *et al.*, 1989; Spanner *et al.*, 1990; Lathrop and Pierce, 1991).

To address this problem, this research has investigated a different approach to proving biophysical estimates from remote sensing data. The approach is based on the derivation of areal fractions of forest components at sub-pixel scales using spectral mixture analysis. The forest scene components of sunlit canopy, sunlit background and shadow fraction have been shown to be useful for providing improved predictions of biophysical parameters compared to conventional methods. These component fractions were derived and tested in two separate study areas at different scales. The first study was conducted at the scale of forest stands using a data set from the NASA COVER Project at the Superior National Forest, Minnesota USA, located near the southern fringe of the North American

boreal forest. Spectral mixture analysis was used to derive component fractions from helicopter MMR radiometer data for 31 stands of black spruce along a gradient of stand densities. Three geometric-optical reflectance models were compared for estimating sunlit canopy component reflectance for input to the analysis together with field measures of background and shadow reflectance. Cylinder, cone and spheroid models of canopy geometry were evaluated as was the importance of solar zenith angle variations in reflectance estimates. Component fractions were evaluated against ground data derived from dense-grid point analyses of coincident high resolution colour photography. In general, the spheroid model of canopy geometry was better than the cone and cylinder models, and the importance of correcting for solar zenith angle (SZA) was illustrated with significant improvements noted for higher SZA as a result of corrections for canopy mutual shadowing. The best overall results were obtained from the shadow fraction using a spheroid model of canopy geometry at SZA 45°. Linear regression analyses showed biomass could be estimated with $r^2$ values of 0.83 and a standard error (S.E.) of 1.7 $kg/m^2$; LAI: $r^2$=0.82, S.E.=0.46; and NPP: $r^2$=0.86, S.E.=0.05 $kg/m^2$/year. These results were a considerable improvement from those obtained using NDVI, for which overall $r^2$ results ranged from 0.40 to 0.47 for all three biophysical parameters.

The successful results from the first analysis provided motivation to explore the application of these techniques to regional scales. That work was performed as part of the Boreal Ecosystem Atmosphere Study (BOREAS), a large international global change research project with sites in Saskatchewan and Manitoba. This research used Landsat Thematic Mapper imagery obtained 2 September 1994 over the BOREAS Southern Study Area. At the regional scale, it was shown that the biophysical analysis needs to be stratified by land cover in order to provide reasonable predictive estimates of these parameters. An

integrated land cover classification and biophysical parameter estimation process was implemented in software to achieve this goal. The approach used a geometric optical reflectance model to produce spectral trajectories of each major forest land cover class instead of the more traditional training area approach. These models allowed an explicit, physical description of forest canopies and trees to be incorporated into the process, as well as the specification of solar angles, viewing positions, topography and other environmental factors. Each trajectory is computed over a full range of tree densities. Associated with each point on the trajectory is a set of pixel level reflectance values together with a set of component fractions (sunlit background, canopy, and shadow), all of which are derived from the geometric-optical reflectance model. Using this physically based method, large training data sets are not required, and further, it is possible to model highly non-linear multispectral distributions of individual forest classes which conventional statistical algorithms are not suited to process. In creating these spectral trajectories, a field spectrometer data collection mission was completed at both BOREAS sites in Saskatchewan and Manitoba during the 1994 late summer Intensive Field Campaign. A new software system was written to provide an automated computing environment for processing field data into surface reflectance end-member values. The end-member spectra, together with forest canopy dimension information, formed the input to the reflectance model for deriving the spectral trajectories. These trajectories formed the input to an evidential reasoning software system, which was upgraded from a supervised training area based land cover classifier to now include two additional options for physically based analysis of trajectories, which includes a hybrid trajectory training mode. Each mode was tested and compared. It was found that higher classification accuracies were obtained using the spectral trajectories compared to training data for the four major forest classes (Old Black Spruce, Old Jack Pine, Old Aspen, mixed forest). This was likely due to the

improved and unbiased characterisation of the full range of stand densities for a class from the trajectory method, as well as the ability to account for forest components and understorey reflectance in the overall signal. A full classification of 12 different forest classes was completed, with the highest accuracy obtained from the hybrid mode with inputs from spectral trajectories for the major forest classes, with training data used for classes for which trajectories were not available. For the mature forest classes, an extensive set of tests for predicting biophysical parameters was performed. Linear regression analyses showed biomass could be estimated with overall $r^2$ values of 0.60 and a standard error (S.E.) of 2.4 kg/m$^2$; and LAI: $r^2$=0.64, S.E.=0.76, compared to NDVI results of $r^2$ = 0.17 and 0.16 for biomass and LAI, respectively. Potential was also shown for predicting tree height and diameter at breast height parameters which, from a remote sensing standpoint, are considerably more difficult to estimate. Major conclusions resulting from these experiments are presented in the following sections.

## 7.2 CONCLUSIONS

A number of major conclusions have been drawn from this thesis research:

- Sub-pixel scale forest component fractions such as sunlit canopy, background, and shadow derived by spectral mixture analysis provided improved predictions of biophysical parameters compared to pixel level reflectance values analysed by vegetation indices.

- Shadow fraction was shown to provide better biophysical predictions than the other forest components. It is important to specify or correct for solar zenith angle variations when deriving these fractions for use in biophysical analyses.

- Geometric optical reflectance models provide important physical descriptions of forest canopies that are useful for modelling end-member reflectance values and for generating spectral trajectories for input to classification and biophysical estimation algorithms. The spheroid based geometric optical reflectance model was shown to be better than cylindrical or conical models of canopy geometry.

- An integrated physically based approach provided a more appropriate framework for land cover classification and biophysical parameter estimation compared to conventional statistical classification methods and vegetation indices. In this research, a modern multi-source evidential reasoning classifier was coupled with physically based model inputs from which both land cover classes and biophysical information was derived.

- Using advanced remote sensing image processing algorithms and models it is possible to provide accurate land cover stratification and good estimates of biophysical parameters such as biomass, leaf area index and net primary productivity.

## 7.3 CONTRIBUTIONS TO RESEARCH

Contributions to the research community from this work are in the areas of methodological advances, software products, environmental applications, as well as data contributions to BOREAS science. These are discussed in turn below.

- Methodological advances

1. The use of spectral mixture analysis has been validated and refined for biophysical parameter estimation in forest stands. Improvements in the areas of optical modelling, solar zenith angle correction, and scene fraction validation have been provided.

2. At the regional scale, a physically based methodology has been implemented which combines optical reflectance models, image classifiers, and the concepts of spectral mixture analysis to provide an integrated method for land cover classification and biophysical parameter estimation.

- Software products

1. A computer macro program has been written for automated processing of field spectrometer data into reflectance values (SPECTRA.XLM, Appendix A).

2. A program was created which provides a direct interface to the geometric optical reflectance model for the purpose of generating spectral trajectories. (BAT_GOMS.C, Appendix B)

3. A significant upgrade to an evidential reasoning software system (MERCURY⊕) has been implemented in software. In addition to the supervised training mode, the new M⊕P software now provides options for full trajectory mode processing as well as a hybrid trajectory-training mode. The full training mode has been shown in other studies to provide improved accuracies for classifying multi-source data sets compared to maximum likelihood, linear discriminant analysis and neural network algorithms, with the new upgraded M⊕P version run in trajectory mode providing the highest accuracies compared to full training mode results in BOREAS (M⊕P code is listed in Appendix C).

- Environmental applications:

1. An improved method for determining land cover and estimating biophysical parameters has been developed. These could be of interest to other scientists who require these parameters for input to ecosystem or carbon models. These methods could also be of interest to forest scientists and managers who require these data

over larger areas. The longer term goal for these efforts is that they might contribute to a better understanding of global change processes over vast tracts of land in the boreal forest, and possibly elsewhere.

- Contributions to BOREAS:

The BOREAS information system (BORIS) contains the full archive of field and remotely sensed data collected by BOREAS investigators. These data are quality checked and are currently available to all BOREAS scientists on the World Wide Web. Access to the general scientific community will be provided after a nominal post experiment period, providing a significant and complete data set to the international scientific and global change research communities. Contributions to BORIS from this research include:

1. Field spectrometer data collected during the BOREAS 1994 FFC-T and IFC-3 field campaigns at both the SSA and NSA study areas have been processed to reflectance and delivered to the RSS-19 central data archive and BORIS.

2. Results from the BOREAS SSA land cover classification and biophysical parameter estimation work completed here will be evaluated for submission to BORIS.

## 7.4 FUTURE RESEARCH

A variety of areas for future research have been identified. These include follow on work using the Superior National Forest and BOREAS data sets, as well as applications to other environments. These are discussed in sequence.

As part of the BOREAS project, a large and comprehensive remote sensing data set from a wide array of airborne and satellite platforms has been assembled. Many options exist for applying the algorithms developed here to other image products such as airborne CASI, AVIRIS, ASAS and MAS as well as satellite SPOT and AVHRR. As the author is a member of BOREAS remote sensing science project RSS-19, the CASI image products collected within this project are of immediate interest. This data set alone offers a wide selection of band sets, resolutions and bi-directional imagery (Miller *et al.*, 1995). The spectral mixture and optical modeling methods implemented here could be applied to these data, and possibly linked to spatial analysis methods such as texture measures which have been useful in studies with CASI elsewhere (e.g. Franklin and McDermid, 1993; Franklin, 1994; Wulder *et al.*, 1996ab; see also the review of texture in Jensen, 1996 p.187-192). For the regional scale, it would be of interest to explore improved radiative transfer models and further develop the integrated physically based classification and biophysical algorithms developed here. It would also be useful to explore new ways of deriving biophysical estimates in a more direct fashion, instead of the regression analysis approach used in this work. A good approach would be to attempt to describe the physical relationships that exist between shadow fractions and biophysical parameters, using an empirical approach to test and refine theoretical hypotheses. The BOREAS project also contains a large multi-temporal data set with acquisitions ranging from winter through late

summer, including a near continuous characterisation of the growing season. It would be particularly interesting to apply the algorithms developed here to the winter time or winter-spring thaw periods (FFC-W, FFC-T) to evaluate the ability to extract forest parameters during these times. The advantage here would be the more homogeneous snow cover understorey, however, the significantly higher solar zenith angles would need to be characterised properly. The mutual shadowing geometric optical reflectance model (Li and Strahler, 1992) used in this research would be well suited for these higher SZA. Field spectrometer data collected by the author during FFC-T could be used in such analysis. The NASA COVER data set from Superior National Forest is also of interest for additional research. These data were acquired over a decade ago and therefore provide an excellent basis for multi-temporal analysis. Further, given the location of the study site near the extreme southern fringe of the boreal forest, this area may be particularly sensitive to global change (Hall *et al.*, 1992).

The methods developed here could also have applications to other forested areas as well as other environments. Of immediate interest here is the application of these methods to the Brazilian Amazon as part of the International Geosphere-Biosphere Programme (IGBP) LBA project (IGBP, 1994), for which the author is a collaborating scientist with NASA GSFC and the Brazilian Space Agency. That work will involve the remote estimation of biophysical properties in the tropical rainforest. Another line of research evolving from this thesis work is to apply methods developed here to high relief, mountainous terrain. This would involve extensive use of digital elevation models and also the modification of the geometric optical reflectance model inputs to incorporate topographic slope and aspect. The author has previous experience with land cover classification in mountainous terrain. For example, the original MERCURY⊕ software

package was developed for alpine land cover classification and permafrost remote sensing experiments (Peddle, 1993, 1995a,b; Peddle and Franklin, 1993), and has since been applied in several studies in the Colorado Rockies (Peddle and Duguay, 1995, 1996; Duguay and Peddle, 1996). Extending the BOREAS biophysical research into a mountainous setting therefore represents an area of immediate interest towards providing a more comprehensive regional scale analysis of forested areas in Canada.

The concepts of spectral mixture analysis have also been shown to be useful in studies of marine environments at several tropical and polar ocean based sites in collaboration with researchers at the University of Waterloo. One line of work involves the analysis of tropical coral reefs in which mixture fractions computed for coral and water targets have been used to adjust coral fractions for the optical attenuation of water, with the longer term goal to assess environmental degradation resulting from coral bleaching (LeDrew *et al.*, 1995b). An initial study completed in Fiji has shown positive results using this technique at individual sites and over larger areas (Peddle *et al.*, 1995a, 1996a). It may be possible to apply new capabilities of the M⊕P algorithm for merging scene stratification with mixture fraction output towards a more regional scale coral reef inventory analysis. A second marine application involves the analysis of multi-temporal Arctic sea ice concentrations. In that work, the idea of spectral mixture analysis has been recast into the time domain to create a time series analysis approach which we have called "Temporal Mixture Analysis" (Piwowar *et al.*, 1996a,b). Beyond this, the intuitive appeal of sub-pixel scale analysis linked to regional scale applications results in the possibility of applying these methods to a variety of other environments.

Clearly, many opportunities for future work have evolved from this thesis research. Of immediate interest is continued work within the forestry context. As described above, the thrust of the next phase of work will involve new dimensions and analysis within the BOREAS project, as well as the development of new approaches for obtaining biophysical estimates in other environments such as mountainous study areas established in the Rocky Mountains of southern Alberta and Colorado, and the tropical rain forest of Brazil. The contribution of the present work sets the context for future research. In this work, the goal has been to implement new approaches to the estimation of biophysical parameters which are important in studies of the carbon cycle and global change. The continued increase in data quality and availability provided through projects such as BOREAS and LBA, together with the approaching launch of the EOS system and other advances in airborne and satellite remote sensing systems create the possibility for new opportunities to further refine these approaches, consider smaller spatial scales (e.g. larger regional areas, continental scales), and transfer these techniques to other environments. These next steps will be important as a contribution towards providing improved land-surface parameterisations as one component within complex numerical models of environmental processes and change. The underlying motivation is to contribute to efforts by the scientific community to provide quality information to society and policy makers regarding the current and future state of the environment.

## REFERENCES

Adams, J.B. and Adams, J.D. 1984. Geologic mapping using Landsat MSS and TM images: Removing vegetation by modeling spectral mixtures. Proceedings of the 3rd Thematic Conference on Remote Sensing for experimental Geology, Colorado Springs, Colorado, (Michigan: ERIM). 615-622.

Adams, J.B., Smith, M.O. and A.R. Gillespie, 1989. Simple models for complex natural surfaces: a strategy for the hyperspectral era of remote sensing. Proceedings of the International Geoscience and Remote Sensing Symposium (IGARSS'89)/12th Canadian Symposium on Remote Sensing. 1:6-21.

Adams, J.B., Smith, M.O. and A.R. Gillespie, 1993. Imaging spectroscopy: interpretation based on spectral mixture analysis. *In* Topics in Remote Sensing 4 Remote Geochemical analysis: Elemental and Mineralogical Composition, p. 145-166. Pieters and Englert (eds.). Cambridge.

Adams, J.B., Smith, M.O. and Johnson, P. 1986. Spectral mixture modeling, a new analysis of rock and soil types at the Viking Lander 1 site. *Journal of Geophysical Research* 91, B8:8098-8112.

Ahern, F.J., J. Sirois, W.D. McColl, R.P. Gauthier, T.T. Alfoldi, W.H. Patterson and T.A. Erdle, 1991. Progress toward improving aerial defoliation survey methods by using electronic imagers. *Photogrammetric Engineering & Remote Sensing*, 57(2):187-193.

Ahern, F.J., D.J. Leckie and J.A. Drieman, 1993. Seasonal changes in relative C-band backscatter of northern forest cover types. *IEEE Transactions on Geoscience and Remote Sensing*, 31(3):668-680.

Ahern, F.J., R.Landry, J.S.Paterson, D.Boucher and I.McKirdy, 1995. Forest landcover information content of multi-frequency multi-polarized SAR data of a boreal forest. In, *Proceedings, 17th Canadian Symposium on Remote Sensing*, Saskatoon, SK, Canada. Vol II, p.537-549.

Ahern, F.J., I.McKirdy and J. Brown, 1996. Boreal forest information content of multi-season, multipolarization C-band SAR data. *Canadian Journal of Remote Sensing.* 22(4): 456-472.

Anger, C.D., S. Mah, and S. Babey, 1994. Technological enhancements to the compact airborne spectrographic imager (casi). In: *Proceedings of the First International Conference on Airborne Remote Sensing*, Strasbourg, France. Vol II, p. 205-213.

Apps, M.J., 1993. NBIOME: A biome-level study of biospheric response and feedback to potential climate changes. *World Res. Rev.* 5(1):41-65.

Apps, M.J., W.A.Kurz, R.J.Luxmoore, I.O.Nilsson, R.A.Sedjo,R.Schmidt, I.G. Simpson, and T.S.Vinson, 1993. The changing role of circumpolar boreal forests and tundra in the global C cycle. *Water, Air and Soil Pollution.* 70:39-53.

Apps, M.J., D.T.Price and J. Wisniewski (eds), 1995. Boreal forests and global change. Kluwer Academic Publishers, Dordrecht. 548 p.

Arai, K. and Terayama, Y. 1992. Label relaxation using a linear mixture model. *International Journal of Remote Sensing*, 13(16):3217-3227.

Arrhenius, S., 1896. On the influence of carbonic acid in the air on the temperature of the ground. *Philosphical Magazine*, 41:237-276.

ASD, 1993. Analytical Spectral Devices Inc. Personal Spectrometer II - Reference Manual. ASD Inc., Boulder, Colorado. Variously paged.

Asrar, G. and J. Dozier, 1994. EOS: NASA Science Strategy for the Earth Observing System. Office of the Mission to Planet Earth. AIP Press, Woodbury NY. 119.

Asrar, G., 1990. Mission to planet Earth: a global change programme. i-v. *In* Remote Sensing and Global Change. Proceedings of the 16th Annual Conference of the Remote Sensing Society. Coulson, M.G. (ed.). University of Nottingham, Nottingham, England. 488.

Babey, S.K. and C.D. Anger, 1989. A Compact Airborne Spectrographic Imager (CASI). Proceedings of the International Geoscience and Remote Sensing Symposium IGARSS'89 / 12th Canadian Symposium on Remote Sensing. 4:1028-1031.

Band, L.E., P. Patterson, R.R. Nemani and S.W. Running, 1991a. Forest ecosystem processes at the watershed scale: incorporating hillslope hydrology. *Agricultural Forest Meteorology* 63:93-126.

Band, L.E., D.L. Peterson, S.W. Running, J.C. Coughlan, R. Lammers, J. Dungan, and R.R. Nemani, 1991b. Forest ecosystem processes at the watershed scale: basis for distributed simulation. *Ecological Modelling* 56:171-196.

Baret, F. and G. Guyot, 1991. Potentials and limits of vegetation indices for LAI and APAR assessment. *Remote Sensing of Environment*, 35:161-173.

Barker Schaaf, C. and A.H. Strahler, 1993. Solar zenith angle effects on forest canopy hemispherical reflectances calculated with a geometric-optical bidirectional reflectance model. *IEEE Transactions on Geoscience and Remote Sensing*, 31(4):921-927.

Birnie, R.V. 1986. Pixel-mixing effects and their significance to identifying snow condition from Landsat MSS data. *International Journal of Remote Sensing*, 7(7):845-853.

Boardman, J.W., 1993. Automated spectral unmixing of AVIRIS data using convex geometry concepts. *In* Proceedings, Fourth Annual JPL Airborne Geoscience Workshop, October 25-29, 1993. R.O. Green (ed.). NASA, Pasadena, California. p. 11-14.

Bolin, B, 1981. Carbon Cycle Modelling. Proceedings and Book Chapters from a Workshop on the Global Carbon Cycle, La Jolla California USA. International Council of Scientific Unions (ICSU),Scientific Committee on Problems of the Environment -SCOPE 16. 390 p.

Bolin, B,. E. Degens, S. Kempe and P. Ketner, 1979. The Global Carbon Cycle. Proceedings and Book Chapters from a Workshop on the Global Carbon Cycle, Ratzeburg, Germany, 1977. International Council of Scientific Unions (ICSU), Scientific Committee on Problems of the Environment - SCOPE 13. 528 p.

Bolle, H.J., 1991. Land surface transformation processes. In, Report of the earth observation user consultation meeting, European Space Agency, Enschede, The Netherlands. Vol. SP-1143, p. 181-192.

Bonan, G.B., 1991a. Atmosphere-biosphere exchange of carbon dioxide in boreal forests. *Journal of Geophysical Research*, 96(D4):7301-7312.

Bonan, G.B., 1991b. Seasonal and annual carbon fluxes in a boreal forest landscape. *Journal of Geophysical Research*, 96(D9):17,329-17,338.

Bonan, G.B., Shugart, H.H. and D.L. Urban, 1990. The sensitivity of some high-latitude boreal forests to climatic parameters. *Climatic Change*, 16(1):9-29.

Bonham, C.D., 1989. Measurements for Terrestrial Vegetation. John Wiley & Sons, New York. 338 p.

BOREAS, 1994. Boreal Ecosystem Atmosphere Study Experiment Plan Version 3.0, May 1994. P.J. Sellers *et al.* (eds.), NASA Goddard Space Flight Center, Greenbelt, MD. 4 volumes, variously paged (orange covers).

Borel, C.C. and S.A.W. Gerstl, 1994. Nonlinear spectral mixing models for vegetative and soil surfaces. *Remote Sensing of Environment*, 47:403-416.

Caselton, W.F., and W. Luo, 1992, Decision making with imprecise probabilities - Dempster Shafer theory and application. *Water Resources Research*, 28(12): 3071-3083.

CGCP, 1989. Canadian Global Change Program, Report # 3: Contributions of Satellite Observations to the CGCP. Royal Society of Canada. Ottawa. 40 p.

Chappellaz, J. J.M. Barnola, D.Raynaud, Y.S.Korotkevich and C.Lorius, 1990. Ice core record of atmospheric methane over the past 160,000 years. *Nature* 345(6271):127-131.

Chen, J.M., and J. Cihlar, 1995. Quantifying the effect of canopy architecture on optical measurements of leaf area index using two gap size analysis methods, *IEEE Transactions on Geoscience and Remote Sensing*, 33(3): 777-787.

Chen, J.M., and J. Cihlar, 1996. Retrieving leaf area index of boreal conifer forests using Landsat TM images, *Remote Sensing of Environment*, 55:153-162.

Chen, J.M., 1996. Evaluation of vegetation indices and a modified simple ratio for boreal applications, *Canadian Journal of Remote Sensing*. 22(3): 229-242.

Chen, Z., Curran, P.J. and J.D. Hansom, 1992. Derivative reflectance spectroscopy to estimate suspended sediment concentration. *Remote Sensing of Environment*, 40(1):67-77.

Chikara, R.S. 1984. Effect of mixed (boundary) pixels on crop proportion estimation. *Remote Sensing of Environment*, 14:207-218.

Cibula, W.G. and M.O. Nyquist, 1987. Use of topographic and climatological models in a geographical data base to improve Landsat MSS classification for Olympic National Park. *Photogrammetric Engineering & Remote Sensing*, 53 (1):67-75.

Cihlar, J., L. St. Laurent and J.A. Dyer, 1991. Relation between the normalized difference vegetation index and ecological variables, *Remote Sensing of Environment*, 35:279-298.

Clark, R.N., G. Swayze, T. King, A. Gallagher, and W. Calvin, 1993. The U.S. Geological Survey Digital Spectral Reflectance Library, Version 1. *In*, Proceedings of the Fourth Annual JPL Airborne Geoscience Workshop, October 25-29, 1993. R.O. Green (ed.). NASA, Pasadena, California. p. 37-39

Cohen, W.B., 1991. Response of vegetation indices to changes in three measures of leaf water stress. *Photogrammetric Engineering & Remote Sensing*, 57(2):195-202.

Craig, M., 1990. Unsupervised unmixing of remotely sensed images. *In* Proceedings of the 5th Australasian Remote Sensing Conference, Perth, Australia. p. 324-330.

Craig, M., 1994. Minimum-volume transforms for remotely sensed data. *IEEE Transactions on Geoscience and Remote Sensing*, 32(3):542-552.

Crist, E.P. and R.C. Cicone, 1984. A physically-based transformation of Thematic Mapper data - the TM tasseled cap. *IEEE Transactions on Geoscience and Remote Sensing*, GE22(3):256-263.

Cross, A.M., J.J. Settle, N.A. Drake, and R.T. Paivinen, 1991. Sub-pixel measurement of tropical forest cover using AVHRR data. *International Journal of Remote Sensing* 12(5), p. 1119-1129.

Curran, P.J. and H.D. Williamson, 1987. GLAI estimation using measurements of red, near infrared, and middle infrared radiance. *Photogrammetric Engineering and Remote Sensing*, 53(2):181-186.

Curran, P.J. and J.L. Dungan, 1989. Estimation of signal-to-noise: a new procedure applied to AVIRIS data. *IEEE Transactions on Geoscience and Remote Sensing*, 27:620-628.

Curran, P.J., 1985. Principles of Remote Sensing. Longman, London. 282 p.

Curran, P.J., 1989. Remote sensing of foliar chemistry. *Remote Sensing of Environment*, 30:271-278.

Curran, P.J., Dungan, J.L., and H.L. Gholz, 1990. Exploring the relationship between reflectance red edge and chlorophyll content in slash pine. *Tree Physiology*, 7:33-48.

Curran, P.J., Dungan, J.L., Macler, B.H. and S.E. Plummer, 1991. The effect of a red leaf pigment on the relationship between red edge and chlorophyll concentration. *Remote Sensing of Environment*, 35:69-79.

D'Arrigo, R., Jacoby, G.C., and I.Y. Fung, 1987. Boreal forests and atmosphere-biosphere exchange of carbon dioxide. *Nature*, 329:321-323.

De Abreu, R.,1995. Personal Communication, Earth Observations Laboratory, University of Waterloo.

Dean, K.G., Kodama, Y. and G. Wendler, 1986. Comparison of leaf and canopy reflectance of subarctic forests. *Photogrammetric Engineering and Remote Sensing*, 52(6):809-811.

Deering, D.W. and P. Leone, 1986. A sphere-scanning radiometer for rapid directional measurements of sky and ground radiance. *Remote Sensing of Environment.* 19: 1-24.

Deering, D.W., Middleton, E.M. and T.F. Eck, 1994. Reflectance anisotropy for a spruce-hemlock forest canopy. *Remote Sensing of Environment*, 47:242-260.

Demetriades-Shah, T.H., Steven, M.D., and J.A. Clark, 1990. High resolution derivative spectra in remote sensing. *Remote Sensing of Environment*, 33:55-64.

Dempster, A.P., 1967, Upper and lower probabilities induced by a multi-valued mapping. *Annals of Mathematical Statistics*, 38:325-339.

Detchmendy, D.M. and W.H. Pace, 1972. A model for spectral signature variability for mixtures. *In* Remote Sensing of Earth Resources, Volume I, F. Shahrokhi (ed.), Tullahoma Tennessee, 596-620.

Dick, K. and J.R. Miller, 1991. Derivative Analysis Applied to High Resolution Optical Spectra of Freshwater Lakes. Proceedings of the 14th Canadian Symposium on Remote Sensing, Calgary, Alberta: 400-403.

Duffett-Smith, P., 1990. Practical Astronomy, Cambridge University Press.

Duguay, C.R. and E.F. LeDrew, 1991. Mapping surface albedo in the east slope of the Colorado Front Range, U.S.A., with Landsat Thematic Mapper. *Arctic and Alpine Research*, 23(2):213-223.

Duguay, C.R. and D.R. Peddle, 1996. Comparison of evidential reasoning and neural network approaches in a multi-source classification of alpine tundra vegetation. *Canadian Journal of Remote Sensing*. 22(4): 433-440.

Farish, D.J., 1986. Introduction to Biology: A Human Perspective. Jones and Bartlett Publishers, Inc., Boston. 574 p.

Farrand, W.H., Singer R.B. and E. Merenyi, 1994. Retrieval of apparent surface reflectance from AVIRIS data: a comparison of empirical line, radiative transfer, and spectral mixture methods. *Remote Sensing of Environment*, 47:311-321.

Fleming, M.D. and R.M. Hoffer, 1979. Machine Processing of Landsat MSS and DMA Topographic Data for Forest Cover Type Mapping. *Proceedings, Fifth Annual Symposium on Machine Processing of Remotely Sensed Data*, LARS, Purdue University, Indiana, USA. p. 377-390.

Foschi, P.G. 1993. Estimating land cover proportions within mixed pixels using a moving-window algorithm. ASPRS/ACSM conference 102-107.

Frank, T.D., 1988. Mapping dominant vegetation communities in the Colorado Rocky Mountain Front Range with Landsat thematic and digital terrain data. *Photogrammetric Engineering and Remote Sensing*, 54(12):1727-1734.

Franklin, J. and A.H. Strahler, 1988. Invertible canopy reflectance modeling of vegetation structure in semiarid woodland. *IEEE Transactions on Geoscience and Remote Sensing*, 26(6):809-825 (plus erratum).

Franklin, J., S.D. Prince, A.H. Strahler, N.P. Hanan and D.S. Simonett, 1991. Reflectance and transmittance properties of West Africa savanna trees from ground radiometer measurements. *International Journal of Remote Sensing*. 12(6):1369-1385.

Franklin, J., 1995. Predictive vegetative mapping: geographic modeling of biospatial patterns in relation to environmental gradients, *Progress in Physical Geography*, 19(4): 474-499.

Franklin, S.E., 1987. Terrain analysis from digital patterns in geomorphometry and Landsat MSS spectral response. *Photogrammetric Engineering & Remote Sensing*, 53(1): 59-65.

Franklin, S.E., 1989. Classification of Hemlock Looper damage using SPOT HRV imagery. *Canadian Journal of Remote Sensing*, 15(3):178-182.

Franklin, S.E., and B.A. Wilson, 1991. Spatial and spectral classification of remote sensing imagery, *Computers & Geosciences*, 17(8): 1151-1172.

Franklin, S.E., 1992. Satellite remote sensing of forest type and land cover in the subalpine forest region, Kananaskis Valley, Alberta. *Geocarto International*. 4:25-35.

Franklin, S.E., and G.J. McDermid, 1993. Empirical relations between digital SPOT HRV and CASI spectral response and lodgepole pine (*Pinus contorta*) forest stand parameters, *International Journal of Remote Sensing*, 14(12): 2331-2348.

Franklin, S.E., 1994. Discrimination of subalpine forest species and canopy density using digital CASI, SPOT PLA, and Landsat TM data, *Photogrammetric Engineering & Remote Sensing*, 60(10):1233-1241.

Franklin, S.E., M.B. Lavigne, B.A. Wilson and E.R. Hunt, 1994. Empirical relations between balsam fir forest stands conditions and ERS-1 SAR data in western Newfoundland, *Canadian Journal of Remote Sensing*, 20(2):124-130.

Franklin, S.E., R.H. Waring, R.W. McCreight, W.B. Cohen, and M. Fiorella, 1995. Aerial and satellite sensor detection and classification of western spruce budworm defoliation in a subalpine forest. *Canadian Journal of Remote Sensing*, 21(3):299-308.

Garvey, T.D., 1987, Evidential reasoning for geographic evaluation for helicopter route planning. *IEEE Transactions on Geoscience and Remote Sensing*, 25(3): 294-304.

Garvey, T.D., J.D. Lowrance, and M.A. Fischler, 1981, An inference technique for integrating knowledge from disparate sources. *Proceedings, Seventh International Conference on Artificial Intelligence*, Vancouver, Canada, p. 319-325.

Gates, D.M., 1990. Climate change and forests. *Tree Physiology*, 7:1-5.

Gates, D.M., Keegan, H.J., Schleter, J.C. and V.R. Weidner, 1965. Spectral properties of plants. *Applied Optics*, 4:11-20.

Goel, N.S. and T. Grier, 1988. Estimation of canopy parameters for inhomogeneous vegetation canopies from reflectance data. III. TRIM: a model for radiative transfer in heterogeneous three-dimensional canopies. *Remote Sensing of Environment*, 25:255-293.

Goel, N.S. Knox, L.B. and J.M. Norman, 1990. From artificial life to real life: computer simulation of plant growth. *International Journal of General Systems*, 18:291-319.

Goel, N.S., 1989. Inversion of canopy reflectance models for estimation of biophysical parameters from reflectance data. p. 205-251. *In* Theory and Applications of Optical Remote Sensing, G. Asrar (ed.). John Wiley & Sons, New York. 734 p.

Goel, N.S., Rozehnal, I. and R.L. Thompson, 1991. A computer graphics based model for scattering from objects of arbitrary shapes in the optical region. *Remote Sensing of Environment*, 36:73-104.

Goetz, A.F., Vane, G., Solomon, J. and B.N. Rock, 1985. Imaging spectrometry for earth remote sensing. *Science*, 228:1147-1153.

Goldberg, M., D.G. Goodenough, M. Alvo, and G. Karam, 1985, A hierarchical expert system for updating forestry maps with Landsat data. *Proceedings of the IEEE.*, 73(6): 1054-1063.

Gong, P. and P.J. Howarth, 1990. An assessment of some factors influencing multispectral land-cover classification. *Photogrammetric Engineering & Remote Sensing*, 56(5):597-603.

Gong, P., J.R. Miller and M. Spanner, 1994. Forest canopy closure from classification and spectral unmixing - multi-sensor evaluation of an open canopy. *IEEE Transactions on Geoscience and Remote Sensing*, 32(5): 1067-1080.

Gong, P., Pu, R., and J.R. Miller, 1992. Correlating leaf area index of ponderosa pine with hyperspectral CASI data. *Canadian Journal of Remote Sensing*, 18(4):275-282.

Goward, S. N., K.F. Huemmrich, and R.H. Waring, 1994. Visible-near infrared spectral reflectance of landscape components in western Oregon. *Remote Sensing of Environment*, 47: 190-203.

Government of Canada, 1991. The State of Canada's Environment. Supply and Services Canada, Ottawa. 27 Sections plus Appendices.

Graham, R.L., Turner, M.G., and V.H. Dale, 1990. How increasing $CO_2$ and climate change affect forests. *BioScience*, 40(8):575-587.

Guyot, G., D. Guyon and D.G.J. Riom, 1989. Factors affecting the Spectral Response of forest canopies: a review. *Geocarto International*, 3:3-18.

Hall, F.G., Huemmrich, K.F. and S.N. Goward, 1990. Use of narrow-band spectra to estimate the fraction of absorbed photosynthetically active radiation. *Remote Sensing of Environment*, 32(1):47-54.

Hall, F.G., Huemmrich, K.F., Strebel, D.E., Goetz, S.J., Nickeson, J.E. and K.D. Woods, 1992. Biophysical, Morphological, Canopy Optical Property, and Productivity Data from the Superior National Forest. NASA Technical Memorandum 104568, Goddard Space Flight Center, Greenbelt, Maryland. Unpaginated.

Hall, F.G., 1994. Remote sensing and regional forest applications - a current assessment. *In* Forest Ecosystem Management: the Role of Remote Sensing and GIS, V.A. Sample (ed.), Island Press.

Hall, F.G., Y.E. Shimabukuro and K.F. Huemmrich, 1995. Remote sensing of forest biophysical structure in boreal stands of *picea mariana* using mixture decomposition and geometric reflectance models. *Ecological Applications*. 5(4): 993-1013.

Hall, F.G., 1996. A physically-based approach to land cover classification and biophysical parameter estimation. Unpublished NASA Internal Document.

Hall, F.G., C.J. Tucker, D. Kimes, D. Peddle, L. Steyaert, Y. Shimabukuro, 1996. An algorithm for integrated classification of land cover and estimation of biophysical characteristics. NASA Earth Observing System, Mission to Planet Earth (EOS-MTPE) MODIS Science Team Proposal (NASA Research Announcement 95-MTPE-03). F.G. Hall, Principal Investigator, 5 Co-investigators.

Halliwell, D. and M.J. Apps, 1995. BOREAS Biometry and Auxiliary Sites: Locations and Descriptions. Report prepared for Northern Forestry Centre, Canadian Forestry Service - Northwest Region. Version 2.0, July 1995. 122 p.

Halliwell, D. and M.J. Apps, 1996. BOREAS Biometry and Auxiliary Sites: Overstorey and Understorey Data. Report prepared for Northern Forestry Centre, Canadian Forestry Service - Northwest Region. Version 2.0, January 1996. 256 p.

Hanan, N.P., Prince, S.D. and Hiernaux, P.H.Y., 1991. Spectral modelling of multi-component landscapes in the Sahel. *International Journal of Remote Sensing*, 12(6):1243-1258.

Hanan, N.P., S.D. Prince, and J. Franklin, 1993. Reflectance properties of West Africa savanna trees from ground radiometer measurements. II. Classification of components. *International Journal of Remote Sensing*. 14(6):1081-1097.

Hare, K.J. and J.C. Ritchie, 1972. The boreal bioclimates. *Geogr. Rev.*, 62(3):333-365.

Harrington, J.B., 1987. Climatic change: a review of causes. *Canadian Journal of Forest Research*, 17:1313-1339.

Hendrickson, O.Q., 1990. How does forestry influence atmospheric carbon. *The Forestry Chronicle*, 66(5):469-472.

Holben, B.N. and Shimabukuro, Y.E. 1993. Linear mixing model applied to coarse spatial resolution data from multispectral satellite sensors. *International Journal of Remote Sensing*, 14(11):2231-2240.

Horler, D.N.H., Dockray, M. and J. Barber, 1983. The red edge of plant leaf reflectance. *International Journal of Remote Sensing*, 4:273-288.

Horwitz, H.M., Nalepka, R.F., Hyde, P.D. and Morgenstern, J.P., 1971. Estimating the proportions of object within a single resolution element of a multispectral scanner. Proceedings, Seventh International Symposium on Remote Sensing of Environment, ERIM, Ann Arbor, MI. 2:1307-1320.

Huete, A.R., 1988. A soil-adjusted vegetation index (SAVI). *Remote Sensing of Environment*, 25:295-309.

IGBP, 1990. International Geosphere-Biosphere Programme: A Study of Global Change. Report 12 - The Initial Core Projects. Graphic Systems Printers, Stockholm, Sweden.

IGBP, 1994. Biosphere-atmosphere field experiment in Amazonia: Lambada / Baterista / Ambiace (LBA). In. Global Change Newsletter: International Geosphere-Biosphere Programme: 18:3-5.

IPCC, 1995. Intergovernmental Panel on Climate Change. Climate Change 1995 - The Science of Climate Change. Summary for Policymakers and Technical Summary of the Working Group I Report from the fifth session of IPCC-WGI, Madrid, Spain, November 1995. 55 p.

Jackson, R.D., Reginato, R.J., Pinter, P.J., and S.B. Idso, 1979. Plant canopy information extraction from composite scene reflectance of row crops. *Applied Optics*, 18(22):3775-3782.

Jasinski, M. F. and Eagleson, P. S., 1989. The structure of red-infrared scattergrams of semi-vegetated landscapes, *IEEE Transactions on Geoscience and Remote Sensing*, 27(4):441-451.

Jasinski, M. F. and Eagleson, P. S., 1990. Estimation of sub-pixel vegetation cover using red-infrared scattergrams, *IEEE Transactions on Geoscience and Remote Sensing* , 28(2):253-267.

Jasinski, M. F., 1990. Functional relation among sub-pixel canopy cover, ground shadow, and illuminated ground at large sampling scales. *In*: Society of Photo Optical Instrumentation Engineers, Orlando, FL. SPIE 1300, Remote Sensing of the Biosphere. p. 48-58.

Jensen, J.R., 1996. Introductory Digital Image Processing - A Remote Sensing Perspective. Second Edition. Prentice Hall Series in Geographic Information Science. Prentice Hall, Upper Saddle River, New Jersey. 316 p.

Johnson, P.E., Smith M.O., Taylor-George, S. and J.B. Adams, 1983. A semi-empirical method for analysis of the reflectance spectra of binary mineral mixtures. *Journal of Geophysical Research*, 88(B4):10,3557-3561.

Jones, A.R., J.J. Settle and B.K. Wyatt, 1988. Use of digital terrain data in the interpretation of SPOT-1 HRV multispectral imagery. *International Journal of Remote Sensing*, 9(4):669-682.

Jordan, C.F., 1969. Derivation of leaf area index from quality of light on the forest floor. *Ecology*, 50:663-666.

Jupp, D.L.B. and A.H. Strahler, 1991. A hotspot model for leaf canopies. *Remote Sensing of Environment*, 38:193-210.

Justice, C.O., Wharton, S.W. and B.N Holben, 1981. Application of digital terrain data to quantify and reduce the topographic effect on Landsat data. *International Journal of Remote Sensing*, 2(2):213-230.

Kaufman, Y.J. and D. Tanre, 1992. Atmospherically resistant vegetation index (ARVI) for EOS-MODIS. *IEEE Transactions on Geoscience and Remote Sensing*, 30(2):261-270.

Kauppi, P. and M. Posch, 1985. Sensitivity of boreal forests to possible climatic warming. *Climatic Change*, 7(1):45-54.

Kauth, R.J. and G.S. Thomas, 1976. The tasseled cap - a graphic description of the spectral-temporal development of agricultural crops as seen by LANDSAT. 4B-41-4B-51. *In* Machine Processing of Remotely Sensed Data.

Keeling, C.D., 1983. The global carbon cycle: what we know and could know from atmospheric, biospheric and oceanic observations. *In* Proceedings of the Carbon Dioxide Research Conference: Carbon Dioxide, Science, and Consensus, DOE CONF-820970, NTIS Springfield Virginia. II.3 - 62.

Kimes, D.S., 1983. Dynamics of directional reflectance factor distributions for vegetation canopies. *Applied Optics*, 22(9):1364-1372.

Kurz, W.A., M.J. Apps, T.M. Webb and P.J. McNamee, 1992. The carbon budget of the Canadian forest sector. Information report NOR-X-326. Forestry Canada, Northwest Region, Northern Forestry Centre, Edmonton. 93 p.

Lathrop, Jr., R.G. and L.L. Pierce, 1991. Ground-based canopy transmittance and satellite remotely sensed measurements for estimation of coniferous forest canopy structure. *Remote Sensing of Environment*, 36:179-188.

Lay, S.R., 1982. Convex Sets and Their Applications. John Wiley and Sons, New York.

Leblon, B., H. Granberg, and S.D. Charland, 1996. Shadowing effects on SPOT-HRV and high spectral resolution reflectances in Christmas tree plantations. *International Journal of Remote Sensing*. 17(2):277-289.

LeDrew, E.F., 1986. Sensitivity of the Arctic climate: a factor in developing planning strategies for our Arctic heritage. *Environmental Conservation*, 13(3):215-228.

LeDrew, E.F., M. Strome, and F.Hegyi (*eds.*), 1995a. The Canadian Remote Sensing Contribution to Understanding Global Change. Department of Geography Publication Series. No. 38, University of Waterloo. Waterloo, Ontario Canada. 434 p.

LeDrew, E.F., H.M. Holden, D.R. Peddle, J.Morrow, R.Murphy, and W.Bour, 1995b. Towards a Procedure for Mapping Coral Stress from SPOT Imagery with *In Situ* Optical Correction. *Third Thematic Conference on Remote Sensing of Marine and Coastal Environments*, Seattle WA, 18-20 September 1995. Vol. I, p.211-219.

Lee, T., J.A. Richards, and P.H. Swain, 1987, Probabilistic and evidential approaches for multi-source data analysis. *IEEE Transactions on Geoscience and Remote Sensing*, 25(3): 283-292.

Lenningston, R.K., Sorensen, C.T. and Heydorn, R.P. 1984. A mixture model approach for estimating crop areas from Landsat data. *Remote Sensing of Environment*, 14:197-206.

Li, X. and A.H. Strahler, 1985. Geometric-optical modeling of a conifer forest canopy. *IEEE Transactions on Geoscience and Remote Sensing*, GE-23(5):705-720.

Li, X. and A.H. Strahler, 1986. Geometric-optical bidirectional reflectance modeling of a coniferous forest canopy. *IEEE Transactions on Geoscience and Remote Sensing*, GE-24:281-293.

Li, X. and A.H. Strahler, 1988. Modeling the gap probability of a discontinuous vegetation canopy. *IEEE Transactions on Geoscience and Remote Sensing*, GE-26(2):161-170.

Li, X. and A.H. Strahler, 1992. Geometric-optical bidirectional reflectance modeling of the discrete crown vegetation canopy: effect of crown shape and mutual shadowing. *IEEE Transactions on Geoscience and Remote Sensing*, 30(2):276-292.

Li, X., A.H. Strahler and C.E. Woodcock, 1995. A hybrid geometric-optical - radiative transfer approach for modeling albedo and directional reflectance of discontinuous canopies. *IEEE Transactions on Geoscience and Remote Sensing*, 33:466-480.

Lillesand, T.M. and R.W. Kiefer, 1979. Remote Sensing and Image Interpretation. John Wiley & Sons, New York. 612 p.

LTER, 1991. Long-Term Ecological Research in the United States: A Network of Research Sites. K. Van Cleve and S. Martin, (*eds*). LTER Publication No. 11, Sixth Edition Revised. LTER Network Office, University of Washington, Seattle, WA., 178 p.

Luvall, J.C. and G.S. Hartshorn, 1990. Estimation of tropical forest canopy temperatures, thermal response numbers, and evapotranspiration using an aircraft-based thermal sensor. *Photogrammetric Engineering and Remote Sensing*, 56(10):1393-1401.

Mah, S, R. Price, S. Achal, C. Palylyk and T. Ivanco, 1995. The acquisition of high resolution airborne hyperspectral imagery with the casi. In: *Proceedings, 17th Canadian Symposium on Remote Sensing*, Saskatoon, SK, Canada. p. 262-267.

Markham, B.L., R.N. Halthorne and S.J. Goetz, 1992. Surface reflectance from satellite and aircraft sensors: results of sensor and algorithm comparisons during FIFE. *Journal of Geophysical Research*. 97(D17):18,785-18,795.

Matsumoto, M., Terayama, Y. and Arai, K. 1992. Image classification from category proportions among mixels. Proceedings of the ISPRS Symposium, Washington, D.C., Commission VII, 588-591.

Miller, J., P.White, J.Chen, D.Peddle, G.McDermid, R.Fournier, P.Shepherd, I.Rubinstein, J.Freemantle, R.Soffer and E.LeDrew, 1996. Seasonal Change in Mean Understorey Reflectance at BOREAS Flux Tower Sites and its Applications to Canopy Vegetation Index Determination. *Journal of Geophysical Research.* (BOREAS Special Issue). [ accepted for publication ]

Miller, J.R., Hare, E.W. and J. Wu, 1990. Quantitative characterization of the vegetation red edge reflectance: 1) an inverted-Gaussian reflectance model. *International Journal of Remote Sensing*, 11(10):1775-1795.

Miller, J.R., J.Freemantle, P.Shepherd, L.Gray, N.O'Neill, A.Royer and E.Senese, 1995. Deployment of CASI to meet the needs of BOREAS science. In: *Proceedings, 17th Canadian Symposium on Remote Sensing*, Saskatoon, SK, Canada. p. 169-175.

Miller, J.R., Wu, J., Boyer, M.G., Belanger, M. and E.W. Hare, 1991. Season patterns in leaf reflectance red edge characteristics. *Int. Journal of Remote Sensing*, 12(7):1509-1523.

Milton, E.J., 1989. On the suitability of Kodak neutral test cards as reflectance standards. *International Journal of Remote Sensing*, 10, p. 1041-1047.

Mitchell, J.F.B., 1989. The "greenhouse" effect and climate change. *Reviews of Geophysics*, 27(1):115-139.

Monteith, J. L. and M.H. Unsworth, 1990. Principles of Environmental Physics, London, Edward Arnold, Ltd.

Moon, W.M., 1990, Integration of geophysical and geological data using evidential belief function. *IEEE Transactions on Geoscience and Remote Sensing*, 28(4): 711-720.

Moon, W.M., 1993, On mathematical representation and integration of multiple spatial geoscience data sets. *Canadian Journal of Remote Sensing*. 19(1): 63-67.

Morassutti, M., 1995. Personal Communication, Earth Observations Laboratory, University of Waterloo.

NASA, 1988. Earth System Science: A Program for Global Change. National Aeronautics and Space Administration, Washington, USA. 208 p.

NBIOME, 1993. Northern Biosphere Observation and Modelling Experiment - Science Plan. Canadian Global Change Program, Incidental Report Series, No. IR93-1. Royal Society of Canada, Ottawa. 61 p.

Nelson, B., V.Kapos, J.Adams, W. Oliveira, O. Braun and I. Amaral, 1994. Forest disturbance by large blowdowns in the Brazilian Amazon. *Ecology*, 75(3):853-858.

Nemani, R.R., L.L. Pierce, S.W. Running and L.E. Band, 1993. Forest ecosystem processes at the watershed scale: sensitivity to remotely sensed Leaf Area Index estimates. *Int. J. Remote Sensing*, 14(13):2519-2534.

Nilson, R. 1990. Approximate analytical methods for calculating the reflection functions of leaf canopies in remote sensing applications, in Photon-Vegetation Interactions: Applications in Optical Remote Sensing and Plant Ecology. R.B. Myneni and J. Ross (eds.), Springer-Verlag, Heidelberg, 162-190.

Nilson, T. and Peterson, U. 1991. A forest canopy reflectance model and a test case. *Remote Sensing of Environment*, 37:131-142.

Observers Handbook, 1994. (*Ed.*: R.L. Bishop), Royal Astronomical Society of Canada.

Pastor, J. and W.M. Post, 1988. Response of northern forests to $CO_2$-induced climate change. *Nature*, 334:55-58.

PCI, 1993, Easi/Pace image analysis system user's manuals. Perceptron Computing Inc., Richmond Hill, Ontario, Canada. Variously paged.

Peddle, D.R., 1993. An Empirical Comparison of Evidential Reasoning, Linear Discriminant Analysis and Maximum Likelihood Algorithms for Alpine Land Cover Classification. *Canadian Journal of Remote Sensing*. 19(1):31-44.

Peddle, D.R. and S.E. Franklin, 1993. Classification of permafrost active layer depth from remotely sensed and topographic evidence. *Remote Sensing of Environment*, 44(1):67-80.

Peddle, D.R., 1995a. Knowledge formulation for supervised evidential classification. *Photogrammetric Engineering & Remote Sensing* 61(4):409-417.

Peddle, D.R., 1995b. MERCURY©: An Evidential Reasoning Image Classifier. *Computers & Geosciences* 21(10):1163-1176.

Peddle, D.R. and C.R. Duguay, 1995. Incorporating Topographic and Climatic GIS Data into Satellite Image Analysis of an Alpine Tundra Ecosystem, Front Range, Colorado Rocky Mountains. *Geocarto International* 10(4):43-60.

Peddle, D.R., E.F. LeDrew and H.M. Holden, 1995a. Spectral Mixture Analysis of Coral Reef Abundance from Satellite Imagery and *In Situ* Ocean Spectra, Savusavu Bay, Fiji. *Third Thematic Conference on Remote Sensing of Marine and Coastal Environments*, Seattle WA, 18-20 September 1995. Vol. II, p.563-575.

Peddle, D.R., H.P. White, R.J. Soffer, J.R. Miller and E.F. LeDrew, 1995b. Reflectance Processing of Field Spectrometer Data in BOREAS. In: *Proceedings, 17th Canadian Symposium on Remote Sensing*, Saskatoon, SK, Canada. Vol. I, p. 189-194.

Peddle, D.R. and C.R. Duguay, 1996. A Rule-Based Algorithm for Advanced GIS Data Analysis in Mountainous Terrain. *8th International Conference on Geomatics and Geographical Information Systems*, Ottawa. May 1996.

Peddle, D.R., E.F. LeDrew and H.M. Holden, 1996a. Optical Correction of Scene Fractions for Estimating Regional Scale Coral Abundance in Fiji. *International Geoscience and Remote Sensing Symposium (IGARSS'96)*, Lincoln, Nebraska, USA. Vol I: 427-429.

Peddle, D.R., F.G. Hall and E.F. LeDrew, 1996b. Spectral Mixture Analysis and Geometric Optical Reflectance Modeling of Boreal Forest Biophysical Structure. *Remote Sensing of Environment.* (accepted for publication).

Piwowar, J.M., D.R. Peddle and E.F. LeDrew, 1996a. Temporal Mixture Analysis of Sea Ice Concentrations in the Canadian Arctic Archipelago. *International Geoscience and Remote Sensing Symposium (IGARSS'96)*, Lincoln, NB, USA. Vol II: 938-940.

Piwowar, J.M., D.R. Peddle and E.F. LeDrew, 1996b. Temporal Mixture Analysis of Arctic Sea Ice Imagery: A New Approach for Monitoring Environmental Change. *Remote Sensing of Environment* (accepted for publication).

Pollard, D.F.W., 1989. Climate Change and its Effects on Forests. *Canadian Forest Industry*, 109(5):56-61.

Portigal, F.P. and R.W. Harrill, 1996. Rio Platano Biosphere Reserve intrusion analysis using linear mixing models, La Mosquitia, Honduras. In: *Proceedings, 26th International Symposium on Remote Sensing of Environment / 18th Canadian Symposium on Remote Sensing*, Vancouver, Canada. p. 439-444.

Quarmby, N.A., Townshend, J.R.G., Settle, J.J., White, K.H., Milnes, M., Hindle, T.L. and Silleos, N. 1992. Linear mixture modelling applied to AVHRR data for crop area estimation. *International Journal of Remote Sensing*, 13(3):415-425.

Ranson, K.J., Daughtry, C.S.T., and L.L. Biehl, 1986. Sun angle, view angle, and background effects on spectral response of simulated balsam fir canopies. *Photogrammetric Engineering and Remote Sensing*, 52(5):649-658.

Ranson, K.J. and C.S.T. Daughtry, 1987. Scene shadow effects on multispectral response. *IEEE Transactions on Geoscience and Remote Sensing*. 25(4):502-509.

Ranson, K.J. and G.Sun, 1994. Northern forest classification using temporal multifrequency and multipolarimetric SAR images. *Remote Sensing of Environment*, 47:142-153.

Ranson, K.J., S.Saatchi and G.Sun, 1995. Boreal forest ecosystem characterization with SIR-C/XSAR. *IEEE Transactions on Geoscience and Remote Sensing*, 33(4):867-876.

Rasool, S.I., 1992. Requirements for terrestrial biospheric data for IGBP core projects. International Geophysical-Biophysical Program, Data Information System, Paris. Working paper number 2.

Rey, M., K.E. Tunaley, and T. Sibbald, 1993, Use of the Dempster-Shafer algorithm for the detection of SAR ship wakes. *IEEE Transactions on Geoscience and Remote Sensing*, 31(5): 1114-1118.

Richey, J.E., Adams, J.B. and R.L. Victoria, 1990. Synoptic-scale hydrological and biogeochemical cycles in the Amazon river basin: a modeling and remote sensing perspective. 249-268. *In* Remote Sensing of Biosphere Functioning, R.J. Hobbs and H.A. Mooney (eds.). Springer-Verlag, New York. 314 p.

Roberts, D.A., Smith, M.O. and J.B. Adams, 1993. Green vegetation, nonphotosynthetic vegetation and soils in AVIRIS data. *Remote Sensing of Environment*, 44:255-269.

Rock, B.N., Hoshaki, T., and J.R. Miller, 1988. Comparison of *in situ* and airborne spectral measurements of the blue shift associated with forest decline. *Remote Sensing of Environment*, 24:109-127.

Rosema, A., W. Verhoef, H.Noorbergen and J.Borgesius, 1992. A new light interaction model in support of forest monitoring. *Remote Sensing of Environment*, 42:23-41.

Rouse, J.W., R.Haas, J.Schell and D.Deering, 1974. Monitoring vegetation systems in the Great Plains with ERTS. Third ERTS Symposium, NASA SP-351, vol. 1, p.309-317.

Running, S.W. and J.C. Coughlan, 1988. A general model of forest ecosystem processes for regional applications: I hydrologic balance, canopy gas exchange and primary production processes. *Ecological Modelling*, 42:125-154.

Running, S.W. and R.R. Nemani, 1988. Relating seasonal patterns of the AVHRR vegetation index to simulated photosynthesis and transpiration of forests in different climates. *Remote Sensing of Environment*, 24:347-367.

Running, S.W., R.R. Nemani, D.L. Peterson, L.E. Band, D.F. Potts, L.L. Pierce and M.A. Spanner, 1989. Mapping regional forest evapotranspiration and photosynthesis by coupling satellite data with ecosystem simulation. *Ecology*, 70:1090-1101.

Running, S.W. and S.T. Gower, 1991. Forest-BGC, A general model of forest ecosystem processes for regional applications. II. Dynamic carbon allocation and nitrogen budgets. *Tree Physiology*, 9:147-160.

Running, S.W. and E.R. Hunt, Jr., 1993. Generalization of a forest ecosystem process model for other biomes, BIOME-BGC, and an application for global scale models. Chapter 8 in, J.R. Ehleringer and C.B. Field (eds.),*Scaling Physiological Processes, Leaf to Globe* p. 141-157. Academic Press Inc.

Sader, S.A., 1987. Forest biomass, canopy structure, and species composition relationships with multi-polarization L-band synthetic aperture radar data. *Photogrammetric Engineering & Remote Sensing*, 53(2):193-202.

Salvato, P., 1973. Iterative techniques to estimate signature vectors for mixture processing of multispectral data. Proceedings of the Symposium on Mach. Pro. of Remotely Sensed Data, IEEE Transactions on Geoscience and Remote Sensing, 73CH0834-2GE, 3B:48-62.

Schowengerdt, R.A., 1983. Techniques for Image Processing and Classification in Remote Sensing. Academic Press, New York. 249 p.

Sedjo, R.A. and A.M. Solomon, 1988. Climate and Forests. p. 105-119. *In* Greenhouse Warming: Abatement and Adaptation. N.J. Rosenberg, W.E. Easterling III, P.R. Crosson and J. Sarmstadter (eds). Resources for the Future, Washington, D.C. 182 p.

Sellers, P., F. Hall, H. Margolis, B. Kelly, D. Baldocchi, J. den Hartog, J. Cihlar, M. Ryan, B. Goodison, P. Crill, J. Ranson, D. Lettenmaier and D. Wickland, 1995. The Boreal Ecosystem-Atmosphere Study (BOREAS): an overview and early results from the 1994 field year. *Bulletin American Meteorological Society* 76(9):1549-1577.

Sellers, P.J. and D. Schimel, 1993. Remote sensing of the land biosphere and biogeochemistry in the EOS era: science priorities, methods and implementation. *Global and Planetary Change*, 7:279-297.

Sellers, P.J., 1985. Canopy reflectance, photosynthesis, and transpiration. *International Journal of Remote Sensing*, 6(8):1335-1372.

Sellers, P.J., 1987. Canopy reflectance, photosynthesis, and transpiration. II. the role of biophysics in the linearity of their interdependence. *Remote Sensing of Environment*, 21:143-183.

Settle, J.J. and Drake, N.A. 1993. Linear mixing and the estimation of ground cover proportions. *International Journal of Remote Sensing*, 14(6):1159-1177.

Shafer, G., 1976, A mathematical theory of evidence. Princeton University Press, Princeton, USA. 297 p.

Shimabukuro, Y.S. and Smith, J.A. 1991. The least-squares mixing models to generate fraction images derived from remote sensing multispectral data. *IEEE Transactions on Geoscience and Remote Sensing* , 29(1):16-20.

Shipman, H. and J.B. Adams, 1987. Detectability of minerals on desert alluvial fans using reflectance spectra. *Journal of Geophysical Research*, 92(B10):10,391-10,402.

Skole, D., 1992. Scientific requirements for a 1km data set. In, J.R. Townshend (ed.), Improved global data for land applications. IGBP, Stockholm, Sweden.

Smith, J.A., Lin, T.L., and K.J. Ranson, 1980. The Lambertian assumption and Landsat data. *Photogrammetric Engineering and Remote Sensing*, 46(9):1183-1189.

Soffer, R.J., J.W. Harron and J.R. Miller, 1995. Characterisation of Kodak gray cards as reflectance reference panels in support of BOREAS field activities. *17th Canadian Symposium on Remote Sensing*, Saskatoon, SK. p. 357-362.

Spanner, M.A., Pierce, L.L., Peterson, D.L. and S.W. Running, 1990. Remote sensing of temperate coniferous forest leaf area index: the influence of canopy closure, understorey vegetation and background reflectance. *International Journal of Remote Sensing*, 11(1):95-111.

SPSS, 1988. SPSS-X User's Guide. Third Edition. SPSS Inc. Chicago Illinois, USA. 1072 p.

Srinivasan, A., and J.A. Richards, 1990, Knowledge-based techniques for multi-source classification. *International Journal of Remote Sensing*, 11(3): 505-525.

Strahler, A.H., and Jupp, D.L.B. 1990, Geometric-optical modelling of forests as remotely sensed scenes composed of three-dimensional, discrete objects, *in* Photon-Vegetation Interactions: Applications in Optical Remote Sensing and Plant Ecology (R.Myneni and J. Ross, Eds.), Springer-Verlag, Heidelberg, pp.162-190.

Strahler, A.H., and Woodcock, C.E. 1986. On the nature of models in remote sensing. *Remote Sensing of Environment*, 20:121-139.

Strahler, A.N. and A.H. Strahler, 1987. Modern Physical Geography. John Wiley & Sons, New York. 544 p.

Swain, P. and S. Davis, 1978. Remote Sensing: The Quantitative Approach. McGraw-Hill, Toronto. 396 p.

Syrén, P., 1994. Reflectance anisotropy for nadir observations of coniferous forest canopies. *Remote Sensing of Environment*, 49:72-80.

Tans, P.P., Fung, I.Y. and T. Takahashi, 1990. Observational constraints on the global atmospheric $CO_2$ budget. *Science*, 247:1431-1438.

Teillet, P.M., 1995. The role of surface observations in support of remote sensing, p. 333--352, In, *The Canadian Remote Sensing Contribution to Understanding Global Change*, E.F. LeDrew, M. Strome, and F. Hegyi (*eds*). Department of Geography Publication Series, no. 38, University of Waterloo. 434p.

Terayama, Y., Ueda, Y. and Arai, K. 1992. A comparative study on the methods for estimation of mixing ratio within a pixel. Proceedings of the ISPRS Symposium, Washington, D.C., Commission VII, 986-989.

Tucker, C.J. and L.D. Miller, 1977. Soil spectra contributions to grass canopy spectral reflectance. *Photogrammetric Engineering and Remote Sensing*, 43(6):721-726.

Tucker, C.J., 1979. Red and photographic infrared linear combinations for monitoring vegetation. *Remote Sensing of Environment*, 8:127-150.

Tucker, C.J., J.R.G. Townshend, T.E. Goff and B.N. Holben, 1986. Continental and Global Scale Remote Sensing of Land Cover, *in* Trabalka, J.R. and D.E. Reichle (eds.), 1986. The Changing Carbon Cycle - A Global Analysis. Springer-Verlag, New York. 592 p.

Tyndall, J., 1861. On the absorption and radiation of heat by gases and vapours, and on the physical connexion of radiation, absorption and conduction. *Philos. Mag.*, 22:169-194 and 273-285.

Ulaby, F.T. and M.C. Dobson, 1993. Radar response of vegetation: an overview. In, *Proceedings, Third Spaceborne Imaging Radar Symposium.* Jet Propulsion Laboratory, Pasadena, CA. Publication JPL 93-16. p. 151-183.

USGCRP, 1994. United States Global Change Research Program - Our Changing Planet. Report to the Committee on Environment and Natural Resources Research of the National Science and Technology Council. Washington. 132 p.

Verhoef, W., 1984. Light scattering by leaf layers with application to canopy reflectance modeling: the SAIL model. *Remote Sensing of Environment*, 16:125-141.

Vermote, E. D. Tanré, J.L. Deuzé, M. Herman and J.L. Morcrette, 1994. 6S User's guide, Version 0. NASA Goddard Space Flight Center, Greenbelt MD, USA. 183 p.

Waring, R.H., J. Way, E.R. Hunt Jr., L. Morrissey, K.J. Ranson, J.F. Weishampel, R. Oren and S.E. Franklin, 1995. Imaging radar for ecosystem studies. *BioScience.* 45(10):715-723.

Wessman, C. A., Aber, J. D., Peterson, D. L. and Melillo, J. M., 1988a. Foliar analysis using near infrared reflectance spectroscopy. *Can. J. For. Res.*, 18:6-11.

Wessman, C. A., Aber, J. D., Peterson, D. L. and Melillo, J. M., 1988b. Remote sensing of canopy chemistry in nitrogen cycling in temperate forest ecosystems. *Nature*, 335(6186):154-156.

Wessman, C.A., Aber, J.D., and D.L. Peterson, 1989. An evaluation of imaging spectrometry for estimating forest canopy chemistry. *Int. Journal of Remote Sensing*, 10(8):1293-1316.

White, H.P, J.R. Miller, J. Chen and D.R. Peddle, 1995. Seasonal change in mean understorey reflectance for BOREAS sites: preliminary results. 17th Canadian Symposium on Remote Sensing, Saskatoon, SK. p. 182-187.

Wickland, D.E., 1989. Future directions for remote sensing in terrestrial ecological research. *In* Theory and Applications of Optical Remote Sensing, p. 691-725. G. Asrar (ed.). John Wiley & Sons, New York. 734 p.

Wilkinson, G.G., and J. Mégier, 1990, Evidential reasoning in a pixel classification hierarchy - a potential method for integrating image classifiers and expert system rules based on geographic context. *International Journal of Remote Sensing*, 11(10): 1963 -1968.

Williams, D.L. 1991. A comparison of spectral reflectance properties at the needle, branch, and canopy level for selected conifer species. *Remote Sensing of Environment*, 35:79-93.

Wilson, B.A. 1996. Estimating coniferous forest structure using SAR texture and tone. *Canadian Journal of Remote Sensing*. 22(4): 382-389.

Woodcock, C.E. and A.H. Strahler, 1987. The factor of scale in remote sensing. *Remote Sensing of Environment*, 21: 311-332.

Wu, Y. and A.H. Strahler, 1994. Remote estimation of crown size, stand density, and biomass on the Oregon transect. *Ecological Applications*, 4(2):299-312.

Wulder, M.A., S.E. Franklin, and M.B. Lavigne, 1996a. Statistical texture properties of forest structure for improved LAI estimates from CASI, *Proceedings, 26th International Symposium on Remote Sensing of Environment and 18th Canadian Symposium on Remote Sensing*, Vancouver, BC. p. 161-164.

Wulder, M.A., S.E. Franklin, and M.B. Lavigne, 1996b. High spatial resolution optical image texture for improved estimates of forest stand leaf area index. *Canadian Journal of Remote Sensing*. 22(4): 441-449.

Zhang, A., 1994. Hyperspectral Image Analysis: A Study on Band Selection Methods and the Sensitivity of Linear Spectral Unmixing. Unpublished Master of Science Thesis, Department of Geomatics Engineering, University of Calgary, Calgary, Alberta. 77 p.

# APPENDICES

**Appendix A.** Reflectance processing files

**Appendix A.1** Header template for BOREAS reflectance output files

/* ASD Header File - Word Text Format. This file MUST contain 20 lines of text (including these first 2 lines [1,2] ). ONLY Lines 3-13 may be edited */
BOREAS DATA
Understorey Reflectance Spectra
BOREAS Project: RSS-19
PI: Dr. John Miller: York University
RSS-19 contact for this file: Derek Peddle
Field Campaign: IFC-3
Field Instrument: ASD Personal Spectrometer II
Panel Calibration: Kodak White Card
REFLECTANCE DATA SPECIFICATIONS
Spectral Range: 400-900 nm
Wavelength Step: 1.4230 nm
Spectrum Description:
Location:
Latitude:
Longitude:
Date:
Time (Local):
Time (GMT):
Solar Zenith Angle:
Solar Azimuth:
Target Description:
Illumination:
Comments:

**Appendix A.2** Example main batch file for input to Excel Macro for processing BOREAS reflectance spectra for all TF sites.
Each section of this file (SSA_BIG.BAT) contains the directory folder location of the next set of spectra to process for each tower flux site, the number of tower flux batch files to be processed per site, and the name of each of those site batch files (Appendix A.3).

```
---------------
SSA_OJP-A
1
ssaojpem.bat
---------------
SSA_OBS-A
1
ssaobsem.bat
---------------
SSA_OA-A
1
ssaoaem.bat
---------------
SSA_YJP-A
1
ssayjpem.bat
```

**Appendix A.3** Example tower flux site batch file for input to Excel Macro for processing BOREAS reflectance spectra for one TF site.
The first section of this file (SSAOBSEM.BAT: SSA study area, Old Black Spruce TF site, End-member batch file) contains the TF site name, latitude and longitude, with each subsequent entry containing the target and KGC reference file names, the target type, illumination conditions, a comment record, and the output reflectance filename.

```
SSA OBS Tower (G8I4T)
53.9854
-105.122
------------------------
sun_ca.000
sun_ca.001
CANOPY
SUNLIT
optically thick stack
S3CASUE.RFL
------------------------
shd_ca.000
shd_ca.001
CANOPY
SHADOW
optically thick stack
S3CASHE.RFL
------------------------
sun_ua.000
sun_ua.001
MOSS
SUNLIT
NONE
S3MOSUE.RFL
------------------------
shd_ua.000
shd_ua.001
MOSS
SHADOW
NONE
S3MOSHE.RFL
```

**Appendix A.4** Description of Excel macro program.

The first task the macro performs is to prompt the user for the name of the batch control file using an Excel interactive dialogue box - this is the only user intervention required when running the program. After the file name has been supplied, the macro runs in stand-alone, unattended batch mode. During program execution, it first reads the latitude and longitude of the field site from the batch file, together with the additional site and data descriptors, and one set of target, panel, and output reflectance file names. The raw spectra digital numbers are read from the target and panel files, and placed in the reflectance file. Using a series of Excel parsing functions, the acquisition date and time for the target spectrum are extracted from the target file header and input to the SZA worksheet together with the site latitude and longitude. The SZA worksheet is then recalculated to compute the SZA for the time of target spectra acquisition. The macro reads the output SZA, and writes it to the spectral and angular interpolation worksheet (Figure 5.1), from which the panel calibration fourth order polynomial BRFs over the field spectrometer wavelengths are computed. The macro then extracts these panel calibrations, and places them in the reflectance file, prior to calculating reflectance using equation 5.1.

Once reflectance has been computed, the macro invokes a number of procedures to compile information describing the data acquisition (mentioned above), taken from the set of worksheets and external files. These are synthesized and formatted into a header template and written to the reflectance output file. Once this has been done, the relevant files are closed, and the entire procedure is repeated using a looping function to process the next set of panel and target spectra, as listed in the batch file. The output reflectance files are produced in ASCII format and are suitable for input to graphics programs or image processing routines for further analysis.

**Appendix A.5** Reflectance processing Excel macro program.

Excel Macro Code

```
Record1 (a)    Derek R. Peddle- BOREAS/RSS-19.  Excel V.4.0 Macro
=Set_Env(1)    Disable Error Messages (custom error checking done here)
=Set_Env(4)
Main_Batchfilename=INPUT("Main Batch Filename: ",2)
Main_Batchfile=FOPEN(Main_Batchfilename)
=Error_Check(Main_Batchfile,1,1,Main_Batchfilename)
home_dir=DIRECTORY()
output_subdir=FREADLN(Main_Batchfile)
output_dir=home_dir&":"&output_subdir

Main_Batchfile_EOF=FALSE
=WHILE(NOT(Main_Batchfile_EOF))
=DIRECTORY(home_dir)
= Set_Env(1)
site_eof=FREADLN(Main_Batchfile)
Main_Batchfile_EOF=Error_Check(site_eof,4,2,Main_Batchfilename)
=IF(Main_Batchfile_EOF,BREAK(),)
nextsite_subdir=FREADLN(Main_Batchfile)
numsite_batchfiles=FREADLN(Main_Batchfile)
site_dir= home_dir&":"&nextsite_subdir
=DIRECTORY(site_dir)

=FOR("bfiles",1,numsite_batchfiles,1)
ASD_Batchfilename=FREADLN(Main_Batchfile)    Get Batch Filename for Tower Site
=Set_Env(1)
Batchfile=FOPEN(ASD_Batchfilename)
=Error_Check(Batchfile,1,2,ASD_Batchfilename)
ts_loc=FREADLN(Batchfile)  Tower Site Location
ts_lat=FREADLN(Batchfile)  Tower Site Latitude
ts_long=FREADLN(Batchfile)         Tower Site Longitude
SSA=IF(VALUE(ts_long)<-102,TRUE,FALSE)    Determine if SSA (SK:CST time
zone) or NSA (MB:CDT) based on longitude (note, time zone for FFC-W differs)
Site_Batchfile_EOF=FALSE

=WHILE(NOT(Site_Batchfile_EOF))         Top of loop: each iteration processes 1 set of
ASD reflectances
=Set_Env(1)   Disable Error Messages
spectra_eof=FREADLN(Batchfile)    Read spectrum set batch file marker
Site_Batchfile_EOF=Error_Check(spectra_eof,4,1,ASD_Batchfilename)
=IF(Site_Batchfile_EOF,BREAK(),)
Field_Panel_filename=FREADLN(Batchfile)         Get filename containing white/grey
field panel data
=Error_Check(Field_Panel_filename,2,1,ASD_Batchfilename)
fp_file=OPEN(Field_Panel_filename)         open reference panel file
=Error_Check(fp_file,3,2,Field_Panel_filename)    Check for file I/O errors
```

```
=SELECT("R32C3:R543C3")          Select & copy panel spectra
=COPY()       (Finished with Field_Panel_file)
=Set_Env(1)
Target_filename=FREADLN(Batchfile)          Get Target Spectra filename
=Error_Check(Target_filename,2,2,ASD_Batchfilename)     Check for Batchfile I/O errors
illum=FREADLN(Batchfile)
target_desc=FREADLN(Batchfile)
comments=FREADLN(Batchfile)
mesg_txt="PROCESSING: "&nextsite_subdir&" / "&ASD_Batchfilename&" /
"&Target_filename     (Parse information into message text)
=MESSAGE(TRUE,mesg_txt) -  Write information to status bar on screen
=Set_Env(1)
t_file=OPEN(Target_filename)          open target spectra file
=Error_Check(t_file,3,2,Target_filename)     Check for file I/O errors
=SELECT("R32C4")  put panel spectra in column next to target spectra in ASD file
=PASTE()
datime=GET.FORMULA(!$A$10)     Get date & time of target spectra acquisition
date_suffix=REPLACE(datime,1,15,"")          Parse sentence to obtain date in correct format
for Excel
asd_date=REPLACE(date_suffix,9,12,"")
asd_time=REPLACE(datime,1,27,"")          Parse sentence to obtain time in correct
format for Excel
=DIRECTORY(home_dir)
=CALCULATION(3,FALSE,100,0.001,TRUE,FALSE,TRUE,FALSE,TRUE,FALSE)
        Minimise recalculation of worksheets
=OPEN("SZAcoeff4.xls",1)  SZA.XLS & Angular Coefficients combined into 1 file (with
link to Panel Calibration file retained)
=FORMULA(asd_date,"R5C19")       Input time & date of spectra data acquisition into
SZA input box
=FORMULA(asd_time,"R6C19")
=FORMULA(ts_lat,"R7C19")
=FORMULA(ts_long,"R8C19")
=CALCULATE.NOW()       Calculate SZA based on supplied Lat/Long, Date & Time of
target spectra acquisition in field
=SELECT("R37C19:R38C19")          Make temp copy of SZA & Az Values
=COPY()
=SELECT("R42C19")
=PASTE.SPECIAL(3,1,FALSE,FALSE)
sza=GET.FORMULA(!$S$42)          Get Solar Zenith Angle
solar_az=GET.FORMULA(!$S$43)  and Azimuth Angle (values only)
=SELECT("R12C19")
=COPY()
=SELECT("R47C19")
=PASTE.SPECIAL(3,1,FALSE,FALSE)
GMT_time=GET.FORMULA(!$S$47)
=SELECT("R60C3:R571C3")
=COPY()
=ACTIVATE(Target_filename)
=SELECT("R32C5")
=PASTE.SPECIAL(3,1,FALSE,FALSE)
```

```
=ACTIVATE("SZAcoeff4.xls")
=Set_Env(1)  Disable Error Messages - (avoid "Save Large Clipboard" Alert Box...)
=CLOSE(FALSE)     Close SZAcoeff.xls
=Set_Env(2)  Enable Error Messages
=ACTIVATE(Target_filename)
=SELECT("R32")     1st ASD Value (340 nm) is noise -  select entire row
=EDIT.DELETE(2)    delete row, & shift cells up
=SELECT("R32C6")  Select location for reflectance computation
=FORMULA("=(RC[-3]/RC[-2])*RC[-1]")  Compute reflectance as Target/Panel *
Calibration
=SELECT("R32C6:R542C6")          Compute reflectance over all ASD wavebands
=FILL.DOWN()
=CALCULATE.NOW()
=SELECT("R32C1:R542C6")          Select entire set of #s,  lambdas,raw ASD spectra,
calibration co-efficients and reflectance values
=COPY()       copy to buffer (finished with Target_file now)
=OPEN("header.asd")          Open Header Template File
=SELECT("R27C1")
=PASTE.SPECIAL(3,1,FALSE,FALSE)     Insert Full ASD & Reflectance Data
=SELECT("R1:R2")  Select first 2 rows of header file (internal comments)
=EDIT.DELETE(2)    Delete and shift cells up
=FORMULA(ts_loc,"R9C3")          Put File specific Info in Output file
=FORMULA(ts_lat,"R10C3")
=FORMULA(ts_long,"R11C3")
=FORMULA(asd_date,"R12C3")
=FORMULA(asd_time,"R13C3")     Specify local time in 24 hour clock
=FORMULA(asd_time,"R13C4")     and also as AM/PM
=FORMULA(IF(SSA,"CST","CDT"),"R13C5")     Specify CST (SK) or CDT (MB) for
local time - based on current study area (SSA T/F (if F: NSA))
=SELECT("R13C3")
=FORMAT.NUMBER("h:mm:ss")
=SELECT("R13C4")
=FORMAT.NUMBER("h:mm AM/PM")
=FORMULA(GMT_time,"R14C3")
=SELECT("R14C3")
=FORMAT.NUMBER("h:mm:ss")
=FORMULA(sza,"R15C3")
=FORMULA(solar_az,"R16C3")
=FORMULA(illum,"R17C3")
=FORMULA(target_desc,"R18C3")
=FORMULA(comments,"R19C3")
=SELECT("R25C3:R535C5")          Select ASD Raw Spectra & Panel Calibration BRFs
=EDIT.DELETE(1)    Delete, and shift cells left
=SELECT("R25C1:R535C1")          Select wavelength counters
=EDIT.DELETE(1)    Delete, and shift cells left
=FORMULA("Wavelength (Start)","R24C1")
=FORMULA("Reflectance","R24C2")
=SELECT("R25C1:R535C1")
=FORMAT.NUMBER("0.00")
=SELECT("R25C2:R535C2")
```

```
=FORMAT.NUMBER("0.000000")
=SELECT("R419C1:R535C2")        Select Wavelengths > 900 nm
=EDIT.DELETE(2)    Delete, shift cells up
=SELECT("R25C1:R65C2")  Select Wavelengths < 400 nm
=EDIT.DELETE(2)    Delete, shift cells up
=SELECT("R25C1")

=Set_Env(1)
Reflectance_filename=FREADLN(Batchfile)  Get name for output reflectance file (from
Batchfile)
=Error_Check(Reflectance_filename,2,2,ASD_Batchfilename)        Check for Batch File
I/O errors
=DIRECTORY(output_dir)
=SAVE.AS(Reflectance_filename,3)  Save results in new reflectance filename
=DIRECTORY(site_dir)
=Set_Env(1)


=Set_Env(1)
=ACTIVATE(Reflectance_filename)
=CLOSE(FALSE)      Close Reflectance file (no need to save changes)
=ACTIVATE(Target_filename)
=CLOSE(FALSE)      Close  file (don't save)
=ACTIVATE(Field_Panel_filename)
=CLOSE(FALSE)      Close  file (don't save)
=Set_Env(2)
=NEXT()        WHILE: process next set of spectra files
=NEXT()        FOR: process next batch file for given site
=NEXT()        WHILE: process next Site from Main Batch File
=Set_Env(1)
=DIRECTORY(home_dir)
=MESSAGE(TRUE,"Processing Complete")
=RETURN()


Error_Check   ~ display file name in error mesg...
=RESULT(6)
=ARGUMENT("Check_file",19)
=ARGUMENT("Check_type",1)
=ARGUMENT("Error_setting",1)
=ARGUMENT("Filename",2)
=Set_Env(1)
Bfile_eof=FALSE
=IF(ISERROR(Check_file))
=IF(Check_type=1,ALERT("1. File not found: "&Filename&" - HALTING MACRO"),)
=IF(Check_type=2,ALERT("2. Batch File: EOF or File I/O Error: "&Filename&" -
HALTING MACRO"),)
=IF(Check_type=3,ALERT("3. ERROR: Spectrum File - Open error ("&Filename&") -
HALTING MACRO"),)
=IF(Check_type=4,SET.NAME("Bfile_eof",TRUE),HALT())
```

```
=END.IF()
=Set_Env(Error_setting)
=RETURN(Bfile_eof)


Set_Env
=ARGUMENT("Env_Par",1)
=IF(Env_Par=1,ERROR(FALSE),)
=IF(Env_Par=2,ERROR(TRUE),)
=IF(Env_Par=3,CANCEL.KEY(FALSE))
=IF(Env_Par=4,CANCEL.KEY(TRUE))
=RETURN()
```

**Appendix A.6** Example output reflectance file from Excel Macro program.
This example is from IFC-3 SSA OJP, and contains the full header specification and information transferred to the RSS-19 central data archive for submission to the BOREAS on-line information system (BORIS) accessed by all BOREAS scientists.

**BOREAS DATA** - Understorey Reflectance Spectra

| | |
|---|---|
| BOREAS Project: | RSS-19 |
| PI: | John Miller |
| RSS-19 contact (this file) | Derek Peddle |
| Field Campaign: | IFC-3 |
| Field Instrument: | ASD Personal Spectrometer II |
| Panel Calibration: | Kodak White Card |

**REFLECTANCE DATA SPECIFICATIONS**

| | |
|---|---|
| Spectral Range: | 400-900 nm |
| Wavelength Step: | 1.4230 nm |
| Spectrum Description: | Average of 10 spectra; 10° FOV |
| Location: | SSA OJP Tower (G2L3T) |
| Latitude (°N): | 53.914 |
| Longitude (-°W; +°E): | -104.6925 |
| Date: | 9/13/94 |
| Time (Local): | 13:50:37 (1:50 PM) |
| Time (GMT): | 19:50:37 |
| Solar Zenith Angle (°): | 51.55 |
| Solar Azimuth (°): | 197.95 |
| Target Description: | LICHEN |
| Illumination: | SUNLIT |
| Comments: | PFL / CLEAR SKIES |

**REFLECTANCE DATA**

| Wavelength (Start) | Reflectance |
|---|---|
| 400.00 | 0.041 |
| 401.41 | 0.039 |
| 402.83 | 0.041 |
| 404.26 | 0.041 |
| :: | :: |
| :: | :: |
| 896.61 | 0.311 |
| 898.03 | 0.306 |
| 899.45 | 0.305 |
| 900.88 | 0.301 |

**Appendix B.** Geometric Optical Reflectance Model files

**Appendix B.1** Description of GOMS Interface Software

For each TF site, the program BAT_GOMS.C prompts the user to supply the necessary inputs to produce the spectral trajectory over the full range of tree densities. The current software interface is designed to produce a full trajectory for each TF site species in each spectral band (here, red and near infrared). The user is first prompted to enter the tree dimension and form parameters which describe the physical model geometry (Table 5.5) for the TF site species being considered. Then, the user is asked to enter the spectral end-member reflectance values for each component for that species for the spectral band being processed (Table 5.3). The program then computes the geometric form factors (Table 5.6) according to the tree dimension inputs. At this point, the software interface processes the input information for each tree density value along the spectral trajectory. At each spectral trajectory point the tree density value is multiplied by the square of the horizontal crown radius (r) to obtain the current model factor input value. For each trajectory point, these values (component reflectance and geometric factors) are output to a GOMS model format parameter file which is read by the model during program execution. This version of GOMS can also correct for topography, however as the BOREAS TF sites being modelled in this research are either flat or have very minor relief, values of zero slope and aspect were entered for all parameter files. The view and illumination angles are stored in a separate file (angles.dat) - these values are constant throughout all model runs. Examples of a GOMS parameter input file and the angle file are listed in this Appendix.

In addition to creating the full set of GOMS format input parameter files, the software interface program BAT_GOMS.C also produces a Unix system command shell file which directs batch mode execution of all the model runs. Each line of this system

command file (goms.bat, listed in this Appendix) contains the full command line specification to run the GOMS model software for the tree density being analysed for each trajectory point. Each command line specifies the GOMS program name (BRDF2.exe), the names of the input parameter file and the trajectory output filename (as generated by BAT_GOMS.C), the angle filename, and whether the model is to be run in forward or inverse mode.

After the software interface program has been run, the system command shell file is executed in either interactive shell or batch modes. The model runs rather efficiently for each trajectory point and therefore in this research the full set of model runs was performed in interactive shell mode (e.g. it took one minute to run the model 100 times to produce a full trajectory for one band, using a DEC-Server 5000 computer running the Ultrix operating system at the University of Waterloo). The output produced from the GOMS model runs includes the component fractions (C,B,S) for each tree density value analysed together with the overall reflectance value obtained. An example trajectory point output file produced by the GOMS model is listed in this Appendix.

One of the final commands in the shell file directs the operating system to combine all of the individual trajectory point output files into one large file for each spectral band per TF site species. A separate program (not listed in Appendix) reads the full set of these GOMS output files produced for all TF site species and for all spectral bands produced, extracts the pertinent output information, performs a variety of data reformatting tasks, and writes it into one large spectral trajectory file for input to the physically based landcover and biophysical software for subsequent processing.

## Appendix B.2 GOMS Interface Software

```
#include <stdio.h>

/*

Program: bat_goms.c

Author: Derek R. Peddle


This C program produces input files and Unix operating system
command files for running the Li-Strahler (1992) GOMS
reflectance model. This program can be used in any situation
where an extensive set of model runs is required. It is used
here for the computation of spectral trajectories over a
range of tree densities as part of the BOREAS project.

For each tree density value, the program creates a parameter
file and also updates the Unix command shell file. The Unix
command shell file created by this program is then executed
as follows using the Unix 'sh' command to evoke the multiple
runs of the GOMS model to produce the spectral trajectory.

% sh goms.bat

*/

float r, r2, td, b,h,dh,Pc,Pb,Ps, br,hb,dhb;
int  i, filec=0;

char output_filename[80], goms_outfilename[80],
par_filename[80];

FILE *par_file, *sh_file, *fopen();

main ()
{
/* open command shell batch file (% sh this file) */
sh_file = fopen ("goms.bat","w");  /* % sh */

/* Obtain user input of tree dimension and form parameters
     for TF site */

printf ("\n Horizontal crown radius (r) ?: ");
scanf ("%f",&r);
printf ("\n Vertical crown radius (b) ?: ");
scanf ("%f",&b);
printf ("\n Height to center of crown (h) ?: ");
```

```
scanf ("%f",&h);
printf ("\n Height distribution of trees: (dh) ?: ");
scanf ("%f",&dh);

/* Obtain end-member reflectance values for each component */

printf ("\n End-member reflectance for \n\t  Sunlit Canopy
(Component signature crown, Pc) ?: ");
scanf ("%f",&Pc);
printf ("\n End-member reflectance for \n\t  Sunlit
Background (Component signature Ground, Pb ?: ");
scanf ("%f",&Pb);
printf ("\n End-member reflectance for \n\t  Shadow
(Component signature shadow, Ps ?: ");
scanf ("%f",&Ps);

printf ("\n Output filename for GOMS output: ");
scanf ("%s",&goms_outfilename);

/* compute input factors from physical tree parameters */

r2 = r*r; /* multiplied by current lambda (td) value below */
br = b/r;
hb = h/b;
dhb = dh/b;

/* Produce spectral trajectory over range of tree density
(lambda) values. */

for (td=0.01; td <= 1.00; td+=0.01)   /* tree density */
{
++filec;

/* Create new output filename and parameter filename for
     current tree density value */

sprintf (output_filename,"fr%d.out",filec);
sprintf (par_filename,"goms%d.par",filec);

/* add next line to Unix command shell file.BRDF2.exe is the
GOMS executable file; angles.dat contains the view and
illumination data, and the model is run in forward mode */

fprintf (sh_file, "BRDF2.exe < angles.dat > %s -forward
-model %s\n", output_filename, par_filename);

par_file = fopen (par_filename, "w");

fprintf (par_file,"#ComponentSignaturesCrown:  %f\n",Pc);
fprintf (par_file,"#ComponentSignaturesGround: %f\n",Pb);
```

```
fprintf (par_file,"#ComponentSignaturesShade:  %f\n",Ps);
fprintf (par_file,"#Slope+SlopeAspect: 0.0  0.0\n");
fprintf (par_file,"#\n");
fprintf (par_file,"#Parameters:  lambda*r^2,  b/r,  h/b,
                  dh/b \n");
fprintf (par_file,"MutShadwTopo {\n");
fprintf (par_file,"    %8.6f        %8.6f         %8.6f
                  %8.6f\n",td*r2,br,hb,dhb);
fprintf (par_file,"}\n");

fclose (par_file);

}  /* for loops */

/* Add cat statement at end of command shell file to combine
all output into 1 large file*/

fprintf (sh_file,"cat ");
for (i=1; i<= filec; ++i) fprintf (sh_file,"fr%d.out ",i);
fprintf (sh_file," > %s\n",goms_outfilename);

/* remove intermediate files */
fprintf (sh_file," rm *.out\n");
fprintf (sh_file," rm *.par\n");


fclose (sh_file);
}
```

**Appendix B.3** GOMS model example input and output files; angles file, batch file, parameter file, output file

**angles.dat**

```
1 1
0.0 0.0 50.71 146.0
```

**goms.bat**

The file goms.bat is a batch file produced by running program bat_goms.c (Appendix B.1). Execution of the Unix shell file goms.bat directs the GOMS model runs for computing spectral trajectories. The GOMS model is run once for each point along a given spectral trajectory, resulting in a large number of model runs, as seen below.

Usage: A spectral trajectory is generated using a Unix operating system shell command (% sh) with input from the goms.bat batch file.

This file is run as follows:

```
% sh goms.bat
```

The contents of the goms.bat file are as follows:

```
BRDF2.exe < angles.dat > fr1.out -forward -model goms1.par
BRDF2.exe < angles.dat > fr2.out -forward -model goms2.par
BRDF2.exe < angles.dat > fr3.out -forward -model goms3.par
     :          :          :        :        :        :
BRDF2.exe < angles.dat > fr98.out -forward -model goms98.par
BRDF2.exe < angles.dat > fr99.out -forward -model goms99.par
BRDF2.exe < angles.dat >fr100.out -forward -model goms100.par

cat fr1.out fr2.out fr3.out ... fr97.out fr98.out fr9
9.out fr100.out  > ojp_red_asd.trj
 rm *.out
 rm *.par
```

The output file produced (in this case, ojp_red_asd.trj) contains the GOMS model fractions and reflectance values produced over the full range of tree densities based on the physical tree dimension parameters and component end-member reflectance values specified. The final two batch shell file commands remove all the intermediate parameter and individual model output files.

**goms99.par**

This is one of the 100 parameter files generated by bat_goms.c for input to the GOMS model runs, as directed by the goms.bat batch file. Each parameter file provides the end-member spectral reflectance values and canopy geometric form parameters, which are computed interactively in bat_goms.c for each tree density value.

```
#ComponentSignaturesCrown:  0.040000
#ComponentSignaturesGround: 0.198000
#ComponentSignaturesShade:  0.019000
#Slope+SlopeAspect: 0.0  0.0
#
#Parameters:  lambda*r^2,  b/r,  h/b,  dh/b
MutShadwTopo {
    1.425599        2.916667        3.160000    2.560000
}
```

**fr99.out**

GOMS model output file for one point along a spectral trajectory, for one spectral band, based on the inputs specified in the parameter file (goms99.par). The component fractions for C, B, and S, as well as the pixel level reflectance values computed by the model are labeled below the three output lines.

```
1 1
0.000000        0.000000        50.710000       146.000000
0.515029  0.000000        0.484971        0.029816

     ^          ^              ^              ^
     C          B              S          red reflectance
```

**Appendix C.** Theory of evidential reasoning and information about M⊕P software.

**Appendix C.1** Theory and Advantages of Evidential Reasoning

Conventional classification algorithms such as maximum likelihood and linear discriminant analysis have become standard components of many commercial image analysis systems. However, the expectations of these systems and algorithms have evolved and increased substantially in recent years as a result of new sensor developments, improved data characteristics, and the need to understand increasingly complex environmental phenomena which require the integrated analysis of multi-source remotely sensed imagery and other digital data sets. However, a number of problems have been encountered in using conventional image classification algorithms with these more modern data sets and complex applications. Firstly, multi-source data sets often contain information at different data scales of measurement (i.e. nominal, ordinal, interval, and ratio level data), or have properties such as directionality (e.g. terrain aspect, wind vectors), however, conventional classifiers can usually handle only ratio level data such as remote sensing imagery. Secondly, conventional classifiers typically rely on a parametric statistical model and therefore require input data to conform to a Gaussian (normal) distribution, however, high resolution imagery and multi-source data sets often do not satisfy this condition and are therefore not suited for parametric algorithms. Thirdly, these classifiers were not designed for the higher dimensionality of modern, hyperspectral image data sets. For example, maximum likelihood classifiers are usually not sufficiently robust to handle more than 7-10 input variables at a time. A fourth problem is that conventional algorithms do not have a method for explicitly handling information uncertainty, data inconsistencies, or errors, which sometimes occur at varying levels in an integrated, multi-source data set.

To address these problems, new approaches and algorithms are required such that the increased information content of modern data sets can be accessed, extracted, and used to help increase our ability to monitor and understand interesting and complex environmental issues. One such approach is based on the mathematical theory of evidence (Shafer, 1976) which has come to be known as evidential reasoning and which, from its general form, can be adapted for the task of image classification. Evidential reasoning provides a powerful framework for integrating and analysing distinct bodies of information

from independent sources without the restrictions imposed by the above mentioned problems. Although the theory of evidence was developed separately from remote sensing and has widespread application to any decision-making problem, it is appropriate to describe it here within the overall context of spatial data processing.

Given a set of input values, such as a multispectral or multi-source pixel, and a set of classes, the task of a digital classification algorithm is to assign the pixel to the proper class. In evidential reasoning theory, the set of classes constitutes a frame of discernment ($\Theta$) within which information processing is to occur, while information from the various data sources is regarded as individual pieces of evidence which must be combined to produce a final decision (pixel labeling). Associated with each piece of evidence is a numerical magnitude of support (s) and plausibility (p) (where $0 \leq s \leq 1$, $0 \leq p \leq 1$, and $s \leq p$), corresponding to the amount of evidence (or mass) in favour of a given class, and the mass which fails to refute that class, respectively (Shafer, 1976). The plausibility represents the upper probability or maximum possible evidence in favour of a proposition (Goldberg *et al.*, 1985), and is calculated as one minus the support for all other propositions (Shafer, 1976). In the context of a remote sensing classification, therefore, plausibility for class $C_i$ would be computed as:

$$p = 1 - s(\neg C_i) \tag{C.1}$$

where s and p represent evidential support and plausibility, respectively. The "true" likelihood of a proposition lies somewhere between its support and plausibility measures (Lee *et al.*, 1987). Utilisation of this range of information, termed the evidential interval of a mass (Garvey, 1987), provides a more realistic framework for representing the actual knowledge available upon which to make a decision. The uncertainty measure ($u_i$) for a given source is computed as the mass not ascribed to any class, and is necessarily assigned to $\Theta$ using the formula (Garvey *et al.*, 1981):

$$u_i = 1 - \sum m(A) \tag{C.2}$$

Once a mass has been computed for each value in a multi-source data pixel, the task remains to combine the evidence into a one dimensional format containing one measure of support per class. This is achieved by orthogonal summation using Dempster's Orthogonal Rule of Combination (Dempster, 1967). This powerful rule can be applied to any number of sources, each of which contains evidence over a set of classes. The orthogonal summation ($\oplus$) of evidence from two sources works by sequentially multiplying the evidence for a given class from one source by the evidence for each class from the other source. Each product of evidence for a given class is then normalised by the sum of the products obtained through multiplication of evidence from non-intersecting classes. The general form of the equation for computing the orthogonal sum of source 1 (with mass $m_1$ over a set of labels A) and source 2 (with mass $m_2$ over a set of labels B) to determine the mass $m'$ assigned to a labeling proposition C is computed using the equation:

$$m'(C) = K^{-1} \sum_{A_i \cap B_j = C} m_1(A_i) m_2(B_j) \tag{C.3}$$

where K is defined as:

$$K = 1 - \sum_{A_i \cap B_j = \phi} m_1(A_i) m_2(B_j) \tag{C.4}$$

The normalizing constant $K^{-1}$ corrects for any mass committed to the empty set ($\phi$), and also provides a measure of the extent of conflict between the two sources considered (Shafer, 1976). Orthogonal summation of additional sources is achieved by repeated application of these formulae. The final step in determining a pixel classification is the application of a decision rule to the resultant evidential mass from the orthogonal summation process. In this research, the decision rule is based on the maximum sum total of evidential support and plausibility values. This process of deriving evidence, orthogonal summation and applying the decision rule is repeated sequentially throughout an image or attribute table to complete a classification.

Note that in the mathematical theory of evidence, formal specifications are only provided for the computation of plausibility, uncertainty measures, and the pooling of evidence from all sources to provide one set of evidential mass from which to base a decision rule (classification). However, no formal specification is provided in the theory for generating the original support values, upon which the computation of plausibility, uncertainty, mass, and orthogonal summation, all are based. This is because of the generality of the theory of evidence. It assumes the data are either already in the form of evidential support, or that they can be rederived into the appropriate evidential framework for use with this technique. From the remote sensing perspective, this is a significant requirement, and much work in this area was required in the first implementation of this method to link the power of evidential reasoning to advanced image analysis. This issue is taken up in Chapter V, when the knowledge specification of trajectory inputs is described as part of a modified Knowledge Look-up Table (K-LUT) structure in software.

**Appendix C.2** Description of M⊕P software modules.

The M⊕P software package is divided logically into five modules, consistent with the MERCURY⊕ software package. The three main programs are: (i) M⊕P_USER.C, a user interface; (ii) M⊕P_TKLUT.C, which builds the trajectory and training knowledge look-up tables for storing and accessing evidence; and, (iii) M⊕P.C, the evidential reasoning program which performs the classification and also produces the trajectory output information. The files GLOBALS.H and FUNCTIONS.H contain variable declarations and a library of program functions accessed by different modules, respectively, however these program modules are not used directly by the user. The software is used by running the programs M⊕P_USER.C, M⊕P_TKLUT.C, and M⊕P.C in sequence. All necessary classification parameters are created through the user interface and stored in a data parameter file on disk (M⊕P_DATA.PAR) for input to both the M⊕P_TKLUT.C and M⊕P.C programs. The parameter file enables user selections to be archived for future use and reference, and also allows the software to be used in either interactive or batch mode. In the latter case, several different analyses can be run concurrently while not impeding interactive work.

In addition to its functionality with both image analysis systems and GIS, mentioned earlier, the software also runs in a variety of computing environments. Through use of C compiler preprocessing directives, the same version of code runs on the Unix, Ultrix, VAX/VMS, MS-DOS, and Apple MacOS operating systems, and is well suited for transport to others. In terms of available data formats and flexibility, the M⊕P program currently supports image format data such as 8-bit and 16-bit binary standard format data and PCI format imagery (PCI, 1993), as well as ASCII format attribute table data.

Another important part of any software system is the user interface. Often, regardless of the capability and ingenuity that any program may possess, if the link between the user and the program is poor the software will typically not be used to its full potential, and sometimes not at all. Considerable effort was put forth in the original MERCURY⊕ software package to provide a clear and informative user interface. It is based upon command line input for compatibility with operating systems that do not support graphical user interfaces (GUI). For the M⊕P update described here, the user interface has been substantially modified to encompass a variety of new functions and capabilities. As the source code for this is rather simple yet tedious, it is not included in the Appendix. Instead, an example user interaction sequence is provided in this Appendix showing the user inputs specified to run the M⊕P program in hybrid trajectory training mode which was used to generate one of the sets of results presented in the thesis.

The computer software upgrades required to create the M⊕P software package from the MERCURY⊕ programs resulted in significant changes to each of the five program modules described above. A number of these changes, while substantial in terms of effort and new code, dealt mostly with lower level functionality and modifications to the MERCURY⊕ code to accept new data formats, provide the required new user interaction sequencing, modify the training mode to be compatible with trajectory mode specifications (particularly for the Hybrid Mode option of the software), and to revise existing data structures to now work with spectral trajectory inputs. The latter two tasks were particularly extensive, however, since this work was directed mostly towards compatibility with an existing set of programs (MERCURY⊕), these updates and changes will not be presented here. Instead, the focus of this software presentation will be on the new code modules implemented specifically to provide the new functionality in "Full Trajectory

Mode", with reference made to the Hybrid Trajectory-Training Mode where appropriate. The new Trajectory Mode involved a separate data structure to be created and linked to the knowledge representation portion of the software (M⊕P_TKLUT.C), as well as additional coding in the M⊕P.C program to compute the trajectory position within a land cover stratification for determining the additional forest attribute outputs (tree density and component fractions). The following sections deal with these aspects of the M⊕P software upgrade.

**Appendix C.3** M⊕P processing sequence and knowledge representation.

In terms of the software code, the function of program M⊕P_KLUT.C is to first read the parameter file (M⊕P_DATA.PAR) to obtain information necessary for trajectory data input (e.g. number of classes and sources, trajectory filenames, formats etc.). It then builds the knowledge look-up table (K-LUT) by compiling the original frequency distributions of all trajectory data, and writes it to the disk file TA.KLT in ASCII format for subsequent input to the M⊕P.C program. Appendix C contains partial code listings of two main functions which perform these tasks. In these code listings, many of the details which pertain to program functioning have been removed, such that only the functionality that pertains to the actual processing of spectral trajectories is presented. The first function, 'allocate_klut_traj' creates a series of pointers to linked lists in memory for each source and each class being considered. Only the root node is created for each element of the circularly linked list, since the dynamic data structure grows in memory (i.e. allocates new memory locations) as required during program execution. This means that, unlike fixed size arrays, there is no upper limit to the number or type of data values that can be represented in the K-LUT. Each memory allocation includes the creation of a hash table, which is where the K-LUT values are actually stored. This permits fast, random access to the data structure, despite the unlimited amount of data that can be stored (as with any program, the system will be limited by the total amount of physical memory space available on a computer, which is usually only an issue with low-end personal computers). A detailed discussion of the memory management routines and dynamic linked list and hash table data structures used in this code is contained in Peddle (1995a,b) and is outside the scope of the present discussion, however, the scaled down functions provided in the appendix have been selected such that additional implementation details are accessible regarding the main functionality relevant to this discussion.

Once the appropriate sectors in memory have been allocated, function 'build_klut_traj' reads the input trajectory values from disk, calculates the proper position in the K-LUT, determines if new memory is needed or if existing memory cells containing the same value being added can be updated, and then inserts or updates the trajectory value into the K-LUT. The raw K-LUT is saved to disk prior to applying any bin transformations or weighting factors to the evidence. This is done so that the frequency distributions from trajectory data need only be computed once, from which any number of classifications could be performed (e.g. testing different bin sizes and source weights to refine a classification). In this way, trajectory data are also retained in a compact format suitable for the M⊕P software for future reference. In hybrid trajectory-training mode, the process is essentially run twice, whereby first the trajectory inputs are processed and input to the K-LUT, and then the supervised training data are read in, processed, and added to the K-LUT. Although the input data sets and formats are very different in each case, the original MERCURY⊕ source code was modified such that a consistent K-LUT format was possible for training and trajectory inputs, and that the two inputs could co-exist in spectral space. This approach was taken since, in hybrid mode, when classifying a given pixel its spectral reflectance values must be compared for evidential support and membership with respect to both training areas and spectral trajectory volumes.

**Appendix C.4** Example user interaction sequence for M⊕P software showing use of hybrid mode inputs for integrated land cover / physically based output. Entries made by the user are shown in bold.

% **M⊕P_USER.EXE**

---

Welcome to ...

M⊕P - Version 2.0.1

- MERCURY⊕ PHYSICAL -

M⊕P: An Integrated Multi-source Evidential Reasoning / Physically Based Image Processing System

Author: Derek R. Peddle 1996 (©)

---

**M⊕P: USER INTERFACE**

Select M⊕P Processing mode:

1. Full Supervised Training Classification Mode
2. Full Spectral Trajectory Classification/End-member Fraction Mode
3. Hybrid Training-Trajectory Mode

Enter Mode [1/2/3]: **3**

Enter Number of Data Sources: **2**

Enter Number of Classes: **13**

Enter Total Number of End-member Fractions and Additional Values
Associated with Reflectance Model Inputs to M+P: **4**

Enter Data Type for Training Data:

Image [i] or Attribute Table [a] -> [I/A]: **A**

Enter Type of Data to be Classified:

Image [i] or Attribute Table [a] -> [I/A]: **A**

Enter Attribute Table Training Area Data Filename: **SSA.TRN**

Enter Trajectory Filename: **SSA.TRAJ**

Use a given trajectory for more than one class ? [y/n]: **N**

Does any data source contain special missing data flags
or undefined data values ? [y/n]: **N**

Enter Name of Attribute Table Test File to be Classified: **SSA.TST**

Output File Type and Format...

Note: Output File Type set to ATTRIBUTE TABLE
to match the input data type being classified.

Enter Classification Output Filename: **SSA_ATB.OUT**

Do you want to Transform the Training Data

Distribution using Weighted Bin Functions? [y/n]: **Y**

The same bin size may be used for all sources,
or you may assign a different bin size for each source...

Note: The bin size must be an odd number.

Do you want to use the same bin size for all sources? [y/n]: **Y**

The bin transformation is only valid for Interval & Ratio
level data. You will now be asked to enter the data level of
each source, and the bin size you specify will only be
applied to those sources that have a valid data level.

Enter the bin size to be used for all valid sources: **121**

Enter the Data Level of Source Number 1 [N/O/I/R]: **R**
A bin size of 121 will be used for this source

Enter the Data Level of Source Number 2 [N/O/I/R]: **R**
A bin size of 121 will be used for this source

Do you want to assign weights to each source ? [y/n]: **N**

Your selections have been stored in the file M⊕P_DATA.PAR,
and will be read by programs M⊕P_TKLUT and M⊕P.

**Appendix C.5** Selected source code functions from M⊕P_KLUT.C

```
/*_____________________________________________________________*/

S_LIST *allocate_klut_traj (s)
S_LIST *s;
/* Create Trajectory Portion of Knowledge Look-up Table */

{
C_LIST *chead;

for (i=0; i < src_num; i++)
 {
  if (i==0)
            { if ( (s = (S_LIST *)
               malloc ((size_t)sizeof (S_LIST)) ) == NULL)
                                          memory_error ();
             shead = s;
            }

  else
            { if ( (s->sn = (S_LIST *)
               malloc ((size_t)sizeof(S_LIST)) ) == NULL)
                                          memory_error ();
              s = s->sn;
            }

  s->snum = i+1;
  s->bin_sz = 1;
  s->bf.d_lev = NOMINAL;

  s->bf.ud_data = s->bf.mi_data = s->bf.ud_inc
      = s->bf.mi_inc = FALSE;

  s->imin = s->imax = s->ud_val = s->mi_val = SMALL;

  /*set last link to point to head of circular list */
  s->sn = shead;

  for (j=0; j < cls_num; j++)
   {
    if (j==0) { if ( (s->c = (C_LIST *)
                malloc ((size_t)sizeof(C_LIST)) )  == NULL)
                                          memory_error ();
                chead = s->c;
               }
    else
               { if ( (s->c->cn = (C_LIST *)
                  malloc ((size_t)sizeof (C_LIST)) )== NULL)
                                          memory_error ();
```

```
                s->c = s->c->cn;
              }

    s->c->cnum = j+1;
    s->c->ta_size = s->c->no_bins = 0;

    /* last link points to head of circularly linked list */
    s->c->cn = chead;

    /* create first bucket of hash table data structure for
          each member of SPREAD */
    for (bk=0; bk < SPREAD; ++bk)
     {
      if ( (s->c->h[bk] = (H_LIST *)
                malloc ((size_t)sizeof (H_LIST)) ) == NULL)
                                              memory_error ();
      s->c->h[bk]->hn = NULL;
      s->c->h[bk]->key = SMALL;
      s->c->h[bk]->freq = s->c->h[bk]->d.wfreq = 0;

     } /* for bk */

   } /* for j */

    s->c = chead;  /* advance to head of list */

 } /* for i */

return (shead);

} /*end of function allocate_klut_traj */

/*_____________________________________________________________*/


S_LIST *build_klut_traj (s)
S_LIST *s;
/* This function reads the spectral trajectory information
     and loads it into the Knowledge Look-up Table (K-LUT) */
{
int x;
float rvalue, xr;
/* structures allocated & set up - ready to receive training
data */

/* tr_mode is >= HYBRID_TRAJECTORY, meaning that trajectory
data are to be included in (or to completely comprise) the
KLUT */
```

```
printf ("\n Building Trajectory Data into KLUT...\n");

while ( (value = get_data (traj_file, AT)) != EOF_FLAG )
{
  s = shead;

  /* current TJ record format is: site#, pixel#, line#, cls,
    fraction 1,fraction 2.. fraction_n, src1 src2... src_n.*/

  /* read Pixel, Line */
  for (i=1; i<=2;++i) x = get_data (traj_file, AT);

  cls = get_data (traj_file, AT);

  for (i=1; i<= num_traj_fr; ++i) x=get_data (traj_file, TJ);

  if ((cls < 0) OR (cls > cls_num))
   { printf ("\n\n Invalid class value: %d\n",cls);
     printf (" The specified valid class range is 0 to
              %d\n",cls_num);
     printf (" (where class 0 is unclassified)\n\n");

     printf(" Note: TRAJECTORY File Format...\n");
     printf("       The first 4 values of each line in the
                    Attribute Table\n");
     printf("       file should be: sample#, pixel#, line#,
                    class\n");
     printf("       followed by the model/fraction values,
                    and then src1 src2 ... src_n\n\n");
     printf("       Please ensure that this format is
                    supplied\n\n");
     printf (" \n\n Program execution terminated\n\n");
     exit (1);
   }

)

  if (cls == 0) for (i=0; i < src_num; ++i)
          x = get_data (traj_file, TJ);

  else   /* cls > 0: its a valid pixel */
   {
    for (i=0; i < src_num; ++i)
     {  /* find class node */
      if (cls != last_cls)
       {
        cls_pos = (cls > last_cls) ?
                cls-last_cls : cls_num-(last_cls-cls);

        /* advance pointer to correct position along
```

```
                circularly linked list */
          for (j=0; j < cls_pos; ++j) s->c = s->c->cn;

         }

        /* read next trajectory training value from file */
        value = get_data (traj_file, TJ);


        /* once linked list cell node position found, determine
             the hash table entry position for that node by
             computing a hashing function using the modulus
             division method */

        bk = value MOD SPREAD;
        if (bk < 0) bk = -bk; /* ensure bk is positive */

        if ( !
             (    ((s->bf.ud_data) AND (value == s->ud_val) AND
                   (!s->bf.ud_inc))
              OR
                  ((s->bf.mi_data) AND (value == s->mi_val) AND
                   (!s->bf.mi_inc))
             )
            )
               /* insert the value into the K-LUT, allocating new
                    memory as needed */

              s->c->h[bk] =
                    add_key (s->c->h[bk], value, 1, NO_WEIGHT);

        s = s->sn;

      }  /* for i=0 to < src_num */

     last_cls = cls;

    } /* end: else its a valid pixel */

} /* while value != EOF_FLAG; */

return (shead);

} /* end function build_klut_traj */

/*_____________________________________________________________*/
```

**Appendix C.6** Selected source code functions from M⊕P.C

```
/*_____________________________________________________________*/

void load_trajectory_LUT (traj_filename)
char traj_filename[80];
/* Load spectral trajectory data from file into Trajectory
   Look-Up Table (TLUT) */

{
short int trj_cls, x;
FILE *traj_file;

for (i=0; i<MAX_TRAJ_CLASSES; ++i)
 for (j=0; j<MAX_TRAJ_POINTS; ++j)
  {
    for (k=0; k<MAX_TRAJ_SOURCES; ++k)
          TLUT_spv[i][j][k]=SMALL;
    for (k=0; k<MAX_TRAJ_FRACTIONS; ++k)
          TLUT_fr[i][j][k]=SMALL;
  }

/* open trajectory input file (ATB format) */
if ( !( traj_file = fopen (traj_filename, "r")) )
   file_open_error (traj_filename,INPUT,0);


/* While not eof Trajectory file do */
while ((x = get_data (traj_file, AT)) != EOF_FLAG) /* ID */
 {
     pixel_num = get_data (input_file,AT);   /* pixel # */
     line_num = get_data (input_file, AT);   /* line # */

     trj_cls = get_data(traj_file, AT); /*Trajectory class */

     if ((trj_cls < 1) OR (trj_cls > cls_num))
      {
        printf ("\n\7 Error in Trajectory file -
                          class out of range \n\n");
        printf ("\n Program execution terminating \n\n\n");
        exit (1);
      }


  /* Search trajectory list for first unused point in this
          trajectory class */
  j = 0;
  while ((j<MAX_TRAJ_POINTS) AND
         (TLUT_spv[trj_cls][j][1] != SMALL)) j++;
```

```
   /* read fractions from trajectory file */

   for (k=1; k <= num_traj_fr; ++k)
      TLUT_fr[trj_cls][j][k] = get_real_data (traj_file, TJ);

   /* read spectral reflectance values from trajectory file */
   for (k=1; k <= src_num; ++k)
    TLUT_spv[trj_cls][j][k]= get_real_data (traj_file, TJ);


}  /* while not EOF traj_file */


printf ("\n======= TRAJECTORY INPUT COMPLETE  =========\n");

fclose (traj_file);

}

/*_____________________________________________________________*/


void analyse_trajectory_LUT (src, mcls)
short int src[MAX_TRAJ_SOURCES], mcls;
{
/* In this function the distance to each point on the
   specified class's trajectory is computed, and the closest
   (min _dist) trajectory point is found. The fraction values
   for this point are then written to the output file. This
   function is called once for each pixel that is classified.
   "src" is the array of values containing pixel DNs for
   current pixel, classified by M+P as being in class "mcls".
*/

float dist, diff, prev_dist, min_dist;
short int closest_pnt, ties=0;
int fr_100;
unsigned char c_fr;

/* use specified trajectory class for this class label
     (some trajectories are used for >1 classes */

if (tr_eq) mcls=tec[mcls]; /* trajectory equivalency class */

printf ("\n----- START OF ANALYSE TRAJECTORY LUT ----- \n");
```

```
if (mcls==0) /* no trajectory for class 0: output undefined*/

 {
  if (cl_dt == AT)
    for (k=1; k <= num_traj_fr; ++k)
        fprintf (output[0].o_file," -999");
  else
   if (cl_dt == IM)
    {
     for (k=1; k <= num_traj_fr; ++k)
      {
       c_fr = 0;
       c_fr &=255;  /* clear 8-bits */
       fprintf (output[k].o_file,"%c",c_fr);
      }
    }
 }

else

/* traverse trajectory for this class, compute distance to
     each point, and track proximity */
{
j=0;
min_dist = (float)BIG;
prev_dist = (float)SMALL;

while ( (j < MAX_TRAJ_POINTS)
     AND (TLUT_spv[mcls][j][1] != SMALL))
{
 if (j < MAX_TRAJ_POINTS)
   {
     /* compute Euclidean distance from input value to
      trajectory point j, using equation 5.10.
     (e.g. from src 1,2 to TLUT[mcls][j][1,2]  */

  dist = 0.0;
  for (k=1; k<=src_num; ++k)
   {
     diff = (float)src[k]-(float)TLUT_spv[mcls][j][k];
     dist += diff*diff;
   }
  dist = sqrt(dist);

  if (dist < min_dist)
    {
      ties = 0;    /* new closest point - reset tie count */
      prev_dist = min_dist;
      min_dist = dist;
      closest_pnt = j;
```

```
    }
   else
    if (dist == min_dist) ties ++;


 }

++j;


} /* while */



/* Note - class label output to file in main() */
if (cl_dt == AT)
 {
  for (k=1; k <= num_traj_fr; ++k)
   fprintf (output[0].o_file,"%d",
     TLUT_fr[mcls][closest_pnt][k]);

  if (ties>max_ties) max_ties = ties;
  tnum_ties += ties;
  a_ties[ties] +=1;
 }
else
 if (cl_dt == IM)
  {
  for (k=1; k <= num_traj_fr; ++k)
   {
    fr_100 = (int)(TLUT_fr[mcls][closest_pnt][k] * 100.0);
    c_fr = fr_100;
    c_fr &=255;
    fprintf (output[k].o_file,"%c",c_fr);
   }
  }

}


} /* end analyse_trajectory_LUT */

/*_____________________________________________________________*/
```

```
/*_____________________________________________________________*/

S_LIST *read_klut (s)
S_LIST *s;
/* Read the Knowledge Look-up Table containing training
     and/or trajectory inputs into the main M+P program */
{
FILE *klut_file;
s = shead;

if ( !(klut_file = fopen ("TA.KLT","r")) )
     file_open_error ("TA.KLT",INPUT,2);

for (i=0; i < src_num; ++i)
 {
  value = get_data (klut_file, KT);

  if (value != (i+1))
     printf ("\n Sources not in order in KLUT file...\n");

  for (j=0; j < cls_num; ++j)
   {
    value = get_data (klut_file, KT);
    if (value != (j+1))
     printf ("\n  Classes not in order in KLUT file...\n");

    while ( ((value=get_data (klut_file,KT)) != EOF_FLAG)
          AND (value != EOC_FLAG) )
     {
      bk = value MOD SPREAD;  /* compute hashing function */
      if (bk < 0) bk = -bk;

      dfreq = get_data (klut_file,KT);
      s->c->ta_size += dfreq;

      /* insert value into KLUT */
      s->c->h[bk] =
          add_key (s->c->h[bk], value, dfreq, NO_WEIGHT);

     } /* while */

    s->c = s->c->cn;  /* advance to next class */
   } /* for j*/

  s = s->sn;  /* advance to next source */

 } /* for i */

fclose (klut_file);
```

```
return (shead);

} /* end of read_klut */
/*_____________________________________________________________*/

S_LIST *bin_klut (s)
S_LIST *s;
/* Compute and apply the bin transformation function to the
     trajectory and/or training data stored in the K-LUT */
{
 short int value,low,high, v,wbk,wf, slot, rv, offset;
 H_LIST *slothead;

 for (i=0; i < src_num; ++i)
  {
  offset = s->bin_sz/2;
  if (s->bin_sz > 1)
   {
   for (j=0; j < cls_num; ++j)
    {
     for (bk=0; bk < SPREAD; ++bk)
      {
      slot = 0;
      while ( (s->c->h[bk] != NULL)
           AND (s->c->h[bk]->key != SMALL) )

       {
        if (slot++ ==0) slothead = s->c->h[bk];

        /* only process original values, but not those
           created during this bin expansion process */
       if (s->c->h[bk]->freq > 0)
       {
        value = s->c->h[bk]->key;

        /* do not apply bin transformation function to
          undefined or missing data values */

        if ( ((s->bf.ud_data) AND (value == s->ud_val)) OR
             ((s->bf.mi_data) AND (value == s->mi_val))    )
           {
             wf = s->bin_sz; /* do base value bin only */

              /* insert from start of list and apply
                     weighting factor (wf) */
             slothead = add_key(slothead, value,
                          s->c->h[bk]->freq*wf, WEIGHT);

             s->c->no_bins += s->c->h[bk]->freq;
           }
```

```
    else
    {
     low  = value - offset;
     high = value + offset;

     /* range value rv += skip */
     for (rv =low; rv <= high; ++rv)
      {
       /* compute weighting factor, in terms of proximity
            to key value using linear distance decay
            function */

       wf = s->bin_sz - (2 * abs(value-rv) );

       if ((s->bf.d_lev == INTERVAL)
            AND (s->imax > s->imin))

         {  if (rv < s->imin)
                 v = s->imax - (s->imin - rv) + 1;
            else if (rv > s->imax)
                 v = s->imin + (rv - s->imax) - 1;
            else v = rv;
         }
       else v = rv;

       wbk = v MOD SPREAD;
       if (wbk < 0) wbk = -wbk;

       if (wbk==bk)  /* insert from start of list, and
                        apply computed weighting factor to
                        evidence */
        slothead = add_key (slothead, v,
                        s->c->h[bk]->freq*wf, WEIGHT);
       else
        s->c->h[wbk] = add_key(s->c->h[wbk], v,
                             s->c->h[bk]->freq*wf,WEIGHT);

      } /* end: for rv = low to high */

     } /* end of: else not missing or undefined data */
    } /* end of: if h[bk]->freq > 0 */


    /* move to next slot in this bucket */
    s->c->h[bk] = s->c->h[bk]->hn;

   }    /* while */
  if (slot > 0) s->c->h[bk] = slothead;
  } /* for bk */
 s->c = s->c->cn;
```

```
    }       /* for j */
   } /* if s->bin_sz >1) */
  s = s->sn;
 }          /* for i */

return (shead);

} /* end bin_klut */

/*_____________________________________________________________*/

S_LIST *normalise_klut (s)
S_LIST *s;
/* normalise evidential support values in K-LUT to account
     for variations in sample size  */
{

 short int jj, bef, b, slot; /* bef - bin expansion factor */
 double tas,  /* ta size, adjusted by bin expansion factor */
        nws;  /* normalised & weighted support */

 float wgt;
 CI_LIST *citemp;
 H_LIST *slothead;

 ci = cihead;

 s = shead;

 if ((sw_flag) AND (same_sw)) citemp = cihead;

 for (i=0; i < src_num; ++i)
  {
   if (s->bin_sz > 1)
    {
      bef = 0;
      b = s->bin_sz - 2;

     while (b >= 1)  /* compute bin expansion factor */
      {
       bef += b;
       b -= 2;
      }
     bef = bef*2 + s->bin_sz + 1;
     /* +1: include original base frequency */

    } /* if bin > 1  */

   ci = cihead;
```

```
for (j=0; j < cls_num; ++j)
 {
  if (s->bin_sz > 1)
     {
       tas = (double)(s->c->ta_size * bef);

       if (s->c->no_bins > 0)
            tas = tas - (double) (s->c->no_bins * bef) +
                        (double) (s->c->no_bins *
                         (s->bin_sz + 1));

     }
  else tas = (double)s->c->ta_size;

  if (sw_flag)
   {
    if (same_sw)
    { if (j == 0)
            { wgt = (double)citemp->w->wgt;
              citemp->w = citemp->w->wn;
             }
            /* weight obtained for first class will be the
                 same for all classes for this source */
     }
    else  /* not same_source weight */
     {

      wgt = (double)ci->w->wgt;
      ci->w = ci->w->wn;  /* advance to next source */
     }
   } /* sw_flag */

  for (bk=0; bk < SPREAD; ++bk)
   {
   slot = 0;
   while ( (s->c->h[bk] != NULL)
            AND (s->c->h[bk]->key != SMALL) )
    {
     if (slot++ ==0) slothead = s->c->h[bk];

     /* include base freq into weighted frequency count */
     s->c->h[bk]->d.wfreq += s->c->h[bk]->freq;

     /* normalise support value by sample size for
            this class */
     nws = (double)s->c->h[bk]->d.wfreq / tas;

     /* adjust by user-specified weight */
```

```
        if ((sw_flag) AND (wgt < 1.0))  nws *= wgt;

        /* assign normalised & weighted support to nsup
                union field */
        s->c->h[bk]->d.n_sup = nws;

        /* advance to next slot in this bucket */
        s->c->h[bk] = s->c->h[bk]->hn;
       } /* while */

      if (slot > 0) s->c->h[bk] = slothead;
      } /* for bk */

    s->c = s->c->cn;  /* move to next class in KLUT */
    ci = ci->cin;  /* advance to class_info for next class */

   } /* for j */
 s = s->sn;

} /* for i */

return (shead);

} /* end normalise_klut */


/*_____________________________________________________________*/


int get_data (d_file, data_type)
FILE *d_file;
enum { IM, AT, KT, TJ } data_type;
/* Read training, trajectory, or image file data */
{
 unsigned char byte_value;
 int int_value, ib1,ib2,i16 ;
 char b1,b2;
 float real_value;

 if (data_type == TJ)
  {
   if ( (fscanf (d_file, "%f", &real_value) != EOF) )
     return (real_value);
   else
     return (EOF_FLAG);
  }
else
 if (data_type == IM)
  {
   if ((file_f == BINARY_IMG) OR (file_f == PCI_FORMAT))
```

```
    {
     if ( (fscanf (d_file, "%c", &byte_value) != EOF) )
      {
       int_value = byte_value;  /* convert byte to integer */
       int_value &= 255;        /* logical bit-wise AND with
                                   255 mask (low 8 bits set */
       return (int_value);
      }
     else return (EOF_FLAG);
    }
  else
   if (file_f == BINARY_IMG_16)  /* 16 bit data */

     if ( (fscanf (d_file, "%c%c", &b1,&b2) != EOF) )
      {
        i16 = ib1 = ib2 = 0;
        ib1 = b1 & 255;
        ib2 = b2 & 255;

        /* flag negative values in high order byte */
        if (ib1==255) ib1 = 0;

        i16 = ib1;
        i16 <<= 8;  /* Left shift high order byte */
        i16 |=ib2;  /* OR-in low order byte */

        if (factor > 0)
          i16 = (int) ((float)i16/(float)factor + 0.5);

        int_value = i16;
        return (int_value);
      }
     else return (EOF_FLAG);

  }

 else   /* AT or KT file type: integer */

 if ((data_type == AT) OR (data_type == KT))
  {
   if ( (fscanf (d_file, "%d", &int_value) != EOF) )
     return (int_value);
   else return (EOF_FLAG);
  }

}    /* end get_data */

/*_____________________________________________________________*/
```

**Appendix D.** BOREAS Biophysical Data

| BOREAS SITE ID | Landcover Class | Biomass kgC/m2 | LAI m2/m2 | DBH cm | Tree Height m |
|---|---|---|---|---|---|
| **OBS:** | | | | | |
| G2L7S | 1 | 1.41 | 2.30 | 9.80 | 4.10 |
| H1E4S | 1 | 3.66 | 6.91 | 5.90 | 2.80 |
| G6K8S | 1 | 4.00 | 4.89 | 15.40 | 15.90 |
| **G8I4T** | 1 | 4.71 | 5.55 | 7.10 | 10.25 |
| D0H6S | 1 | 5.22 | 6.81 | 15.00 | 15.80 |
| G2I4S | 1 | 7.47 | 11.72 | 7.80 | 6.10 |
| H2D1S | 1 | 7.53 | 10.59 | 20.10 | 18.10 |
| **OJP:** | | | | | |
| G8L6P | 2 | 0.62 | 0.27 | 4.70 | 3.70 |
| **G2L3T** | 2 | 3.02 | 1.23 | 12.90 | 14.56 |
| F5I6P | 2 | 3.75 | 1.63 | 10.50 | 12.00 |
| G7K8P | 2 | 3.99 | 1.60 | 22.40 | 14.40 |
| I2I8P | 2 | 4.77 | 3.49 | 11.50 | 11.30 |
| G9L0P | 2 | 5.70 | 2.25 | 22.50 | 18.10 |
| G4K8P | 2 | 5.98 | 2.26 | 28.40 | 19.90 |
| G1K9P | 2 | 6.03 | 2.34 | 24.40 | 18.60 |
| F7J1P | 2 | 9.02 | 4.63 | 23.00 | 24.20 |
| F7J0P | 2 | 10.42 | 8.78 | 25.10 | 20.20 |
| **MIX:** | | | | | |
| G4I3M | 3 | 8.68 | 9.74 | 46.60 | 32.60 |
| F1N0M | 3 | 8.69 | 7.88 | 30.50 | 23.40 |
| H2D1M | 3 | 11.62 | 12.97 | 31.20 | 23.30 |
| **OA:** | | | | | |
| D6L9A | 4 | 4.42 | 1.42 | 10.90 | 10.60 |
| D9I1M | 4 | 4.44 | 2.22 | 18.70 | 21.70 |
| D9G4A | 4 | 4.80 | 1.69 | 19.70 | 25.00 |
| E7C3A | 4 | 7.28 | 2.66 | 34.00 | 24.10 |
| B9B7A | 4 | 8.73 | 3.08 | 21.20 | 18.30 |
| **C3B7T** | 4 | 8.76 | 3.18 | 20.50 | 23.16 |

Biophysical ground data for BOREAS SSA for biomass, leaf area index (LAI), tree diameter at breast height (DBH), and tree height. Data grouped by land cover class from Tower Flux Sites (shown in bold) and Auxiliary Sites.

# GLOSSARY

Sorted by alphabetical theme.

*Agencies and Organisations*

| | |
|---|---|
| CCRS: | Canada Centre for Remote Sensing |
| CFS: | Canadian Forestry Service |
| NFC: | Northern Forestry Center (CFS, Edmonton) |
| NOAA: | National Oceanic and Atmospheric Administration, USA |
| NASA: | National Aeronautics and Space Administration, USA |
| GSFC: | NASA Goddard Space Flight Center (Greenbelt Maryland USA) |
| USRA: | Universities Space Research Association (GSFC) |
| ISTS: | Institute for Space and Terrestrial Science (Ontario) |

*Biophysical Parameters*

| | |
|---|---|
| BIO: | biomass |
| DBH: | tree diameter at breast height |
| HGT: | tree height |
| LAI: | leaf area index |
| NPP: | net primary productivity |

*Boreal Ecosystem Atmosphere Study (BOREAS)*

| | |
|---|---|
| AFM: | Airborne Flux and Meteorology |
| AUX: | Auxiliary site |
| BORIS: | BOREAS Information System (Internet) |
| FFC: | Focused Field Campaign |
| FFC-T: | FFC - Thaw |
| FFC-W: | FFC - Winter |
| HYD: | Hydrology |
| IFC: | Intensive Field Campaign |
| IFC-1: | Early Summer IFC |
| IFC-2: | Mid-summer IFC |
| IFC-3: | Late summer IFC |
| NSA: | Northern Study Area |
| OA: | Old Aspen |
| OBS: | Old Black Spruce |
| OJP: | Old Jack Pine |
| P.I.: | Principal Investigator |
| RSS: | Remote Sensing Science |
| SSA: | Southern Study Area |
| TE: | Terrestrial Ecology |
| TF: | Tower Flux science team / Tower Flux site |
| TGB: | Trace Gas Biogeochemistry |
| YJP: | Young Jack Pine |

*Geometric Optical Reflectance Models*

| | |
|---|---|
| b | vertical crown radius |
| CYL: | Cylinder model |
| dh | height distribution |
| GOMS: | Geometric Optical Mutual Shadowing model |
| h | height to center of crown |
| h:w | height:width ratio |
| r | horizontal crown radius |

*Global Change Programs and Projects*

| | |
|---|---|
| BOREAS: | Boreal Ecosystem Atmosphere Study |
| CGCP: | Canadian Global Change Program |
| COVER: | Characterization of Vegetation with Remote Sensing (NASA SNF field experiment) |
| FIFE: | First ISLSCP Field Experiment |
| IGBP: | International Geosphere Biosphere Program |
| ISLSCP: | International Satellite Land Surface Climatology Project |
| LBA: | Lambada / Baterista / Ambiace (Brazil, IGBP) |
| LTER: | Long Term Ecological Research program (USA) |
| MTPE: | NASA Mission to Planet Earth |
| NBIOME: | Northern Biosphere Observation and Modelling Experiment (Canada) |
| SNF: | Superior National Forest, Minnesota USA |
| USGCRP: | United States Global Change Research Program |

*Remote Sensing Terms, Instruments, and Techniques*

| | |
|---|---|
| ASAS: | Advanced Solid-state Array Spectrometer |
| ASD: | Analytical Spectral Devices, Inc - field spectrometer |
| AVHRR: | NOAA Advanced Very High Resolution Radiometer |
| AVIRIS: | Airborne Visible Infrared Imaging Spectrometer |
| CASI: | Compact Airborne Spectrographic Imager |
| EOS: | Earth Observing System |
| MAS: | MODIS Airborne Simulator |
| MMR: | Modular Multi-band Radiometer |
| MODIS: | Moderate Resolution Imaging Spectrometer |
| MSS: | Landsat Multi-Spectral Scanner |
| NDVI: | normalised difference vegetation index |
| NIR: | near infrared |
| PFL: | Portable Field Laboratory |
| SPOT: | System Pour L'observation de la Terre (France) |
| TM: | Landsat Thematic Mapper |
| TMS: | Thematic Mapper Simulator |

*Spectral Mixture Analysis*

| | |
|---|---|
| Rp: | pixel level reflectance |
| Rc: | sunlit canopy end-member reflectance |
| Rb: | sunlit background end-member reflectance |
| Rs: | shadow end-member reflectance |
| C: | sunlit canopy fraction |
| B: | sunlit background fraction |
| S: | shadow fraction |
| EM: | end-member |
| SMA: | spectral mixture analysis |

*Software*

| | |
|---|---|
| HYBRID: | hybrid trajectory training mode of M⊕P software |
| K-LUT: | Knowledge Look-up Table |
| MERCURY⊕: | Image processing software - Multi-source Evidential Reasoning Classification by Orthogonal Summation (⊕) |
| M⊕P: | MERCURY⊕ Physically-based software system |
| TRAJ: | trajectory mode of M⊕P software |
| TRN: | training mode of M⊕P software |
| ⊕ | mathematical symbol for orthogonal summation |